Robust analysis and optimization process for simulation-enhanced design of flexible aircraft

Marco Saporito

ONERA

THE FRENCH AEROSPACE LAB

UNIVERSITY OF SOUTHAMPTON

Faculty of Engineering and Physical Sciences
School of Aeronautics and Astronautics

Robust analysis and optimization process for simulation-enhanced design of flexible aircraft

by

Marco Saporito

MEng

ORCiD: 0000-0003-1975-2811

A thesis for the degree of
Doctor of Philosophy

April 2023

University of Southampton

Abstract

Faculty of Engineering and Physical Sciences
School of Aeronautics and Astronautics

Doctor of Philosophy

Robust analysis and optimization process for simulation-enhanced design of flexible aircraft

by Marco Saporito

A main challenge in modern aeronautics is to achieve disruptive design solutions for a greener and affordable aviation. One way towards this target is to increase aerodynamic efficiency through very high wing aspect ratios, involving lighter and flexible structures to reduce weight. A main obstacle in this path is to provide trustable predictions at the early design stage, where the conventional approaches fail due to insufficient knowledge, and limited room for high-fidelity analyses. Considerable progress has already been achieved by embedding more efficient, physics-based methods into the process. However, in most cases the effort of studying complex phenomena is not accompanied by an assessment of the inherent uncertainty. And yet, uncertainty can be critical especially in early design, as its negative realization in the advanced phases may produce serious consequences (such as the need to fully redesign the aircraft). The aim of this project is therefore to address this gap, by developing some suitable analysis tools in support of the conceptual design of highly flexible aircraft, with the capability of propagating some relevant uncertainty through the optimization process and finally provide information on the reliability of the results. To this end, we leverage physics-based simulation as the most complete source of information, capable of capturing non-linearities and complex disciplinary interactions typical of flexible airplane dynamics. The project is built around four objectives: 1) the development of a set of adequate models for aerodynamics, flight dynamics and structural dynamics; 2) the integration of the above modules with an aircraft sizing tool to broaden the design exploration capabilities by taking into account discipline-related uncertainty and constraints; 3) the expansion of the analysis capabilities and set of constraints by enabling coupled aero-structural analyses under uncertainty; 4) the demonstration of a robust design and optimization process for a highly flexible aircraft concept. After a detailed discussion of the background and relevant literature, this document continues presenting and discussing the development, validation and integration of the different analysis tools. Then, it introduces a first application where some of the analysis and

simulation capabilities are exploited for an aircraft multi-disciplinary design & optimization process, where uncertainty is allowed to be propagated into some key performance indices. A second, more complex architecture is subsequently presented, where static and dynamic aeroelasticity is taken into account, with and without uncertainty. Finally, some studies are performed demonstrating how the proposed framework can be successfully employed in a robust analysis and optimization process of high-aspect-ratio flexible aircraft. Conclusions and future perspectives are then elaborated in the final chapter.

Contents

List of Figures **ix**

List of Tables **xxi**

Declaration of Authorship **xxv**

Acknowledgements **xxvii**

Definitions and Abbreviations **xxxi**

1 Introduction **1**
1.1 Background . . . 2
1.2 Project outline, aim and objectives . . . 5
1.3 Thesis structure . . . 7

2 Literature review **9**
2.1 Overview . . . 10
2.2 Flight simulation at conceptual design . . . 13
2.2.1 Flying qualities constraints . . . 14
2.2.2 Flight simulation of flexible aircraft . . . 15
2.3 Sizing of high-aspect-ratio wings . . . 19
2.4 Dynamic aeroelasticity . . . 22
2.4.1 The flutter problem . . . 23
2.4.2 Dynamic gust loads . . . 25
2.4.3 Dynamic aeroelasticity for conceptual aircraft MDAO . . . 28
2.5 Multi Disciplinary Optimization . . . 32
2.5.1 Bayesian optimization and Efficient Global Optimization . . . 33
2.5.2 Super-Efficient Global Optimization . . . 36
2.6 Design under uncertainty: optimization, reliability, robustness . . . 37
2.6.1 General considerations . . . 37
2.6.2 Uncertainty Quantification and Sensitivity Analysis . . . 39
2.6.3 Monte Carlo and Quasi-Monte Carlo method . . . 41
2.6.4 Polynomial Chaos Expansion . . . 42
2.6.5 Applications in aircraft conceptual design . . . 43
2.7 Summary . . . 45

3 Formulation and analysis tools **47**
3.1 Overview . . . 48

3.2 Aerodynamics . . . 52
3.2.1 Linear derivative-based aerodynamics . . . 53
3.2.2 Linear unsteady strip theory . . . 55
3.2.3 The steady Vortex Lattice Method . . . 57
3.2.3.1 Theoretical background . . . 57
3.2.3.2 Applicability and limitations . . . 60
3.2.3.3 Validation of the VLM solver . . . 62
3.2.4 The Unsteady Vortex Lattice Method . . . 67
3.2.4.1 Theoretical background . . . 67
3.2.4.2 Validation of the UVLM solver . . . 69
3.2.5 Compressibility corrections . . . 75
3.3 Structural dynamics . . . 78
3.3.1 Linear beam Finite Element Model . . . 78
3.3.2 Nonlinear Geometrically-Exact Beam Theory (GEBT) . . . 80
3.4 Aeroelasticity . . . 82
3.4.1 Linear aeroelasticity by 1D-beam FEM and unsteady strip aerodynamics . . . 82
3.4.1.1 Discretized aeroelastic equations . . . 82
3.4.1.2 Validation . . . 84
3.4.2 Nonlinear aeroelasticity . . . 88
3.4.2.1 Fluid-structure interface . . . 89
3.4.2.2 Validation - static aeroelasticity . . . 95
3.5 Flight dynamics . . . 97
3.5.1 Validation of the flight dynamics module . . . 99
3.5.2 Coupling flight dynamics with VLM aerodynamics . . . 101
3.6 System identification for nonlinear systems . . . 107
3.7 Sensitivity analysis and uncertainty quantification approaches . . . 110
3.7.1 Problem definition and tool selection . . . 110
3.7.2 Validation - mathematical example . . . 111
3.8 Aircraft conceptual sizing and optimization . . . 112
3.9 Summary . . . 115

4 Aircraft MDAO under flying qualities reliability constraints 117
4.1 Overview . . . 118
4.2 Aerodynamics and flight dynamics . . . 121
4.3 Surrogate modelling of the aircraft sizing process and aerodynamic characterization . . . 124
4.4 Reliability constraints . . . 126
4.5 Optimization results . . . 128
4.6 Conclusions . . . 130
4.7 Summary . . . 131

5 MDAO framework for flexible transport aircraft 133
5.1 Overview . . . 134
5.2 Flexible wing sizing . . . 140
5.2.1 Initial sizing of a wing-box structure . . . 140
5.2.2 Beam model generation for aeroelastic analysis . . . 145

5.2.3 Sizing load case definition . . . 150
5.2.4 Static structural optimization of flexible wings . . . 152
5.2.4.1 Application and verification on the baseline test case . . 153
5.2.4.2 Application on high aspect ratio wing . . . 159
5.2.5 Consistency against overall aircraft sizing . . . 164
5.3 Dynamic aeroelastic constraints under uncertainty . . . 168
5.3.1 Deterministic flutter speed on low and high aspect ratio configurations . . . 170
5.3.2 Sensitivity of flutter speed with respect to aeroelastic parameters 175
5.3.2.1 Problem definition . . . 178
5.3.2.2 Application to the baseline and the high aspect ratio test-cases . . . 181
5.3.3 Dynamic gust response . . . 187
5.3.3.1 Implementation of specifications requirements . . . 188
5.3.3.2 Deterministic loads on low and high aspect ratio configurations . . . 190
5.3.4 Sensitivity of gust loads to aeroelastic parameters . . . 197
5.3.4.1 Problem definition . . . 197
5.3.4.2 Application to the baseline and the high aspect ratio test-cases . . . 198
5.4 Summary . . . 205

6 Robust MDAO studies 207
6.1 Overview . . . 208
6.2 Rigid aircraft optimization . . . 209
6.3 Deterministic MDAO results . . . 214
6.3.1 Optimization under flutter constraint only . . . 214
6.3.2 Optimization under gust loads constraints only . . . 219
6.3.3 Optimization under flutter and gust loads constraints . . . 225
6.4 Robust MDAO results . . . 231
6.4.1 Optimization under flutter reliability constraint only . . . 232
6.4.2 Optimization under gust loads reliability constraints only . . . 238
6.4.3 Optimization under flutter and gust loads reliability constraints . 245
6.5 Results review and discussion . . . 251
6.6 Conclusions . . . 261
6.7 Summary . . . 263

7 Conclusions 265
7.1 Thesis summary . . . 266
7.2 Achievements . . . 268
7.2.1 Tools development, integration and validation . . . 268
7.2.2 Application: MDAO of rigid aircraft under flying qualities reliability constraints . . . 270
7.2.3 MDAO framework for the design of flexible aircraft under uncertainty . . . 271
7.2.4 Application: MDAO of flexible aircraft under aeroelastic reliability constraints . . . 271
7.3 Perspectives . . . 273

7.3.1 Possible improvements and future work 273
7.3.2 Flight simulation of very flexible aircraft 274

Appendix A Unsteady strip theory formulation 277
Appendix A.1 Expressions for unsteady lift and moment 278
Appendix A.1.1 Contribution of aerofoil pitch-plunge motion 278
Appendix A.1.2 Contribution of flap rotation 278
Appendix A.1.3 Contribution of gust encounter 279
Appendix A.2 Transformation of Integro-Differential Equations into Ordinary Differential Equations 279
Appendix A.3 Total aerodynamic loads 279
Appendix A.3.1 Aerodynamic variables 282
Appendix A.3.2 Formulation of discretized aerodynamics 283
Appendix A.3.3 Unsteady aileron hinge moment 284

Appendix B Verification of the surrogate modelling approach 287

Appendix C Initial analytical sizing of the main wing-box components 291
Appendix C.1 Skin sizing 292
Appendix C.2 Web sizing 292
Appendix C.3 Stringers sizing 293
Appendix C.4 Ribs sizing 293
Appendix C.5 Reinforcements and secondary parts 294

Appendix D Numerical methods for solving nonlinear equations 295
Appendix D.1 Classic chord method 296
Appendix D.2 Regula falsi method 296

References 299

List of Figures

1.1 Examples of unconventional aircraft concepts featuring highly-efficient wing configurations. . . . 2
1.2 Traditional vs integrated design approaches (adapted from [1]). . . . 4
1.3 Integrated multidisciplinary design process versus traditional design process. When decisions are made earlier, they can have a high impact at a relatively low cost (from [2]). . . . 5

2.1 Uncertainty in multidisciplinary flight vehicle modeling, from [3]. . . . 11
2.2 Design Process Paradigm Shift, from [4]. . . . 12
2.3 Short-period characteristics predicted during sizing and optimization loops in SDSA, plotted against the specification categories (from [5]). . . . 15
2.4 Spiral trajectory predicted by three different levels of fidelity, for three different stiffness parameter values (σ =4, 10 and 50), from [6]. . . . 17
2.5 Relative error of linearized and mean-axes models with respect to fully-coupled nonlinear model with varying stiffness prameter σ, from [6] . . 17
2.6 Comparison of responses to lateral controls with three levels of fidelity, from [7]. . . . 18
2.7 Wing-box cross section idealization used in [8]. . . . 21
2.8 Effects of linear and nonlinear structural models on overall aircraft figures of merit, from [8]. . . . 22
2.9 Superposition of manoeuvre and gust envelopes, from [9]. . . . 25
2.10 Typical '1-Cosine' design gust velocity profiles, from the FAA Advisory Circular 25.341-1 [10]. . . . 28
2.11 Variations of optimum fuel burn and maximum take-off weight with specific allowable stress and effects of a flutter constraint in the loop (from [11]). . . . 30
2.12 Examples of gust encounter setups for dynamic aeroelastic simulations, as implemented in the MDO framework proposed in [12, 13]. . . . 32
2.13 Illustration of the Bayesian optimization mechanism, from [14]. The top figure shows the Gaussian Process regression of a 1D function in terms of mean (solid line) and 95% confidence interval (dashed envelope). The model is derived after three function evaluations, indicated by blue circles. The bottom figure plots the associated Expected Improvement acquisition function. The point that maximizes the EI (represented by an 'x') is selected for the next objective function evaluation. . . . 34
2.14 Different possible design and optimization approaches in presence of uncertainty, from [15]. . . . 39

3.1 Generic XDSM[1]scheme representing the overall structure of the present framework for robust design and optimization under reliability constraints. The specific disciplinary blocks to be included and the list of inputs and outputs will depend on the particular study to be performed. The structure can slightly change accordingly. 51
3.2 Typical format of aerodynamic database, from [5]. 54
3.3 Mean-line of the aerofoil. ϑ and h denote pitch and plunge, respectively. 56
3.4 Horseshoe vortex lattice model for a lifting-line problem, from [16]. . . . 59
3.5 Vortex ring model for the VLM, from [16]. 60
3.6 Interactive Boundary Layer iterative procedure, from [17]. 61
3.7 Geometrical issue with panel discretization, from [16]: all four corner points of a surface panel seldom lay in the same plane. 62
3.8 Panel discretization for wake rollup, from [16]. 62
3.9 Iteration loop with or without boundary layer calculation and wake shape calculation, from [17]. 63
3.10 Predictions from the two solvers of the variation of the flat wing pitching moment coefficient C_m against sweep angle. 64
3.11 Comparison between a horizontal wing with angle of attack $\alpha = 3°$ and the same wing in vertical position with sideslip angle $\beta = 3°$, for validation of the side force coefficient. 65
3.12 Panel models with pressure coefficient distribution from the two compared solvers. Main wing: sweep angle $\lambda_S = 10°$, dihedral angle $\gamma_D = 10°$. Tail: span $b_H = 5$ m, chord $c_H = 1$ m, tilt angle $\tau_H = -3°$, root leading edge distance from main wing root leading edge $d = 6$m. Angle of attack $\alpha = 2°$, sideslip angle $\beta = 2°$. 66
3.13 Panel models with pressure coefficient distribution from the two compared solvers. Main wing: sweep angle $\lambda_s = 0°$, dihedral angle $\gamma = 10°$. Horizontal tabiliser: span $b_h = 5$ m, chord $c_h = 1$ m, tilt angle $\tau_h = -3°$. Fin: span $b_f = 3.5$ m, chord $c_h = 1$ m. Angle of attack $\alpha = 2°$, sideslip angle $\beta = 2°$. 67
3.14 Validation of the UVLM solver. Lift coefficient of 3D thin wings of different aspect ratios in sudden forward motion. The simulated conditions correspond to $\alpha = 5°$ and $V\Delta t/c = 1/16$. Comparison against data from [16]. 70
3.15 Validation of the UVLM solver. Time history of lift coefficient of a 3D wing in sinusoidal plunging motion for three reduced frequencies. $\mathcal{AR}$= 4, $h = \infty$, $\alpha = -5°$. Comparison against data from [16]. 70
3.16 Validation of the UVLM solver. Lift coefficient of a 2D thin profile in harmonic plunging oscillations, for three reduced frequencies. Comparison against the theoretical model of Theodorsen [18], data from [19]. 71
3.17 Validation of the UVLM solver. Flapping wing test-case. 72
3.18 Validation of the UVLM solver. Flapping wing at $k = 0.1$. Comparison against data from Murua [19]. 73
3.19 Validation of the UVLM solver. Qualitative comparison of contour plots of the wake circulation Γ_{wake} for the flapping wing test-case. Reduced flapping frequency $k = 0.1$. The reference figure (a) shows only the last flapping cycle, whereas the present model (b) reports one additional cycle, showing that the conditions are already practically stationary, with no visible transient effects from one cycle to the other. 73

3.20 Validation of the UVLM solver. Flapping wing at $k = 0.75$. Comparison against data from Murua [19]. 74
3.21 Validation of the UVLM solver. Qualitative comparison of contour plots of the wake circulation Γ_{wake} for the flapping wing test-case. Reduced flapping frequency $k = 0.75$. The reference figure (a) shows only the last flapping cycle, whereas the present model (b) reports two additional cycles, showing that the conditions are already practically stationary, with no visible transient effects from one cycle to the other. 75
3.22 Equivalent straight and swept planforms obtained by the Prandtl-Glauert transformation, from [20]. 77
3.23 Beam coordinate system. 79
3.24 Representative layout and discretization for the linear aeroelastic model. The real wing in grey is represented by a flat surface, discretized in N 2D strips (blue). Each strip undergoes pitch and plunge motion according to the structural deformation. No interaction (crossflow) exists among the different wing sections. Only the main wing is modeled. 82
3.25 Schematic representation of a free wing-fuselage system experiencing aeroelastic oscillations, from [20]. 85
3.26 Planform, discretization, and mass distribution for the test-case in [20]. . 85
3.27 Time response of the root bending moment per unit gust amplitude following a sharp-edged gust. The curves are compared with those reported in [20]. 86
3.28 Evolution of the first 5 modal frequencies with air speed for the Goland wing. A red vertical line marks the speed at which the flutter instability is reached. 87
3.29 Evolution of the first 5 modal damping ratios with air speed for the Goland wing. A red vertical line marks the speed at which the flutter instability is reached. 87
3.30 Evolution of the first 6 modal frequencies with air speed for the Patil wing. A red vertical line marks the speed at which the flutter instability is reached. 88
3.31 Evolution of the first 6 modal damping ratios with air speed for the Patil wing. A red vertical line marks the speed at which the flutter instability is reached. 89
3.32 Visualization of the aeroelastic model for the Patil wing. Overview showing the undeformed aerodynamic mesh (grey), the deformed one, including the wake (black), the beam model with the additional auxiliary nodes (red), and the aerodynamic forces acting on the deformed wing (blue arrows). 92
3.33 Visualization of the aeroelastic model for the Patil wing. Overview showing the pressure coefficient distribution over the deformed wing. 93
3.34 Visualization of the aeroelastic model for the Patil wing. Detail view showing the aerodynamic forces (blue) generated in the aerodynamic domain (black) and the equivalent forces transferred to the structural domain (red). 93

3.35 Visualization of the aeroelastic model for the Patil wing. Detail view showing the wing geometry (thick black lines), the vortex lattice discretization (thin grey lines), the VLM collocation points (represented by an 'x') and the aerodynamic forces (blue), applied at the midpoint of the leading vortex line of each vortex ring. 94
3.36 Validation of the present nonlinear aeroelastic model: spanwise vertical displacement of the Patil wing's elastic axis, compared against data from [21] and [22]. 96
3.37 Validation of the present nonlinear aeroelastic model: spanwise twist of the Patil wing, compared against data from [21] and [22]. 96
3.38 Evolution of angle of attack and elevation due to an elevator doublet of amplitude $\delta_e = \delta_{e_0} \pm 2.0°$, with $\delta_{e_0} = -9.2184°$ performed between 1.0 and 2.0 seconds. 99
3.39 Evolution of angle of attack and elevation due to a throttle doublet of amplitude $\Delta T/T = \pm 0.1$ performed between 1.0 and 7.0 seconds. 100
3.40 Evolution of angle of attack due to step aileron actuation δ_a, starting from a pitch-down initial condition with elevator deflection set to $\delta_e = 2.0°$. . 101
3.41 Evolution of sideslip angle due to step aileron actuation δ_a, starting from a pitch-down initial condition with elevator deflection set to $\delta_e = 2.0°$. . 101
3.42 Evolution of roll rate due to step aileron actuation δ_a, starting from a pitch-down initial condition with elevator deflection set to $\delta_e = 2.0°$. . . 102
3.43 Single wing test-case, from [23]. The CG position is identified by the $*$ symbol. The figure has a representational purpose only, and the contour plot does not provide any relevant information. 103
3.44 Evolution of pitch angle of the free-to-pitch wing due to an initial condition of $\theta = 5$ deg. Validation against data from [23]. 104
3.45 Two-wing conventional glider 105
3.46 Two-wing conventional glider test-case, from [23]. The figure has a representational purpose only, and the contour plot does not provide any relevant information. 105
3.47 Evolution of pitch angle of the glider configuration due to an initial condition of $\theta = 5$ deg. Validation against data from [23]. 106
3.48 Example curve fitting of a 4th-order oscillator function via the Prony method. 109
3.49 Comparison of the PDF obtained with the present approach against data from [24]. 112
3.50 Structure of the `FAST-OAD` overall aircraft design suite, from [25]. 114

4.1 CeRAS baseline planform, from [26]. 119
4.2 Framework for aircraft multidisciplinary design and optimization under reliability constraints. 121
4.3 Identification of lift coefficient time history under forced pitch oscillations. 123
4.4 Snapshot during unsteady simulation of the CeRAS A320 baseline, run with the present UVLM solver. 124
4.5 Example of aerodynamic responses to pitch oscillations and their identification via linear derivatives. 125

4.6 Framework for robust design and optimization under reliability constraints, where the aircraft sizing, aerodynamic and flight dynamic modules are replaced by a surrogate model. 126
4.7 Thumb print criterion reporting the pilot opinion contours related to the short period characteristics. The dashed red lines show the bounds used in this work. 127
4.8 Validation of the PCE approach for a reference configuration ($t_{rW} = 0.3$, $\Lambda_W = 25°$, $t_{rT} = 0.28$, , $\Lambda_T = 28°$). 128
4.9 Monitor plot of the DOE runs and optimization history. 129
4.10 Radar plot summarizing all the evaluations during the DOE and the optimization iterations. 130

5.1 Extended design structure matrix of the present MDAO framework for aeroelastic sizing and fuel burn optimization of a transport aircraft. Deterministic approach. 138
5.2 Extended design structure matrix of the present MDAO framework for aeroelastic sizing and fuel burn optimization of a transport aircraft. Probabilistic approach. 139
5.3 Cross section idealization adopted in this work. 141
5.4 Cross section idealization used in [8]. 141
5.5 Cross section idealization used in [27]. 142
5.6 Wing primary structure idealization and loads partitioning, as proposed in [27]. 142
5.7 Spars and elastic axis location on the baseline wing planform. 143
5.8 View of the 3D wing-box idealization adopted in this work. The particular example is from a kinked $\mathcal{AR}$ 15 wing configuration. 143
5.9 Span-wise distributions of the beam stiffness properties derived for the CeRAS baseline wing. The out-of-plane bending stiffness EI^{A}_{yy} and torsional stiffness GJ are plotted in (a), whereas the in-plane bending stiffness EI^{A}_{zz} is shown in (b). 148
5.10 Verification of the computed span-wise distributions of the out-of-plane and in-plane bending stiffness (EI^{A}_{yy} and EI^{A}_{zz}, respectively) for an $\mathcal{AR}$ -18 wing. The comparison is against data from [8]. 149
5.11 3D views of the aeroelastic model employed, showing both the VLM discretization and the beam model, including the auxiliary structural points needed for the fluid-structure interpolation. 151
5.12 Flexible wing structural optimization process under static loads constraints over the CeRAS baseline configuration. Evolution of the current best wing mass objective function (a) and the corresponding static loads constraints (b) through the SEGOMOE optimization iterations. 155
5.13 Flexible wing structural optimization process under static loads constraints over the CeRAS baseline configuration. Evolution of the current best variables through the SEGOMOE optimization iterations. 156
5.14 Flexible wing structural optimization process under static loads constraints over the CeRAS baseline configuration. Monitor plot of the wing mass objective function (a) and the corresponding static loads constraint (b) through the SEGOMOE optimization iterations. 157

5.15 Flexible wing structural optimization process under static loads constraints over the CeRAS baseline configuration. Monitor plot of the design variables through the SEGOMOE optimization iterations. 158
5.16 Wing structural mass buildup for the CeRAS baseline. Three sets of data are compared: the FEM data for the initial guess structural layout (blue), the FEM data for the optimal structural layout (red) and the estimation for the rigid aircraft by FAST-OAD (green). 158
5.17 Flexible wing structural optimization process under static loads constraints over the '$\mathcal{AR}$ 15' configuration. Evolution of the current best wing mass objective function (a) and the corresponding static loads constraints (b) through the SEGOMOE optimization iterations. 160
5.18 Flexible wing structural optimization process under static loads constraints over the $\mathcal{AR}$ 15 configuration. Evolution of the current best variables through the SEGOMOE optimization iterations. 161
5.19 Flexible wing structural optimization process under static loads constraints over the $\mathcal{AR}$ 15 configuration. Monitor plot of the wing mass objective function (a) and the corresponding static loads constraint (b) through the SEGOMOE optimization iterations. 162
5.20 Flexible wing structural optimization process under static loads constraints over the $\mathcal{AR}$ 15 configuration. Monitor plot of the design variables through the SEGOMOE optimization iterations. 163
5.21 Wing structural mass buildup for the $\mathcal{AR}$ 15 configuration. Three sets of data are compared: the FEM data for the initial guess structural layout (blue), the FEM data for the optimal structural layout (red) and the estimation for the rigid aircraft by FAST-OAD (green). 163
5.22 Highlight from the overall XDSM scheme of Figure 5.1. Detail of the iterative aeroelastic sizing approach, designed to ensure consistency between the wing mass W_{w1}, considered in the overall aircraft sizing, and the wing mass optimized to sustain the prescribed aeroelastic loads, W_{w2}. The design is considered consistent when the two values differ by less than 2%. 166
5.23 Sizing and optimization iterations for an aircraft configuration with $\mathcal{AR} = 17.6$, $t_r = 0.34$ and $k_{sr} = 0.33$. The traced quantities correspond to the wing empty weight estimated by FAST-OAD (W_{w1}), by the initial guess, and by the aeroelastic structural optimization (W_{w2}). 167
5.24 Sizing and optimization iterations for an aircraft configuration with $\mathcal{AR} = 19.1$, $t_r = 0.30$ and $k_{sr} = 0.26$. The traced quantities correspond to the wing empty weight estimated by FAST-OAD (W_{w1}), by the initial guess, and by the aeroelastic structural optimization (W_{w1}). 168
5.25 Sizing and optimization iterations for an aircraft configuration with $\mathcal{AR} = 19.6$, $t_r = 0.32$ and $k_{sr} = 0.27$. The traced quantities correspond to the wing empty weight estimated by FAST-OAD (W_{w1}), by the initial guess, and by the aeroelastic structural optimization (W_{w1}). 168
5.26 Evolution of the first 10 modal frequencies with air speed for the CeRAS wing model. A red vertical line marks the speed at which the flutter instability is reached. 173
5.27 Evolution of the first 10 modal damping ratios with air speed for the CeRAS wing model. A red vertical line marks the speed at which the flutter instability is reached. 173

5.28 Evolution of the first 10 modal frequencies with air speed for the '$\mathcal{AR}$ 15' wing model. A red vertical line marks the speed at which the flutter instability is reached. 175
5.29 Evolution of the first 10 modal damping ratios with air speed for the '$\mathcal{AR}$ 15' wing model. A red vertical line marks the speed at which the flutter instability is reached. 175
5.30 First six wing structural modes of the baseline configuration. The red line identifies the elastic axis. The reported frequencies correspond to flutter speed. Each shape is scaled freely in order to give a better visual understanding. 176

5.31 First six wing structural modes of the '$\mathcal{AR}$ 15' configuration. The red line identifies the elastic axis. The reported frequencies correspond to flutter speed. Each shape is scaled freely in order to give a better visual understanding. 177

5.32 Flutter speed Probability Distribution Function following the uncertainty propagation on the baseline test-case. The area shed in red indicates the imposed flutter-safe region: the probability of flutter occurring within this region should be lower than 5%. The baseline results robust enough with respect to such condition. 184
5.33 Main statistical and sensitivity indices from the flutter sensitivity analysis on the baseline configuration. 184
5.34 Flutter speed distribution following uncertainty propagation on the '$\mathcal{AR}$ 15' test case. The area shed in red indicates the imposed flutter-safe region: the probability of flutter occurring within this region should be lower than 5%. This configuration does not appear to be robust enough with respect to such condition. 186
5.35 Main statistical and sensitivity indices from the flutter sensitivity analysis on the aspect ratio 15 configuration. 186
5.36 Example of gust profiles used for preliminary studies on dynamic gust response. 189
5.37 Bending stress responses to discrete gusts from the baseline test case. . . 190
5.38 Vertical shear stress responses to discrete gusts from the baseline test case. 190
5.39 Torsional shear stress responses to discrete gusts from the baseline test case. 191
5.40 Bending stress responses to discrete gusts from the aspect ratio 15 test case. 192
5.41 Vertical shear stress responses to discrete gusts from the aspect ratio 15 test case. 192
5.42 Torsional shear stress responses to discrete gusts from the aspect ratio 15 test case. 193
5.43 Bending stress responses to discrete gusts from the empty weight baseline test case. 194
5.44 Vertical shear stress responses to discrete gusts from the empty weight baseline test case. 194
5.45 Torsional shear stress responses to discrete gusts from the empty weight baseline test case. 195
5.46 Bending stress responses to discrete gusts from the empty weight aspect ratio 15 test case. 195

5.47 Vertical shear stress responses to discrete gusts from the empty weight aspect ratio 15 test case. 196
5.48 Torsional shear stress responses to discrete gusts from the empty weight aspect ratio 15 test case. 196
5.49 Gust loads distributions following uncertainty propagation on the CeRAS baseline wing. The area shed in red indicates the imposed safe region: the probability of loads occurring within this region should be lower than 5%. The baseline results robust enough with respect to all constraints. 200

5.50 Main statistical figures from the sensitivity analysis and uncertainty quantification on the gust-induced loads at wing root for the CeRAS baseline wing. 201

5.51 Gust loads distributions following uncertainty propagation on the '$\mathcal{AR}$ 15' wing. The area shed in red indicates the imposed safe region: the probability of loads occurring within this region should be lower than 5%. This configuration does not result robust enough with respect to the bending loads. 203

5.52 Main statistical figures from the sensitivity analysis and uncertainty quantification on the gust-induced loads at wing root for the '$\mathcal{AR}$ 15' wing. . 204

6.1 Optimization process using the conventional FAST-OAD approach. Monitor plot of the fuel mass objective function through the SEGOMOE optimization iterations. 211
6.2 Optimization process using the conventional FAST-OAD approach. Monitor plot of the three design variables through the SEGOMOE optimization iterations. 212
6.3 Optimization process using the conventional FAST-OAD approach. Evolution of the current best fuel mass through the SEGOMOE optimization iterations. 212
6.4 Optimization process using the conventional FAST-OAD approach. Evolution of the current best design variables through the SEGOMOE optimization iterations. 213
6.5 Best wing planform from the unconstrained rigid aircraft optimization. The baseline wing planform is also reported for comparison. 213
6.6 MDAO process for flexible aircraft under deterministic constraint on flutter speed. Monitor plot of the fuel mass objective function (a) and the flutter constraint (b) through the SEGOMOE optimization iterations. . . 216
6.7 MDAO process for flexible aircraft under deterministic constraint on flutter speed. Monitor plot of the three design variables through the SEGOMOE optimization iterations. 217

6.8 MDAO process for flexible aircraft under deterministic constraint on flutter speed. Evolution of the current best fuel mass (a) and the corresponding flutter constraint (b) through the SEGOMOE optimization iterations. 218
6.9 MDAO process for flexible aircraft under deterministic constraint on flutter speed. Evolution of the current best design variables through the SEGOMOE optimization iterations. 219
6.10 Best wing planform from the MDAO results under flutter deterministic constraint. The baseline and the best planform from the FAST-OAD rigid aircraft optimization are also reported for comparison. 219
6.11 MDAO process for flexible aircraft under deterministic constraints on gust loads. Monitor plot of the fuel mass objective function (a) and the gust loads constraints (b) through the SEGOMOE optimization iterations. . 222
6.12 MDAO process for flexible aircraft under deterministic constraints on gust loads. Monitor plot of the three design variables through the SEGOMOE optimization iterations. 223
6.13 MDAO process for flexible aircraft under deterministic constraints on gust loads. Evolution of the current best fuel mass (a) and the corresponding gust loads constraints (b) through the SEGOMOE optimization iterations. 224
6.14 MDAO process for flexible aircraft under deterministic constraints on gust loads. Evolution of the current best design variables through the SEGOMOE optimization iterations. 225
6.15 Best wing planform from the MDAO results under gust loads deterministic constraints. The baseline and the best planform from the FAST-OAD rigid aircraft optimization are also reported for comparison. 225
6.16 Best wing planform from the MDAO results under flutter and gust loads deterministic constraints. The baseline and the best planform from the FAST-OAD rigid aircraft optimization are also reported for comparison. . 227
6.17 MDAO process for flexible aircraft under deterministic constraints on flutter speed and gust loads. Monitor plot of the fuel mass objective function (a) and the flutter and gust loads constraints (b) through the SEGOMOE optimization iterations. 228
6.18 MDAO process for flexible aircraft under deterministic constraints on flutter speed and gust loads. Monitor plot of the three design variables through the SEGOMOE optimization iterations. 229
6.19 MDAO process for flexible aircraft under deterministic constraints on flutter speed and gust loads. Evolution of the current best fuel mass (a) and the corresponding flutter and gust loads constraints (b) through the SEGOMOE optimization iterations. 230
6.20 MDAO process for flexible aircraft under deterministic constraints on flutter speed and gust loads. Evolution of the current best design variables through the SEGOMOE optimization iterations. 231
6.21 Best wing planform from the MDAO results under flutter reliability constraints. The baseline and the best planform from the FAST-OAD rigid aircraft optimization are also reported for comparison. 234
6.22 MDAO process for flexible aircraft under reliability constraint on flutter speed. Monitor plot of the fuel mass objective function (a) and the flutter constraint (b) through the SEGOMOE optimization iterations. 235

6.23 MDAO process for flexible aircraft under reliability constraint on flutter speed. Monitor plot of the three design variables through the SEGOMOE optimization iterations. 236
6.24 MDAO process for flexible aircraft under reliability constraint on flutter speed. Evolution of the current best fuel mass (a) and the corresponding flutter constraint (b) through the SEGOMOE optimization iterations. 237
6.25 MDAO process for flexible aircraft under reliability constraint on flutter speed. Evolution of the current best design variables through the SEGOMOE optimization iterations. 238
6.26 MDAO process for flexible aircraft under reliability constraint on flutter speed. Juxtaposition of all evaluated flutter speed distributions during the optimization process. 238
6.27 Best wing planform from the MDAO results under gust loads reliability constraints. The baseline and the best planform from the FAST-OAD rigid aircraft optimization are also reported for comparison. 240
6.28 MDAO process for flexible aircraft under reliability constraints on gust loads. Monitor plot of the fuel mass objective function (a) and the gust loads constraints (b) through the SEGOMOE optimization iterations. 241
6.29 MDAO process for flexible aircraft under reliability constraints on gust loads. Monitor plot of the three design variables through the SEGOMOE optimization iterations. 242
6.30 MDAO process for flexible aircraft under reliability constraints on gust loads. Evolution of the current best fuel mass (a) and the corresponding gust loads constraints (b) through the SEGOMOE optimization iterations. . 243
6.31 MDAO process for flexible aircraft under reliability constraints on gust loads. Evolution of the current best design variables through the SEGOMOE optimization iterations. 244
6.32 MDAO process for flexible aircraft under reliability constraints on gust loads. Juxtaposition of all evaluated bending loads distributions (a) and vertical shear loads (b) during the optimization process. 245
6.33 Best wing planform from the MDAO results under flutter speed and gust loads reliability constraints. The baseline and the best planform from the FAST-OAD rigid aircraft optimization are also reported for comparison. . 247
6.34 MDAO process for flexible aircraft under reliability constraints on flutter speed and gust loads. Monitor plot of the fuel mass objective function (a) and the flutter and gust loads constraints (b) through the SEGOMOE optimization iterations. 248
6.35 MDAO process for flexible aircraft under reliability constraints on flutter speed and gust loads. Monitor plot of the three design variables through the SEGOMOE optimization iterations. 249
6.36 MDAO process for flexible aircraft under reliability constraints on flutter speed and gust loads. Evolution of the current best fuel mass (a) and the corresponding flutter and gust loads constraints (b) through the SEGOMOE optimization iterations. 250
6.37 MDAO process for flexible aircraft under reliability constraints on flutter speed and gust loads. Evolution of the current best design variables through the SEGOMOE optimization iterations. 251

6.38 Best wing planforms from the different optimization cases previously presented. The baseline and the best planform from the FAST-OAD rigid aircraft optimization are also reported for comparison. 252
6.39 Scatter plots of the fuel mass with respect to the three design variables: aspect ratio (a), taper ratio (b) and kink span ratio (c). The data are those collected during the 6 MDAO cases presented above. 253
6.40 One-dimensional tracking of the fuel-vs-$\mathcal{AR}$ relationship over the studied space. The two curves correspond to the rigid aircraft sizing process obtained with FAST-OAD alone (dashed line), and to the flexible aircraft approach enabled by the developed methods (solid line). The taper ratio and kink span ratio are fixed to $t_r = 0.25$ and $k_{sr} = 0.4$. 255
6.41 Overlap of multiple runs over the $\mathcal{AR}$ interval 12 - 15 showing the effect of numerical uncertainty in the flexible aircraft sizing process. 255
6.42 Scatter plots of the flutter constraint with respect to the three design variables: aspect ratio (a), taper ratio (b) and kink span ratio (c). The data are those collected during the 6 MDAO cases presented above, including the deterministic and probabilistic cases. 257
6.43 Scatter plots of the gust loads constraints with respect to the three design variables: aspect ratio (a), taper ratio (b) and kink span ratio (c). The data are those collected during the 6 MDAO cases presented above, including the deterministic and probabilistic cases. 258
6.44 Examples showing the impact of introducing a safety factor in the reliability-constrained MDAO. For each case, the scatter plots of the constraints-vs-$\mathcal{AR}$ and fuel-vs-$\mathcal{AR}$ distributions are reported. The first case (a and b) has no safety factor, corresponding exactly to the MDAO case number 6 discussed above; the second and third case correspond respectively to a safety factor of 8% (c and d) and 10% (e and f). The safety factor is applied to all constraints, and its effect is highlighted by different red-shaded areas in the left Figures, as well as by different numbers of valid points, highlighted in green in the right figures. 259
6.45 Best wing planforms corresponding to different safety increments applied on the constraint definitions. The baseline and the best planform from the FAST-OAD rigid aircraft optimization are also reported for comparison. 260

7.1 Snapshot from an unsteady aeroelastic simulation of the response of a flexible wing-plus-stabilizer configuration to a step-change in the angle of attack. The contour plot highlights the distribution of vorticity over the wing, stabilizer and their wakes. 275
7.2 Snapshot from an unsteady aeroelastic simulation of the response of a flexible wing-plus-stabilizer configuration to a step-change in the angle of attack. The contour plot highlights the distribution of lift over the wing and stabilizer. Their discretized wakes are also represented by a black uncoloured mesh. 276

Appendix B.1 Validation of the surrogate models - Lift coefficient derivatives. 288
Appendix B.2 Validation of the surrogate models - Moment coefficient derivatives. 289
Appendix B.3 Validation of the surrogate models - Aircraft parameters. . . . 290

Appendix D.1 *Classic chord* method, from Reference [28]. 296
Appendix D.2 *Regula falsi* method, from Reference [28]. 297

List of Tables

3.1 List of the developed and integrated tools available in the proposed MDAO framework. . . . 50
3.2 Aerodynamic coefficients obtained with the two solvers for the 5° sweep test case. The resolution is adapted to that of XFLR5, which is limited to the third decimal. . . . 64
3.3 Aerodynamic coefficients obtained with the two solvers for the test case of Figure 3.12. Notice that the Fortran solver gave a non-zero yawing coefficient $C_n = 0.00028$, which is not reported because of the resolution of XFLR5, limited to three decimals. . . . 65
3.4 Aerodynamic coefficients obtained with the two solvers for the test case of Figure 3.13 . . . 66
3.5 Aeroelastic properties of the Goland wing, as given in [19]. . . . 86
3.6 Flutter speed of the Goland wing. Note that **e** denotes the relative difference with respect to the present model. . . . 86
3.7 Aeroelastic properties of the Patil wing, from [29]. . . . 88
3.8 Flutter speed and frequency of the Patil wing. . . . 88
3.9 Parameters for the free-to-pitch wing. . . . 103
3.10 Parameters for the free-to-pitch wing-stabilizer glider. . . . 105
3.11 Uncertain ranges and distributions of variables for the test-case in Equation (3.56). . . . 111
3.12 Comparison of output metrics from the UQ module for the validation test-case. . . . 112

4.1 CeRAS baseline parameters, from [26]. . . . 119
4.2 Definition of the MDAO problem under flying qualities reliability constraints. . . . 120
4.3 Uncertainty distributions on the input parameters. $\overline{x}_{CG}$ is the CG location for a prescribed load case defined in FAST-OAD. I_{yyB} is the moment of inertia of the baseline configuration. . . . 128
4.4 Short period damping and natural frequency constraints adopted for the present case study. . . . 128
4.5 Fuel mass optimization results compared with baseline data. The optimized configuration offers an improvement of 1.4%. . . . 130

5.1 Material properties for the wing-box components. Values typical of aeronautical aluminium alloy. . . . 143
5.2 Definition of the simplified structural optimization problem for the flexible wing. . . . 153

5.3 Optimization results for the flexible wing structural optimization process over the CeRAS baseline configuration. The data for the initial guess structure, as well as from the corresponding rigid configuration sized by FAST-OAD are reported for comparison. 156
5.4 Optimization results for the flexible wing structural optimization process over the $\mathcal{AR}$ 15 configuration. The data for the initial guess structure, as well as from the corresponding rigid configuration sized by FAST-OAD, are reported for comparison. 159
5.5 Uncertain parameters and corresponding distributions adopted for the flutter sensitivity analysis. All distributions are Gaussian. Symbols denoted with a bar $\bar{(\,)}$ represent the nominal values produced by the sizing and optimization process. The symbol ς indicates the standard deviation. 181
5.6 Mean (nominal) values of the 6 selected uncertain parameters for the flutter speed sensitivity studies on the CeRAS baseline and the '$\mathcal{AR}$ 15' wings. 182
5.7 Main statistical figures from the sensitivity analysis and uncertainty quantification on the flutter speed for the baseline configuration. 185
5.8 Main statistical figures from the sensitivity analysis and uncertainty quantification on the flutter speed for the aspect ratio 15 configuration. 187
5.9 Uncertain parameters and corresponding distributions adopted for the gust loads sensitivity analysis. All distributions are Gaussian. Symbols denoted with a bar $\bar{(\,)}$ represent the nominal values produced by the sizing and optimization process. The symbol ς indicates the standard deviation. 198
5.10 Main statistical figures from the sensitivity analysis and uncertainty quantification on the gust-induced bending loads at wing root for the baseline configuration. 201
5.11 Main statistical figures from the sensitivity analysis and uncertainty quantification on the gust-induced vertical shear loads at wing root for the baseline configuration. 202
5.12 Main statistical figures from the sensitivity analysis and uncertainty quantification on the gust-induced torsional shear loads at wing root for the baseline configuration. 202
5.13 Main statistical figures from the sensitivity analysis and uncertainty quantification on the gust-induced bending loads at wing root for the '$\mathcal{AR}$ -15' configuration. 202
5.14 Main statistical figures from the sensitivity analysis and uncertainty quantification on the gust-induced vertical shear loads at wing root for the '$\mathcal{AR}$ -15' configuration. 203
5.15 Main statistical figures from the sensitivity analysis and uncertainty quantification on the gust-induced torsional shear loads at wing root for the '$\mathcal{AR}$ -15' configuration. 204

6.1 Definition of the fuel mass optimization problem for a rigid aircraft. . . . 210
6.2 Definition of the MDAO problem for the flexible aircraft with a deterministic constraint on flutter speed. . . . 215
6.3 Best point from the MDAO results under flutter deterministic constraint. 219
6.4 Definition of the MDAO problem for the flexible aircraft with deterministic constraints on dynamic gust loads. . . . 220
6.5 Best point from the MDAO results under gust loads deterministic constraints. . . . 225
6.6 Definition of the MDAO problem for the flexible aircraft with deterministic aeroelastic constraints on flutter and gust loads. . . . 226
6.7 Best point from the MDAO results under flutter and gust loads deterministic constraints. . . . 226
6.8 Definition of the MDAO problem for the flexible aircraft with reliability constraint on flutter speed. . . . 233
6.9 Best point from the MDAO results under flutter reliability constraint. . . 233
6.10 Definition of the MDAO problem for the flexible aircraft with reliability constraint on flutter speed. . . . 240
6.11 Best point from the MDAO results under gust loads reliability constraints. 240
6.12 Definition of the MDAO problem for the flexible aircraft with reliability constraint on flutter speed and gust loads. . . . 246

6.13 Best point from the MDAO results under flutter speed and gust loads reliability constraints. . . . 246
6.14 Summary of the optimization results from the different cases previously presented. . . . 252
6.15 MDAO under flutter and gust loads reliability constraints. Optimization results corresponding to different safety increments applied on the constraint definitions. . . . 260

Declaration of Authorship

I declare that this thesis and the work presented in it is my own and has been generated by me as the result of my own original research.

I confirm that:

1. This work was done wholly or mainly while in candidature for a research degree at this University;
2. Where any part of this thesis has previously been submitted for a degree or any other qualification at this University or any other institution, this has been clearly stated;
3. Where I have consulted the published work of others, this is always clearly attributed;
4. Where I have quoted from the work of others, the source is always given. With the exception of such quotations, this thesis is entirely my own work;
5. I have acknowledged all main sources of help;
6. Where the thesis is based on work done by myself jointly with others, I have made clear exactly what was done by others and what I have contributed myself;
7. Parts of this work have been published as: [30], [31], [32], [33]

Acknowledgements

I would like to express my sincerest gratitude to all the people that contributed, in a way or another, to the accomplishment of this PhD.

First of all, I want to acknowledge the fundamental contribution of my supervisors, Andrea Da Ronch, Nathalie Bartoli, Sébastien Defoort, who shared with me invaluable knowledge, skills and advice, with wisdom and passion. I also immensely value their human attitude and friendship, which enriched this PhD journey with happy memories at work and several adventures outside. I also include in this list Peter Shmollgrüber, who had to abandon its supervisory role too early, officially, but who in practice was always there whenever I needed his help.

My gratitude goes also to all the colleagues and friends from the University of Southampton and the ONERA of Toulouse that crossed my path over these years. Each of them carries part of the merit of my personal and professional maturation. In particular, from the University, I refer to Jerney, Guangda, Riccardo, Ben, Yan Sun, Daniel. In addition, I want to dedicate a big thank you to Ben, for his kind help during my move to Toulouse. From the ONERA of Toulouse, thanks for your support to Alessandro, Gabriel, Tiphaine, my dear friend Luiz, and to all the kind and welcoming people of the M2CI department.

A special thanks goes to Vincenzo and Tania. You guys welcomed me and Sabrina in Toulouse in a moment of hardship, and supported us for weeks when trying to settle down in the city. At least, that period sealed the beginning of a strong friendship. In this context, I found in Vincenzo a companion with whom I could fully share not only joys and sorrows of our PhD journey, but also many other wonderful adventures.

Of course, this PhD would not have been possible without the love and support of my family, that since my first steps has always encouraged me to learn, explore, and follow my dreams and my passion wherever they may take me.

Finally, I want to express my profound gratitude to Sabrina, my love. You lived with me every single emotion of this journey, and were always there to revive my focus and motivation whenever they were faltering. Together we went through many hard challenges, but you could always brighten the darkest room by recalling me that few things really, deeply matter in life, and we are one of them.

To Sabrina,
for her endless love and support,
and to my beloved dad, mom and brother,
my splendid family.

Definitions and Abbreviations

Abbreviations

CG	Center of Gravity
DLM	Doublet Lattice Method
DOE	Design of Experiments
EA	Elastic Axis
EAS	Equivalent air speed
EI	Expected Improvement
FDM	Fight Dynamics Model
GP	Gaussian Process
MC	Monte Carlo (method)
MDAO	Multi-Disciplinary Analysis & Optimization
MDO	Multidisciplinary Design Optimization
MTOW, MZFW	Maximum Take-Off Weight and Maximum Zero-Fuel Weight
PCE	Polynomial Chaos Expansion
PDF	Probability Distribution Function
QoI	Quantity of Interest
SA	Sensitivity Analysis
SEGO	Super Efficient Global Optimization
TLAR	Top-Level Aircraft Requirements
UQ	Uncertainty Quantification
VLM, UVLM	Vortex Lattice Method and Unsteady Vortex Lattice Method
WB2, WB2S	Watson and Barnes infill criteria
XDSM	eXtended Design Structure Matrix

Symbols

a	Elastic axis chord-wise location
$\mathcal{AR}$	Aspect ratio
A	Wing-box and beam cross section area
$\boldsymbol{A}$	Dynamic matrix of the linear aeroelastic system
$\mathcal{A}$	Aerodynamic influence matrix
A_1, A_2	Coefficients used in the Wagner's function
A_s, A_{s0}	Stringer's cross section area and its initial guess value

b	Wing span
b_1, b_2	Coefficients used in the Wagner's function
c	Chord
$\boldsymbol{C}$	Damping matrix
c_b	Wing-box chord
c_f	Friction coefficient
c_{MGC}	Mean geometric chord
C_L, C_m, C_D	Lift, moment and drag coefficients
C_{L_α}, $C_{L_{\dot{\alpha}}}$, $C_{L_{\ddot{\alpha}}}$	Lift coefficient derivatives with respect to α
C_{m_α}, $C_{m_{\dot{\alpha}}}$, $C_{m_{\ddot{\alpha}}}$	Moment coefficient derivatives with respect to α
d	Distance of CG from EA
EI^{A}_{yy}, EI^{A}_{zz}	Out-of-plane and in-plane bending stiffness
g	Gravitational acceleration
GJ	Torsional stiffness
h_w	Wing-box web height
$\boldsymbol{H}$	Fluid-structure interface matrix
I_{yy}	Aircraft moment of inertia around pitch axis
J	Torsion constant
k	Reduced frequency
$k_{()}$	Correction factors used by `FAST-OAD` (subscripts indicate quantities affected)
$k_s r$	Kink location (span ratio)
$\boldsymbol{K}$	Stiffness matrix
ℓ, m, n	Rolling, pitching and yawing moments in body axes
m	Aircraft mass
M	Mach number
$\boldsymbol{M}$	Mass matrix
$\boldsymbol{n}$	Surface normal vector
P	Aerodynamic pressure
$\boldsymbol{P}$, P_x, P_y, P_z	Linear momentum vector and its components in inertial frame
$\boldsymbol{Q}$, Q_x, Q_y, Q_z	Angular momentum vector and its components in inertial frame
p, q, r	Roll, pitch and yaw rates
$\boldsymbol{q}$	Generalized displacements
S	Wing surface
t	Time
t_r	Taper ratio
t_s, t_w, t_{s0}, t_{w0}	Skin and web thickness and respective initial guess values
U, U_{ds}	Vertical gust velocity, vertical design gust velocity
$\boldsymbol{V}$, V_x, V_y, V_z	Velocity vector and its components in inertial frame
V_C	Cruise speed
V_g	Geometric optimization variables
V_F	Flutter speed

$\boldsymbol{w}$	DOFs vector of the linear structural FEM
W	Aircraft weight (= $m\,g$)
W_g	Wing geometric parameters
W_{w1}, W'_{w1}	Wing structure and primary structure weight, respectively, from the `FAST-OAD` sizing process
W_{w2}, W'_{w2}	Wing structure and primary structure weight, respectively, from the aeroelastic sizing process
$\boldsymbol{x}$	DOFs vector of the linear aeroelastic FEM
x_{CG}	Aircraft center of gravity location
X, Y, Z	Total external forces in body axes
y_{CG}, z_{CG}	Components of CG distance from EA, in structural coordinates
α	Angle of attack
Γ	Velocity circulation
μ	Mass per init length
ξ, ξ_{sp}	Generic damping ratio, short period damping ratio
ρ	Air density
ρ_m	Material density
σ_b	Bending stress
σ_m	Material yield strength
τ_m	Material shear strength
τ_v	Vertical shear stress
τ_t	Torsional shear stress
$\boldsymbol{n}$	local normal vector of the solid surface
Φ	Velocity potential
ϕ_W	Wagner's function
ϕ, θ, ψ	Euler's angles
$\boldsymbol{\Omega}$, Ω_x, Ω_y, Ω_z	Angular rates vector and its components in inertial frame
ω, ω_{sp}	Generic angular frequency, short period angular frequency

Operators

$\mathbb{E}$	Expected value
$\mathbb{P}$	probability
$\mathbb{V}$	Variance
ς	Standard deviation
$\hat{(\,)}$	Distribution
$\overline{(\,)}$	Nominal value
$P_5(\,)$, $P_{95}(\,)$	5th and 95th percentiles of distribution

Chapter 1

Introduction

1.1 Background

As environmental requirements become more and more stringent, reduction of emissions in commercial aviation is targeted with increasing pressure both by research and industry [34–36]. A large effort is put on the exploration of disruptive technologies and configurations that may lead to a new generation of highly efficient aircraft [37, 38]. Most innovation strategies arise at the three levels of propulsion, structures and aerodynamics. Technologies such as electric/hybrid propulsion and distributed propulsion are receiving large attention [39], as well as cutting-edge structural solutions including composites-rich structures, bio-inspired materials, morphing structures [40], foldable wings [41, 42], to just name a few. From the aerodynamic side, the tendency is to promote efficient layouts such as blended wing-body configurations [43, 44], box-wing configurations [45–47], boundary layer ingestion [48], very high aspect ratio truss-braced wings [49–52] or semi-aeroelastic hinged wing tips [53] (see Figure 1.1).

(a) Strut-braced high-aspect-ratio wings, from [49]

(b) Double-bubble fuselage, high-aspect-ratio wing configuration, from [54, 55]

(c) Airbus AlbatrossONE semi-aeroelastic hinged wing tips, from [53]

FIGURE 1.1: Examples of unconventional aircraft concepts featuring highly-efficient wing configurations.

As usual in aerospace design, the implementation of such choices involves important implications on several disciplines. It is evident that future aircraft candidate concepts all present the challenge of a stronger interaction among disciplines that are traditionally treated as independent, at least at preliminary and conceptual design stages. Such a standard design approach is no longer convenient for these kinds of configurations. For instance, high aspect ratio wings accentuate aero-structural issues, such as flutter, divergence, limit-cycle oscillations (LCO) and gust loads, and affect stability, control

strategies and pilot coupling [1]. Therefore, an effective exploration of disruptive concepts needs to be accompanied by analysis and optimization frameworks as multidisciplinary as possible, even at conceptual or preliminary design stages [56]. For this reason, a new paradigm of physics-based and integrated aircraft conceptual design is being introduced to replace the classical approach of knowledge-based sectorial design. The new approach aims to take into account the interactions among the different disciplines by increasing the level of detail and retaining the relevant disciplinary couplings (see Figure 1.2). The shift towards this design philosophy indeed offers economic advantages. In fact it is widely accepted that integrated design approaches handling an increased amount of information and knowledge during the early design phases have a positive impact on the overall design cost. The cost of any design change grows considerably with the advancement of the process, and modern integrated conceptual design represents the opportunity to anticipate the events of design changes and contain the costs in a relevant way [57, 58] (see Figure 1.3). To report a relevant case, after finding that divergent flutter may occur under certain conditions in the Boeing B747-8 and B747-8F, reparations and software updates had to be applied [59], with costs for the company and the operators and damage to the company image. Failing to provide adequate multidisciplinary capabilities early in the design may lead to severe consequences not just limited to expensive late corrections, but could even entail the failure of the whole process [1]. Fortunately modern computational power and numerical methods (such as surrogate modelling) encourages increasing efforts on the development of analysis tools and their mutual integration to corroborate aircraft conceptual design procedures with physics-based predictions. Such strategy inevitably calls for advanced tools capable of resolving the desired level of complexity, with the constraint of keeping affordable computational costs and time suitable for the early stage of the design.

Due to the promising potential advantages and to the availability of computational power, multidisciplinary analysis and optimization (MDAO) for aircraft design has shown in recent years significant progress. Together with the numerous achievements, though, several issues still remain challenging and stimulate ongoing efforts in the research community.

For instance, as aircraft design involves several disciplines, each of which requires different tools and handling a large body of information, the exchange of data between modules represents a crucial question [60]. The definition of common programming languages, interfaces and data management strategies becomes a key enabler for the effectiveness of the whole framework [61–63].

Another critical point is the choice of an appropriate model and numerical strategies for each of the involved disciplines. The design team, as well as the single specialist, have at their disposal a broad set of analysis methods of different levels of fidelity (accuracy

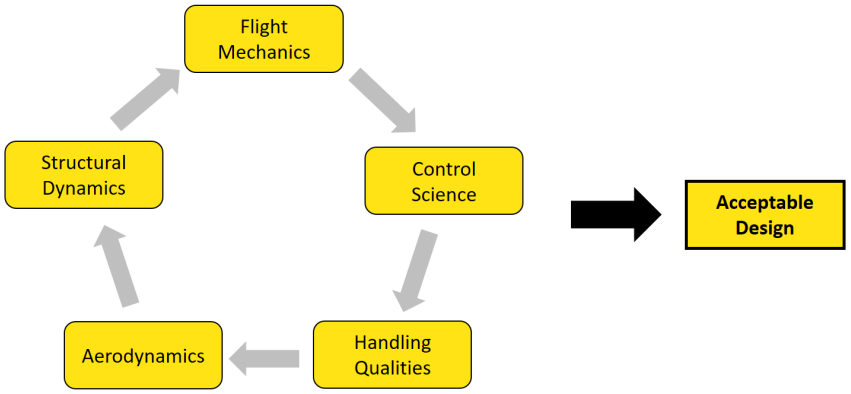

(a) Traditional design approach

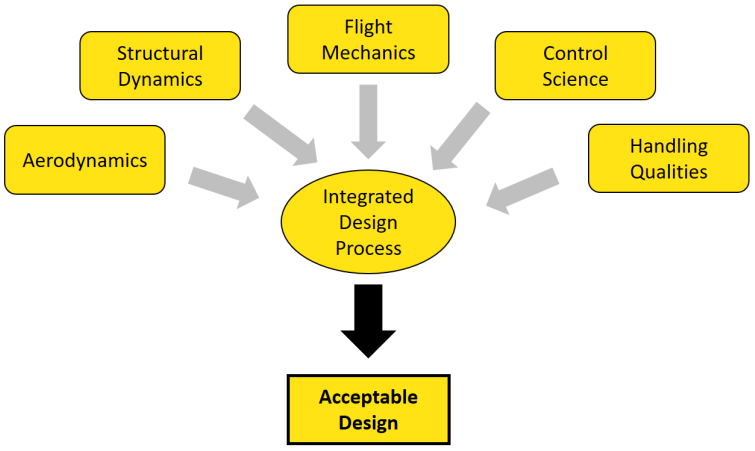

(b) Integrated design approach

FIGURE 1.2: Traditional vs integrated design approaches (adapted from [1]).

to capture the physical phenomena) . A proper design framework should be implemented in such a way that the appropriate fidelity level is employed for each maturity status of the design process. Often, effort is put on introducing as much physics as possible from the earliest stages by some clever multifidelity approaches. The strategy is to exploit information from a few expensive higher-fidelity analyses to correct and enrich the results of the lower-fidelity tool. This can be done either by directly merging the two solvers in a new hybrid tool [64–66], or by deriving a surrogate model through data sets from multiple tools [67, 68]. The adoption of such strategies and the choice of the appropriate fidelity levels for different design purposes are widely discussed in [69]. When developing an MDAO framework, the assessment of the applicability of all the different analysis tools and their impact in terms of accuracy of the results is a necessary task. In fact, it is desirable to provide the highest possible flexibility towards the exploration of wide design spaces, and all the integrated tools should prove capable to handle large ranges of variables, ideally including discrete variables or topological

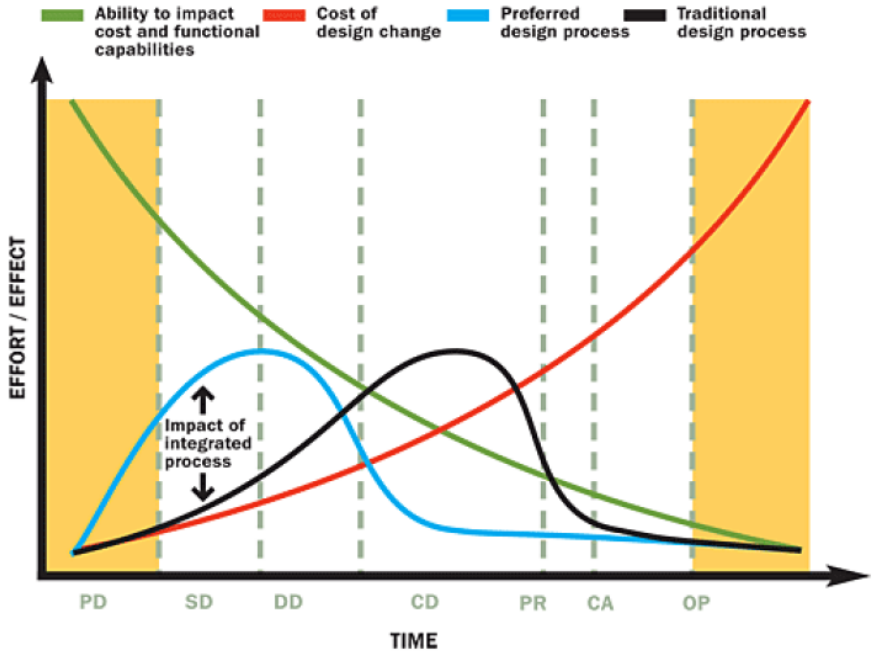

FIGURE 1.3: Integrated multidisciplinary design process versus traditional design process. When decisions are made earlier, they can have a high impact at a relatively low cost (from [2]).

decisions (such as presence/absence of wing braces) and represent a variety of physical conditions and phenomena, while keeping the computational time reasonable.

The complexity of the MDAO tasks is even increased by the fact that any engineering model is inherently affected by uncertainties. This is especially true at conceptual design, where the level of detail requires to retain a lot of unknowns, and where virtually all the methods must introduce approximations in order to meet a compromise between speed and accuracy. For this reason, uncertainty quantification and management in MDAO applications is an interesting challenge, at the centre of several research activities [70, 71]. If properly addressed, it would improve the quality of the design outcomes providing key information on the robustness and reliability of the results.

1.2 Project outline, aim and objectives

The present work aims to provide some of the necessary tools within the above broad context of new generation multidisciplinary conceptual design, with special attention given to high-aspect-ratio configurations where structural flexibility induces a potentially significant risk. The project belongs to a wide framework development plan for multidisciplinary conceptual design of novel aircraft configurations which is carried out at both the founding centres: a) the University of Southampton, where advanced efficient methods for aerodynamic computations have been developed and are currently

under further refinement, b) the ONERA centre of Toulouse, where parallel development is in progress for advanced aircraft sizing tools - covering for example blended-wing-body, hybrid, turboelectric and distributed propulsion configurations - as well as numerical methods for robust multidisciplinary design and optimization procedures. All of the mentioned research is bound to be integrated within a large multidisciplinary framework for conceptual design of novel aircraft concepts. Some example applications can be found in [72–74].

Within the given panorama, the present project aims in particular to develope some analysis and simulation tools, suitable for conceptual design level, to capture relevant static and dynamic phenomena affected by large airframe flexibility, and to treat them in a stochastic way by taking into account the uncertainties linked to the unavoidably imperfect knowledge typical of the early design stage.

Specifically, we want to retain as much information as possible regarding the core disciplines of aerodynamics, structural dynamics and flight dynamics (and their possible coupling) in order not only to understand in what measure the behaviour of the vehicle is affected by structural flexibility, but also in what measure the uncertainties relative to the three mentioned domains affect such a behaviour. Of course, the generic term 'behaviour' needs to be translated into quantifiable parameters of interest, such as flying qualities, loads, or fuel consumption. Also, each uncertain quantity of interest has to be associated to a stochastic range, and compared to design constraints to be met with a certain probability. The disciplinary modules need to fully allow a mutual coupling, but also be capable to run as stand-alone modules for those cases where coupling is negligible. Therefore, the development is oriented towards a modular approach, in the sense that different models for different disciplines can be interfaced to address different coupled problems. For example, steady or unsteady aerodynamics could be coupled with linear or nonlinear structural dynamics, or with the flight dynamics module, according to different specific needs. Moreover, the analysis and simulation package has to allow a practical interface to be plugged into a wider framework, typically an external sizing and optimization architecture.

The core idea behind the project could be summarized by the following research question:

Can we develop an analysis and simulation framework to investigate aeroelastic and flight performance of new generation flexible aircraft, capable of handling and propagating input uncertainty, in support of a robust design and optimization process at conceptual design phase?

The project is built around four technical objectives:

I the development of a set of adequate analysis tools for the disciplines of interest, namely aerodynamics, flight dynamics and structural dynamics, in response to the need of more physics-based methods for unconventional design exploration;

II the integration of the above modules with an aircraft sizing tool to broaden the design exploration capabilities, including the possibility of taking into account discipline-related uncertainty and constraints;

III the further expansion of the framework's capabilities and set of constraints by enabling coupled aero-structural analyses under uncertainty;

IV the demonstration of a robust design and optimization process for a highly flexible aircraft concept.

The development of such analysis tools paves the way for at least two desirable applications: a) the usage within a robust multidisciplinary design & optimization framework for unconventional aircraft configurations; b) the exploitation of the fast flexible aircraft flight dynamics simulation capabilities to be run on a fixed-base research flight simulator, present at the University of Southampton, for handling qualities assessment and other simulation campaigns. However, only the first type of application is addressed in this project, whereas the second type is seen as a secondary perspective that would benefit from the implemented tools, but that would still require further developments to be considered in future research activities.

1.3 Thesis structure

Considering the above aim and objectives, the present Thesis is structured as follows.

Chapter 2 gives a more detailed description of the background of this project, with focus on the key aspects that we want to address and on the relative state of the art.

The first technical objective (I) is addressed in Chapter 3, where the development, validation and integration of a list of necessary tools is presented.

Chapter 4 demonstrates a first aircraft robust MDAO application using some of the developed tools, fulfilling the second technical objective (II). In particular, the test case is for a transport aircraft wing planform optimization to minimize the fuel mass for a give mission. Uncertainty is included through a couple of aircraft input parameters, and it is propagated into some flying qualities reliability constraints.

The third technical objective (III) is addressed in Chapter 5, where a more complex architecture for robust MDAO of flexible aircraft is proposed. Static and dynamic aeroelasticity is considered, and uncertainty can be introduced and propagated into flutter and dynamic gust response constraints.

Finally, Chapter 6 presents some flexible aircraft MDAO case studies performed using the above-mentioned framework. Several cases are covered, including deterministic and probabilistic cases, involving flutter and/or gust loads constraints. Results are compared against a conventional rigid-aircraft design approach. This covers the last technical objective (IV), in fulfillment of the global PhD project aim.

Conclusions are then drawn in Chapter 7, which summarizes the main achievements of this project and discusses the most interesting perspectives.

Chapter 2

Literature review

Contents

1.1 Background 2
1.2 Project outline, aim and objectives 5
1.3 Thesis structure 7

2.1 Overview

The project objectives stated in the previous Chapter require a multidisciplinary framework covering different technical capabilities. In the first instance, there is a need for effective analysis and simulation tools for the involved flight physics disciplines. These tools should be able to interact with an overall aircraft sizing process, so that information regarding geometry, weight & balance, or performance can be exchanged and made available to an optimizer. Then, it is necessary to have in place adequate methods for robust optimization of complex and costly objective functions. This means that not only modern and efficient optimization methods are required, but also some uncertainty quantification techniques that minimize the computational burden of uncertainty propagation. It becomes clear then that the technical domain is quite vast and complex. This Chapter seeks to clarify the background from which this project evolves, and to identify more in details the bounds enforced on the present investigations. This is done with the support of relevant literature offering instructive and inspiring insights on the state of the art, with attention on both the success and limitations of the discussed approaches. After a brief overview given below in this Section, more details are discussed in Sections 2.2 to 2.6.

To start with, simulation in aerospace applications is a fundamental task which is addressed for various purposes and in different contexts, spanning from design to verification, testing, training, etc. In this work, three core and interrelated disciplines are mainly involved, namely flight mechanics, aerodynamics, and structural mechanics. These three domains are often treated separately and differently. In fact, while flight mechanics is well described by low-order models and low frequencies, structural mechanics problems involve high frequencies and higher-order models. In both cases the simulation is aimed at visualizing the system response following certain inputs or disturbances. On the other hand, aerodynamics simulations are aimed at computing loads and energy transformations due to the interaction with the surrounding flow, and a variety of methods are available with different complexity and computational cost. However, aerodynamics is in general identified as the most challenging discipline. The resulting aerodynamic loads can be used for design and optimization purposes.

In contrast with the above disciplinary cases, a broader simulation approach is required when the three main areas play all a relevant role. This is the case for aeroelastic studies, and even more when controls and actuators are taken into account, in which case we adopt the more general term of aeroservoelasticity (ASE). When all these disciplines are expected to be relevantly involved, an adequate interdisciplinary, higher-order simulation model needs to be employed encompassing the wider range of frequencies. However, as a general trend, higher-order systems, such as aeroelastic or aero-servoelastic

systems, involve increased complexity and therefore increased uncertainty (see Figure 2.1). Therefore, two coexisting needs emerge: on the one hand, the need for multidisciplinary simulation arises in order to address the analysis of complex systems characterized by potentially important interactions between flight physics disciplines traditionally treated as independent; on the other hand, such simulation capabilities should be employed in a robust approach where deterministic analyses are accompanied by some uncertainty propagation techniques that provide the designer with an awareness of the impact that the inevitable lack of knowledge may have on the final outcome.

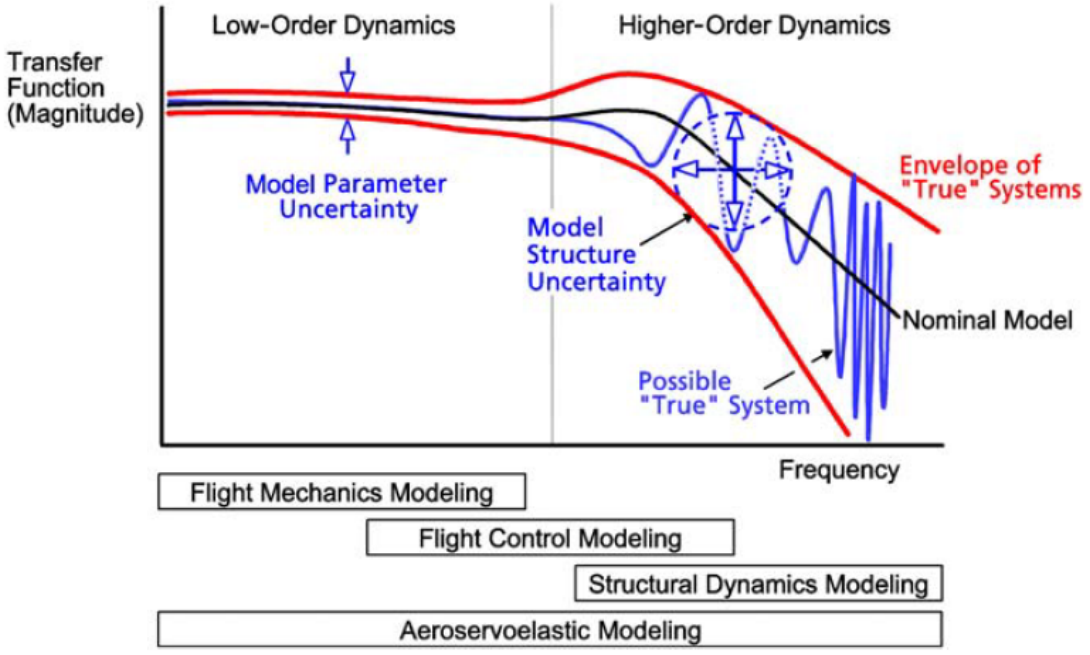

FIGURE 2.1: Uncertainty in multidisciplinary flight vehicle modeling, from [3].

The role of the inherent uncertainty is especially important during the early design phases. Figure 2.2 clarifies this statement by showing a qualitative trend of the 'amount' of uncertainty and how this decreases with the increasing knowledge through the design maturation. The figure also points out how crucial the conceptual phase is in the whole process: despite the high level of uncertainty, it is during this phase that the most relevant decision making takes place, fixing most of the relevant variables and therefore reducing abruptly the design 'freedom'. Also, consequently to the decisions taken at this stage, a great deal of the costs are committed, and this is why the cost curve experiences a steep increase at this same phase. This simple but effective analysis underlines the impact that the conceptual design phase has on the final outcome. Being able to capture the relevant sources of uncertainty and to map their effect into the analysis predictions can be a powerful strategy for estimating costs and risks of novel designs. The subject is further detailed in [75] and [4].

The uncertainty ranges can be large due both to aleatory causes, related with the randomness of certain operational conditions, and to epistemic ones, arising from the lack of knowledge or from the unavoidable approximations underlying the models employed. The difficulty of considering and propagating uncertainty through the design process is exacerbated when the disciplinary couplings and complex models are taken into account [76] (see again Figure 2.1). This is confirmed by the fact that, although considerable progress has been achieved on multidisciplinary aircraft conceptual design, many of the proposed frameworks in the literature fail at identifying the key sources of uncertainty and do not convey any information about the robustness/reliability of the design outcomes.

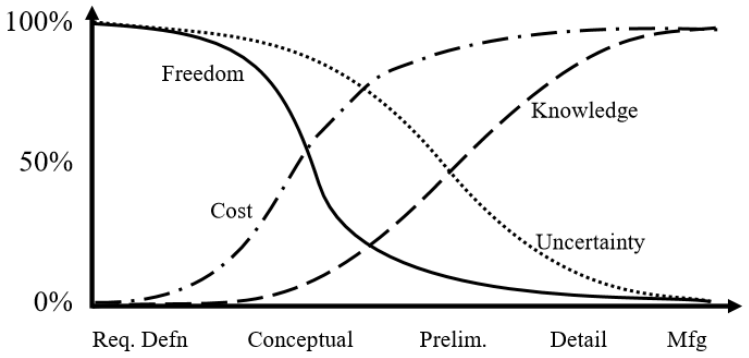

FIGURE 2.2: Design Process Paradigm Shift, from [4].

The development of simulation capabilities adequate to the above needs and suitable for modern aircraft design and optimization represents a huge challenge that requires the investment of a lot of expertise, time and computational power. The list of possible interesting applications is virtually unlimited, covering for example investigations on new generation real-time flight simulators, handling qualities assessment of flexible aircraft, stability and control analysis, control system design (autopilot functions, load alleviation, stability augmentation), manoeuvre loads assessment for structural sizing and optimization, overall aircraft design and optimization. Addressing all these kinds of studies is clearly out of the scope of a single PhD program. Instead, given this wide range of possible applications, the interest here is more on the development and the proof-of-concept of the main building-blocks of a multidisciplinary aircraft design framework, paving the way for further developments and more detailed investigations on several research cases.

In terms of demonstrative applications, where simulation is used in support of a robust analysis and optimization process for flexible aircraft, this work restricts its focus on a few domains. A first interest is to perform flight simulation for flying qualities assessment. This would represent a key initial step before moving to more complex tasks, such as pilot-in-the-loop simulations or control design, which will not be addressed here. A second target is aeroelastic simulation, both static and dynamic, in order to

capture the most critical aspects of fluid-structure interaction, such as flutter or gust-induced loads.

Therefore, the following Sections concentrate on a review of relevant literature on these domains. In particular, Section 2.2 addresses the topic of flight simulation investigations at the level of conceptual design, covering approaches for both rigid and flexible aircraft. Then, Section 2.3 explores the problem of aircraft sizing involving flexible high-aspect-ratio wings. This mainly concerns static aeroelasticity and aircraft sizing techniques. Dynamic aeroelastic issues, and in particular flutter and gust loads, are discussed in Section 2.4. Next, Section 2.5 presents the most interesting optimization strategies to be considered for this project, with particular focus on MDO. Finally, Section 2.6 focuses on the problem of sensitivity analysis and uncertainty quantification, with attention on aircraft design applications.

2.2 Flight simulation at conceptual design

The traditional aircraft design approach seldom relies on flight simulation. This is historically due to the lack of computational power, that made the simulation an expensive task. Additionally, it is difficult to produce a simulation framework which is robust in all the design space and at all flight conditions. Most approaches therefore rely on simplified analytical models or on empirical relationships. With the advent of modern digital computers, with increasingly powerful performance, the importance of flight simulation has continuously increased over the years [77]. Simulators are increasingly used not only for pilot training but also for other applications such as flight planning, envelope expansion, design and analysis of control laws, handling qualities investigations, and pilot-in-the-loop studies.

Nowadays, several studies have already included flight simulation and flight dynamics information into modern conceptual design tools, with the aim of supporting the design with more physics when empirical data are not sufficient. Relevant examples of such applications can be found in [5, 78–81], just to mention a few.

The main benefits of including multidisciplinary flight simulation capabilities during the design process are: a) the possibility to perform sizing manoeuvres with a higher fidelity than the standard methods, and b) the opportunity to investigate the effect of the disciplinary interactions on flying qualities, handling qualities, stability and control characteristics of the design candidates.

The following parts of this Chapter give further details on the state of the art and relevant issues related with these tasks. In particular, Section 2.2.1 gives a review of recent work on flying qualities constraints at aircraft conceptual design. Then, Section 2.2.2

reviews the state-of-the-art modeling methods for multidisciplinary simulation of air vehicles.

2.2.1 Flying qualities constraints

Compliance with flying qualities requirements is a mandatory task of the certification process. Typically the analysis of flying qualities is done in the latest stages of the design, when most of the features are fixed, and configuration changes in the attempt to improve the dynamic characteristics may not be affordable. If this approach is acceptable for conventional aircraft design, where the high level of knowledge ensures a certain degree of confidence, this is not necessarily true for unconventional concepts. For this reason, some effort has been put by industries and research to include flight dynamics constraints earlier in the design process [82]. The work of Mieloszyk et al. [82] represents a relevant example of such an effort, and the approach is here briefly summarized. The paper aims to use design constraints based on airworthiness specifications on the dynamic properties of an unconventional box-wing configuration. In this case the authors refer to the MIL-STD acceptability criteria [83] and to the CS-23 Airworthiness requirements [84]. These requirements concern the 6-degrees-of-freedom dynamics of the vehicle, and more exactly they involve the flight dynamics modal characteristics such as phugoid, short-period and dutch-roll damping ratios, dutch-roll frequency and spiral mode time to double. The dynamic stability data on the design candidates were computed automatically during an optimization [85]. The computation was done through the use of the Simulation and Dynamic Stability Analysis (`SDSA`) software [86]. Several flight conditions were used with variable flight speed and altitude. The stability analysis was carried out by extracting the eigenvalues of the full 6-DOFs rigid body dynamic matrix from the linearised equations of motion [87]. The added value of this work is to have shown the feasibility of introducing a comprehensive list of flight dynamics constraints during an overall aircraft design and optimization problem. In this way, the authors manage to address the problem of granting satisfactory flying qualities from the earliest design phase, even for an unconventional configuration.

A similar approach is used in the SimSAC Project, as reported in [5], where the CEASIOM advanced analysis tools employed during the conceptual design are used also for higher fidelity verification of the compliance with the ICAO recommendations or the MIL-STD acceptability criteria [83]. After computing all the needed aerodynamic and inertial characteristics through the appropriate CEASIOM modules, the evaluation of the overall dynamic properties of the vehicle leverages also in this case on the `SDSA` software [86]. An example of the software output during a sizing and optimization cycle on a Boeing 747-like baseline is reported in Figure 2.3, where short-period damping and natural frequency are compared with the certification specifications. It can be seen that some candidates under some flight conditions exhibit unacceptable characteristics,

calling for alternative design solutions. The figure demonstrates how flying qualities could potentially be an active constraint during aircraft design. The work offers another successful example of a multidisciplinary design and optimization framework for aircraft conceptual design, where stability & control characteristics are considered as constraining features during the overall design process.

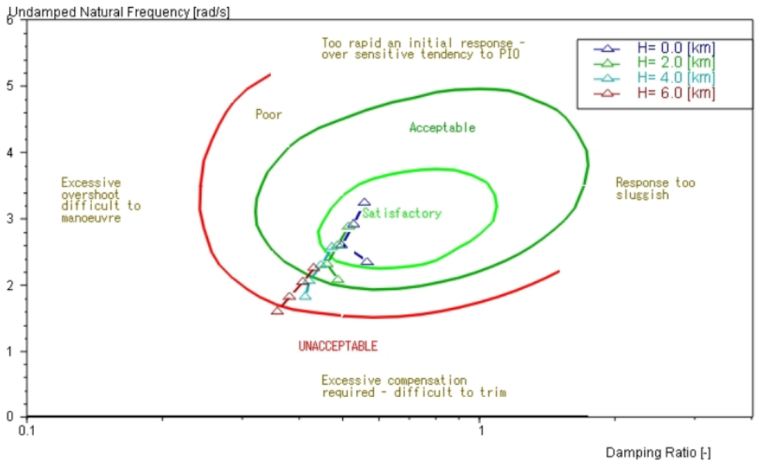

FIGURE 2.3: Short-period characteristics predicted during sizing and optimization loops in SDSA, plotted against the specification categories (from [5]).

Other approaches can be found in the literature to tackle the assessment of specification-compliance during aircraft conceptual design, such as in [26, 88, 89]. However, not much has been done to the writer's knowledge to assess the impact of uncertainty on the design outcome. Even less so if the design concerns flexible aircraft. Therefore, one contribution of this project is to fill this gap, proposing a framework with similar functionalities as those just mentioned, but with the additional capabilities of propagating uncertainty, from a user-selected set of inputs, with the possibility of treating also flexible aircraft concepts.

2.2.2 Flight simulation of flexible aircraft

The subject of flight simulation of flexible aircraft is wide and complex, as it encompasses various disciplines, namely flight dynamics, structural dynamics, aerodynamics and aeroelasticity. Since different approaches, tools and levels of fidelity are available for each of these disciplines, several combinations have been developed in the literature according to different specific needs or objectives and availability of resources of each case.

In general flight simulation capabilities can bring several advantages, including the ability to investigate flying qualities, handling qualities, stability, pilot coupling effects, as well as to perform manoeuvre loads assessments and control design at various levels (stability augmentation, autopilot, loads alleviation). Moreover, a simulation tool

implementing the most interesting disciplinary coupling (such as aero-structural coupling in the case of this project) can be used as a reference to determine the accuracy and the domain of validity of lower-fidelity approaches, such as those based on uncoupled models.

This Section summarizes the most interesting approaches for flight dynamics investigations on flexible aircraft, at a level that could potentially suit conceptual design analyses. A large amount of work exists in literature on this topic (such as in [1, 90–95]), and a thorough review would be excessively long for the purpose of this work. Therefore, just a couple of relevant examples are here discussed. These have been chosen because they seem sufficiently representative to draw out the main conclusions about the most relevant phenomena to be captured and the adequate tools to be employed.

The first example is from [19], based on previous work from [6, 96]. The authors developed a model to simulate the open loop dynamics of very flexible aircraft. High flexibility of the structure was allowed by a geometrically-exact composite beam formulation. Structural rotations are parameterized using the Cartesian Rotation Vector with respect to a body-attached reference frame. Fully three-dimensional orientation of the body reference frame is achieved by quaternions representation. Aerodynamics is modelled through an unsteady vortex lattice method, where thickness of aerodynamic surfaces is neglected, whereas camber is allowed. An implementation of wake roll-up is also included. The degrees of freedom of the fully-coupled non-linear system are the circulation vector of the vortex lattice model and its first time derivative, the structural deformations and their first time derivatives, the position and orientation of the structural nodes and the respective first time derivatives with respect to the body reference frame, the position and orientation of the body frame with respect to the inertial frame, and the translational and rotational velocities of the body reference frame. The full inertial coupling between elastic and rigid body motion is enforced including also the effect of gyroscopic forces due to structural rotation. Such an effect is found to be relevant for example when yaw rate is present (as stated by Hesse and Palacios [6, 96]). The proposed approach proved able to show the limitations of the mean-axes formulation, which fails to account for large deformations. Figure 2.4 compares the evolution of a spiral manoeuvre computed with a full non-linear model, a linearized model and a mean-axes model, and shows some inaccuracy of the mean-axes formulation at low stiffness values. The varying stiffness E is parameterized with respect to a reference value E_0 through the parameter σ, defined as $\sigma = E/E_0$, with $\sigma = 10$ corresponding to the rigid body stiffness of the test-case employed. It is seen that even in the case of high stiffness, when the hypothesis of small deformations is satisfied, inaccurate performance predictions are obtained when rotation rates are relevant. This happens because the impact of gyroscopic effect is completely neglected by the mean-axes approximation, and it is visible in Fig. 2.5, where a constant relative error is produced even at high values of the stiffness parameter.

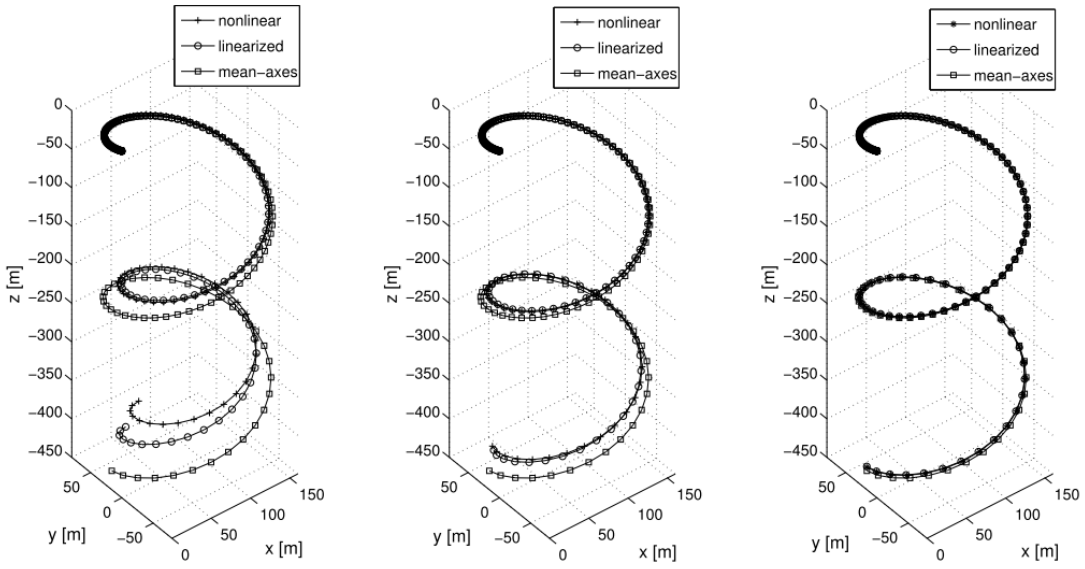

(a) $\sigma = 4$ (b) $\sigma = 10$ (c) $\sigma = 50$

FIGURE 2.4: Spiral trajectory predicted by three different levels of fidelity, for three different stiffness parameter values (σ=4, 10 and 50), from [6].

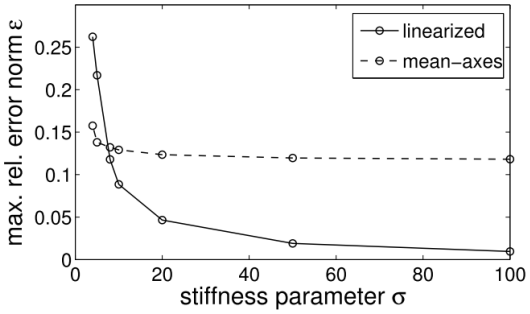

FIGURE 2.5: Relative error of linearized and mean-axes models with respect to fully-coupled nonlinear model with varying stiffness prameter σ, from [6]

In [7], the equations of motion are derived from the principle of virtual work, where geometrical non-linearities are allowed, and the structural model relies on a finite element discretization where each element is assumed to experience constant strain. A two-dimensional inviscid incompressible unsteady aerodynamic model is used, where a span-wise lift distribution function is adopted as a correction for flow three-dimensionality (a so-called 2.5D approach). The simulations of the complete test-case aircraft were carried out considering only the flexibility of the main wing, the fuselage and tail being treated as rigid surfaces. The model was implemented in a MATLAB toolbox at the University of Michigan. An interesting comparison of three levels of fidelity was performed to assess the respective range of validity. The lowest fidelity model simulated the rigid body dynamics of the statically-deformed aeroplane, where the static

deflection was pre-calculated around a certain equilibrium condition; the middle fidelity model retained the elastic degrees of freedom, but they were computed from a linearised approximation under steady-state conditions; the highest-fidelity model was the fully-coupled non-linear unsteady system. It was found that for simple symmetric manoeuvres, linearised solutions may be acceptable to capture the main aircraft dynamics, whereas for asymmetric manoeuvres a non-linear approach is required for an adequate description, especially of the lateral-directional states. Some significant results are shown in Fig. 2.6, where the response to a combined aileron and rudder input is reported for the three levels of fidelity.

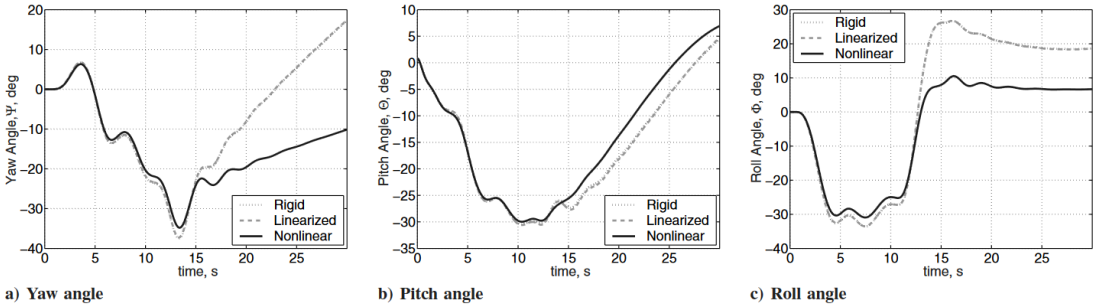

FIGURE 2.6: Comparison of responses to lateral controls with three levels of fidelity, from [7].

The above examples allow to extrapolate a few important observations.

First, they give an idea of the tools that are commonly used for these kinds of simulations. In virtually all cases, the aerodynamic models rely on inviscid, incompressible, potential, unsteady flow assumptions, such as the UVLM or unsteady strip theory. The structural model is only a beam method, preferably nonlinear to capture the effects of large deformations. The 6-degrees-of-freedom dynamics for time-marching trajectory calculation is retained in exact form (no linearization of the rigid-body equations of motion is enforced). This allows to correctly capture the system evolution over relatively long time windows.

Second, in many cases flexiblity is only taken into account for the wings, and the rest of the aircraft is considered rigid. This is a widely accepted approximation, as the most relevant aeroelastic effects are due to wing deformation, and it is especially valid for large tube-and-wing aircraft, where the main body is abundantly reinforced and rigid.

Lastly, as it can be seen from the time histories in Figures 2.4 and 2.6, the effect of flexibility does not seem to impact significantly the instantaneous overall aircraft response. This means that the 'rigid-body' modes remain sufficiently separated from the aeroelastic ones, so that no relevant interaction is observed to affect the aircraft stability characteristics. On the other hand, the effect of flexibility is seen in the long-term, after the dynamics is propagated for a few seconds. In particular, the main impact is seen in

the lateral-directional behaviour. Therefore, it appears that when the interest is mainly on the stability characteristics, or on the sudden response to a short disturbance (such as gust encounter), the aircraft motion and the structural response could be reasonably decoupled, at least on a first instance. On the other hand, if a long manoeuvre or flight phase has to be simulated, such as for guidance and control or pilot-in-the-loop studies, it is advisable to retain the fully-coupled system, including the nonlinear coupling between longitudinal and lateral-directional degrees of freedom.

From these considerations, the following conclusions are drawn:

- Potential flow methods such as VLM and strip theory and beam methods are the most suitable for the required aeroelastic analysis capabilities;
- Flexibility can be considered to affect uniquely the wings, and ignored for the rest of the aircraft structure;
- It is convenient to develop a modular framework with an aeroelastic module and a nonlinear flight dynamics module to be implemented separately and allowed to be coupled only when needed.

2.3 Sizing of high-aspect-ratio wings

The potential significant increase in aerodynamic efficiency deriving from high-aspect-ratio lifting surfaces has motivated a great research effort over time. In fact, as lift-induced drag can account for 40-50% of the aircraft's total drag in cruise [97], the reduction of this drag component, attainable by the adoption of more slender wings, still represents a highly attractive target, both from an economic and environmental point of view. However, one fundamental drawback is that a high-aspect-ratio wing inevitably features a long bending arm with respect to the wing root, requiring a strong and well-designed structure to cope with the increased loads. This would ultimately result in an increase of weight, with the risk of offsetting the aerodynamic benefits. The elongated wing would also imply higher deformations, especially if the structural mass has to be minimized at the expense of stiffness. This undoubtedly accentuates concerns about the aeroelastic safety of such wings, both in terms of static and dynamic behaviour.

Therefore, any effort to address the design of high-aspect-ratio wings has the mission to provide a trade-off between these conflicting aspects. In order to do that, it is necessary to take into account all the above issues, requiring significant analysis capabilities and computational resources. Indeed, the designer has to address different problems simultaneously, such as aero-structural analysis and optimization, dynamic aeroelastic simulations - where even the selection of appropriate methods and of a convenient

parameterization are not trivial tasks - as well as the integration within an overall aircraft design logic, since the design of an isolated wing does not insure the feasibility or the optimality of the solution found. In fact, the final assessment of the design success is in reality related not to the wing itself, but to the entire aircraft configuration, as the final objective is usually a global performance index such as fuel consumption, range, passenger capacity, etc. It becomes clear, then, how such a mission is rather a multidisciplinary problem.

The above considerations are true no matter what design phase is under examination. However, as already stated, this work is focused on the conceptual design level. This poses a two-fold problem, because on one hand there is a need to select and impose some simplifying assumptions in order to maintain the computational burden affordable while exploring the design space, but on the other hand it is necessary to implement the capabilities to address the main aeroelastic issues and assess whether or not they are critical for each particular design.

A relevant example of how the problem could be addressed is the approach proposed in [8]. The case is particularly pertinent first because the context is conceptual design, consistently with the present case, and second because the adopted baseline, adapted from the Airbus A320 series, is very similar to the CeRAS configuration that will be used throughout this project as a reference. Here, the authors tackle the problem in an effort to retain the effects of geometrical non-linearity on the aero-structural computation, demonstrating that they may significantly affect the sizing outcome. Apart from this conclusion, which is already a substantial contribution, it is interesting to present some more details about the adopted tools and methodology.

The overall objective of the paper is to develop a framework that enables parametric studies - such as the dependence on aspect ratio - for the Breguet range over a relatively simple aircraft model. To accomplish this, the wing is first sized and optimized from an aeroelastic perspective, in the sense that the sizing static manoeuvre loads are computed on the deformable wing.

Concerning the choice of the aeroelastic model, the VLM is adopted for the aerodynamic part. Lifting surfaces are represented by a flat plate approximation, following [16]. Only lift forces are taken into account in the aeroelastic evaluations. Drag is computed separately using semi-empirical relationships, following [98–100], and it is only used for the calculation of the Breguet range. The wing structure is modeled by two consecutive levels of abstraction. The first one is a simplified representation of a three-dimensional wing-box, considered rectangular and composed by two identical spars, the upper and lower skin and a series of identical and equally spaced stringers (see Figure 2.7), all made of the same aluminium alloy. This model serves in the first instance as a base to derive some 'condensed' properties for an equivalent finite element beam model, which constitutes the second level of abstraction. Each beam element is defined

by a series of mass and stiffness parameters that are calculated via some analytical expressions from the wing-box geometry.

It is the beam model that is coupled to the aerodynamic model for the aeroelastic analyses. The mapping between the structural and aerodynamic discretization is based on Radial Basis Functions (RBF), following the approach used in Neocass [78, 79]. When computing the sizing manoeuvre loads the structural model retains geometrical nonlinearity, and the static solution is found iteratively using the Newton-Raphson method. Once the nonlinear equilibrium is found, the beam forces and moments are transferred to the wing-box model, which is then used to evaluate the stress on the different components. The box-to-beam reduction approach significantly speeds-up the aeroelastic analyses. This is easily understood as a non-linear analysis based on a three-dimensional finite element model of the wing-box representation would imply an enormous increase of the structural degrees of freedom, as well as additional complexity in terms of numerical convergence and stability. The use of equivalent beam models (also known as stick models) to speed up aeroelastic studies on large aircraft wing structures has widespread support, as confirmed by several prominent modern works on flexible aircraft MDAO [11, 78, 79, 94, 101]. For the interested reader, a thorough investigation of different possible approaches is provided for example by [102].

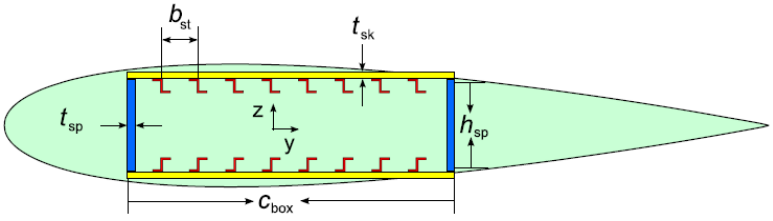

FIGURE 2.7: Wing-box cross section idealization used in [8].

The structural optimization is performed by using as variables the three geometrical quantities that define the wing-box geometry at each section: the spar thickness, skin thickness and stringers' area. The objective is to minimize the wing mass under a series of structural failure constraints, including the Von Mises stress, the skin buckling stress, the crippling and buckling stresses in the stringers.

Some conclusions are worth mentioning here. The authors state that a strong correlation was found between structural displacement and final wing mass, as well as structural displacement versus range. These aspects are better understood by looking at Figure 2.8. In particular, it is stated that the adoption of a geometrically nonlinear structural model brought a mass reduction of over 5% compared to the linear analysis. Also, it can be seen again from Figure 2.8 that the optimal configuration, in their case providing the longest range, varies depending on whether a linear or nonlinear model is used. These findings suggest that a nonlinear structural representation may be desirable, especially if mass minimization and fuel minimization are to be performed. The importance of nonlinear structural models is confirmed also by other studies on

high-aspect-ratio wings, such as in [29, 103, 104]. A less clear correlation was found instead between displacement and aerodynamic efficiency, indicating that a more approximated approach may still be adequate for cruise drag evaluation. Finally, it is interesting to note that in one study they identify an optimal aspect ratio of 19, which is reduced if some wing span constraints are applied. This looks quite a high value for a full-aluminium structure, considering that an Airbus A320 has an aspect ratio of about 9.5. These interesting results motivate further studies on similar high-aspect-ratio wings with adequate analysis tools.

Overall, the work clearly shows a remarkable maturity in addressing a complex multidisciplinary design and optimization task, where both aeroelastic issues and overall aircraft design aspects are taken into account. The proposed methodology is certainly inspiring in the context of the present project. Nevertheless, it should be pointed out that some limits still emerge. In fact, there is no actual optimization at the aircraft level, but rather a few simple parametric studies. Also, dynamic aeroelasticity is not taken into account at all, nor is the impact of uncertainty of any sort. Therefore, it is believed that the present research objectives remain challenging and relatively unexplored.

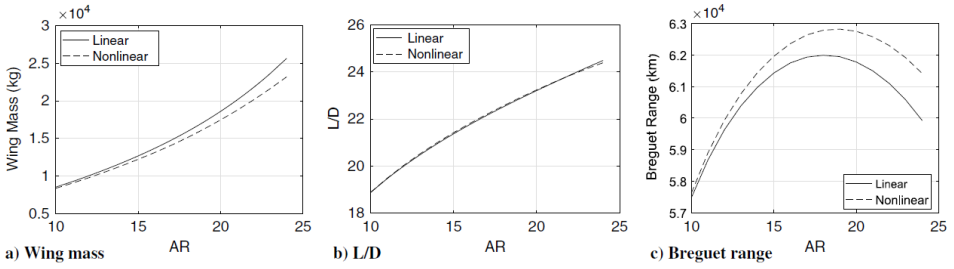

FIGURE 2.8: Effects of linear and nonlinear structural models on overall aircraft figures of merit, from [8].

2.4 Dynamic aeroelasticity

An important and challenging aspect to be considered when dealing with flexible airframes, especially lifting surfaces, is dynamic aeroelasticity. In fact, on one hand there are important safety implications, because dynamic effects such as flutter and gust response are potentially dangerous phenomena that need to be cautiously analyzed. On the other hand, dynamic aeroelasticity requires significant computational capabilities, both in terms of model complexity and computational time. Therefore, including an assessment on these aspects during the conceptual design of high-aspect-ratio aircraft remains a research challenge, and it represents one of the main gaps that this project seeks to address.

The following Sections give some background on the two main dynamic aeroelastic problems this work focuses on: the flutter problem in Section 2.4.1, and dynamic gust

loads in Section 2.4.2. Also, a review of some relevant examples of aircraft MDAO studies where these aspects are taken into account is given in Section 2.4.3.

2.4.1 The flutter problem

Aeroelastic flutter is undoubtedly one of the major sources of concern when exploring flexible high-aspect-ratio wings. This is true not only because flutter is a very dangerous phenomenon, but also because it is difficult to accurately predict. Reliable tools exist today, of course, but they are in general high-fidelity, expensive methods, in most cases tuned and validated against experiments on existing configurations. The main challenges arise when addressing conceptual design of unconventional configurations, where less data and less time are available. For example, divergent modes could differ from one configuration to another, and this requires to retain a sufficiently large number of modes for all calculations. For these reasons, flutter is in most cases ignored during the traditional conceptual design steps, and it is only studied in later phases of the process. However, one limit of this approach, as discussed in Section 2.6.5, is the commitment of considerable costs in those advanced phases, due to the high expense of analyses and eventual design adjustments carried out at that point of the development. Therefore, one interest of the present project is to develop and test an alternative approach for the conceptual design of high-aspect-ratio configurations where the main aeroelastic issues, including flutter, can be taken into account. It is clearly impossible to completely perform in advance all the preliminary and advanced studies at a much lower cost. The objective here is rather to be able to derive some trends - of the desired objective function and aeroelastic constraints - with respect to critical design variables (such as aspect-ratio, or wing structural parameters) in order to anticipate the main hazards connected to unconventional configurations and reject the most risky ones from the set of optimal solutions. This would ultimately mitigate the cost and risks of advanced studies by reducing the design space around a conceptual optimum which is already expected to be free from flutter - albeit not with 100% confidence.

With this aim in mind, this Section continues with a brief review of the theory and the main methods available in the literature for flutter analysis, by focusing on those compatible with the stated conceptual design requirements.

By definition, flutter is *a dynamic instability of a flight vehicle associated with the interaction of aerodynamic, elastic, and inertial forces* [105]. As such, it is convenient to treat the problem from the perspective of dynamic system stability, which consists of deriving a suitable model of the physics behind, express it in linear form and infer its stability characteristics by studying its eigenspectrum. The general form of what is known as the flutter equation, describing the equilibrium between the above three types of forces, is given in Equation (2.1) (from [106]).

$$\left[\frac{V^2}{c^2}\boldsymbol{M}p^2 + \boldsymbol{K} + \frac{1}{2}\rho V^2 \boldsymbol{A}(p)\right]\boldsymbol{q} = \boldsymbol{0} \tag{2.1}$$

The matrices $\boldsymbol{M}$, $\boldsymbol{K}$ and $\boldsymbol{A}(p)$ relate the generalized displacements $\boldsymbol{q}$ with the generalized inertial, elastic and unsteady aerodynamic forces, respectively. The variable p can be seen as the nondimensional differential operator $c/V\,(\frac{d}{dt})$ in the time domain, or, equivalently, the Laplace variable in the Laplace domain.

Of course many different physical models, combining a variety of structural and aerodynamic theories, can be expressed in the form of Equation (2.1). However, according to how the aerodynamic formulation depends on p, the approaches can be grouped in most cases in three main categories:

- p methods: If the aerodynamic forces can be expressed as a sufficiently simple function of p, at any fixed value of density and speed, Equation (2.1) can be solved as a classical eigenvalue problem, where each possible solution $p = \lambda + i\,k$ is a complex number related to the frequency and damping of a particular mode. These methods offer a practical solution of the flutter problem, and are potentially valid anywhere below and above the flutter speed, provided that the aerodynamic model remains valid at the corresponding flow conditions. However, the method is not the most popular, because not many aerodynamic models allow such a general and simple dependence on p. A classical example can be found in [107].

- k methods: More sophisticated aerodynamic formulations, such as from the kernel function or doublet lattice approach or the supersonic Mach box, lead to aerodynamic matrices valid only for harmonic motion, $p = ik$. These methods are able to provide the exact flutter speed, at which in effect the hypothesis of harmonic motion is realistic because oscillations become undamped, but they cannot offer an accurate view of the migration of modal frequencies and damping ratios with varying speed. Also, they are not guaranteed to predict what is the real mode to first become unstable.

- p-k methods: These methods represent an extension of the basic k methods. It is assumed that for sinusoidal motion with slowly decreasing or increasing amplitudes the aerodynamic model based on harmonic motion remains a good approximation. This allows to somewhat extend the sophisticated frequency domain aerodynamic theories in the neighbourhood of the zero-damping flutter speed.

Other slightly different approaches to solve the flutter problem have been proposed, but their thorough examination is out of the scope of this work. The interested reader can find additional information for example in [108, 109]. The interest here is just to

give an overview of the problem and the available solution methods. Some applications involving dynamic aeroelastic constraints, including flutter, during conceptual aircraft MDAO are discussed in Section 2.4.3. Before that, Section 2.4.2 introduces another important issue in dynamic aeroelasticity, namely gust-induced loads.

2.4.2 Dynamic gust loads

Gust response is a critical aeroelastic issue in aircraft sizing. The static manoeuvre loads are never considered sufficient in any sizing approach, even in traditional conceptual design. Moreover, recent evidences show that modern climate changes can have a significant worsening impact on wind gust, such as a 20-30% increase in the daily or hourly occurrences of high-speed gust events. Such a trend may lead to increased attention to gust loads in the future aircraft sizing and certification processes. And even at present, specifications always impose to combine the static manoeuvre flight envelope with the gust envelope, and pick the most critical conditions among the two. This is shown in Figure 2.9. For a rigid aircraft the effect of a vertical gust can be considered with good approximation proportional to the flight speed [110]. This is why the gust envelope is represented by straight lines whose slope depends on the gust intensity, and which are superimposed to the steady level flight condition, represented by a load factor $n = 1$. Common discrete values of vertical gust speed used for initial sizing are U1 = 50 ft/s and U2 = 25 ft/s.

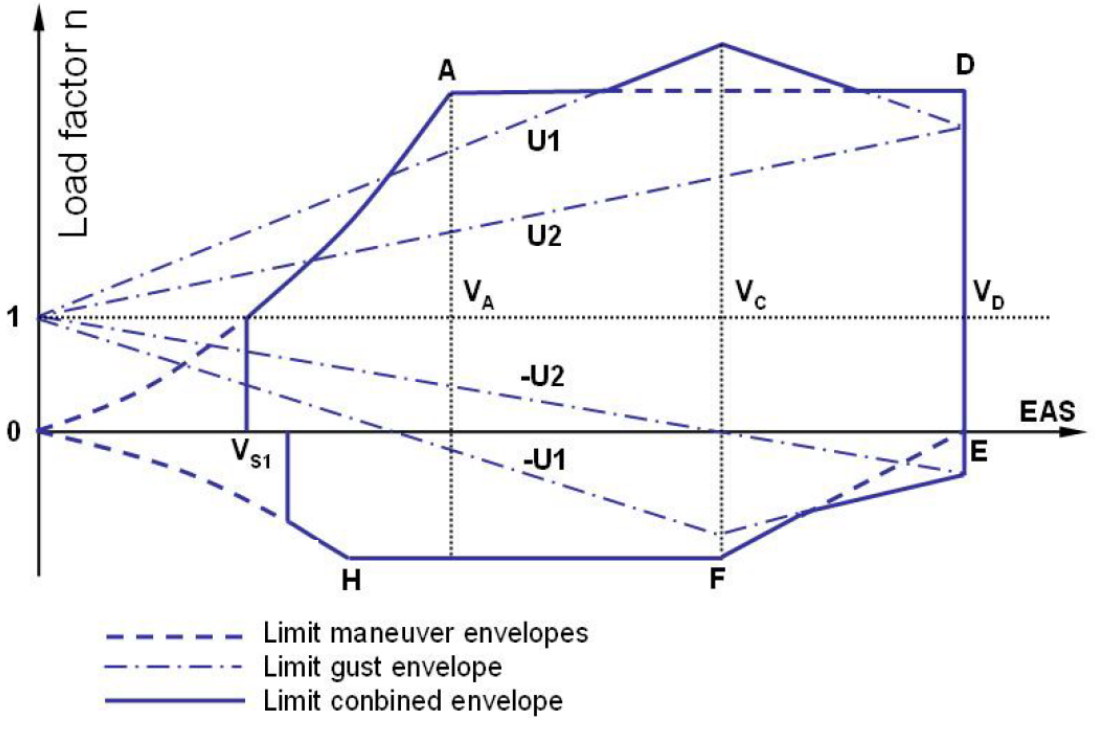

FIGURE 2.9: Superposition of manoeuvre and gust envelopes, from [9].

However, even for rigid aircraft, the actual dependence of the load factor on the gust speed should be corrected to account for the alleviation arising from unsteady aerodynamic effects. In the conventional conceptual design approaches, this is done through some semi-empirical relationships. For example, reference [9] adopts the experimental alleviation factor proposed by Pratt and Walker [111] k_g, so that the gust-induced load factor is:

$$n_{\text{gust}} = \frac{\rho}{2\,g}\,k_g\,U\,\frac{V_{\text{C(EAS)}}C_{L_\alpha}}{m/S} \tag{2.2}$$

$$k_g = \frac{0.88\,\mu_g}{5.3 + \mu_g} \tag{2.3}$$

$$\mu_g = \frac{2\,m}{\rho\,S\,c_{\text{MGC}}C_{L_\alpha}} \tag{2.4}$$

where ρ is the air density, U is the vertical gust speed, $V_{\text{C(EAS)}}$ is the cruise equivalent air speed, C_{L_α} is the aircraft lift-curve slope, m is the aircraft mass, S the aircraft reference surface, c_{MGC} the wing mean geometric chord.

The objective of the conceptual sizing is to estimate the worst gust loads and the mass of an appropriately sized structure to sustain them. From Equations (2.2) to (2.4) it emerges that a nonlinear relationship relates the load factor to the aircraft mass. This means that the worst mass case for gust loads is not known a priori, and several cases should be analyzed. In practice, it is acceptable, at the earliest stage, to compute the two extreme cases of lowest and highest mass [9]. In particular, the lowest mass to be considered is the maximum zero-fuel weight (MZFW), increased by 5% to account for a minimum quantity of fuel always remaining onboard. The maximum mass case, instead, corresponds to the maximum take-off weight (MTOW). However, in this case the mass of the fuel stored in the overhanging part of the wing reduces the bending moment at the wing root, so its contribution to the total load factor has to be subtracted. This contribution is given by its mass, denoted as MCV, multiplied by the distance of its center of gravity from the root chord. Reference [9] approximates this distance as 55% of the distance from the point of application of the aerodynamic loads, so that ultimately, the mass considered in this case is MTOW - 0.55 MCV.

Once the two load factors are calculated, they are compared to the manoeuvre limit load factor of 2.5, and the highest is used to estimate the required structural mass.

Such a semi-empirical approach can be considered quite accurate when dealing with conventional designs, but there is no guarantee that it holds valid for unconventional configurations. Especially when flexible high aspect ratio wings are involved, the subject becomes risky, as these wings are more prone to high gust-induced aeroelastic

loads. For this reason, it is of interest in this work to investigate the effects of gust loads, in addition to flutter, when included as dynamic aeroelastic constraints during a flexible aircraft MDAO.

When addressing the problem in a more physics-based perspective, where semi-empirical formulas are of no interest, useful indications can be found in the certification specifications (EASA CS25 [112] or FAA part 25 [113]). These regulations indicate two main approaches to verify airworthiness with respect to gust loads. The first one consists in determining the dynamic response to prescribed discrete gust inputs. The second demands to verify the response to a continuous turbulence model, provided in frequency domain. Of course verifying full compliance with regulations is definitely out of the scope of this work, and in general of any conceptual design task. Here, regulations are just used as a reference to define realistic design constraints, and no attempt is made to enforce a thorough assessment of compliance. This work only focuses on the first of the two approaches.

The discrete gust shape prescribed by regulations has the '1-cosine' form described in Figure 2.10. The disturbance is assumed to be one-dimensional with the gust velocity acting normally (vertically in this case) to the airplane advancing direction. The one-dimensional assumption constrains the instantaneous vertical gust velocities to be the same at all points in planes normal to the direction of airplane travel. The disturbance is considered frozen in space while the airplane crosses its field. The shape is defined by two main parameters: the gust gradient, H, corresponding to half of the wavelength, and the gust amplitude, or design gust velocity, U_{ds}, indicating the maximum vertical velocity. The latter is given as a function of the gust gradient, extrapolated according to experimental evidences, so the two parameters are not independent. The curve describing this dependence is also shown in Figure 2.10. In order to assess the structural safety with confidence, it is recommended to compute the responses to a sufficient number of different gust gradients, because the worst combination of frequency and amplitude is in general not known a priori.

The appropriate design gust velocity depends not only on the gust gradient, but also on the flight altitude and on the aircraft mass properties. In particular, the expression provided by regulations is:

$$U_{ds} = U_{\text{ref}} F_{\text{g}} \left(\frac{H}{350} \right)^{1/6} \tag{2.5}$$

where the reference speed U_{ref}, to be expressed in ft/s, is provided by the specifications, and only depends on the altitude and on whether the flight speed is set to the cruise speed V_C or the dive speed V_D. F_g is called the flight profile alleviation factor, and introduces the dependence on different aircraft properties as follows:

$$F_g = 0.5 \left(F_{gz} + F_{gm}\right) \tag{2.6}$$

where:

$$F_{gz} = 1 - \frac{Z_{mo}}{76200} \tag{2.7}$$

$$F_{gm} = \sqrt{R_2 \tan\left(\frac{\pi R_1}{4}\right)} \tag{2.8}$$

$$R_1 = \frac{\text{Maximum Landing Weight}}{\text{Maximum Take-off Weight}} \tag{2.9}$$

$$R_2 = \frac{\text{Maximum Zero Fuel Weight}}{\text{Maximum Take-off Weight}} \tag{2.10}$$

$$Z_{mo} = \text{Maximum operating altitude} \tag{2.11}$$

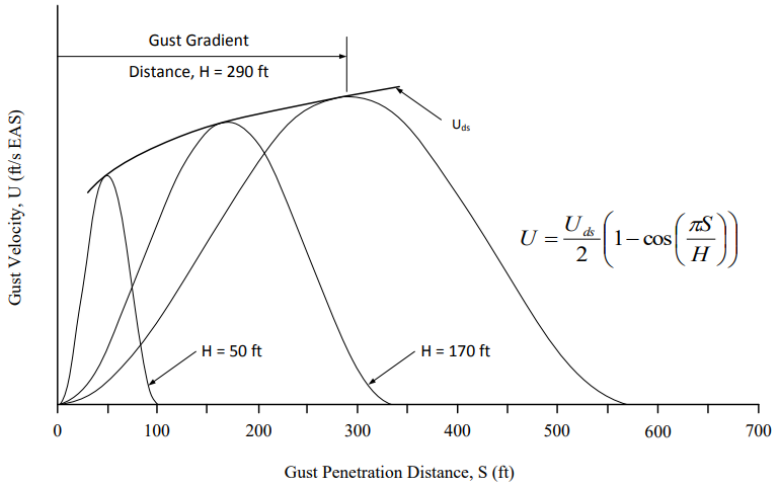

FIGURE 2.10: Typical '1-Cosine' design gust velocity profiles, from the FAA Advisory Circular 25.341-1 [10].

The above expressions can be used to enforce some realistic simulation-based constraints on dynamic gust loads.

2.4.3 Dynamic aeroelasticity for conceptual aircraft MDAO

It is of interest here to show that some solutions involving the above methods are suitable and have been successfully applied to aircraft design and optimization cases. In

particular, the Neocass framework [78, 79] allows the computation of flutter speed using an aeroelastic model based on a stick model for the structure, derived from a wing-box representation as discussed in Section 2.3, and the DLM to model the aerodynamics. Another interesting application where flutter speed is calculated at conceptual level in support of aircraft design is the one proposed in [11]. Here the aeroelastic model is based on a frequency-domain unsteady strip theory formulation, with a proposed correction to capture some compressibility effects in the transonic domain, and again a beam model derived from a wing-box geometry. It should be underlined that in both cases certain limitations had to be retained as a compromise to address a conceptual-level problem. For example, the DLM in itself is only valid for incompressible, irrotational and inviscid flow, and is effective under the hypothesis of small deformations. However, under these limitations, it captures well the unsteady three-dimensional aerodynamics, and is therefore generally accepted for aeroelastic computations at conceptual design. The same is true for the unsteady strip theory, especially if applied to high-aspect-ratio wings. In fact, as stated in [11], although it fails to capture the three-dimensional wing tip effects, strip theory remains an accepted method for the aerodynamic response of high-aspect-ratio wings [114, 115], thoroughly validated in the literature [29, 116].

Regarding how flutter speed calculations are integrated within the aircraft design process, the two frameworks follow different approaches. In Neocass, flutter can be included as a constraint only during the inner structural sizing phase, with the overall aircraft variables being kept fixed. An example application is provided in [117]. In short, their approach consists of individuating in Equation (2.1) the dependence on the prescribed structural variables and evaluate by use of finite differences the eigenvalues derivatives with respect to the structural variables. These in turn are used to finally calculate the derivative of the flutter constraint with respect to structural variables, so that they can be employed during a gradient-based optimization.

The approach of [11], instead, demonstrates how the newly-developed aeroelastic solver was coupled into an existing aircraft design tool, namely the Transport Aircraft System OPTimization (TASOPT) tool [118], developed at MIT. As a first coupling of two initially separated programs, the approach is kept simpler: the flutter speed is calculated for each design candidate during the overall aircraft optimization process, and a cost function is defined to penalize each candidate that approaches or reaches instability. The monitored quantity is the highest real part of the eigenvalues obtained by solving Equation (2.1). Although being a less sophisticated approach compared to the one in [117] just discussed, it represents a more straightforward way to couple an external solver to an existing aircraft design platform. This allows greater flexibility for plugging and testing different solvers. An important conclusion reported from [11] is that a flutter constraint may have a decisive impact on the design of a high-aspect-ratio aircraft. In fact, the proposed demonstrative application, carried out around a Douglas

D8 baseline, shows that flutter speed effectively limits the optimal feasible aspect ratio, resulting in a 3.3% higher fuel burn compared to the unconstrained optimum. Also, the study continues by investigating the effect of possible new material technology improving the allowable stress, with respect to the standard aluminium baseline. Results show that the impact of a flutter constraint on fuel burn and maximum take-off weight would be more and more significant with increasing material performance (see Figure 2.11). Reference [117] does not provide such a comparative analysis, but states that the flutter-constrained structural sizing process managed to move the flutter speed of the optimized baseline from 100 m/s to above 250 m/s.

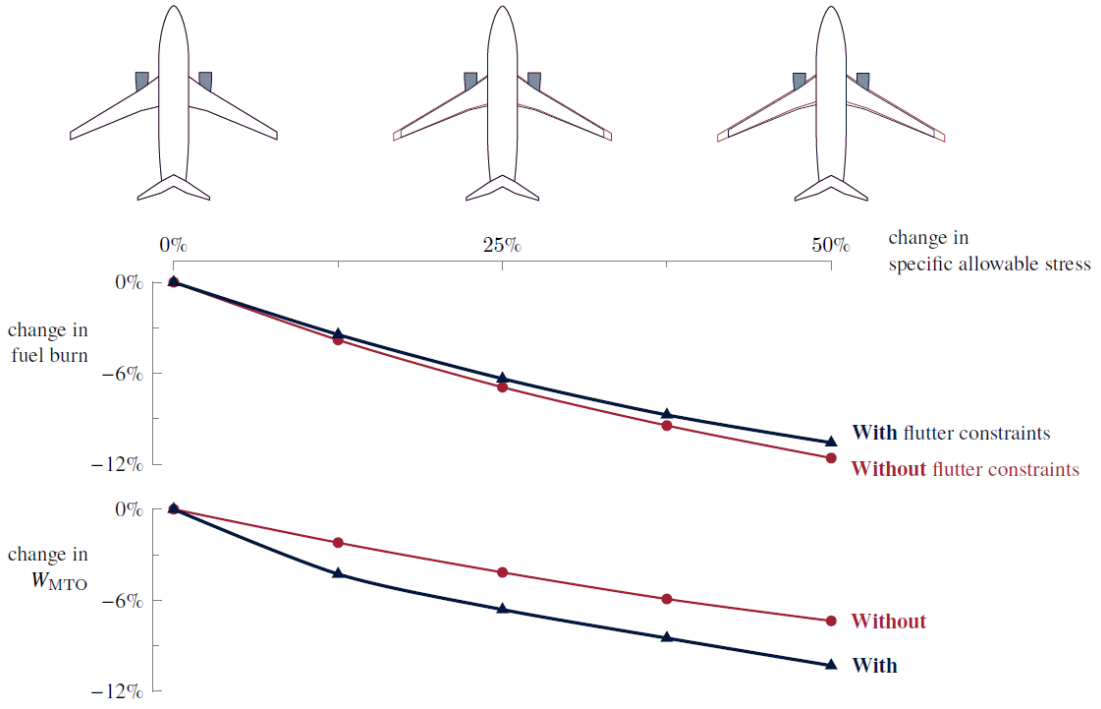

FIGURE 2.11: Variations of optimum fuel burn and maximum take-off weight with specific allowable stress and effects of a flutter constraint in the loop (from [11]).

These examples are not the only ones available in literature, but they were chosen to be discussed here because they give a good idea of the state of the art at the time of writing. In particular they turn out to be relevant example because both of them show validated applicability to modern transport aircraft, which is the main focus of this work. However, there are other successful applications of multidisciplinary optimization applied on aircraft design that are at least worth mentioning, such as [12, 13, 119]. One in particular, presented in [12, 13] deserves appreciation for the remarkable maturity and complexity. The work presents an MDO framework for the conceptual-preliminary design of solar HALE unmanned drones, where several disciplines, including flight dynamics and aeroelasticity, are treated with physics-based approaches. A few applications are presented, demonstrating the capability of performing a multi-objective optimization - mass minimization and endurance maximization - constrained by several disciplinary

constraints, including worst-case stresses, static margin, control reversal, tip stall margin at cruise, dynamic and aeroelastic stability, and battery charge. It should be noted that such a wide coverage of disciplines is probably enabled by the fact that the study is conducted at an industrial level, where all the relevant expertise is promptly available with a well-developed and mature technological know-how. Although the present project is developed in a different, research-level environment, and such a wide multidisciplinarity is not envisaged, it is still worth to note that: first, this example further confirms the interest of including static and dynamic aeroelasticity, as well as flight dynamic performance, in the optimization loop; second, the methods proposed to address aeroelastic analyses confirm an establishment in the state of the art, as they are not significantly different from those identified above. In fact, the aeroelastic model is taken from the MIT `ASWING` code [120, 121], and consists of an unsteady strip theory model coupled with a nonlinear beam. The beam properties, in turn, are derived from the two-dimensional characteristics of a wing-box representation, allowed to include composite layers, by use of the dedicated software `Co-Blade` [122].

Another interesting aspect to underline from [12, 13] is the use of dynamic aeroelastic constraints in the loop. In particular, the implementation of the flutter constraint is treated similarly as discussed above, with the worst-case damping ratio identified from the eigenvalues (for all altitudes) and returned to the optimizer. Also, in addition to what already seen, this time also the dynamic aeroelastic response to gust is included as a constraint. This is implemented by allowing time-marching simulations at certain prescribed flight conditions. The reported examples show the possibility of simulating either a one-dimensional linear gust ramp, or a two-dimensional '1-cosine' shape (see Figure 2.12). As gust encounter simulations may turn out to be quite expensive, especially if intended to be run several times during optimization loops, for each of the gust case, an offline study was carried to derive worst case non-dimensional gust shape parameters - e.g. longitudinal characteristic length over chord - and therefore reduce the number of simulations required.

It is not clear how relevant the impact of all these constraints was in the reported case studies, compared to a more conventional unconstrained approach. However the authors state that the constraints were active and contributed to shape the final optimal configuration. In [13] they even discuss the effect of including an Active Flutter Suppression (AFS) system, demonstrating that such a technology would allow a 10% weight saving compared to a passive solution, consisting in a more robust structure with increased stiffness. Although this result cannot be taken as a general conclusion, it is still useful to show how critical it is to enable an aircraft design framework with aeroelastic analysis capabilities.

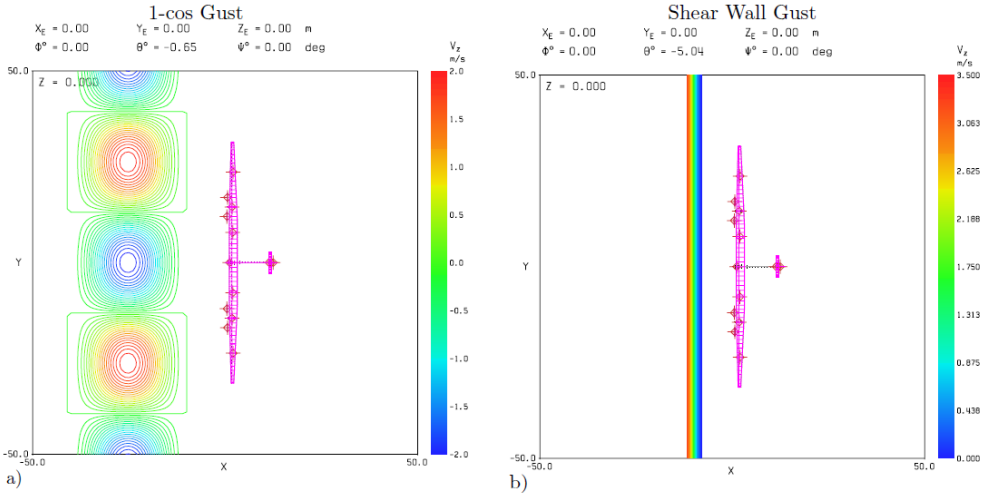

FIGURE 2.12: Examples of gust encounter setups for dynamic aeroelastic simulations, as implemented in the MDO framework proposed in [12, 13].

2.5 Multi Disciplinary Optimization

As Multidiscipinary Design and Optimization (MDO) is in general linked to complex and expensive problems, the choice of the optimization approach to adopt is of critical importance. In fact, despite the physical phenomena to be analyzed in the aerospace domains are in most cases adequately addressed by a variety of modern computational methods and tools, the computational time required for the different analyses still represents a challenging obstacle. Therefore, the efficiency of the optimization algorithm managing the analysis iterations can determine the success of the design approach. For this reason, great effort has been invested in the development of efficient MDO architectures and optimization algorithms. One significant example is the establishment of the AGILE European project[1], which collects contributions from many important European aerospace research and industrial institutions. An extensive discussion on this wide topic could easily be the subject of an entire dedicated manuscript, which is clearly not the objective of this work. Some relevant and detailed literature can be found for example in [94, 123–126].

Here, the focus is restricted on one of the best performing approaches successfully applied to large and complex MDO problems [127, 128], namely Bayesian optimization, for which an overview is provided in Section 2.5.1. Moreover, some efficient extensions of this approach, leading to the so-called Super-Efficient Global Optimization, are discussed in Section 2.5.2, as they appear particularly promising for the aims of this project.

[1] https://www.agile4.eu, 2019-2022

2.5.1 Bayesian optimization and Efficient Global Optimization

Bayesian optimization is a machine learning technique best-suited to optimizing expensive objective functions which in general lack known special structure - like concavity or linearity - and for which derivatives are not available [14]. Because of this lack of knowledge, such functions are often referred to as 'black-box' functions. Bayesian Optimization is effective for global optimization over continuous domains and may tolerate stochastic noise in function evaluations. According to [14], the best use of this class of methods is for problems of less than 20 dimensions, although such a value is actually problem-dependent, and therefore should probably be seen only as indicative. The optimization of a coupled MDA often lies in this class of problems, because the analysis can be nonlinear, expensive, sometimes noisy, and with a limited set of design variables.

One key ingredient that makes this approach effective is the use of surrogate models to represent the expensive objective function. In particular, differently from other surrogate-based optimization methods, Bayesian optimization surrogates are developed using Bayesian statistics, and the decision on where to evaluate the objective derives from a Bayesian interpretation of these surrogates.

A Bayesian optimization algorithm consists of two main components: a Bayesian statistical metamodel approximating the true objective function, and an acquisition function used to decide where the real function should be sampled after each iteration. The statistical model is a Gaussian process (GP) [129], also known as Kriging, that associates to any point in the design space a probability distribution for the corresponding true value of the objective function. It is first built based on an initial set of function evaluations, usually selected according to a Design of Experiments (DOE), and then updated at each new observation during the enrichment process. The acquisition function (or infill criterion, or acquisition criterion), instead, is aimed at selecting the point with the best chance to approach the optimum. The most common acquisition function is the Expected Improvement (EI), which seeks to return as a choice for the next evaluation the point representing the best combination of large local uncertainty and promising mean value of the surrogate objective function, as it will be clarified later. The basic pseudocode for a Bayesian optimization process is provided in Algorithm 1. A graphical example of a Bayesian optimization step based on Expected Improvement is given in Figure 2.13.

The GP regression is based on the hypothesis that, for any point $\boldsymbol{x}$, the unknown objective $f(\boldsymbol{x})$ can be expressed as a multivariate normal probability distribution, with a particular mean value $\mu_0(\boldsymbol{x})$ and a covariance matrix given by a *covariance function* or *kernel* $\Sigma_0(\boldsymbol{x}_i, \boldsymbol{x}_j)$ that can be evaluated for each pair of points $\boldsymbol{x}_i$, $\boldsymbol{x}_j$. The kernel is chosen so that points $\boldsymbol{x}_i$, $\boldsymbol{x}_j$ that are closer in the input space have a large positive correlation, reflecting the assumption that their function values should be more similar than points

Algorithm 1 Basic pseudocode for Bayesian optimization

Input: Objective function f, initial DOE of size n_0, maximum number of iterations N
  Define a Gaussian Process to represent the objective function f
  Define an appropriate acquisition function
  Observe f at n_0 points according to an initial DOE
  while $n \leq N$ **do**
    Update the GP surrogate model
    Find $\boldsymbol{x}_{n+1}$ maximizing the acquisition function
    Evaluate the objective function $f(\boldsymbol{x}_{n+1})$
    Update current best $f^*(n)$
    Increment n
  end while
Output: Point corresponding to the best evaluated objective function

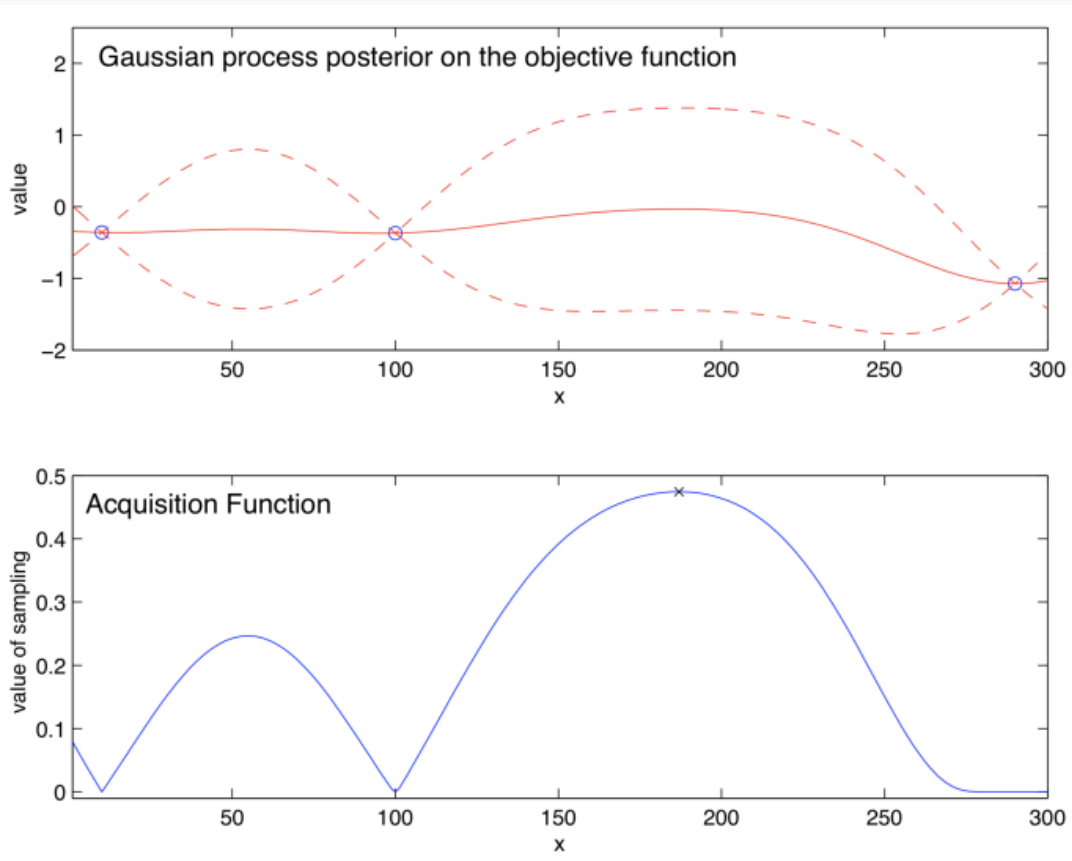

FIGURE 2.13: Illustration of the Bayesian optimization mechanism, from [14]. The top figure shows the Gaussian Process regression of a 1D function in terms of mean (solid line) and 95% confidence interval (dashed envelope). The model is derived after three function evaluations, indicated by blue circles. The bottom figure plots the associated Expected Improvement acquisition function. The point that maximizes the EI (represented by an 'x') is selected for the next objective function evaluation.

that are far apart. Different formulations are possible for the mean and kernel functions. For example, the mean can be expressed by a constant value, or by a simple polynomial in $\boldsymbol{x}$, the latter being more useful when representing an objective function expected to have some specific trend. Different options are also commonly used for the kernel function, such as the *power exponential* or *Gaussian* kernel, or the *Màtern* kernel [14].

The most commonly used acquisition function is the Expected Improvement. Its definition follows a simple reasoning: it is desired that each sample at which the true, expensive objective function is evaluated corresponds to a large improvement with respect to the best values among the previous evaluations. Such improvement is of course unknown until the next evaluation is done. However, it is possible to have an estimation of this improvement based on the assumed GP surrogate. If n evaluations have already been performed, and f_n^* is the best collected value at the moment, the Expected Improvement is a measure of such estimation, defined as in Equation (2.12).

$$\mathrm{EI}_n(\boldsymbol{x}) \;:=\; E_n\left[[f(\boldsymbol{x}) - f_n^*]^+\right] \tag{2.12}$$

Here, E_n indicates the expectation based on the knowledge of the previous n evaluations, and the apex $[\ ]^+$ indicates that the value is retained only if positive, and is set to zero otherwise.

A closed form to compute the expected improvement based on the statistical properties of the Gaussian Process (mean and variance as functions of $\boldsymbol{x}$) is described in [130] or [131]. The mathematical development is not reported here, but the main outcome is that with an available expression for $\mathrm{EI}_n(\boldsymbol{x})$ it is possible to select the next sample as the one that maximizes it:

$$\boldsymbol{x}_{n+1} \;=\; \arg\max(\mathrm{EI}_n(\boldsymbol{x})) \tag{2.13}$$

The EI function is inexpensive to compute, despite it can present issues in its numerical differentiation. However, solving Equation (2.13) remains a relatively fast task that can be addressed by several classical optimization methods. This approach, first introduced by Močkus [132], was revived by Jones [131] under the name of Efficient Global Optimization (EGO).

The methodology just discussed represents one of the main approaches for efficient global optimization of expensive black-box functions. However, other variants have been proposed in the literature. For example, other acquisition functions can be used in alternative to the Expected Improvement, such as Knowledge Gradient (KG), Entropy Search (ES), Predictive Entropy Search (PES) or Multi-Step Optimal Acquisition Functions. Moreover, the basic logic of Bayesian optimization just discussed was extended to more complex problems, such as those involving noisy evaluations, parallel

computations, multi-fidelity approaches and others. The interested reader can find further information in [14].

2.5.2 Super-Efficient Global Optimization

Recent developments have allowed further improvements of the EGO approach. In particular, a first method addressing the incorporation of constraints, not contemplated by the original EGO, was proposed by [133]. The method allows solving general nonlinearly mixed constrained problems, and was named Super-Efficient Global Optimization (SEGO). Further improvements have been discussed by [134, 135], concerning the handling of a large number of design variables, the introduction of more efficient infill criteria, improving the original formulation based on the Expected Improvement, and the combination of Mixture of Experts (MOE) in order to adapt the approach to more complex multidisciplinary problems. A better way to handle constraints was also proposed by [128, 136], where a demonstration is presented over an aircraft MDO application.

One key idea of SEGO, which determines its great potential, is the handling of mixed equality and inequality constraints by introducing additional metamodels, one for each constraint function. This is of great benefit especially when those constraints imply the evaluation of other expensive functions. This would be the case for example when introducing dynamic aeroelastic constraints within an overall aircraft sizing and optimization framework.

However, taking constraints into account by means of their Bayesian surrogate models is not a trivial task. One problem, for example, is that the estimation of feasibility obtained only via the mean of their GPs does not grant feasibility with respect to the true constraint functions. Nevertheless, satisfactory results have been obtained by means of the so-called Upper Trust Bound technique [136], which encourages exploration of the feasible domain by combining the mean prediction and the associated uncertainty function given by the GP.

Another challenge is the solution of the optimization problem to maximize the Expected Improvement acquisition function over the feasible domain. This problem can easily become very difficult, as the acquisition function EI is highly multimodal, as visible in Figure 2.13. For this reason, some modified acquisition functions have been proposed. One example is the one proposed by Watson and Barnes, which subtracts the GP mean from the EI, as shown in Equation (2.14). Such a function was shown to ease the solution of the optimization problem with a significant increase in efficiency.

$$\mathrm{WB2} = \mathrm{EI}(\boldsymbol{x}) - \mu(\boldsymbol{x}) \tag{2.14}$$

One additional modification of this criterion, proposed by [135], consists of adding a scale factor s to the EI, which has a smoothing effect on the acquisition function with additional benefit in terms of optimization cost. The new criterion is indicated as WB2S, and is expressed as in Equation (2.15).

$$\text{WB2S} = s\,\text{EI}(\boldsymbol{x}) - \mu(\boldsymbol{x}) \tag{2.15}$$

These characteristics are among the main and most recent improvements of the SEGO strategy, making it a cutting-edge solution for efficient optimization of expensive black-box functions under mixed, expensive black-box constraints. Therefore, it is probably the most suitable and flexible technique for the kind of Multi Disciplinary Optimization problems to be addressed in this project. Moreover, the ONERA center of Toulouse, which has supported this project as research partner, has given a large contribution to the latest evolution of the SEGO approach [128, 134–136], and has developed its own SEGO suite, named `SEGOMOE`. For this reason, this tool was selected to address the most complex MDAO cases presented later in this manuscript.

2.6 Design under uncertainty: optimization, reliability, robustness

2.6.1 General considerations

One main driver motivating the present research project is the fact that complex design problems inevitably imply uncertainty and risks, and the more complex the problem, the higher the uncertainty. Investigating the impact of uncertainty is in many cases of fundamental importance, at research level as well as at industrial level. The problem is that such investigations significantly increase the computational cost compared to deterministic studies. This is why uncertainty quantification and design under uncertainty are still very active research topics. This Section is aimed at highlighting the main aspects of this problem, discussing the possible formulations, and clarifying the concepts of reliability and robustness in the context of design under uncertainty. Then, Section 2.6.5 further discusses the issue with more specific focus on aircraft multidisciplinary design, providing also some example applications from the recent literature.

A useful classification of design and optimization problems in the context of uncertainty is provided by Levrière [15]. It is based on the fact that any design problem depends on two kinds of functions; the objective function and the constraint function. The proposed classification distinguishes the cases where uncertainty is propagated

into the objective function from those where it is propagated into the constraint function. The first case involves the concept of 'robustness', defined as the quality of a system's response (objective function) of being insensitive to small variations in system parameters. The second case is linked to the idea of 'reliability', intended as the ability of a system to ensure its functions in a given uncertain context, where non-admissible solutions are tolerated as long as they remain unlikely.

Depending on the specific needs, the objective and constraint functions can be given three possible states: function not needed, deterministic function, function subject to uncertainty. The possible combinations of these states applied to the objective and constraint functions give origin to different design classes with corresponding different outcomes. This is well illustrated in Figure 2.14. In particular, in the context of deterministic approaches, the design can be: a) admissible, if deterministic constraints are applied but no optimization is addressed; b) optimal, if a deterministic objective function is optimized without imposing any constraints; c) optimal and admissible, if a deterministic optimization is performed under deterministic constraints. In presence of uncertainty, some additional categories can be defined. If uncertainty affects only the constraint function, the design is said: d) reliable, if no optimization is carried out; e) optimal and reliable, if uncertainty is propagated only to the constraints, and the optimization is run over a deterministic objective function. On the contrary, if uncertainty only concerns the objective function, the design is called: g) robust, if it the objective function can be optimized with a sufficiently high probability; h) robust and admissible, if in addition some deterministic constraints are satisfied. Ultimately the most complex design class is: i) robust and reliable, if both the objective function is optimized and the constraint are satisfied with a satisfactory probability.

The type of approach to be used depends of course on the specific needs of each problem and on the available resources. Ideally, any designer aims at a robust and reliable optimal design. In reality, this cannot always be ensured, and the choice is the result of a trade-off between the need to minimize risks and the limited computational or time budget. In this project, we aim at developing a flexible framework that can easily be adapted to any of the discussed approaches. However, as one main challenge to be addressed is the introduction of dynamic aeroelasticity within an overall aircraft design problem, the investigations will prioritize the dynamic aeroelastic analyses. As it will be shown later, these are taken into account as performance constraints during the overall MDO. Consequently, the focus is primarily to investigate the impact of uncertainty on these constraints, and the preferred approach will be for optimal and reliable design. However, a change for a different approach, such as robust and admissible design, or robust and reliable design, could be easily attained without any significant implementation effort.

It should be noted that the terms 'robust' and 'robustness' are occasionally used in this manuscript in a generic sense indicating 'resilience' against uncertainty, but it is worth

pointing out that in accordance to the described definitions the more appropriate terms are 'reliable' and 'reliability'.

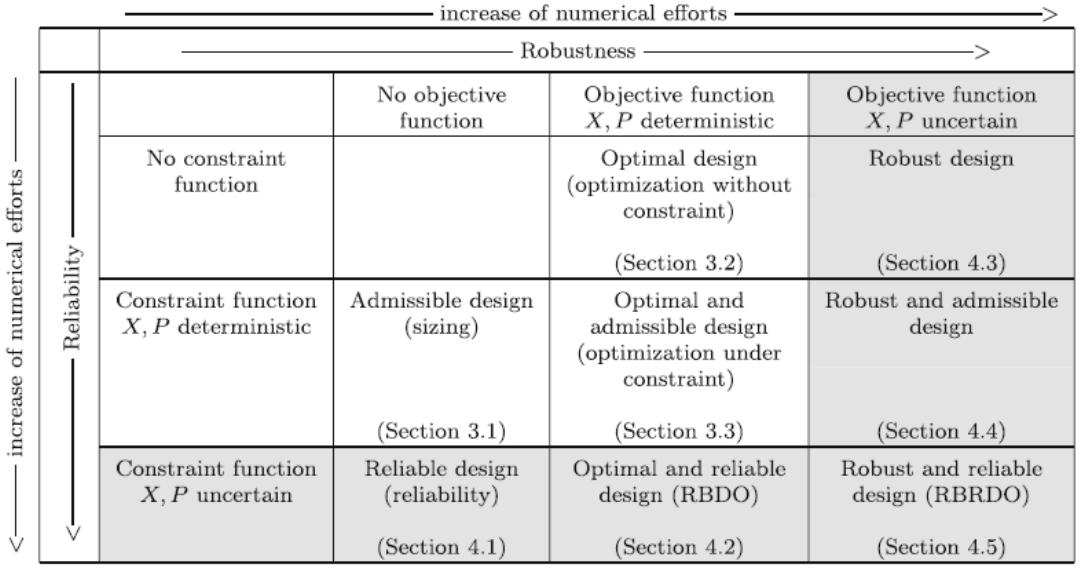

	No objective function	Objective function X, P deterministic	Objective function X, P uncertain
No constraint function		Optimal design (optimization without constraint) (Section 3.2)	Robust design (Section 4.3)
Constraint function X, P deterministic	Admissible design (sizing) (Section 3.1)	Optimal and admissible design (optimization under constraint) (Section 3.3)	Robust and admissible design (Section 4.4)
Constraint function X, P uncertain	Reliable design (reliability) (Section 4.1)	Optimal and reliable design (RBDO) (Section 4.2)	Robust and reliable design (RBRDO) (Section 4.5)

FIGURE 2.14: Different possible design and optimization approaches in presence of uncertainty, from [15].

2.6.2 Uncertainty Quantification and Sensitivity Analysis

After having clarified the definitions of robust and reliable design, it is now useful to enter in the details of the mathematical problem concerning how the input uncertainty can be propagated into the desired outputs - whether these are objective or constraint functions. This basically involves the domain of what are called Uncertainty Quantification (UQ) and Sensitivity Analysis (SA). The following discussion is based on reference [137], which offers a useful overview of the main theoretical aspects of these topics.

To start with, let us consider a generic function F giving the output Y and depending on a space $\boldsymbol{x}$ and on a set of uncertain parameters $\boldsymbol{Q}$, as in Equation (2.16).

$$Y = F(\boldsymbol{x}, \boldsymbol{Q}) \tag{2.16}$$

The output Y may have values belonging to the output space Ω_Y according to an unknown probability distribution, denoted as ρ_Y. The objective of UQ is to determine this output distribution, knowing the input distributions on the vector $\boldsymbol{Q}$. The following discussion is limited to the case where all the uncertain parameters are statistically independent, so that each of them is represented by a separate univariate probability distribution.

The desired information about the output probability distribution usually involves a few common statistical metrics: the mean, or expectation, $\mathbb{E}$, and the variance $\mathbb{V}$. These are defined as in Equations (2.17) and (2.18), respectively.

$$\mathbb{E}[Y] = \int_{\Omega_Y} y\,\rho_Y(y)\,dy \tag{2.17}$$

$$\mathbb{V}[Y] = \int_{\Omega_Y} (y - \mathbb{E}[Y])^2\,\rho_Y(y)\,dy \tag{2.18}$$

The mean represents the expected value of the model output Y, whereas the variance is an indication of how much the output is expected to vary around the mean. An additional useful index is the percentile P_x of Y, which defines the value below which the model outputs are located with a probability of x percent. Mathematically, this corresponds to the definition given in Equation (2.19).

$$x = \int_{-\infty}^{P_x} \rho_Y(y)\,dy \tag{2.19}$$

In some cases, however, the interest may go beyond the computation of the above quantities. In particular, one may want to know what parameters among the set $\boldsymbol{Q}$ have the most impact on the variation of the output Y. In fact, it is possible that the output is very sensitive to some of these parameters, and insensitive to others. The quantification of how much each parameter is responsible for the output uncertainty is exactly the scope of what is called Sensitivity Analysis (SA). Several metrics have been proposed to mathematically define this sensitivity. A review of different methods is given by [138]. However, the most common indices are those proposed by Sobol [139], known as Sobol indices, which are based on the concept of variance. The idea is to estimate how much of the output variance is due to each uncertain input. Therefore, such an index should be low for a given parameter whose variation results in a comparatively small variation of the final output. Conversely, if a change in one parameter leads to a large variation of the output, the index should be high. Following this reasoning, one main index, known as first-order Sobol sensitivity index, S_i, is defined as in Equation (2.20).

$$S_i = \frac{\mathbb{V}[\mathbb{E}[Y|Q_i]]}{\mathbb{V}[Y]} \tag{2.20}$$

where $\mathbb{V}[\mathbb{E}[Y|Q_i]]$ is the expected value of the output Y when the parameter Q_i is fixed. This index represents therefore the expected reduction in the variance of the model when the parameter Q_i is kept constant. It can be shown that the sum of the first-order Sobol indices cannot exceed one, and is only equal to one if there is no interaction

between the uncertain parameters [140]. Two parameters are said to interact if they have a non-additive effect on the output.

Higher order Sobol indices exist and give information about the interactions between each parameter with several others. Usually, enough information is given by the first-order indices and what are called total-order indices S_{Ti} [141]. These include not only the sensitivity of first-order effects, but also the sensitivity due to interactions between a certain input Q_i and all combinations of the remaining ones [142]. The definition is given in Equation (2.21).

$$S_{Ti} = 1 - \frac{\mathbb{V}[\mathbb{E}[Y|Q_{-i}]]}{\mathbb{V}[Y]} \tag{2.21}$$

Here, Q_{-i} indicates all uncertain parameters except Q_i. The sum of the total Sobol sensitivity indices is equal to or greater than one, and is only equal to one if there are no interactions between the parameters [140].

Now that a clear definition of the needed quantities of interest has been presented, the following Section is dedicated to the main methods employed in literature for their computation.

2.6.3 Monte Carlo and Quasi-Monte Carlo method

The simplest method to derive the required statistical metrics for UQ and SA is the Monte Carlo method. The idea is to evaluate the model thousands of times in correspondence of randomly sampled (according to their probability distribution) parameter sets. The collected series of model outputs is then used to compute the needed statistical indices. The advantage of this approach is the simplicity and applicability to any problem, without requiring any assumptions about the model. However, a critical drawback is that it is extremely expensive, often prohibitively. This major disadvantage can be somehow mitigated by the so-called quasi-Monte Carlo approach, which reduces the number of model evaluations by more efficient sampling techniques covering the parameter space more evenly. Examples of such techniques are the Sobol sequence [143] and the Hammersley sequence [144].

After N model evaluations, the mean and the variance can be computed as in Equations (2.22) and (2.23).

$$\mathbb{E}[Y] \approx \frac{1}{N}\sum_{i=1}^{N_s} Y_i \tag{2.22}$$

$$\mathbb{V}[Y] \approx \frac{1}{N-1}\sum_{i=1}^{N} (Y_i - \mathbb{E}[Y])^2 \tag{2.23}$$

Clearly, the accuracy increases with increasing number of samples. To compute Sobol indices from a Monte Carlo, Reference [137] favors the Saltelli's method [141], which is not documented here for brevity. With this approach, if N is the number of samples needed by the quasi-Monte Carlo method to achieve a certain accuracy in the UQ, the corresponding number of samples required to compute the Sobol indices is $N_s = N(d + 2)$, with d denoting the number of uncertain parameters.

2.6.4 Polynomial Chaos Expansion

A much more efficient way to perform UQ and SA, representing the current standard in most applications, is through the use of Polynomial Chaos Expansion (PCE). This method consists of creating a surrogate model $\hat{F}$ of the true function F of Equation (2.16) based on a polynomial expansion structured as in Equation (2.24).

$$F \approx \hat{F} = \sum_{n=0}^{N_p-1} c_n(\boldsymbol{x})\, \phi_n(\boldsymbol{Q}) \tag{2.24}$$

where c_n are expansion coefficients and ϕ_n are the polynomials. The number of expansion factors N_p depends on the number of uncertain inputs D and on the chosen polynomial order p as in Equation (2.25).

$$N_p = \binom{D+p}{p} = \frac{(D+p)!}{D!\,(D+p)!} \tag{2.25}$$

It is convenient to choose the polynomials $\phi_n(\boldsymbol{Q})$ so they are orthogonal with respect to the multivariate probability density function $\rho_{\boldsymbol{Q}}$, and one method to do this by using the so-called three-term recurrence relation [145]. The following step is to find the expansion coefficients c_n. If this is to be accomplished by treating the true function as a black-box, which means that nothing can be inferred by knowledge of the true function's properties, then the approach is said non-intrusive. This is the preferred approach here, as it allows greater flexibility to treat different problems. Non-intrusive methods can be divided into two main classes: point-collocation methods and pseudo-spectral projection methods.

Point-collocation methods demand that the polynomial approximation is equal to the true model at a set of prescribed collocation nodes. This condition allows the problem of finding the coefficients c_n through a set of linear equations. The number of collocation points suggested by [137] is $N_c = 2\,N_p + 2$.

Pseudo-spectral projection methods, instead, are based on a least square minimization of the error between the true and surrogate model, and requires numerical integration

to find the expansion coefficients c_n. The number of model evaluations needed varies according to the integration scheme, for which several options are available [137].

The choice of the polynomial chaos expansions method is problem dependent. In general, the pseudo-spectral method is faster than point-collocation, but has lower stability. Moreover, point-collocation (as well as the quasi-Monte Carlo method) is robust towards missing values as long as the number of results remaining is high enough. Therefore, the point-collocation method is here preferred.

Once the PCE is generated, several statistical metrics can be directly obtained from it. For example, the mean and variance can be calculated as in Equations (2.26) and (2.27), respectively.

$$\mathbb{E}[Y] \approx c_0 \tag{2.26}$$

$$\mathbb{V}[Y] \approx \sum_{n=1}^{N_p-1} \gamma_n \, c_n^2 \tag{2.27}$$

where γ_n is a normalization factor defined as $\gamma_n = \mathbb{E}[\phi_n^2(\boldsymbol{Q})]$.

The first- and total-order Sobol indices can either be derived analytically from the PCE, as shown in [146, 147], or with the Monte Carlo procedure described above, with the difference that the Monte Carlo approach would be much faster because the sampling would be on the polynomial surrogate $\hat{F}$, and not on the true, expensive function F.

Polynomial chaos expansions are recommended as long as the number of uncertain parameters is small (typically < 20), as they are much faster than Monte Carlo methods [137].

2.6.5 Applications in aircraft conceptual design

Despite most studies on aircraft conceptual design and optimization rely on deterministic processes, assuming the feasibility of their results and ignoring the concept of robustness, some studies do face the issue of uncertainty quantification and propagation, although not necessarily including aeroelasticity-related issues.

For example, Reference [148] introduces environmental and operational uncertainty within the design and optimization process of a combat air vehicle. The key uncertain parameters, all of aleatory nature, are identified for the particular application to be the combat altitude, the combat Mach number, the number of turns and the angle of turn. There is no a-priori evaluation of the input parameters uncertainty. Instead, the distribution shapes are chosen by the authors only according to reasonable assumptions. The

uncertainty is always represented with a normal distribution around a nominal value with standard deviations of approximately 0.5% of the nominal value, except for the number of turns, which is considered as a more random variable, and for this reason is assumed to vary with a uniform distribution. The multidisciplinary design exploration is based on surrogate modelling techniques, the most effective of which has been identified by the authors in the non-deterministic Kriging (or GP) [149]. The surrogate model is built through standard Monte Carlo simulations based on a simple uniform Design of Experiment (DOE). Although some of the adopted methods could be improved - such as the Monte Carlo simulations or the uniform DOE, which are quite inefficient - the paper represents a good example where the uncertainty propagation successfully supports the exploration providing a robust design outcome.

Differently from the previous approach, the work of Mines [75] tries to derive information on the distributions and correlations of the key uncertainty sources from model- and data- based considerations, instead of assuming prescribed independent distributions without justification. To this purpose, the author identifies the main uncertainty sources with epistemic model uncertainty, and more precisely with the uncertainty due to the finite element discretization in the adopted physics-based models. In addition, the work includes wing-level reliability constraints (such as on tip deflection), which means that the constraint compliance is affected by uncertainty. The work demonstrates the added value of including design robustness and reliability information early on the design, which can help saving a large amount of money in comparison to the case where a realization of negative uncertainty late in the design process results in the non-compliance to some constraints/requirements.

In these examples and in all similar ones, some limitations are of course necessary: it is not practical to take all the possible problem inputs as uncertain, and propagate dozens, or hundreds, or thousands of uncertain parameters across the entire design and optimization process. Therefore, depending on the main objectives of each study, the priority is given to a restricted set of quantities (aerodynamic coefficients, geometry, weight and balance, structural properties, etc), and to a restricted set of constraints or figures of merit (performance, flying qualities, fuel mass, structural safety, etc). The idea is to show that if the framework can be adapted to different, particular robust multidisciplinary analysis and optimization problems, then it can be easily applied to several other studies involving similar figures of merit or different combinations of the disciplinary modules, for example different aerodynamic model coupled with the same flight dynamics model, or the same aerodynamic model coupled with rigid or flexible structure, etc.

2.7 Summary

This Chapter covered a literature review on the following points:

- Applications involving flight simulation during conceptual design studies, including flying qualities assessment and simulation of flexible aircraft dynamics;
- Efficient methods for sizing and optimization of high-aspect-ratio wings at conceptual design level;
- The issues of flutter and dynamic gust loads, and how they can be taken into account in overall aircraft conceptual design;
- Bayesian Optimization and Super Efficient Global Optimization to tackle complex MDO problems;
- How to perform design and optimization under uncertainty: the main Uncertainty Quantification techniques and some example applications in aircraft conceptual design.

Advanced and effective methods exist for all the individual topics above, but their smart combination into an efficient framework for robust MDAO for the design of flexible aircraft is still lacking of mature and comprehensive applications. This represents the main research gap that this work aims to fill. The proposed approach is detailed in the following chapters.

Chapter 3

Formulation and analysis tools

Contents

2.1 Overview 10
2.2 Flight simulation at conceptual design 13
2.2.1 Flying qualities constraints 14
2.2.2 Flight simulation of flexible aircraft 15
2.3 Sizing of high-aspect-ratio wings 19
2.4 Dynamic aeroelasticity 22
2.4.1 The flutter problem 23
2.4.2 Dynamic gust loads 25
2.4.3 Dynamic aeroelasticity for conceptual aircraft MDAO 28
2.5 Multi Disciplinary Optimization 32
2.5.1 Bayesian optimization and Efficient Global Optimization 33
2.5.2 Super-Efficient Global Optimization 36
2.6 Design under uncertainty: optimization, reliability, robustness . . . 37
2.6.1 General considerations 37
2.6.2 Uncertainty Quantification and Sensitivity Analysis 39
2.6.3 Monte Carlo and Quasi-Monte Carlo method 41
2.6.4 Polynomial Chaos Expansion 42
2.6.5 Applications in aircraft conceptual design 43
2.7 Summary 45

3.1 Overview

This chapter presents a set of tools that were chosen to be part of the analysis and simulation framework suitable for conceptual design of flexible aircraft. Some of them were developed by the author when no suitable solution was found off-the-shelf for the identified needs. As the aim is to cover a range of applications as wide as possible, including estimations for non-conventional vehicles, the attempt here is to provide tools with large adaptability, offering a variety of features that could be switched on or off according to the particular needs. For instance, linear and nonlinear methods can be selected at the aerodynamic, flight dynamics and structural dynamics levels. Also, the disciplinary modules can be used as stand-alone applications with their own input-output channels, or they could be interfaced for coupled analyses. The source code can be compiled (with or without multidisciplinary coupling) either into a stand-alone application or into a Python shared object. This latter option allows the tools to be plugged into a multidisciplinary environment, for which a Python interface has been developed.

In this context, the most challenging task is generally recognized to be the prediction of aerodynamic loads. In this work, some methods have been selected because considered suitable for conceptual design applications, according to most of the related literature (see Section 2.2.2). Since it is assumed that limited knowledge is available at this design phase - which is not necessarily true for conventional concepts, but it is surely a fair assumption when coping with novel concepts - it was decided to have a small set of different fidelity levels, which the analyst can choose according to the complexity of the particular case. The choice shall follow a preliminary assessment based on experience, theoretical inference or on representative test simulations. The available aerodynamic modules are presented in Section 3.2, together with their validation for those that have been developed by the author.

Similarly, the approaches to model the structural dynamics and its interface with the aerodynamic methods are presented in Section 3.3 and Section 3.4.

Time-domain simulation capabilities were also given particular attention for the following reasons: a) they have the advantage to capture and clearly show the effects of possible nonlinearities and/or transient responses, b) they enable to simulate sizing scenarios (manoeuvres, gust encounters) to improve the quality of the structural sizing process; c) they allow flying and handling qualities predictions to be verified or to be extracted from the time history results; d) virtual flight simulation within a fixed-base new generation flight simulator, recently installed at the University of Southampton, is envisioned as a desirable outcome of the research project, because it would pave the way to further research on handling qualities and pilot-coupling assessment. For these reasons, a flight simulation tool was developed during this project, and its formulation

and validation are presented in Section 3.5. Also, its coupling with the aerodynamic modules is described in Section 3.5.2.

To best exploit the nonlinear time-domain results, a system identification module has been put in place with the aim of automatically extracting some relevant figures from the output data. In this way the simulations can be automatically iterated multiple times and used within sensitivity analyses, sizing loops or optimisation loops. The idea is to provide a general tool to tackle a variety of tasks, such as the extraction of flying qualities figures of merits, the identification of maximum loads during prescribed manoeuvres or the evaluation of maximum control surface deflection. Nevertheless, the proposed method is being currently applied on the first mentioned category, namely the flying qualities extraction, because in line with the gradual maturation of the framework development it offers the opportunity to test the strategies without necessarily requiring a full disciplinary coupling, which risks to obfuscate the research progress with excessive complexity. The investigated system identification strategies are presented in Section 3.6.

As already stated earlier in this work, the problems faced here are not merely related with the capability of predicting certain nominal behaviours or characteristics of the design candidates, but we aim at going further and corroborating such predictions with information on the reliability of the results. To do so, it is important first to identify for each task of interest (flying qualities estimation, loads prediction, etc) the relevant sources of uncertainty, and then to set up an analysis framework to propagate the uncertainty through the design process into the output quantities of interest. In other words, some sensitivity analysis and uncertainty quantification capabilities are needed, and for this reason some available tools have been selected to be part of the developed framework. These are introduced in Section 3.7.

Of course, all of these tools need to be integrated with an aircraft sizing and optimization process. To this purpose, this work took advantage of the expertise of the ONERA centre, which provided the `FAST-OAD` aircraft sizing tool [150] and the `SMT` and `SEGOMOE` libraries for surrogate modelling and optimization techniques. These are discussed in Section 3.8.

To give a better overview of the framework architecture, its main building-blocks are here summarized. The main modules are:

- A choice of aerodynamic models, including a classical analytical model based on linear aerodynamic derivatives, and a steady or unsteady implementation of the Vortex Lattice Method (VLM or UVLM);
- A nonlinear structural mechanics solver (`GEBT`, Geometrically Exact Beam Theroy)
- Two possible aeroelastic solvers: *a*) a linear solver based on potential unsteady strip theory coupled with linear beam theory, mainly required for flutter analysis;

b) a linear/nonlinear model coupling the `GEBT` structural solver with the VLM or UVLM aerodynamic solvers;

- A flight dynamics simulation module (FDM) implementing the 6DOFs nonlinear equations of motion;
- A post-processing module to extract the desired quantity of interest (amplitude, frequency, damping) out of the simulation history by use of a Least Square best fit technique of the time-domain data;
- An uncertainty quantification and sensitivity analysis module that wraps the above modules and propagates the uncertainty from the input parameters into the desired outputs. It returns the desired statistical metrics to be used in the reliability evaluation;
- An aircraft conceptual sizing tool (`FAST-OAD`) performing the necessary loops until convergence to a consistent configuration (i.e. satisfying the TLARs);
- An optimization environment (`SEGOMOE`) to be interfaced with the sizing process and with the implemented multidisciplinary deterministic or stochastic constraints (such as flying qualities constraints, flutter speed, gust loads).

Table 3.1 clarifies which solvers were developed by the author and which ones were integrated from existing open-source resources.

Implemented by the author	**Off-the-shelf software**
VLM (Vortex Lattice Model)	`GEBT` (nonlinear beam model)
UVLM (Unsteady VLM)	`FAST-OAD` (aircraft sizing tool)
Unsteady strip theory	`SEGOMOE` (Bayesian optimization)
Linear aeroelastic solver	`Uncertainpy` (UQ & SA tool)
Nonlinear aeroelastic solver	
FDM (Flight Dynamics Module)	
Post-processing module	

TABLE 3.1: List of the developed and integrated tools available in the proposed MDAO framework.

The global architecture (for a fictitious, generic task) is summarized in Figure 3.1. The process starts with the definition of an optimization problem based on a set of design variables - here they will mostly concern geometric variables - denoted as V_g and an objective function, here identified with the fuel mass. According to the input geometry, and on a series of top-level aircraft requirements (TLAR), `FAST-OAD` performs the

conceptual sizing of a rigid aircraft, based on low-fidelity models (especially for aerodynamics and structure). Some parameters of the converged configuration, here denoted as W_g as they usually involve wing characteristics, are then passed to the flight physics disciplinary modules. These can include the flight dynamics module, or an aerodynamic module, or an aeroelastic module, or a combination of them. The actual structure corresponding to the 'Flight Physics Modules' block depends on the specific task to be addressed, and on the required performance to be evaluated. The output of this simulation block can be a set of scalar quantities or their time history, if time simulation is performed. In this second case, the time series can involve some displacement $X(t)$ or load $F(t)$. These output can be fed to the processing module in order to derive the required figures of merit, such as the generic frequency and damping ratio ω and ξ, or some target structural loads σ and τ. If uncertainty has to be considered, the uncertainty quantification (UQ) module shall be included to propagate it to those outputs. Typical uncertain inputs could be the aircraft center of gravity location Δx_{CG}, the longitudinal moment of inertia I_{yy}, the wing elastic axis location a, and its offset d from the wing center of gravity axis. The uncertainty distributions of those parameters are indicated by a hat $\hat{(\,)}$, and would be the inputs of the UQ module. The output distributions of the desired figures of merit ($\hat{\xi}$, $\hat{\omega}$, $\hat{\sigma}$, $\hat{\tau}$) can then be used to define a set of reliability constraints, for example targeting for each output a certain mean or variance or the probability to overshoot a certain threshold. A similar variant of this architecture, not shown in Figure 3.1, can propagate the uncertainty to the objective function, in which case the problem could more properly be defined as *robust* optimization, according to the definition given earlier in Section 2.6.1.

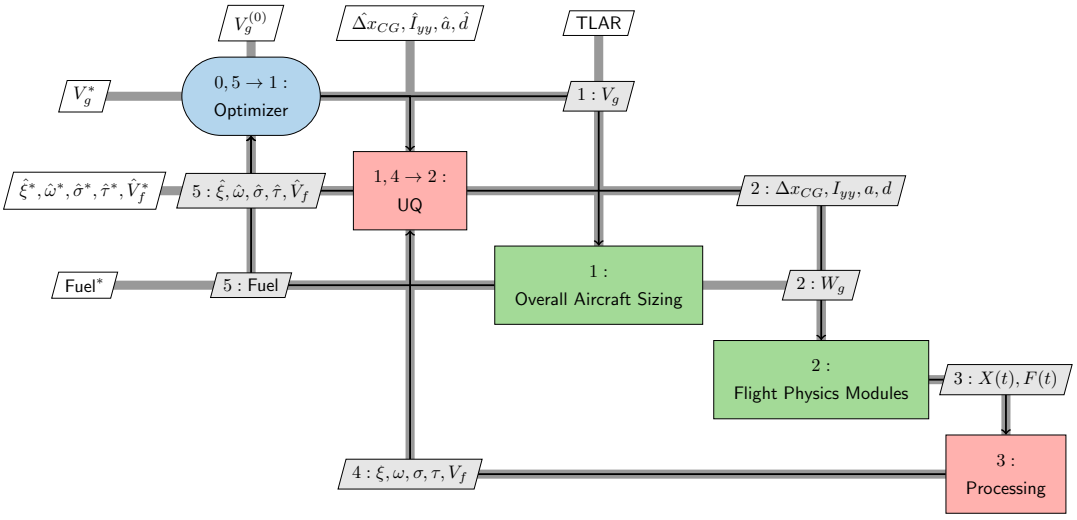

FIGURE 3.1: Generic XDSM[1] scheme representing the overall structure of the present framework for robust design and optimization under reliability constraints. The specific disciplinary blocks to be included and the list of inputs and outputs will depend on the particular study to be performed. The structure can slightly change accordingly.

3.2 Aerodynamics

Chosing and implementing the appropriate aerodynamic solvers requires a good understanding of the assumptions and limitations behind the available theories and methods. Therefore, to provide a deeper understanding of the adopted strategy, this section not only describes the numerical approaches implemented in this work, but also revises the relevant theoretical principles behind them.

The most general description of the fluid dynamics problem is given by the Navier-Stokes equations, expressing the conservation of momentum in differential form:

$$\rho\left(\frac{\partial q_i}{\partial t}+\boldsymbol{V}\cdot\nabla q_i\right)=\rho f_i-\frac{\partial}{\partial x_i}\left(P+\frac{2}{3}\mu\nabla\cdot\boldsymbol{V}\right)+\frac{\partial}{\partial x_j}\mu\left(\frac{\partial q_i}{\partial x_j}+\frac{\partial q_j}{\partial x_i}\right) \qquad (i=1,2,3) \tag{3.1}$$

where ρ is the density, $\boldsymbol{V}$ is the velocity vector, f_i is the body force in the i-th direction, P is the pressure and μ the viscosity. The typical boundary conditions associated with Equation (3.1) require that the normal and tangential velocity components decay to zero at the solid boundary:

$$q_n=0 \qquad \text{(on solid surface)} \tag{3.2}$$

$$q_t=0 \qquad \text{(on solid surface)} \tag{3.3}$$

These equations must be combined with the continuity equation, that in its most general form is:

$$\frac{\partial\rho}{\partial t}+\boldsymbol{V}\cdot\nabla\rho+\rho\nabla\cdot\boldsymbol{V}=0 \tag{3.4}$$

For high speed problems also the energy equation has to be used, which is not reported since it is not of interest for the present case.

Because of the complexity of the Navier-Stokes equations, analytical solutions are available only for very simple cases, and numerical methods with some sets of assumptions have to be used according to the problem approached and the requirements in terms of accuracy, time and computational power available.

[1] EXtended Design Structure Matrix: in this work, the graphical convention follows the one from [151]. For a reader not familiar with the matter, it is important to know that in these charts all inputs are on vertical lines, all outputs on horizontal lines, gray lines represent data exchange between modules, and black arrow lines indicate the process flow.

The most advanced computational methods (Direct, Eddy, RANS simulations, etc.) for solving the fluid dynamics equations are to be abandoned at conceptual design phase for at least two reasons: 1) the computational cost and time is in general too high to allow vast design exploration; 2) being sensible to low-scale effects, they are of value mostly when a high level of geometric detail (airfoil leading-edge curvature, fillets, roughness) is involved, which is not the case during conceptual design.

Typically, the approaches recognized as affordable, or promising, for conceptual design applications neglect the viscous effects, or approximate them relying on pre-computed data [152–154]. The methods employed in this work belong to this category, and are introduced in the following sections.

3.2.1 Linear derivative-based aerodynamics

The most basic and still powerful aerodynamic model is the traditional approach of Bryan [155], based on the assumption of linear dependency on flight state variables, where each contribution is linearly superimposed to build up the total aerodynamic force/moment. The total aerodynamic coefficients are given by expressions such as in Equations (3.5) and (3.6).

$$C_i = C_{i_0} + C_{i_\alpha}\,\Delta\alpha + C_{i_V}\,\frac{\Delta V}{V_e} + C_{i_q}\,\frac{q\,c_{\mathrm{MGC}}}{2\,V} + C_{i_z}\,\frac{2\,\Delta z}{c} + C_{i_\delta}\,\delta \qquad (3.5)$$
$$(i = D, L, m)$$

$$C_i = C_{i_0} + C_{i_\beta}\,\Delta\beta + C_{i_p}\,\frac{b\,p}{2\,V} + C_{i_r}\,\frac{r\,c_{\mathrm{MGC}}}{2\,V} + C_{i_\delta}\,\delta \qquad (3.6)$$
$$(i = C, \ell, n)$$

The assumption is usually applicable to a large portion of the flight envelope, at least for most conventional aircraft, and even when linearity is no longer present, such as when approaching stall, or in transonic regimes, local linearization is often successfully used in many applications. This approach ensures very fast computations and, in combination with the linearized equations of motion, allows the classical stability & control analysis to be quickly performed through eigenvalue and eigenvector computation. For these reasons, the approach is the standard in industry and many flight simulation applications [156–158].

The predictions rely on a database of pre-computed aerodynamic derivatives, in a form similar to that illustrated in Figure 3.2. The structure reveals the limits of the approach: first, a large amount of data is to be computed; second, to reduce such a number, some interactions between the state variables are usually neglected.

Moreover, the reliability of the approach strictly depends on the quality of the data sources. When data comes from extensive simulation or testing campaigns the predictions can be highly accurate. At conceptual design, although these sources are not available, data from analytical and semi-empirical relationships give satisfactory results, at least for conventional configurations. For this reason, the first aerodynamic model considered in this work is based on the classical Bryan's approximation (Equations (3.5) and (3.6)), where the needed aerodynamic coefficients are computed through analytical and semi-empirical relationships from [9, 159–161]. In addition, most of the needed coefficients could also be computed by use of the Vortex Lattice Method that will be discussed later in this chapter.

(a) Stability coefficients table

Alpha	*Mach*	*Beta*	Q	P	R	C_L	C_D	C_m	C_Y	C_ℓ	C_n
x	x	x	-	-	-	x	x	x	x	x	x
x	x	-	x	-	-	x	x	x	x	x	x
x	x	-	-	x	-	x	x	x	x	x	x
x	x	-	-	-	x	x	x	x	x	x	x

(b) Control coefficients table

Alpha	*Mach*	δ_e	δ_r	δ_a	C_L	C_D	C_m	C_Y	C_ℓ	C_n
x	x	x	-	-	x	x	x	x	x	x
x	x	-	x	-	x	x	x	x	x	x
x	x	-	-	x	x	x	x	x	x	x

(c) Unsteady coefficients table

Mach	$C_{m_{\dot{\alpha}}}$	$C_{Z_{\dot{\alpha}}}$	$C_{X_{\dot{\alpha}}}$	$C_{Y_{\dot{\beta}}}$	$C_{\ell_{\dot{\beta}}}$	$C_{n_{\dot{\beta}}}$
x	x	x	x	x	x	x

FIGURE 3.2: Typical format of aerodynamic database, from [5].

It is worth mentioning here a few details about the computation of drag, as it is directly linked to the key performance indicator of fuel burn. The present approach follows the drag build-up of [9], where the total drag is given by four contributions: viscous drag C_{D0}, compressibility drag C_{Dc}, induced drag C_{Di}, and trim drag C_{Dtrim}. The total drag build-up is obtained as in Equation (3.7):

$$C_D = k_{C_D}\left(k_{C_{D0}}C_{D0} + k_{C_{Dc}}C_{Dc} + k_{C_{Di}}C_{Di} + k_{C_{D_{trim}}}C_{D_{trim}}\right) \tag{3.7}$$

where the coefficients k_i, when available, account for additional corrections due to particular technologies such as winglets. The viscous drag is obtained by summing and normalizing the friction contributions of all the wet areas as in Equation (3.8), with the friction coefficients given by the Prandtl-Schlichting correlation [162] as in Equation (3.9).

$$C_{D0} = \sum_i c_{fi}\, k_{fi}\, \frac{S_{wet,i}}{S_i} \tag{3.8}$$

$$c_f = \frac{0.455}{(1 + 0.126\, M^2)\left(\log_{10} \mathrm{Re}\right)^{2.58}} \tag{3.9}$$

The compressibility term is estimated by a semi-empirical formula taking as inputs only Mach number and lift coefficient [9]. Although its validity is not general, the correction is considered acceptable as far as the Mach number does not exceed 0.8 [72].

The remaining two contributions, namely induced and trim drag, are evaluated employing simple analytical functions and semi-empirical corrections. The induced drag is given by Equation (3.10) [163], and the Oswald factor e is estimated as in [164]. The contribution due to trim is computed by Equation (3.11) as indicated in [9].

$$c_{Di} = \frac{C_L^2}{\pi \mathcal{A}\mathcal{R} e} \tag{3.10}$$

$$C_{D_{trim}} = 5.89 \cdot 10^{-4}\, C_L \tag{3.11}$$

3.2.2 Linear unsteady strip theory

A common approach to model the aerodynamic loads for aeroelastic applications is to treat each wing section through unsteady 2-dimensional potential aerodynamics [165, 166]. In this way any cross-flow and viscous effects are neglected. The computational burden is therefore reduced and suitable for preliminary evaluations, especially when dealing with high aspect-ratio configurations, where the cross-flow effects are limited to a small region around the wing tips (as reported in Section 2.4.3). The potential flow assumption is valid for linear aerodynamic regimes, i.e. moderate angles of attack and subsonic speed [167]. Within this range, even the unsteady effects can be included with a linear model. A linear unsteady aerodynamic model becomes an useful tool for treating aeroelastic systems flying in relatively simple conditions (small angles of attack, small gust amplitude or control deflections, negligible cross-flow or sideslip), because it allows the full aero-structural system to be described linearly, and this, in turn, allows standard eigenvalue analysis or control studies to be performed [30, 168–170]. Therefore, the method enables, for instance, fast predictions of flutter/divergence speed, including open-loop and closed-loop cases.

For these reasons, this method has been included as one of the options available for this work. The main interest, within the time frame of this project, is to use it for flutter predictions, although it can be - and it has been - successfully employed also for other applications (see [30, 171]).

The formulation is here briefly reported, and refers to the flow around a thin, uncambered profile, identified with its straight mean-line as in Figure 3.3.

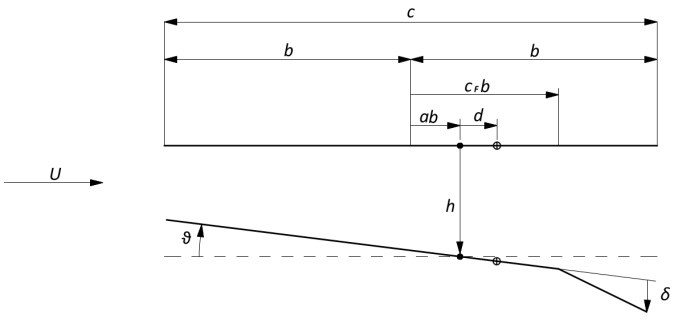

FIGURE 3.3: Mean-line of the aerofoil. ϑ and h denote pitch and plunge, respectively.

The aerodynamic loads are derived from the two-dimensional unsteady potential theory of Theodorsen [18], and considered continuously distributed along the wing span. The arbitrary motion of the aerofoil and the flap deflection can be evaluated by means of convolution of the Wagner's function, and the same procedure is applied for the gust encounter with the Kussner's function, as reported in [20].

According to this, the total lift and pitch moment can be expressed as a summation of the contributions of aerofoil motion, flap deflection and gust encounter:

$$L = L_a + L_\delta + L_g \tag{3.12}$$

$$M = M_a + M_\delta + M_g \tag{3.13}$$

The expressions for the three terms are treated separately in the Appendix A.1. Lift and moments are evaluated at the elastic axis.

For the Wagner's function $\phi_W(t)$, the exponential approximation of Jones is used [172], which reads as in Equation (3.14).

$$\phi_W(t) = 1 - A_1\, e^{-b_1 \frac{U}{b} t} - A_2\, e^{-b_2 \frac{U}{b} t}; \tag{3.14}$$

where the coefficients are $A_1 = 0.165$, $A_2 = 0.335$, $b_1 = 0.0455$, $b_2 = 0.3$.

The effect of gust can be accounted for using the Kussner's solution, with the following exponential approximation of the Kussner's function $\psi_K(t)$:

$$\psi_K(t) = 1 - A_3\, e^{-b_3 \frac{U}{b} t} - A_4\, e^{-b_4 \frac{U}{b} t}; \tag{3.15}$$

where the coefficients, proposed by Leishman [173], are $A_3 = 0.5792$, $A_4 = 0.4208$, $b_3 = 0.1393$, $b_4 = 1.802$.

Further details on the model formulation are given in Appendix A. In the present work, this model is only applied for flutter analysis of a clamped wing with no control surfaces' deflections. Therefore, only the contribution of aerofoil motion, L_a, is retained.

3.2.3 The steady Vortex Lattice Method

3.2.3.1 Theoretical background

This method arises from a series of assumptions that considerably simplify the fluid dynamics problem of Equations (3.1) and (3.4). The simplifying approach leading to the definition of the VLM will be briefly summarised here.

A first common hypothesis is that of constant viscosity μ. When viscosity is completely neglected, the flow is said to be inviscid, and the introduction of such an assumption in the Navier-Stokes equations leads to the Euler equation:

$$\frac{\partial \boldsymbol{V}}{\partial t} + \boldsymbol{V} \cdot \nabla \boldsymbol{V} = \mathbf{f} - \frac{\nabla P}{\rho} \tag{3.16}$$

Another common assumption, valid at low speed regimes, is that of incompressibility ($\rho =$ constant). Enforcing this condition in Equation (3.4) leads to the incompressible continuity equation:

$$\nabla \cdot \boldsymbol{V} = \frac{\partial V_x}{\partial x} + \frac{\partial V_y}{\partial y} + \frac{\partial V_z}{\partial z} = 0 \tag{3.17}$$

It can be shown that at subsonic flow regimes the flow around wings can be represented with sufficient accuracy by the Euler Equation (3.16) and the incompressible continuity Equation (3.17). Such an approximation is only valid out of the thin boundary layer surrounding the surface. Within the boundary layer viscosity plays a relevant role as it is responsible for the generation of the so-called viscous drag, which cannot be predicted by the Euler equation.

Another important approximation that is made to further simplify the fluid dynamic equations is that of irrotational flow, which means that the fluid particles do not experience rotation, so that $\nabla \times \boldsymbol{V} = 0$. Under this assumption it can be demonstrated

that the velocity is an exact differential of a potential Φ which is independent of the integration path, and is only a function of the location:

$$\Phi(x, y, z) = \int_{R_0}^{R} V_x\, dx + V_y\, dy + V_z\, dz \tag{3.18}$$

where R_0 is an arbitary starting point. The velocity at each point can therefore be obtained by the gradient of the velocity potential:

$$\boldsymbol{V} = \nabla\Phi \tag{3.19}$$

Thus, for an incompressible irrotational flow the continuity equation can be expressed as:

$$\nabla \cdot \boldsymbol{V} = \nabla \cdot \nabla\Phi = \nabla^2\Phi = 0 \tag{3.20}$$

Equation (3.20) is known as Laplace's equation, and the flow described by this equation is referred to as potential flow. When viscosity is also neglected, the only boundary condition to be satisfied is that the normal component of the relative velocity on the solid surface must be zero:

$$\nabla(\Phi - \Phi_\infty) \cdot \mathbf{n} = 0 \tag{3.21}$$

where $\mathbf{n}$ is the local normal vector of the surface. A boundary condition must be set also at the farfield (infinity). For a fluid originally at rest, the perturbation introduced by a moving body should decay far from the body ($\mathbf{r} \to \infty$):

$$\lim_{r\to\infty} \nabla(\Phi - \Phi_\infty) = 0 \tag{3.22}$$

Equations (3.20) to (3.22) form the theoretical basis for the Vortex Lattice Method, which therefore is valid for incompressible inviscid irrotational flow.

The basic idea behind the method is that a solution to the Laplace equation (3.20) can be obtained by a distribution of elementary solutions on the problem boundaries (body surface and wake). In fact, because of the principle of superposition, if each elementary function is a solution of the Laplace equation, their linear combination will also be a solution for that equation. They are also called singular solutions because they feature zero velocity at infinity (satisfying the boundary condition (3.22)) but singular velocity at $\mathbf{r} = 0$. The solution of the global problem is found by integrating those singular solutions over the boundaries. The problem is thus reduced to finding an appropriate set of singular solutions that fulfils the boundary condition (3.21). Several singular solutions are suitable for this purpose, such as sources, doublets, polynomials and vortices. The 3D VLM relies on vortex segments, for which the velocity field is given by the Biot-Savart law.

The method in brief prescribes to cover the solid surface with a lattice of vortices whose circulations $\mathbf{\Gamma}$ are initially unknown, and will be determined after enforcing the boundary condition (3.21) on some discrete locations, named collocation points. Once the circulations are known, the aerodynamic force can be computed by means of the Kutta-Jukowsky theorem:

$$\mathbf{F} = \rho \, \boldsymbol{V}_\infty \times \mathbf{\Gamma} \tag{3.23}$$

where $\mathbf{F}$ is the aerodynamic force per unit length and $\boldsymbol{V}_\infty$ the free stream speed.

A first basic application is that of the horseshoe vortex lattice model, where the wingspan is modelled through a series of horseshoe-shaped vortices as in Figure 3.4. A more accurate discretization of the lifting surface is achieved by vortex ring elements, represented in Figure 3.5. This last approach is the one referred to as VLM in this work. The problem is set up by reformulating the boundary condition (3.21) in terms of the normal velocity components induced by the vortex distribution on the wing and wake and the free-stream speed, which means:

$$\nabla\Phi \cdot \mathbf{n} = \nabla\Phi_\infty \cdot \mathbf{n} \qquad \rightarrow \qquad \mathcal{A}\,\mathbf{\Gamma} = \boldsymbol{V}_\infty \cdot \mathbf{n} \tag{3.24}$$

In Equation (3.24), $\mathcal{A}$ is called the aerodynamic influence matrix, where any element (ij) represents the velocity induced in the collocation point of panel i by a unit vortex ring in panel j, and $\mathbf{\Gamma}$ is the vector of all the unknown circulations.

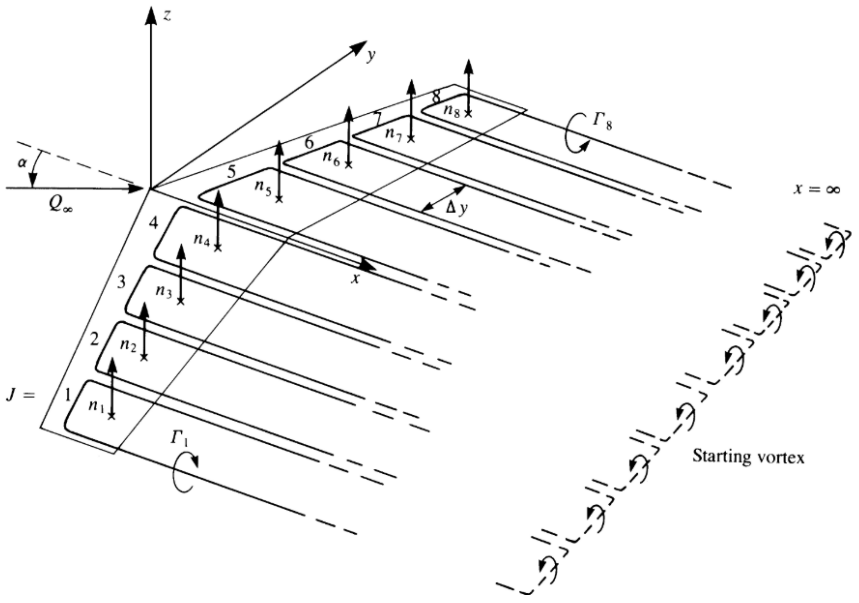

FIGURE 3.4: Horseshoe vortex lattice model for a lifting-line problem, from [16].

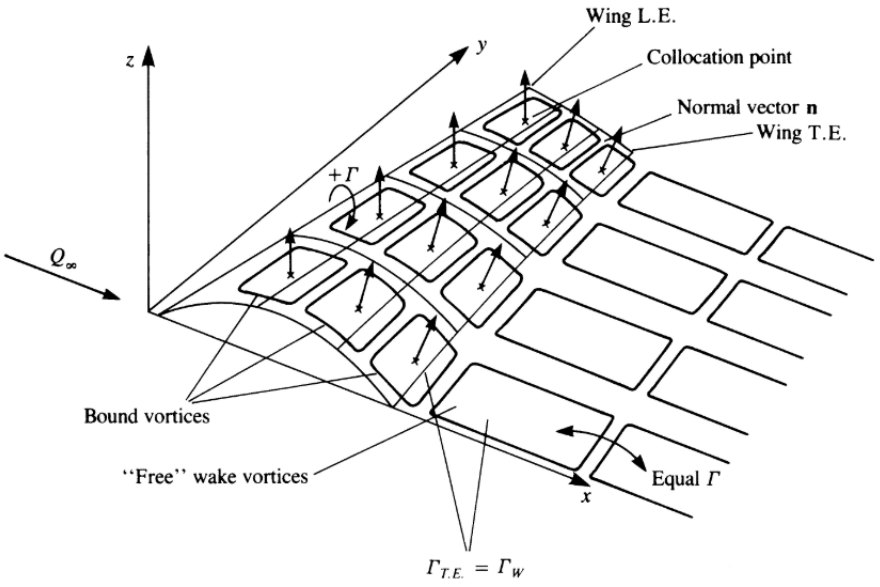

FIGURE 3.5: Vortex ring model for the VLM, from [16].

3.2.3.2 Applicability and limitations

The VLM is an useful tool to predict lift and induced drag for three-dimensional lifting surfaces. Depending on the accuracy required, it can describe flat plates, cambered surfaces or a complete three-dimensional body with any kind of thickness and camber. It is very common because of its flexibility on the geometrical description and its fastness - it just solves a linear system of equations. Nevertheless, the method must be used with awareness of its limitations, due the assumptions made for its derivation. The three main reasons that limit the accuracy of the VLM are compressibility, viscosity, panel modelling and wake model. As far as compressibility is concerned, a correction is possible, named the Prandtl-Glauert rule, and it will be discussed later in Section 3.2.5. The three remaining problems are briefly described here.

The equations implemented in the VLM are derived with the assumption of inviscid flow. This means that all the boundary layer phenomena are completely neglected. In particular, the lift remains a linear function of the angle of attack, without any capability of predicting flow-separation, and low Reynolds number calculations should be avoided. An iterative way to couple the potential flow equations of the VLM and the viscous boundary layer equations exists: the Interactive Boundary Layer method (IBL). It consists in an iterative loop where a boundary layer thickness is estimated after the potential flow solution. The boundary layer modifies the geometry of the previous potential model, requiring a new iteration. After each loop the boundary layer thickness and potential flow solution are updated until both the potential and viscous models have converged (see Figure 3.6). Although this procedure is in principle implementable, the increase in computational effort and time offsets the gain in accuracy.

Also, an appropriate modelling of viscous effects requires a refined geometrical description, including profile shapes, junctions, fairings, etc, otherwise it could lead to imprecise predictions [174]. On the other hand, potential flow solvers are generally recognized to provide much more reliable predictions about lift force, even with simplified geometries [16, 98, 163]. Since aeroelastic phenomena are mainly triggered by lift forces [20], many authors successfully addressed aeroelastic problems assuming no drag at all [7, 19, 92, 96, 175]. Following this philosophy, no effort was put in this work to further enhance the VLM implementation with viscous effects, with the reminder of restricting its application to problems where the latter are of minor relevance.

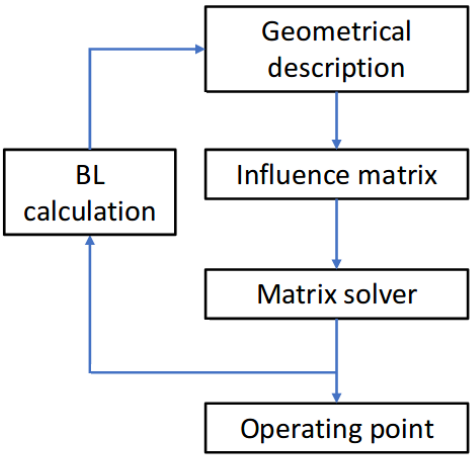

FIGURE 3.6: Interactive Boundary Layer iterative procedure, from [17].

Panel modelling also implies some loss of accuracy due to an imperfect geometrical description of the desired surface. In fact, three-dimensional surfaces in general cannot be decomposed into flat quad panels [17] (see Figure 3.7). This results in some numerical error, which is expected to be small, but still difficult to evaluate [19]. Also, the standard panel approach implies constant singularity distribution (sources, doublets, etc.) over the panel. Higher-order panel methods can be formulated, where linear or non-linear distribution of elementary solutions and/or geometries may be described [16]. Nevertheless, also in this case the increased accuracy may not be worth the augmented computational time. Another limit due to panel discretization is the difficulty modeling wing-body interactions, so that usually only lifting surfaces are analysed, without accounting for fuselage and nacelles.

The third major limit of the panel methods is the model of the wake, usually treated as flat. In reality, the wake follows the shape of the streamlines. An iterative loop can be used to achieve the so-called wake rollup, that would give a more realistic model (see Figures 3.8 and 3.9). As before, the choice of whether to implement this feature or not depends on the required degree of accuracy and on the availability of time for the simulations.

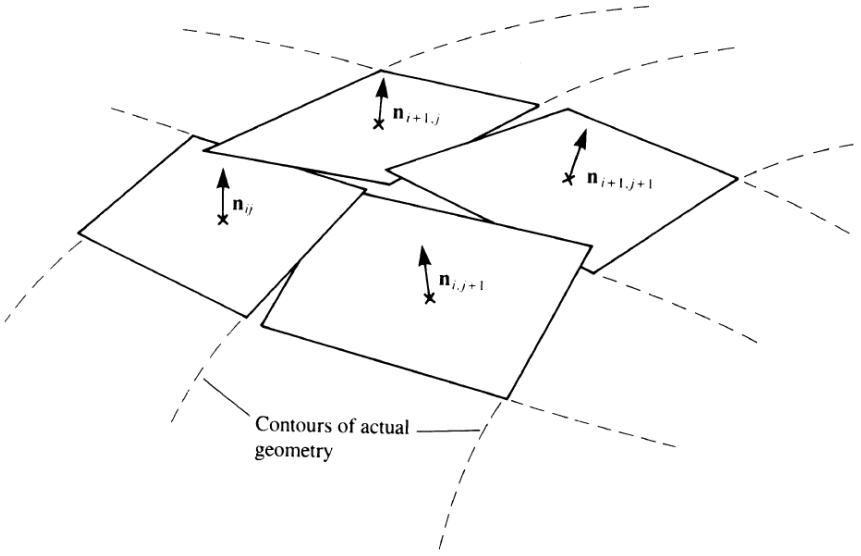

FIGURE 3.7: Geometrical issue with panel discretization, from [16]: all four corner points of a surface panel seldom lay in the same plane.

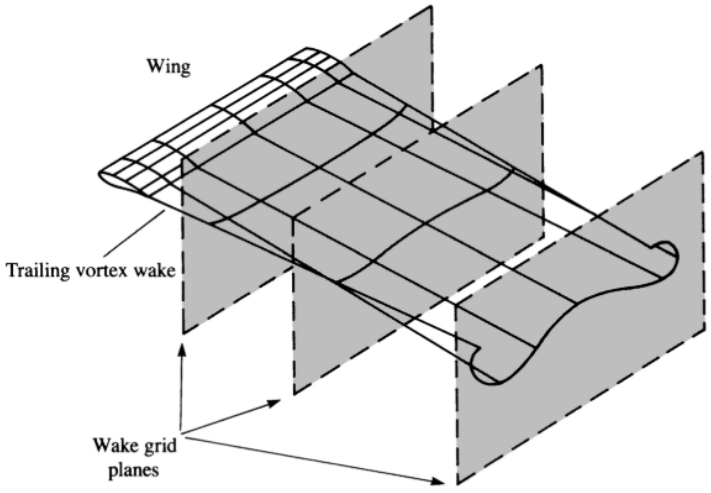

FIGURE 3.8: Panel discretization for wake rollup, from [16].

3.2.3.3 Validation of the VLM solver

Several VLM programs are available online, such as [17, 154, 176, 177]. However, the adoption of these tools was not found of practical benefit to the project, for different reasons. In some of the above programs, the scope is to provide an advanced model suited for high geometrical detail, including propellers and non-lifting bodies interaction, boundary layer approximated predictions, etc. All these features, not necessarily required for the present work, make the code architecture very large and complex to be accessed by external developers, especially as the developer documentation is always poor if not completely missing. Furthermore, most of those tools are aimed at rigid body modelling, so even if accessing the source code had been a trivial task, a non-trivial implementation work would have still been demanded to include unsteady

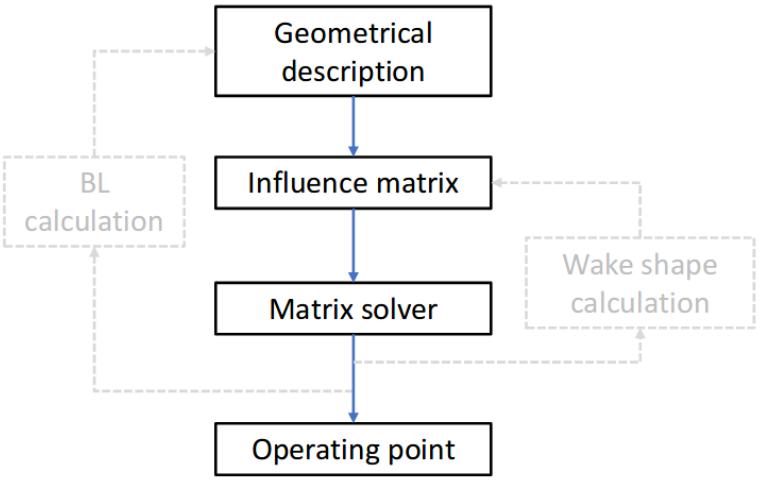

FIGURE 3.9: Iteration loop with or without boundary layer calculation and wake shape calculation, from [17].

aerodynamics and mesh deformation routines. On the other hand, a basic VLM Fortran implementation existed from previous work in our team at the University of Southampton, limited to a flat, horizontal, single wing in symmetric flow. Such a Fortran model was already predisposed to be interfaced with the FALCon procedure [64] to allow two-dimensional viscous corrections through RANS simulation data. Although this is something not required here, it could still be of interest for future research. Considering all of these aspects, it was preferred to start from the simple, in-house Fortran implementation and improve it only with the features considered of interest for the present project and its possible developments (arbitrary 3D wing shape and orientation, multiple wings, asymmetric flow, control surfaces, mesh deformation, interfaces to external solvers). This necessary implementation work was considered more beneficial for an efficient and aware development process than a tedious decryption, interpretation and adaptation of large, poorly documented platforms of unnecessary complexity.

The present section reports the validation process of the developed VLM solver, which was accomplished gradually in parallel with the implementation progress. The validation has been carried out by comparison with one of the tools mentioned above, the `XFLR5` program [17], a well-established VLM solver freely available online under the GNU General Public License. All lifting surfaces are modeled by planar surfaces generated by all the profile mean lines. In the present model, the wake is represented by straight vortex lines developing downstream from each trailing edge vortex ring, as in Figure 3.4, whereas in `XFLR5` the wake vortex lines are deformed by a roll-up procedure. It was found that for the following static cases this difference does not add significant mismatch in the results.

The validation was accomplished through a series of steps, from simple to complex configurations.

Flat wing with varying sweep angle

The first, simplest validation case was aimed at validating the aerodynamic results for a planar wing at different sweep angles in simple symmetric flow conditions. The sweep angle was varied from zero to 15 °. The aerodynamic coefficients corresponding to a sweep of 5° are compared in Table 3.2. The variation of pitching moment coefficient with respect to sweep angle is reported in Figure 3.10.

	XFLR5	Validated model
C_L	0.193	0.192
C_D	0.001	0.001
C_m	-0.090	-0.089

TABLE 3.2: Aerodynamic coefficients obtained with the two solvers for the 5° sweep test case. The resolution is adapted to that of XFLR5, which is limited to the third decimal.

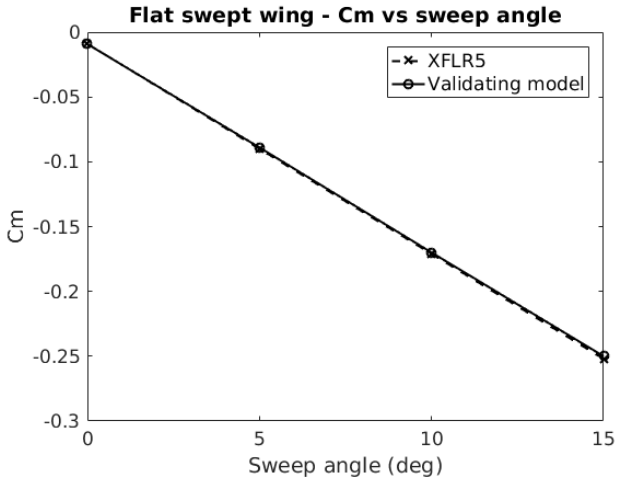

FIGURE 3.10: Predictions from the two solvers of the variation of the flat wing pitching moment coefficient C_m against sweep angle.

Side force validation

Since XFLR5 does not compute side force, the validation of the side force coefficient computed by the Fortran solver was accomplished by comparing results from the same wing simulated first in horizontal position with angle of attack $\alpha = 3°$ and then in vertical position with sideslip angle $\beta = 3°$(see force contour plots in Figure 3.11). The calculations matched perfectly, with force coefficients $C_{L,\mathrm{h}} = C_{Y,\mathrm{v}} = 0.26595$ and rolling moment coefficients $C_{\ell,\mathrm{h}} = C_{\ell,\mathrm{v}} = 0.06528$.

Two-wing configuration with main wing and horizontal stabiliser

This case was aimed at validating the interaction between two wings. A flat swept horizontal tailplane was added to the configuration, both located at the same height. Details on the geometry are given in Figure 3.12. The obtained aerodynamic coefficients

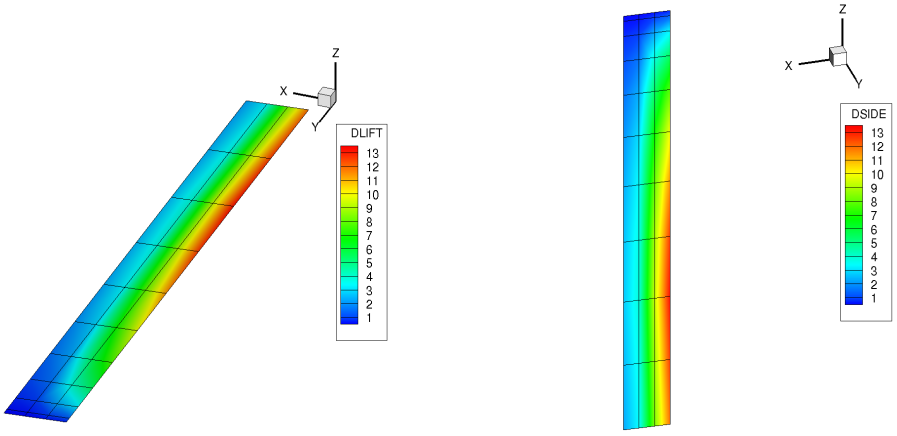

(a) Wing in horizontal position with $\alpha = 3°$.

(b) Wing in vertical position with $\beta = 3°$.

FIGURE 3.11: Comparison between a horizontal wing with angle of attack $\alpha = 3°$ and the same wing in vertical position with sideslip angle $\beta = 3°$, for validation of the side force coefficient.

are compared in Table 3.3, showing again good agreement with the reference, with less than 1% error.

	XFLR5	Validated model
C_L	0.130	0.130
C_D	0.001	0.001
C_m	0.241	0.239
C_l	0.006	0.006
C_n	0.000	0.000

TABLE 3.3: Aerodynamic coefficients obtained with the two solvers for the test case of Figure 3.12. Notice that the Fortran solver gave a non-zero yawing coefficient $C_n = 0.00028$, which is not reported because of the resolution of XFLR5, limited to three decimals.

Three-wing configuration

The last validation considered asymmetric flow around a full three-wings configuration with main wing plus horizontal and vertical stabilisers. The main wing featured both in-plane and out-of-plane displacements through sweep and dihedral angles. Geometrical details are given in Figure 3.13. A good match of the aerodynamic coefficients was achieved, with a maximum of 1.5% error on the C_m, as reported in Table 3.4.

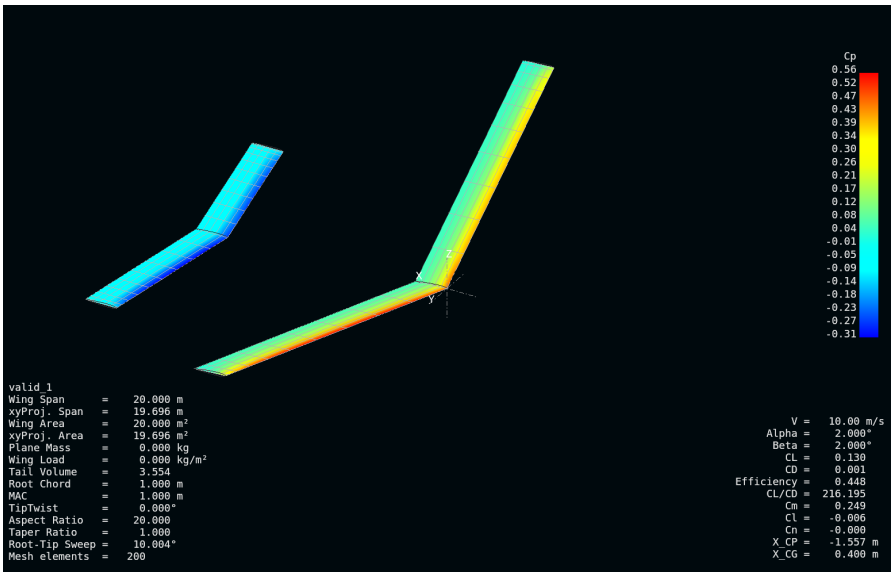

(a) XFLR5.

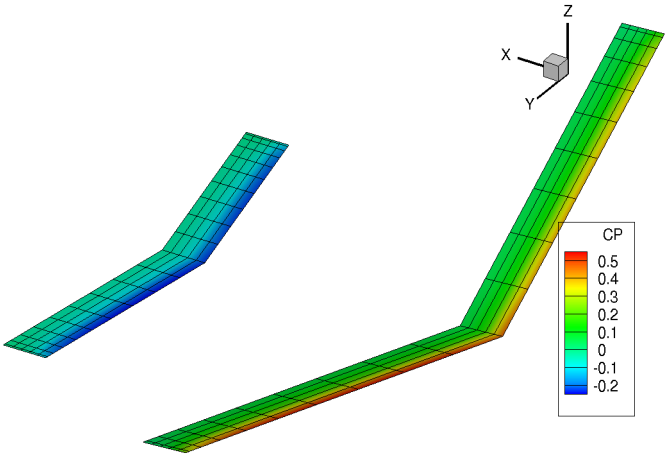

(b) Validated model.

FIGURE 3.12: Panel models with pressure coefficient distribution from the two compared solvers. Main wing: sweep angle $\lambda_S = 10°$, dihedral angle $\gamma_D = 10°$. Tail: span $b_H = 5$ m, chord $c_H = 1$ m, tilt angle $\tau_H = -3°$, root leading edge distance from main wing root leading edge $d = 6$m. Angle of attack $\alpha = 2°$, sideslip angle $\beta = 2°$.

	XFLR5	Validated model
C_L	0.132	0.131
C_D	0.001	0.001
C_m	0.384	0.378
C_l	0.006	0.006
C_n	0.009	0.009

TABLE 3.4: Aerodynamic coefficients obtained with the two solvers for the test case of Figure 3.13

.

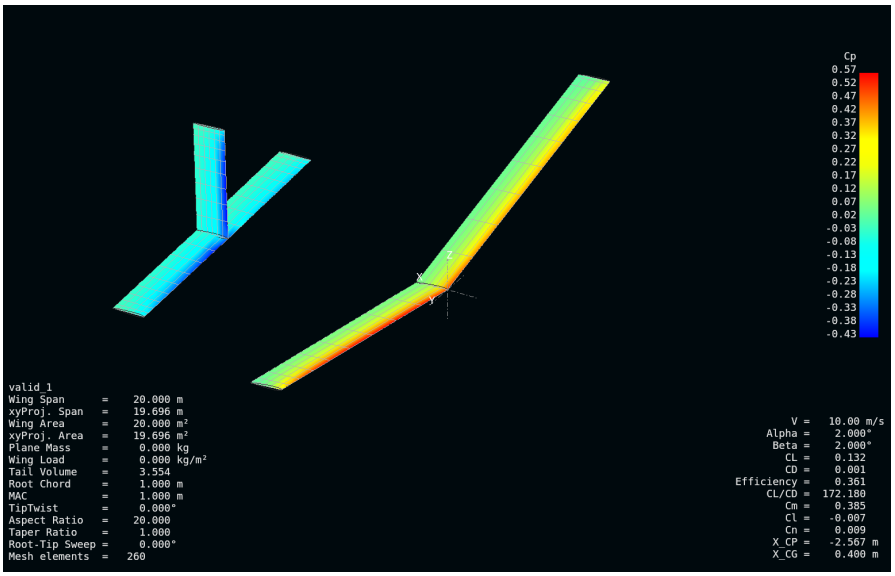

(a) XFLR5.

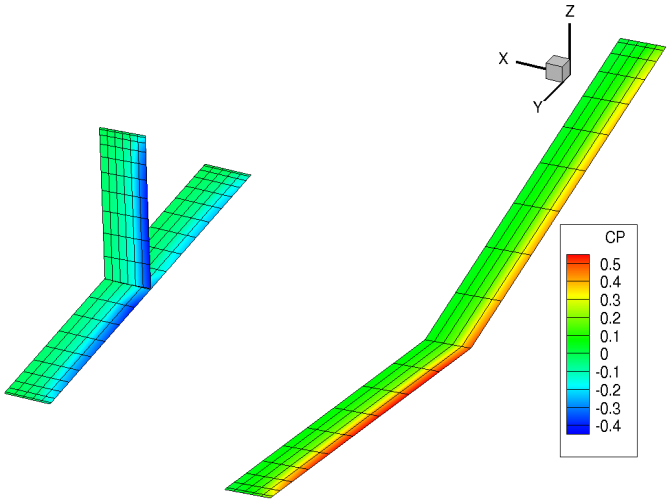

(b) Validated model.

FIGURE 3.13: Panel models with pressure coefficient distribution from the two compared solvers. Main wing: sweep angle $\lambda_s = 0°$, dihedral angle $\gamma = 10°$. Horizontal tabiliser: span $b_h = 5$ m, chord $c_h = 1$ m, tilt angle $\tau_h = -3°$. Fin: span $b_f = 3.5$ m, chord $c_h = 1$ m. Angle of attack $\alpha = 2°$, sideslip angle $\beta = 2°$.

3.2.4 The Unsteady Vortex Lattice Method

3.2.4.1 Theoretical background

As most aeroelastic dynamic problems require the capability to model flow unsteadiness [20], the unsteady version of the VLM described in Section 3.2.3 was implemented in addition to the above methods. The advantage of this method, compared to the unsteady strip theory in Section 3.2.2 is in that the former allows three-dimensional flow and flow interactions between multiple surfaces to be modeled.

Another method often used for 3D unsteady aerodynamic computations is the Doublet Lattice Method (DLM). Although being faster than the UVLM, the DLM is a linear method limited to small out-of-plane harmonic motion with a flat wake, and it is formulated in the frequency domain. On the contrary, the UVLM has a wider applicability because any 3D motion and deformation in the time domain of the lifting surface is allowed, and the 3D shape of the force-free wake is obtained as part of the solution procedure and contributes to it. These characteristics make the latter a more attractive option for applications where complex geometries and large structural motion are envisioned, calling for more flexible analysis tools.

Here follows a brief description of how this formulation differs with respect to the steady one already given.

First, the boundary condition (3.21) needs to account for the contribution of the instantaneous body motion, and therefore it is expanded as follows:

$$(\nabla \Phi_B + \nabla \Phi_W - \nabla \Phi_\infty - \boldsymbol{V}_{\text{rel}} - \boldsymbol{\Omega} \times \boldsymbol{r}) \cdot \mathbf{n} = 0 \tag{3.25}$$

where Φ_B and Φ_W are the velocity potential due to body and wake circulation, respectively, Φ_∞ is the free-stream potential, $\boldsymbol{V}_{\text{rel}}$ is the velocity component due to the body translation with respect to the fluid (excluding the free-stream speed, already accounted for by Φ_∞, but including both rigid body and elastic motion, if any) and the last term inside the brackets accounts for the velocity at $\boldsymbol{r}$ due to the rigid body angular rates $\boldsymbol{\Omega}$.

A second main difference is in the computation of the aerodynamic force at each panel. Instead of using the Kutta-Jukowsky formula (3.23), whose extension to unsteady conditions is controversial [19], the loads are obtained by computing the pressures through the unsteady Bernoulli equation [16]:

$$\frac{P_\infty - P}{P} = \frac{V_B^2}{2} + \frac{|\boldsymbol{V}_\infty + \boldsymbol{V}_{\text{rel}} + \boldsymbol{\Omega} \times \boldsymbol{r}|^2}{2} + \frac{\partial \Phi}{\partial t} \tag{3.26}$$

where $\boldsymbol{V}_B = \nabla \Phi_B$ is the local velocity due to the body circulation, and V_B is its magnitude.

Third and last fundamental difference with respect to the steady version, the UVLM requires a discretization of the wake into vortex rings as done for the body surfaces. This is done by creating a new row of vortex segments at each time step placed in the space covered by the wing trailing edge during the step in question (see Figure 3.5). The new shed wake vortex rings are assigned the same circulation value as the one of the respective trailing edge vortex at the previous step. This is done in order to comply with Kelvin's theorem, stating that in the potential flow region the angular momentum cannot change, and thus the circulation around a fluid curve enclosing the

wing and its wake is conserved. In this way, the memory of the past flow conditions is retained through the wake circulation, which remains unchanged in absence of viscous dissipation.

The validation of the present implementation of the UVLM is reported in the following Section.

3.2.4.2 Validation of the UVLM solver

This section reports the validation of the present implementation of the Unsteady Vortex Lattice Method. As done for the steady part, some validation cases of increasing complexity were chosen progressively with the maturation of the program.

The first case, from [16], is for the sudden forward acceleration of flat wings. The initial flow conditions are influenced by the starting vortex shed by the trailing edge. This induces a downwash on the wing with decreasing intensity as the vortex is left downstream, according to the Biot-Savart law [163]. For this reason, the local instantaneous angle of attack is lower than the nominal steady-state one, the latter being approached asymptotically as the starting vortex moves to infinity downstream.

The simulations are repeated for several aspect ratios, and this gives an idea of the three-dimensional effect of wing tip vorticity. The results are reported in Figure 3.14. As expected, low-aspect-ratio wings experience lower lift because the tip-induced downwash reduces the local effective angle of attack along the span.

It should be noted that the very first values of lift coefficient given by the UVLM are affected by a singularity at $t = 0$ in the time derivative of the velocity potential, needed in the unsteady Bernoulli equation for pressure computation. The singularity is propagated by the finite difference method in the first time steps. The error is due to the fact that a sudden variation of this term happens in a short time, producing a very high value of the velocity potential time rate, and a few steps are needed for its effect to vanish. The error could be reduced by reducing the time step of the time-marching numerical scheme.

A second validation case, again from [16], is for a 3D wing in forced sinusoidal motion at three different reduced frequencies k. Figure 3.15 compares the simulated results for the lift coefficient during steady oscillations (after the transient is vanished), compared against data from [16]. Good agreement was found in all cases, again with less than 1% error.

Further confirmation of the adequacy of the model in the case of harmonic oscillations has been obtained by comparison with the unsteady theory of Theodorsen [18]. In this case, as the theory concerns two-dimensional flow around thin airfoils, a very high aspect ratio ($\mathcal{AR}$= 100) was used in the 3D UVLM model. The frequencies investigated

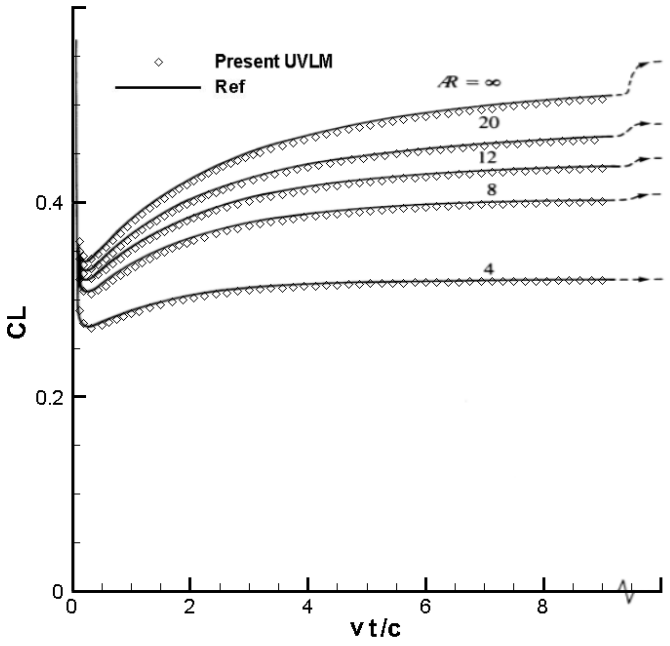

FIGURE 3.14: Validation of the UVLM solver. Lift coefficient of 3D thin wings of different aspect ratios in sudden forward motion. The simulated conditions correspond to $\alpha = 5°$ and $V\,\Delta t/c = 1/16$. Comparison against data from [16].

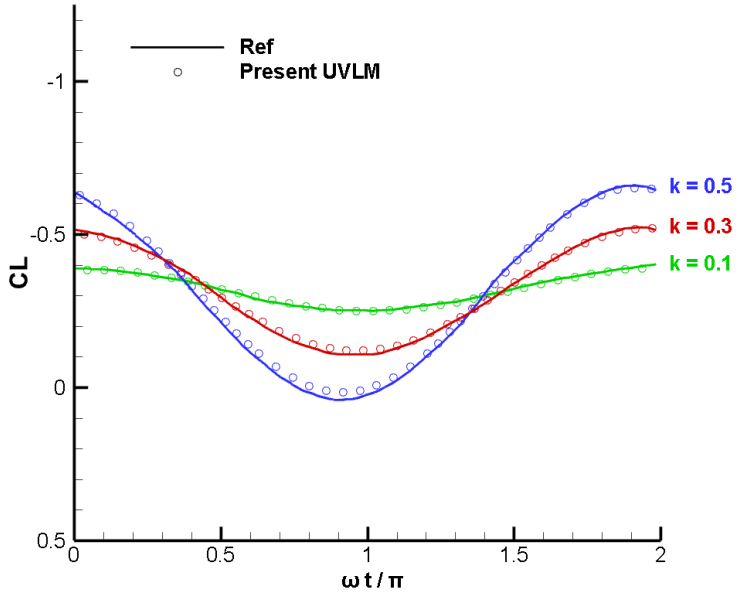

FIGURE 3.15: Validation of the UVLM solver. Time history of lift coefficient of a 3D wing in sinusoidal plunging motion for three reduced frequencies. AR= 4, $h = \infty$, $\alpha = -5°$. Comparison against data from [16].

correspond to $k = 0.25$, $k = 0.5$ and $k = 0.75$. Again, a good matching was obtained as shown in Figure 3.16.

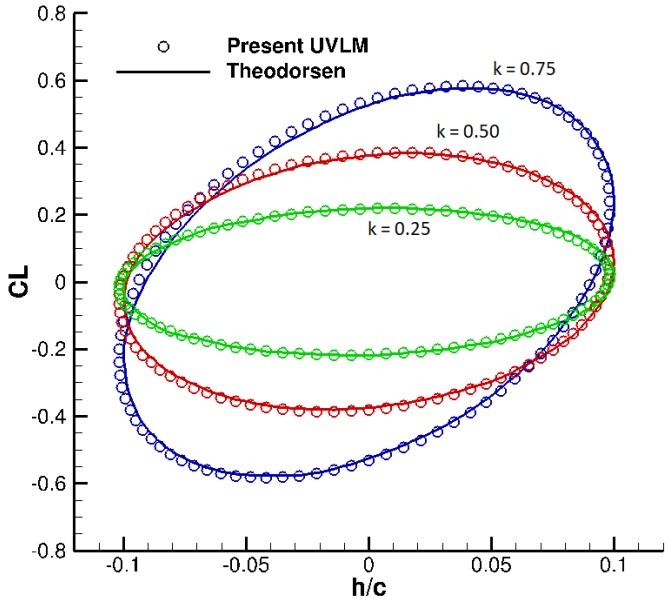

FIGURE 3.16: Validation of the UVLM solver. Lift coefficient of a 2D thin profile in harmonic plunging oscillations, for three reduced frequencies. Comparison against the theoretical model of Theodorsen [18], data from [19].

A more complex case, first introduced in [178] and studied also in [179], was simulated to test the developed model more thoroughly. This time in fact large 3D geometrical variations are considered, and curved surfaces are treated instead of planar wings. The test-case is for two curved symmetric wings flapping in a bird-like sense while moving forward at constant speed. For a better understanding, this is represented in Figure 3.17, where five snapshots are taken from one flapping cycle. Each wing has an aspect ratio $\mathcal{AR} = 3$, and the curvature is that of the NACA 83xx airfoils, where the first two digits refer to maximum camber value and location, and the last two are irrelevant as they relate to the thickness, which is not modeled in this formulation. The configuration presents a geometric angle of incidence with respect to the free-stream direction of $\alpha_0 = 5°$, and the flapping motion is given by the harmonic law $\phi(t) = 45 \cos(\omega t)$, where ϕ is the flapping angle, expressed in degrees.

A first case, corresponding to moderate frequency ($k = 0.1$), and a second one at high frequency ($k = 0.75$) are considered. In both cases, as done by the reference authors, each wing is discretized with 6 chord-wise and 10 span-wise vortex rings, and the flapping cycle is resolved through 40 time steps.

The lift coefficient time history for the low-frequency case is reported in Figure 3.18 and compared with the data from Murua [19]. A semi-quantitative comparison is also reported in Figure 3.19, where the contour plot of wake circulation is compared with that from [178]. The distributions look qualitatively identical.

Similarly, the lift coefficient variation for the high-frequency case is reported in Figure 3.20 and validated against reference [19], whereas the wake circulation contour plot is compared in Figure 3.21 with reference [178]. Again, the same range of circulation values and the same distribution can be qualitatively observed. It should be noted that the two compared methods cannot be assessed as exactly equivalent because some fine-tuning parameters from [178] were not explicitly given (such as the numerical cut-off radius that eliminates the vortex-line singularity, which impacts the precision and the stability of the method, or the exact definitions for the local reference systems on each panel, such as the local lift direction or the surface normal direction).

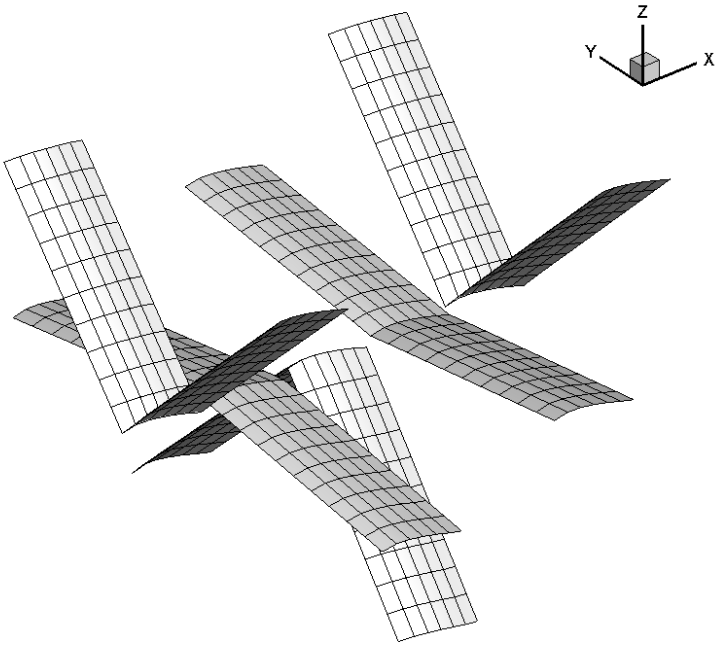

FIGURE 3.17: Validation of the UVLM solver. Flapping wing test-case.

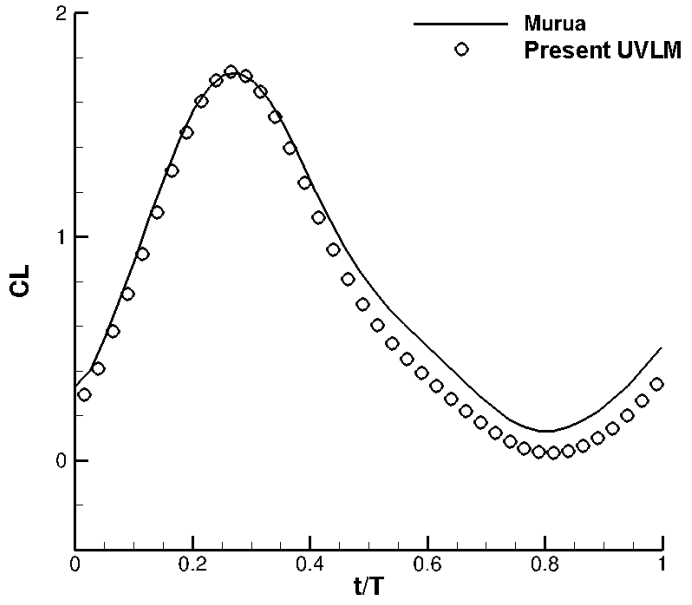

FIGURE 3.18: Validation of the UVLM solver. Flapping wing at $k = 0.1$. Comparison against data from Murua [19].

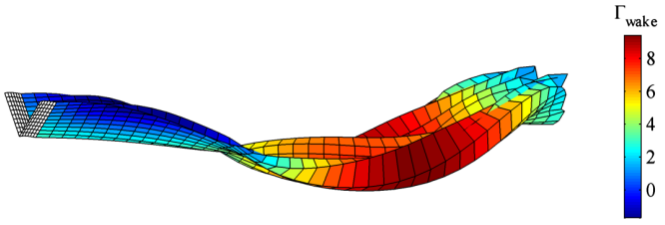

(a) Reference [178].

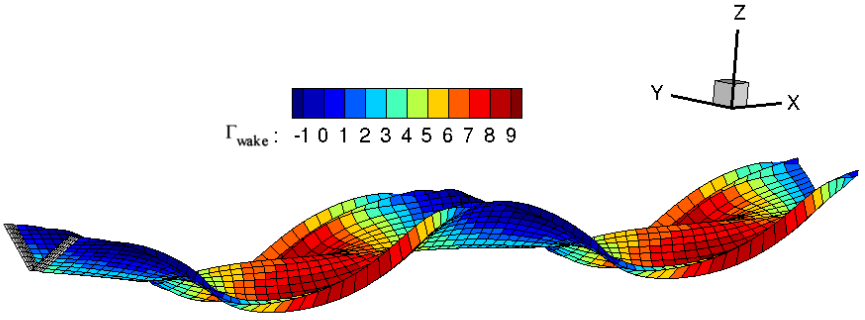

(b) Present UVLM.

FIGURE 3.19: Validation of the UVLM solver. Qualitative comparison of contour plots of the wake circulation Γ_{wake} for the flapping wing test-case. Reduced flapping frequency $k = 0.1$. The reference figure (a) shows only the last flapping cycle, whereas the present model (b) reports one additional cycle, showing that the conditions are already practically stationary, with no visible transient effects from one cycle to the other.

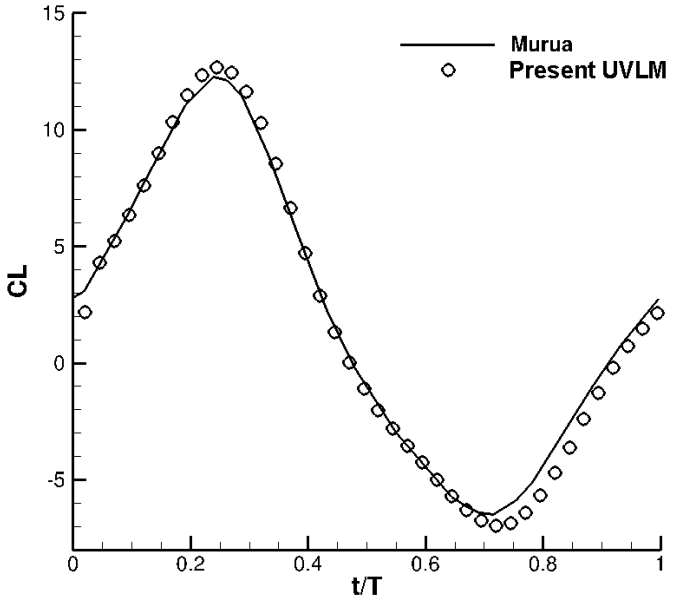

FIGURE 3.20: Validation of the UVLM solver. Flapping wing at $k = 0.75$. Comparison against data from Murua [19].

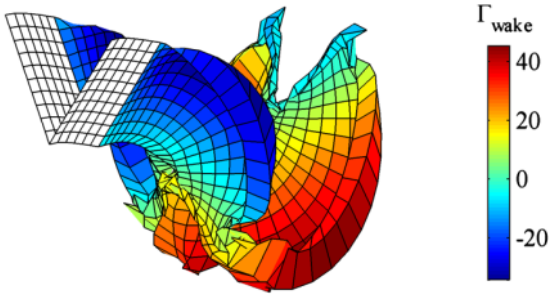

(a) Reference [178].

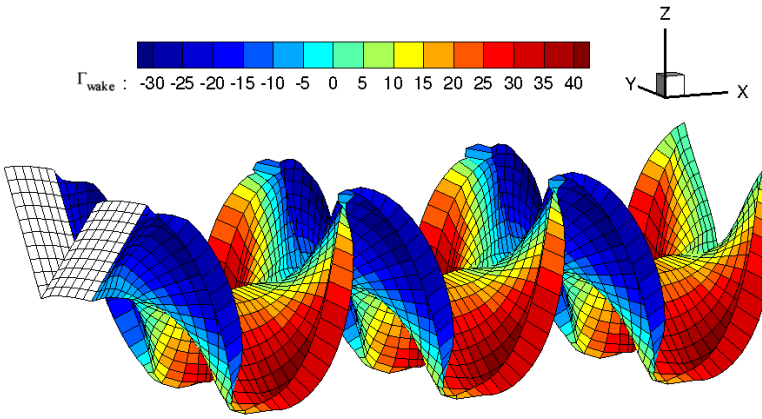

(b) Present UVLM.

FIGURE 3.21: Validation of the UVLM solver. Qualitative comparison of contour plots of the wake circulation Γ_{wake} for the flapping wing test-case. Reduced flapping frequency $k = 0.75$. The reference figure (a) shows only the last flapping cycle, whereas the present model (b) reports two additional cycles, showing that the conditions are already practically stationary, with no visible transient effects from one cycle to the other.

3.2.5 Compressibility corrections

The derivation of the governing equations for both the VLM and the strip theory method implied the hypothesis of incompressible (low-speed) flow. Nevertheless, a correction accounting for a certain degree of compressibility can be introduced, named the Prandtl-Glauert rule. Such correction relies on the assumptions of steady flow and small perturbations, which means that the perturbation on the free stream flow induced by the moving body is small:

$$\left|\frac{\partial \Phi}{\partial x}\right|, \left|\frac{\partial \Phi}{\partial y}\right|, \left|\frac{\partial \Phi}{\partial z}\right| \ll V_\infty \tag{3.27}$$

Under these conditions, it can be shown that the same Laplace equation of the incompressible case holds if applying the simple coordinate transformation:

$$x_0 = \frac{x}{\sqrt{1 - M_\infty^2}} \tag{3.28}$$

$$y_0 = y \tag{3.29}$$

$$z_0 = z \tag{3.30}$$

$$\Phi_0(x_0, y_0, z_0) = \Phi(x, y, z) \tag{3.31}$$

$$\tag{3.32}$$

This transformation implies that the numerical value of the disturbance potential Φ_0 at the point (x_0, y_0, z_0) equals the one of Φ in the original coordinates at point (x, y, z). But it is important to note that the original wing planform in compressible flow differs from the one in equivalent incompressible flow, because its x_0-dimensions have been stretched by $1/\sqrt{1 - M_\infty^2}$, whereas the dimensions in the other two directions remain unchanged. These differences are shown in Figure 3.22. In particular, it is important to note that the transformation produces a change in the wing aspect ratio and sweep.

The equivalence between the two domains means that, once the geometry is transformed in the $(x_0, y_0, z - 0)$ frame, the velocity and pressure distributions can be calculated using the incompressible methods already discussed, and then the pressure field can be transferred back to the corresponding points in the original wing. This means that the forces acting on the mesh of the wing in compressible flow are equal to the corresponding forces on the transformed wing in incompressible flow, which has a different aspect ratio and sweep angle. However, as the dimensions are different, the non-dimensional coefficients are different, and it can be shown that the high speed coefficients are obtained as:

$$C_{L(M>0)} = \frac{C_{L(M=0)}}{\sqrt{1 - M_\infty^2}} \tag{3.33}$$

$$C_{m(M>0)} = \frac{C_{m(M=0)}}{\sqrt{1 - M_\infty^2}} \tag{3.34}$$

It is important to note that, because of the inherent geometrical distortion, when a three-dimensional solution is required, as for the VLM case, there is no alternative to analyzing a new wing planform for each different Mach number. Instead, for a two-dimensional approximation, as the strip theory, the original geometry can be kept, and only the corrections of Equations (3.33) and (3.34) are required. These can simply be implemented by replacing the incompressible thin-plate lift-curve slope of $2\,\pi$ with the compressible one of $2\,\pi/\sqrt{1 - M_\infty^2}$.

The Prandtl-Glauert correction is valid for steady or quasi-steady flow up to $M = 0.7$ [163]. For unsteady aerodynamics some corrections have also been proposed. However, they require the definition of several additional coefficients or indicial functions, that introduce additional complexity, uncertainty and computational cost. On the other hand, as far as strip theory is concerned, it is known that applying the Prandtl-Glauert correction to the lift-curve slope results in conservative flutter speed predictions [20]. Therefore, it was decided that:

- For steady, 3D compressible analysis, the VLM with the Prandtl-Glauert transformation will be used;
- For time-marching gust response simulations the approximation of quasi-steady flow is assumed, and the VLM with the Prandtl-Glauert transformation will be used;
- For flutter analysis, the strip theory with the Prandtl-Glauert correction applied to the lift-curve slope will be used;
- No effort is done to correct the UVLM for compressibility, and therefore its use will be limited to incompressible regimes.

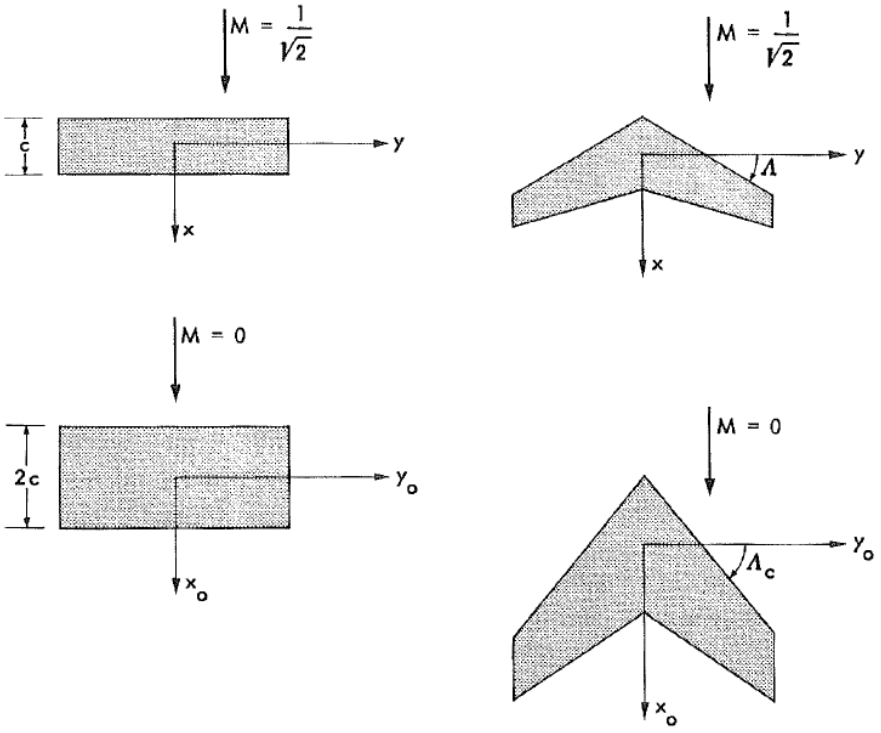

FIGURE 3.22: Equivalent straight and swept planforms obtained by the Prandtl-Glauert transformation, from [20].

3.3 Structural dynamics

This section provides the details of the structural dynamics models to be employed for aeroelastic analyses. Following Chapter 2, 1-dimensional structural models are in general adequate for aeroelastic applications targeted in this project. For this reason, only 1-D beam theory is here taken into account. First, a linear Finite Element Model developed by the author in previous work [171] is presented in Section 3.3.1. The model, originally conceived for clamped, uniform beams, was adapted here to unconstrained wings with varying section properties. This model is useful in particular for its capability to provide quick estimation on the structure dynamic properties via eigenvalue analysis. This model is also coupled with the linear unsteady aerodynamic strip theory introduced in Section 3.2.2, enabling linear aeroelasticity computations. This is further discussed in Section 3.4.1.

These tools are especially useful when dealing with moderate deformations. In the future steps of this project, a non-linear structural solver will also be included to enable aeroelastic computation in the case of higly flexible aircraft. This is briefly mentioned in Sections 3.3.2 and 3.4.2.

3.3.1 Linear beam Finite Element Model

The linear beam model employed in this work is based on the hypothesis of small displacements and on the Euler-Bernoulli beam theory, which considers the shear strain negligible compared to the bending strains and assumes that each beam cross section rotates rigidly around its neutral axis. A complete description of this formulation can be found in [30, 171]. Here only the main features are outlined.

First, it is worth pointing out that all the below equations relating to linear or nonlinear structural models are expressed in a structural reference frame, which is fixed at the beam clamped end. It is a right-handed frame whose first axis x_s is directed along the undeformed beam axis, and y_s and z_s represent the horizontal and vertical directions, with z_s positive upwards (see Figure 3.23). The subscript $(\,)_s$ will be dropped in the following equations to ease the notation, but the reader shall have no doubt that all the structural equations and definitions refer to this frame.

The model considers only two structural responses: a) the bending response, involving the vertical deformation u and the rotation φ around the bending axis, and b) the twist response, involving the twist rotation ϑ. The corresponding dynamic equations for bending and twist are obtained writing the equilibrium (in terms of forces per unit span) between the inertial loads, the elastic forces and the external (aerodynamic) loads (F_z and M_x). If the beam elastic axis (EA) and its center-of-gravity axis (CG) are not coincident, the bending and twisting degrees of freedom are inertially coupled, and the

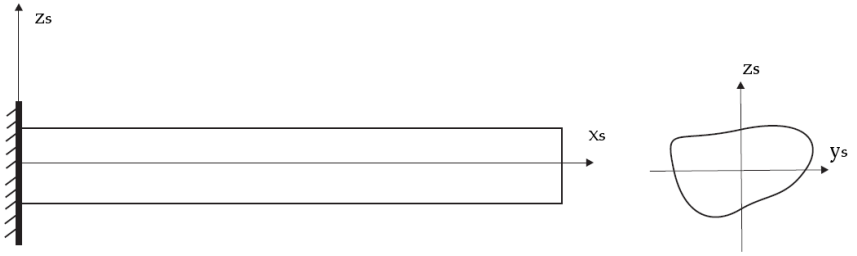

FIGURE 3.23: Beam coordinate system.

importance of this coupling increases with the GC to EA distance d. This linear model is restricted to the out-of-plane bending, and therefore only the horizontal component of this offset, namely y_{CG}, is taken into account.

The resulting structural model, according to a classical derivation (such as from [105]), is described by the following set of equations:

$$\begin{cases} \mu(x)\frac{\partial^2 u(x,t)}{\partial t^2} - \mu(x)\, y_{\mathrm{CG}}(x)\frac{\partial^2 \vartheta(x,t)}{\partial t^2} + \frac{\partial^2}{\partial x^2}\left(EI^{\mathrm{A}}_{yy}(x)\,\frac{\partial^2 u(x,t)}{\partial x^2}\right) = \frac{\partial F_z(x,t)}{\partial x} \\ \mu(x)d(x)\frac{\partial^2 u}{\partial t^2}(x,t) + \left[I_p(x) + \mu(x)\, y^2_{\mathrm{CG}}(x)\right]\frac{\partial^2 \vartheta}{\partial t^2}(x,t) - GJ(x)\frac{\partial^2 \vartheta}{\partial x^2}(x,t) = \frac{\partial M_x(x,t)}{\partial x} \end{cases} \tag{3.35}$$

Here, I^{A}_{yy} and I^{A}_{zz} are the two section area moments of inertia, and its product with the Young's modulus E gives the bending stiffness. GJ is the torsional stiffness, with J being the cross-section torsion constant. μ denotes the local mass per unit length, I_p is the polar moment of inertia around the CG, and y_{CG} indicates the shift of the local center of gravity from the beam axis.

The analytical model described above has been implemented in a finite element model, following the Weak Galerkin Method [180]. The shape functions used for bending variables are the third-order polynomials of the Euler's beam formulation, while linear functions were used to model twist.

For each element the vector $\boldsymbol{w_e}$ contains all the nodal displacements of the element:

$$\boldsymbol{w_e}(t) = \left[\boldsymbol{w_{e1}} \;\middle|\; \boldsymbol{w_{e2}}\right]^T = \left[u_1(t) \quad \varphi_1(t) \quad \vartheta_1(t) \;\middle|\; u_2(t) \quad \varphi_2(t) \quad \vartheta_2(t)\right]^T, \tag{3.36}$$

where $u_i(t)$, $\varphi_i(t)$ and $\vartheta_i(t)$ are the vertical displacement, bending slope and twist of the i-th node, respectively.

The system is then assembled for N elements and the constrained degrees of freedom are conveniently removed, giving:

$$\boldsymbol{M}\,\ddot{\boldsymbol{w}} + \boldsymbol{K}\,\boldsymbol{w} = \boldsymbol{F_a} \tag{3.37}$$

3.3.2 Nonlinear Geometrically-Exact Beam Theory (GEBT)

As discussed in Section 2.3, the effects of large deformations may be important, and therefore it is desirable to have the capability to capture them. For this reason, this framework includes a non-linear structural solver interfaced with the steady and unsteady VLM modules. More precisely, it is a geometrically-nonlinear solver, which models correctly the nonlinear deformations, but retains the linearity of the constitutive relationships. This serves as the highest fidelity tool in this framework for aeroelastic analysis of very flexible airplanes.

The chosen structural dynamics software is the `GEBT` program (standing for Non-linear Geometrically-Exact Beam Theory), freely available at [181] and documented in [182, 183]. The software, developed in Fortran, has already been successfully employed on aeroelastic applications, such as in [6, 22, 96, 179, 184].

It is a general-purpose tool designed to address the challenging analysis of highly-flexible, slender structures, where the hypothesis of small displacement, bringing to the common and simple linear models, are significantly violated. The main feature of the approach is that displacements, forces and moments are transferred between the deformed and undeformed beam frames according to exact, nonlinear kinematic relationships involving all the translation and rotation degrees of freedom in space. The nonlinear equilibrium is found iteratively using the Newtown-Raphson method.

The material, however, is still supposed to be in its linear elastic domain, which is why the constitutive relationships remain linear. A detailed description of the analytical formulation can be found in [182, 183, 185].

`GEBT` requires the cross-sectional properties at each element node to be provided in the form of flexibility and mass matrices. The flexibility matrix $\boldsymbol{S}$ expresses the link between nodal loads and structural strains as in Equation (3.38). The notation follows the structural reference frame shown in Figure 3.23.

$$\begin{bmatrix} \gamma_{xx} \\ 2\,\gamma_{xy} \\ 2\,\gamma_{xz} \\ \kappa_x \\ \kappa_y \\ \kappa_z \end{bmatrix} = \underbrace{\begin{bmatrix} S_{11} & S_{12} & S_{13} & \cdots & S_{16} \\ S_{21} & S_{22} & S_{23} & \cdots & S_{26} \\ S_{31} & S_{32} & S_{33} & \cdots & S_{36} \\ \vdots & \vdots & \vdots & \ddots & \vdots \\ S_{61} & S_{62} & S_{63} & \cdots & S_{66} \end{bmatrix}}_{S} \begin{bmatrix} F_x \\ F_y \\ F_z \\ M_x \\ M_y \\ M_z \end{bmatrix} \tag{3.38}$$

Here, the first axis is the beam axis, so that γ_{11} are the axial strains, γ_{12} and γ_{21} are the shear strains, and $\kappa_x = \partial\vartheta/\partial x$ measures the twist per unit length and $\kappa_y = \partial\varphi_y/\partial x$ and $\kappa_z = \partial\varphi_z/\partial x$ are the two curvatures per unit length. The user can model any type of material, including anisotropic ones, by providing an appropriately populated

flexibility matrix. To suppress unneeded deformation mechanisms it is sufficient to put the corresponding elements S_{ij} equal to zero. For example, for an isotropic cross-section at its shear center, the flexibility matrix would be:

$$\boldsymbol{S} = \begin{bmatrix} \frac{1}{EA} & 0 & 0 & 0 & 0 & 0 \\ 0 & \frac{1}{GK_{xy}} & 0 & 0 & 0 & 0 \\ 0 & 0 & \frac{1}{GK_{xz}} & 0 & 0 & 0 \\ 0 & 0 & 0 & \frac{1}{GJ} & 0 & 0 \\ 0 & 0 & 0 & 0 & \frac{1}{EI^{\mathrm{A}}_{yy}} & 0 \\ 0 & 0 & 0 & 0 & 0 & \frac{1}{EI^{\mathrm{A}}_{zz}} \end{bmatrix} \tag{3.39}$$

Here, EA is the cross-section axial rigidity, with A denoting the cross-section area, and GK_{xy} and GK_{xz} are the shearing rigidity in the horizontal and vertical planes. Note that the assumption of negligible vertical and horizontal shear deformation is enforced by considering infinite shearing rigidity ($1/GK_{xy} = 1/GK_{xz} = 0$), so K_{xy} and K_{xz} do not need to be computed. Again, GJ is the torsional rigidity, with J being the cross-section torsion constant. I^{A}_{yy} and I^{A}_{zz} are the two section area moments of inertia, which multiplied by the Young's modulus E give the bending rigidity around the structural y_s and z_s axes.

If dynamic analysis has to be performed, linear and angular momenta have to be included for dynamic simulations. Equation (3.40) relates the structural velocities to the linear and angular momentum via the mass matrix $\boldsymbol{M}$.

$$\begin{bmatrix} P_x \\ P_y \\ P_z \\ Q_x \\ Q_y \\ Q_z \end{bmatrix} = \underbrace{\begin{bmatrix} \mu & 0 & 0 & 0 & \mu z_{\mathrm{CG}} & -\mu y_{\mathrm{CG}} \\ 0 & \mu & 0 & -\mu z_{\mathrm{CG}} & 0 & 0 \\ 0 & 0 & \mu & \mu y_{\mathrm{CG}} & 0 & 0 \\ 0 & -\mu z_{\mathrm{CG}} & \mu y_{\mathrm{CG}} & I_p & 0 & 0 \\ \mu z_{\mathrm{CG}} & 0 & 0 & 0 & I_{yy} & 0 \\ -\mu y_{\mathrm{CG}} & 0 & 0 & 0 & 0 & I_{zz} \end{bmatrix}}_{\boldsymbol{M}} \begin{bmatrix} V_x \\ V_y \\ V_z \\ \Omega_x \\ \Omega_y \\ \Omega_z \end{bmatrix} \tag{3.40}$$

Here, μ denotes the local mass per unit length, y_{CG} and z_{CG} indicate the shift of the local center of gravity from the beam axis. The terms I_{yy}, I_{zz} and I_p denote the two mass moments of inertia and the polar moment of inertia, respectively. P_i and Q_i are the linear and angular momenta, and V_i and Ω_i are the linear and angular velocities.

`GEBT` allows different types of analysis to be performed on slender structures with constant or varying section properties along the beam axis, including:

- Linear or nonlinear static analysis;

- Linear or nonlinear steady-state dynamic simulation (neglecting all time derivatives)
- Linear or nonlinear transient dynamic simulation;
- Eigenvalue analysis of small motions about a linearized nonlinear steady state.

In the context of this project, the most interesting applications are the nonlinear static analysis and the linear transient dynamic analysis starting from a static nonlinear equilibrium.

3.4 Aeroelasticity

3.4.1 Linear aeroelasticity by 1D-beam FEM and unsteady strip aerodynamics

A linear aeroelastic model has been developed and validated as an intermediate fidelity level tool for aeroelastic applications, especially time simulation and flutter prediction through eigenvalue analysis. The model relies on the unsteady strip theory presented in Section 3.2.2 for the aerodynamic loads, and on the linear beam FEM of Section 3.3.1.

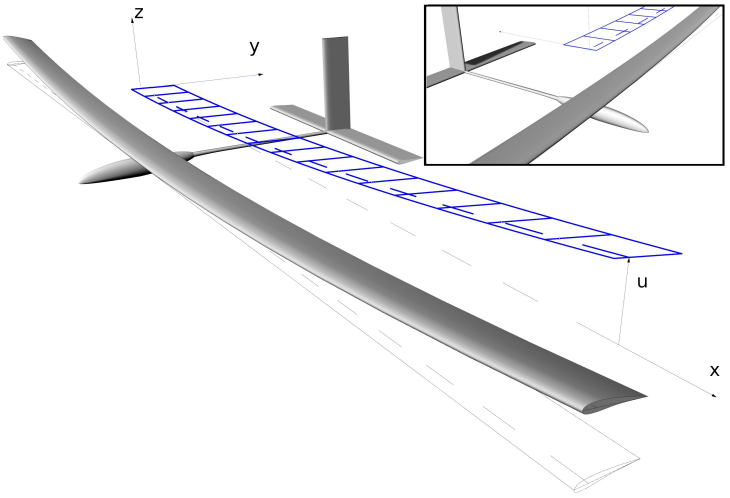

FIGURE 3.24: Representative layout and discretization for the linear aeroelastic model. The real wing in grey is represented by a flat surface, discretized in N 2D strips (blue). Each strip undergoes pitch and plunge motion according to the structural deformation. No interaction (crossflow) exists among the different wing sections. Only the main wing is modeled.

3.4.1.1 Discretized aeroelastic equations

The complete coupled set of equations describing the aeroelastic model is found combining the above aerodynamic model with Equation (3.37). A full derivation of the

matrix formulation was already published in [30, 171], and therefore only a synthetic overview is reported here. Once all the aerodynamic matrices are available, and the additional aerodynamic states $\boldsymbol{z}$ are included in the global equilibrium, Equation (3.37) is expanded as follows:

$$\begin{cases} \boldsymbol{M}^{(3N\times 3N)}\,\ddot{\boldsymbol{w}} + \boldsymbol{K}^{(3N\times 3N)}\,\boldsymbol{w} = \boldsymbol{A}_M^{(3N\times 3N)}\,\ddot{\boldsymbol{w}} + \boldsymbol{A}_C^{(3N\times 3N)}\,\dot{\boldsymbol{w}} \\ \qquad\qquad + \boldsymbol{A}_K^{(3N\times 3N)}\,\boldsymbol{w} + \boldsymbol{A}_z^{(3N\times 8N)}\,\boldsymbol{z} \\ \dot{\boldsymbol{z}} = \boldsymbol{\Psi}^{(8N\times 3N)}\,\boldsymbol{w} + \boldsymbol{E}^{(8N\times 8N)}\,\boldsymbol{z} \end{cases} \tag{3.41}$$

The right-hand side of the first line in Equation (3.41) represents the total aerodynamic force $\boldsymbol{F_a}$, which arises from the aerodynamic stiffness, damping and added masses (accounted for by the $\boldsymbol{A}_K$, $\boldsymbol{A}_C$ and $\boldsymbol{A}_M$ matrices, respectively) and from the unsteady aerodynamic effects included via the last term $\boldsymbol{A}_z\,\boldsymbol{z}$. The second line of Equation (3.41) describes the dynamics of the aerodynamic states, which involves the additional coupling matrix $\boldsymbol{\Psi}$ and the dynamic matrix $\boldsymbol{E}$. It should be noted that this formulation attributes all the required variables to each beam node. This means that each node is assigned with 3 structural displacements (with the respective velocities and accelerations), and 8 additional aerodynamic states. Therefore, the size of each matrix is proportional to the number of nodes. With the hypothesis of clamped wing, enforced hereafter, the number of free nodes equals the number of elements N, which is used in Equation (3.41) to specify the matrices' dimensions.

This system is then re-assembled in state-space form. To this aim, the three following matrices are introduced for convenience:

$$\begin{aligned} \boldsymbol{M}_T &= \boldsymbol{M} - \boldsymbol{A}_M \\ \boldsymbol{C}_T &= \boldsymbol{C} - \boldsymbol{A}_C \\ \boldsymbol{K}_T &= \boldsymbol{K} - \boldsymbol{A}_K \end{aligned} \tag{3.42}$$

Here, $\boldsymbol{C}$ is the structural damping matrix, which was set to zero in this work as a conservative simplifying assumption, but that could be easily populated to include any damping model eventually required. The desired state-space representation is of the kind:

$$\dot{\boldsymbol{x}} = \boldsymbol{A}\,\boldsymbol{x} \tag{3.43}$$

Equations (3.41) are turned into the form of Equation (3.43) with by implementing the following matrix structure:

$$x = \begin{bmatrix} w \\ v \\ z \end{bmatrix}; \qquad A = \begin{bmatrix} \mathbf{0} & \boldsymbol{I} & \mathbf{0} \\ -\boldsymbol{M}_T^{-1}\boldsymbol{K}_T & -\boldsymbol{M}_T^{-1}\boldsymbol{C}_T & -\boldsymbol{M}_T^{-1}\boldsymbol{A}_z \\ \boldsymbol{\Psi} & \mathbf{0} & \boldsymbol{E} \\ \mathbf{0} & \mathbf{0} & \mathbf{0} \end{bmatrix}$$

It is worth specifying that the state vector w represents the structural nodal variables (vertical displacement, bending slope and twist), $v = \dot{w}$ represents their velocities, z contains the aerodynamic variables coupled to the structural degrees of freedom.

3.4.1.2 Validation

The model described above can be applied either to a restrained wing (typically a clamped wing) or to a wing-fuselage system, where the center of gravity is free to plunge vertically according to the applied external forces, namely the gravitational, inertial and aerodynamic loads (see Figure 3.25). A validation case for a wing-fuselage system has been chosen from [20], for which the planform, discretization and mass distribution are illustrated in Figure 3.26. All the data describing the test-case can be found in the reference text.

In the book, torsional motion is neglected, so that the structure can only experience heaving oscillations. This restriction is enforced in the present model by constraining to zero the torsional degree of freedom of all the elements.

Additionally, the reference example approximates the response by retaining only the rigid body, the first symmetric and the first asymmetric bending modes. The same approximation is therefore enforced in the present model, by applying a classical modal projection technique to the structural dynamic matrix. More details on this procedure can be found in [171].

Figure 3.27 shows the comparison of the root bending moment per unit gust amplitude after a sharp-edged gust encounter. The results are computed for both the rigid airplane case, where any structural vibration is constrained, and the elastic airplane case. It can be seen that the two models capture the same behaviour, despite not showing an exact match (especially regarding the flexible response). This is attributed to a main difference in the discretization method: while in reference [20] the exact analytical modal shapes are used, in the present case the modal shapes depend on the finite element representation. Also, in the present model the added masses can only be attributed to the element nodes. Since only a uniform discretization scheme is allowed, the added masses cannot be placed exactly in the same locations as in Figure 3.26. This mismatch only influences the inertial loads in the elastic case, as in the rigid case the mass distribution is irrelevant.

An important observation is that the elastic case undergoes higher structural stresses, and this is due to the inertial loads transferred from the wing structure to the center of gravity through the wing root. Other than serving as a validation case, this example provides further confirmation of the critical role that structural flexibility plays in aircraft design, and of the importance of underpinning the design with aeroelastic evaluations.

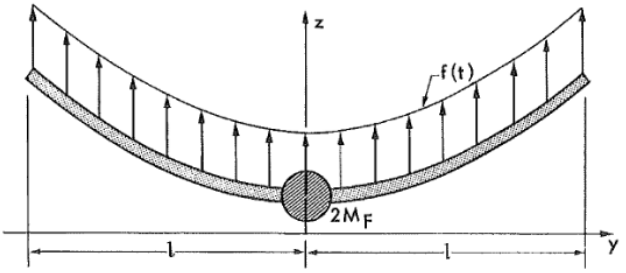

FIGURE 3.25: Schematic representation of a free wing-fuselage system experiencing aeroelastic oscillations, from [20].

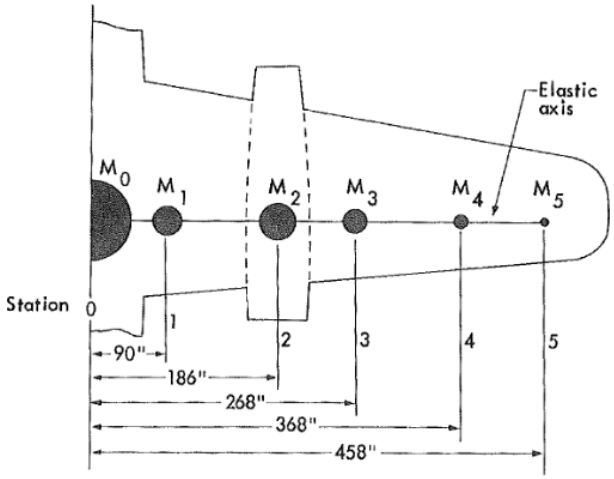

FIGURE 3.26: Planform, discretization, and mass distribution for the test-case in [20].

A couple of validation cases were also investigated to verify the correctness of the proposed model for flutter predictions. Two wing models with opposite characteristics were selected from the literature: the Goland wing [186] which is a quite rigid, low-aspect-ratio wing, and the Patil wing [29], very slender and flexible.

The Goland wing properties are given in Table 3.5. The evolution of its stability characteristics with increasing air speed is traced in Figures 3.28 and 3.29, showing, respectively, the frequencies and damping ratios of the first 5 modes. Figure 3.28 shows that above 100-110 m/s the frequencies of the first bending mode and the first torsional mode start to coalesce. This progressive modal coupling is the cause of the flutter instability, which is reached at 134.6 m/s (marked by a red vertical line). From the damping

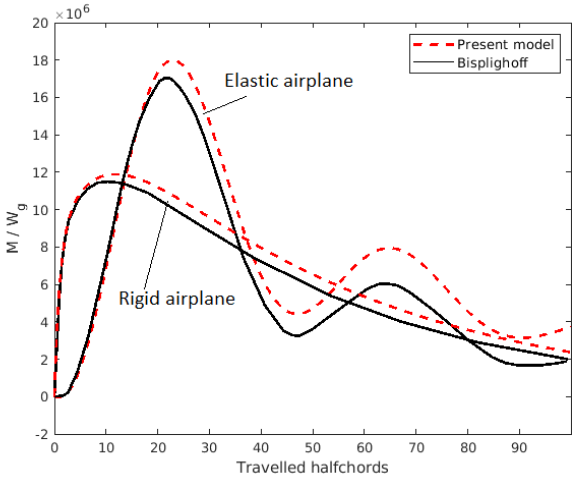

FIGURE 3.27: Time response of the root bending moment per unit gust amplitude following a sharp-edged gust. The curves are compared with those reported in [20].

ratio plot of Figure 3.29, it can be seen that at that speed the first torsional mode (in orange) crosses the x axis, becoming negatively damped. At the crossing point, the mode has a frequency of 10.9 Hz. On the other hand, the first bending mode shows a steep increase in its damping, which is a common behaviour in such aeroelastic systems. These results indicate that the physical instability phenomenon is captured correctly. This is confirmed by the data found in the literature, where the flutter speed predictions are very close to the one found here, where (see Table 3.6).

Property	**Unit**	**Value**
Semispan	m	6.096
Chord	m	1.8288
Mass per unit length	kg/m	35.71
Elastic axis (from l.e.)	-	33% chord
Center of gravity (from l.e.)	-	43% chord
Bending rigidity	$N{\cdot}m^2$	$9.77 \cdot 10^6$
Torsional rigidity	$N{\cdot}m^2$	$0.99 \cdot 10^6$
Moment of inertia	kg·m	8.64

TABLE 3.5: Aeroelastic properties of the Goland wing, as given in [19].

Source	**Model**	V_f [m/s]	**e** [%]
Goland [186]	Analytical	137.2	1.9
Patil [187]	Beam + strip theory	135.6	0.7
Present model	Beam + strip theory	134.6	0.0

TABLE 3.6: Flutter speed of the Goland wing. Note that **e** denotes the relative difference with respect to the present model.

Similar conclusions are drawn from the second flutter investigation, this time on the more flexible Patil wing. The aeroelastic properties are summarized in Table 3.7. Again, the convergence between the first bending (blue) and the first torsional (green) modes

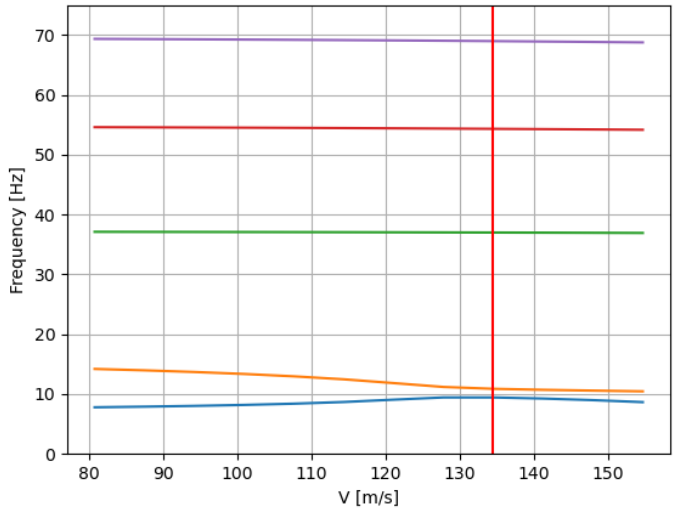

FIGURE 3.28: Evolution of the first 5 modal frequencies with air speed for the Goland wing. A red vertical line marks the speed at which the flutter instability is reached.

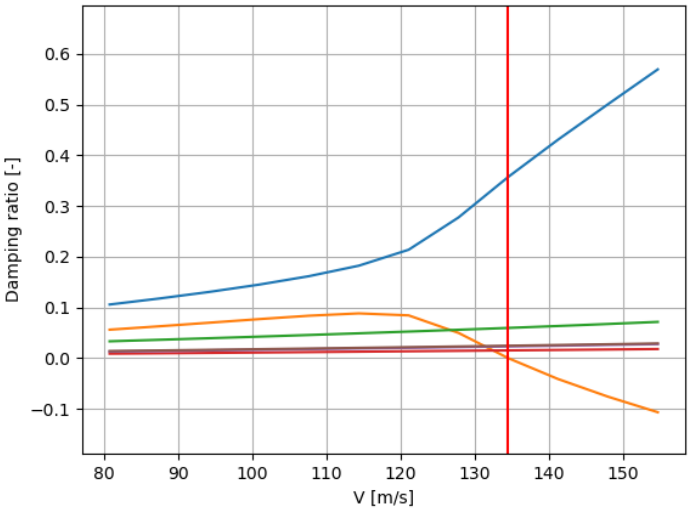

FIGURE 3.29: Evolution of the first 5 modal damping ratios with air speed for the Goland wing. A red vertical line marks the speed at which the flutter instability is reached.

is quite evident from Figure 3.30. This time, the second bending mode (orange) is between the two, but it does not participate in the flutter mechanism. From Figure 3.31, it can be seen that the unstable mode is again the first torsional mode, whose damping becomes negative above 31.4 m/s, at the frequency of about 3.4 Hz. It is also interesting to note that because of the high flexibility (low stiffness), the first bending frequency is so low that at some point, around 26 m/s, it almost looses its oscillatory nature, touching the critical damping 1.0, before turning again into a highly damped oscillatory state, with a damping ratio above 0.9. The qualitative and quantitative differences

between these two plots and those for the Goland wing (Figures 3.28 and 3.29) reflect the relevant physical differences between a slender, flexible wing and a stout, rigid one. However, also for the Patil wing the results are satisfactory when compared to other studies. Data from three reference papers are collected in Table 3.8, and all demonstrate a very good match with respect to the present results.

Property	**Unit**	**Value**
Semispan	m	16.0
Chord	m	1.0
Mass per unit length	kg/m	0.75
Elastic axis	-	50% chord
Center of gravity	-	50% chord
Bending rigidity	Nm^2	$2 \cdot 10^4$
Torsional rigidity	Nm^2	$1 \cdot 10^4$

TABLE 3.7: Aeroelastic properties of the Patil wing, from [29].

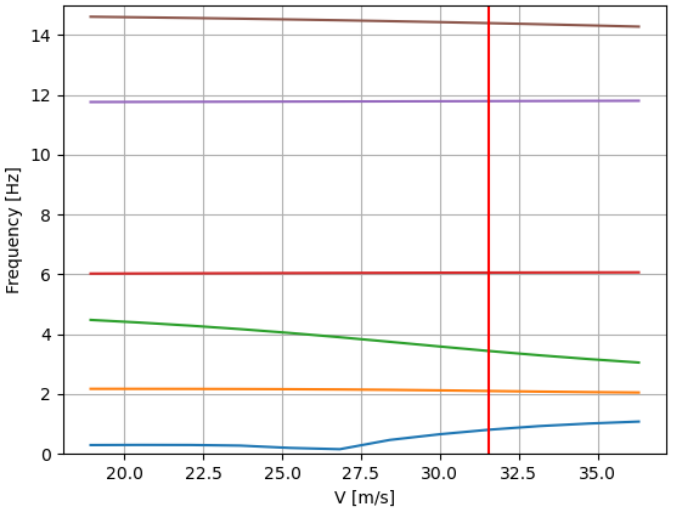

FIGURE 3.30: Evolution of the first 6 modal frequencies with air speed for the Patil wing. A red vertical line marks the speed at which the flutter instability is reached.

Source	**Model**	V_f [m/s]	f [Hz]
Patil [187]	Beam + 3D panel	31.8	3.7
Patil [188]	Beam + strip theory	32.2	3.6
Present model	Beam + strip theory	31.4	3.4

TABLE 3.8: Flutter speed and frequency of the Patil wing.

3.4.2 Nonlinear aeroelasticity

The highest fidelity model developed in this project for aeroelastic simulations is one coupling the `GEBT` nonlinear structural model presented in Section 3.3.2 with the steady

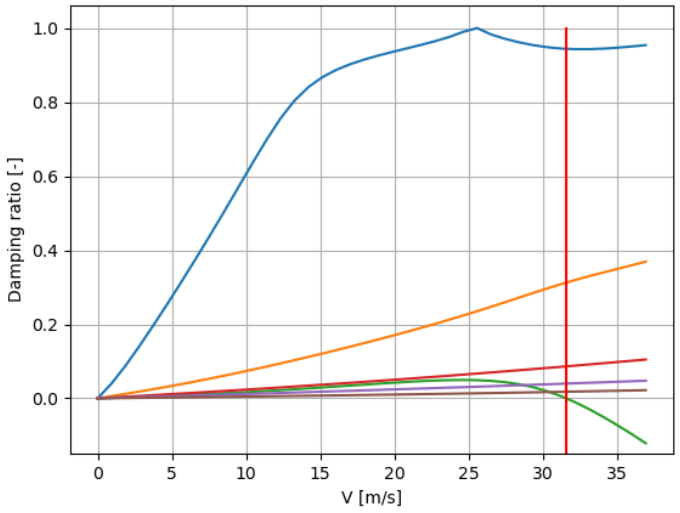

FIGURE 3.31: Evolution of the first 6 modal damping ratios with air speed for the Patil wing. A red vertical line marks the speed at which the flutter instability is reached.

and unsteady VLM of Sections 3.2.3 and 3.2.4. This model brings the framework the capability of dealing with flexible slender lifting surfaces in an efficient way, suitable for supporting the conceptual design phase, in line with the current state of the art, discussed in Sections 2.3 and 2.4. In particular, it enables to address the nonlinear static analysis needed for the structural sizing and optimization of flexible wings, as well as to perform dynamic response to gust by superimposing the aeroelastic transient response to the nonlinear static equilibrium corresponding to level flight.

3.4.2.1 Fluid-structure interface

In order to put such disciplinary coupling in place, it is essential to interface the two domains in an effective and robust way. This means that aerodynamic loads must be transferred to the structural model and structural deformations and velocities must be tracked back to the aerodynamic mesh by maintaining physical consistence. In the linear model presented in Section 3.4.1, this was a trivial task because the aerodynamic and structural meshes are coincident: the aerodynamic strips are located exactly at the beam nodes, so that loads and deformations are all directly calculated and applied at the same points, without requiring any transformation or interpolation process.

However, as the VLM and beam discretizations are completely different, an interpolation technique is required. The approach here adopted follows the method proposed by [189]. The basic idea is that we need a relationship that allows to derive the displacements in the fluid domain mesh, indicated here as $\delta \boldsymbol{y}_f$, knowing those in the structural domain, $\delta \boldsymbol{y}_s$. Provided that the fluid domain consists of N_f nodes, and the structural

domain of N_s nodes, this relationship is commonly expressed in the form of Equation (3.44).

$$(\delta \boldsymbol{y}_f)_i \;=\; \sum_{j=1}^{N_s} h_{ij}\,(\delta \boldsymbol{y}_s)_j \tag{3.44}$$

The elements h_{ij} can be grouped in a matrix $\boldsymbol{H}$ known as interpolation matrix. A common requirement is that the interpolation of displacements and forces between the two domains guarantees the conservation of energy. This is usually obtained by imposing that the virtual work of the aerodynamic loads on the virtual displacement in the aerodynamic domain equals the virtual work of the corresponding structural loads on the virtual structural displacements. It is well known that this condition translates into the fact that the loads on the structural nodes can be derived from the loads in the aerodynamic domain by multiplying the latter by the transpose of $\boldsymbol{H}$. Despite this does not include the conservation of momentum, the approach is still satisfactory in most applications and remains one of the most commonly applied.

To understand how the adopted approach brings to the calculation of the required matrix $\boldsymbol{H}$, it is worth starting from a simple statement of the problem. The objective is to reconstruct a function f, defined in a compact space Ω, that allows to find a set of nodes $Y = [\boldsymbol{y_1}, \boldsymbol{y_2}, \ldots, \boldsymbol{y_{N_f}}]$ from the knowledge of the function values $f(\bar{\boldsymbol{x}}_1), f(\bar{\boldsymbol{x}}_2), \ldots, f(\bar{\boldsymbol{x}}_{N_s})$ on scattered distinct centers $X = [\bar{\boldsymbol{x}}_1, \bar{\boldsymbol{x}}_2, \ldots, \bar{\boldsymbol{x}}_{N_s}]$. The first step is to build a local approximation of f, $\hat{f}$ as a sum of basis functions $p_i(\boldsymbol{x})$:

$$\hat{f} \;=\; \sum_{i=1}^{m} p_i(\boldsymbol{x})\, a_i(\boldsymbol{x}) \;=\; \boldsymbol{p}(\boldsymbol{x})\, \boldsymbol{a}(\boldsymbol{x}) \tag{3.45}$$

with m being the chosen number of basis functions and $a_i(\boldsymbol{x})$ denoting their coefficients.

The proposed solution to find a suitable set of coefficients $a_i(\boldsymbol{x})$ derives from the weighted least square fit for the approximation, as in Equation (3.46).

$$\text{Minimize } J(\boldsymbol{x}) \;=\; \int_{\Omega} \phi(\boldsymbol{x} - \bar{\boldsymbol{x}}) \left(\hat{f} - f(\bar{\boldsymbol{x}})\right)^2 d\Omega(\bar{\boldsymbol{x}}) \tag{3.46}$$

with the linear constraint:

$$\hat{f}(\bar{\boldsymbol{x}}) \;=\; \sum_{i=1}^{m} p_i(\hat{\boldsymbol{x}})\, a_i(\boldsymbol{x}) \tag{3.47}$$

The weight functions $\phi(\boldsymbol{x})$ are called Radial Basis Functions (RBF) [190].

The solution of Equation (3.46), detailed in [189], brings to a function of the form:

$$\hat{f}(\boldsymbol{x}) = \sum_{j=1}^{N_s} \psi_j(\boldsymbol{x})\, f(\hat{\boldsymbol{x}}) \tag{3.48}$$

where $\psi_j(\boldsymbol{x})$ are called shape functions.

Equation (3.48) represents the required solution, analogous to Equation (3.44). The shape functions, evaluated at the different nodes, can be finally assembled into the interface matrix $\boldsymbol{H}$.

The computation of the interface matrix $\boldsymbol{H}$ needs to be done only once at the beginning of the analysis. Then, the same matrix allows to transform geometry and forces forth and back between the two domains during the nonlinear iterations or time domain iterations. The size of the matrix is fixed by the number of aerodynamic and structural nodes. It should be noted that for the beam discretization, the number of beam nodes is not sufficient, because the interpolation function would fail to capture rotations around the beam axis, leading to an ill-conditioned matrix. To overcome this issue, it is convenient to add some auxiliary nodes outside the beam axis, forming a 'fish-bone' mesh that allows to capture rotations very effectively. Here two nodes are added for each beam node, creating one forward and one backward arm along the local wing chord. Of course these are only used for the interpolation procedure, and are not part of the structural model. An example of the discretization of a high-aspect-ratio wing is given in Figure 3.32. Here, the deformed VLM mesh, including the trailing vortex lines, is represented in black, whereas the undeformed shape is in grey. The deformed beam is reported in red, and the auxiliary points are highlights as red circles. In addition, to give a better idea of what the loads distribution looks like, the aerodynamic lift forces on the VLM panels are shown by blue arrows. An alternative view, showing the pressure coefficient distribution over the deformed aerodynamic mesh, is reported in Figure 3.33. Some more details are reported in Figure 3.34, where a closer view of the wing is given showing both the aerodynamic forces, in blue, and the corresponding equivalent forces on the structural domain, in red, obtained through the transpose of the interpolation matrix $\boldsymbol{H}$. The moduli of the structural forces are higher than the aerodynamic ones because the contributions of many aerodynamic panels have to be concentrated into a smaller number of structural points. Also, it can be noted that in order to achieve the correct amount of twisting moment with the given arms, the structural forces on the aft points result downward, opposite with respect to the total resulting force, which is upward. This is just a numerical artifice that depends on the chosen arm length, and different distributions would result from different arms. In all cases, the total lift and moments would remain consistent with the aerodynamic loads, by respecting the equivalence of the virtual works between the two domains.

Some finer details, this time about the aerodynamic model, are given in Figure 3.35, which shows the aerodynamic force distribution over a small portion of the wing. What is interesting here is that the application points of these forces is crucial for the accuracy

of the simulation. In particular, the figure shows the VLM grid in thin grey lines, the wing geometrical leading and trailing edges in thick black lines, the midpoints of the bound vortex segments denoted by circles, and the VLM collocation points denoted by small crosses. It is important that the aerodynamic forces are placed on the vortex segments' midpoints, as the theory requires, and not elsewere, for example at the collocation points, or at the leading edge of the geometrical grid. In fact, it should be noted that in many cases a VLM model can be quite accurate even with just a few chordwise panels - strip theory, for example, is almost equivalent to one single chordwise panel - and this translates into a benefit in computational speed. But when decreasing the number of chordwise panels, an error in the chordwise location of the aerodynamic force would be amplified, with a significant cascading effect on the twisting moment, twisting deformation, local lift, and therefore on the final aeroelastic solution.

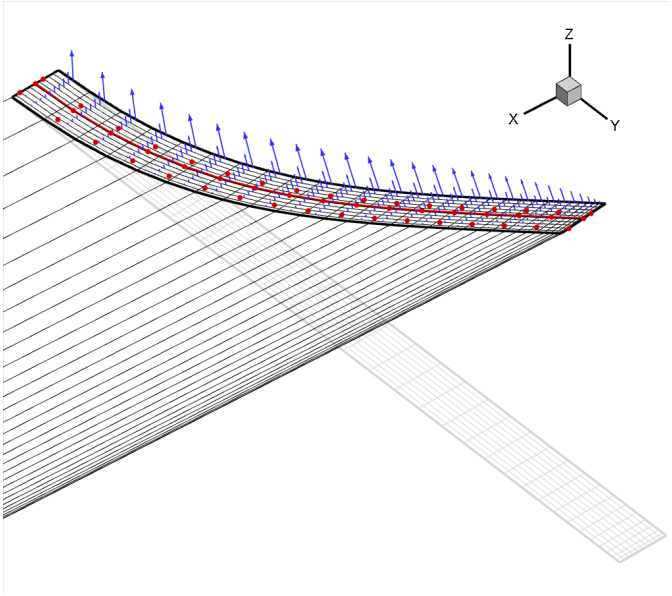

FIGURE 3.32: Visualization of the aeroelastic model for the Patil wing. Overview showing the undeformed aerodynamic mesh (grey), the deformed one, including the wake (black), the beam model with the additional auxiliary nodes (red), and the aerodynamic forces acting on the deformed wing (blue arrows).

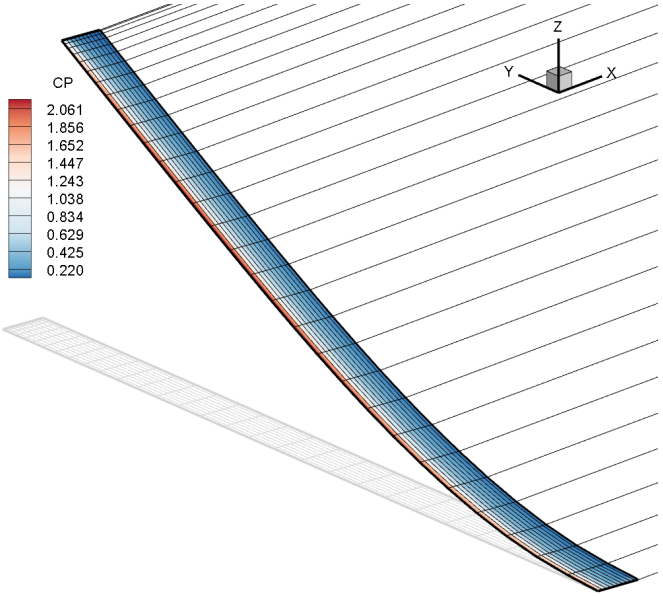

FIGURE 3.33: Visualization of the aeroelastic model for the Patil wing. Overview showing the pressure coefficient distribution over the deformed wing.

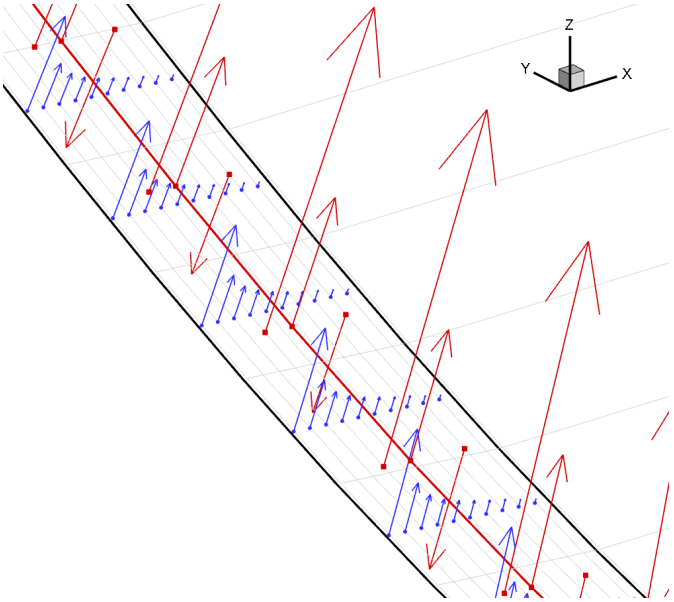

FIGURE 3.34: Visualization of the aeroelastic model for the Patil wing. Detail view showing the aerodynamic forces (blue) generated in the aerodynamic domain (black) and the equivalent forces transferred to the structural domain (red).

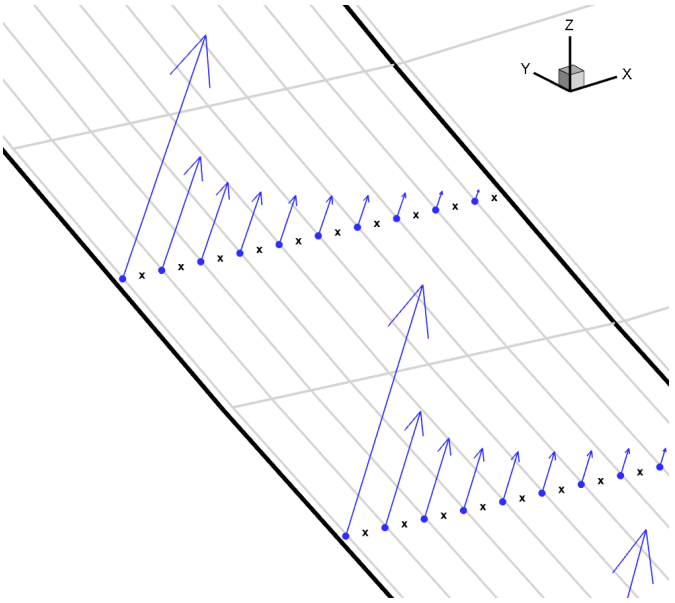

FIGURE 3.35: Visualization of the aeroelastic model for the Patil wing. Detail view showing the wing geometry (thick black lines), the vortex lattice discretization (thin grey lines), the VLM collocation points (represented by an 'x') and the aerodynamic forces (blue), applied at the midpoint of the leading vortex line of each vortex ring.

3.4.2.2 Validation - static aeroelasticity

Figures 3.32 to 3.35 are taken from the aeroelastic model of the Patil wing, from [21]. This model was used for a validation case for the nonlinear aeroelastic tool just discussed. The wing is quite appropriate for this purpose because of its slenderness and flexibility, and it has already been employed as a reference test case by others [22, 29, 41, 104]. The wing characteristics and flow conditions are summarized in Table 3.7. Figures 3.36 and 3.37 report the spanwise bending and twist deformation, respectively, measured at the wing elastic axis. The flow conditions are defined by the air speed and density $V = 25.0\,\mathrm{m/s}$ and $\rho = 0.0889\,\mathrm{kg/m^3}$, and two different angles of attack are examined: $\alpha = 2\,\mathrm{deg}$ and $\alpha = 4\,\mathrm{deg}$. The results obtained with the present model are compared against those from the `FALCon` tool of [22] and those from [21]. Both references adopted an analogous aeroelastic model, coupling an inviscid, incompressible panel method with a geometrically-nonlinear beam. As it can be noted, the results from the present model match satisfactorily with the reference data. Only the twist curve at $\alpha = 4\,\mathrm{deg}$ shows some visible error, especially with respect to Smith [21]. However, as the corresponding vertical deformation is practically identical, the differences in the twist data are probably to be attributed to the reference frame in which structural rotations are expressed, and not to a relevant difference in the physical model. The present model adopts a global reference frame fixed to the undeformed configuration, but it is not clear what frame was used by [21] to produce its plots, nor whether it was a global frame or a local one. However, the validation is considered successful. It is worth noting that the tip of the deformed wing moves towards a lower spanwise abscissa for higher deformations, so that the total length of the curved wing remains constant. This is a clear effect of the geometric nonlinearity. A linear model would have only given a higher vertical displacement at the same spanwise abscissa, resulting in an unnaturally longer wing.

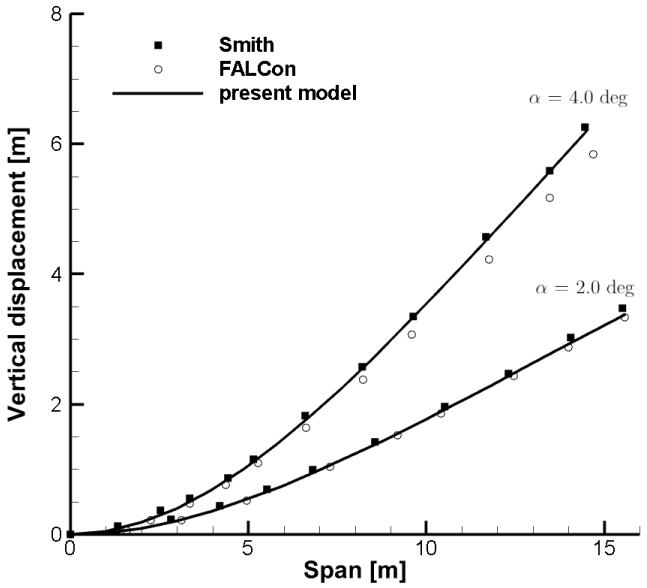

FIGURE 3.36: Validation of the present nonlinear aeroelastic model: spanwise vertical displacement of the Patil wing's elastic axis, compared against data from [21] and [22].

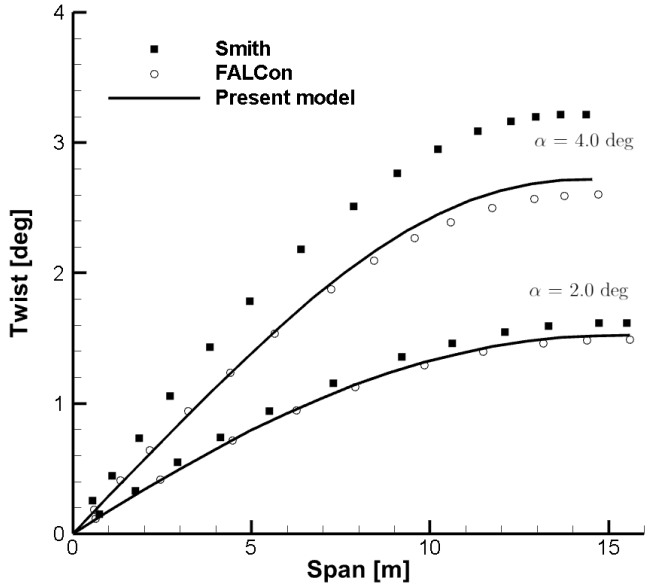

FIGURE 3.37: Validation of the present nonlinear aeroelastic model: spanwise twist of the Patil wing, compared against data from [21] and [22].

3.5 Flight dynamics

This section presents the implemented model for flight dynamics simulation. The choice to implement this module rather than adapt existing programs was motivated by the preference for a simple, minimal and easy to interface software, compatible with the aerodynamic and aeroelastic modules described previously. In fact, off-the-shelf software, such as JSBSim [158], usually comes with a variety of secondary functionalities and a large number of inputs and settings which would add unnecessary complexity and increased risk of errors or inconsistency in the input, output and inner variable definitions. The formulation of the 6-DOFs flight dynamics follows from the well-known rigid-body equations for atmospheric flight, as could be found for instance in [156, 157]. As the purpose of simulation here is to test brief manoeuvres or short aircraft responses, quite limited in time and space, and certainly at non-supersonic speeds, Earth rotation and curvature are neglected as they would add no relevant effects. All the following equations are expressed in body axes. The force equations read as follows:

$$\begin{cases} X - m\,g\,\sin\theta = m\,[\dot{V}_x + q\,V_z - r\,V_y] \\ Y - m\,g\,\cos\theta\sin\phi = m\,[\dot{V}_y + r\,V_x - p\,V_z] \\ Z - m\,g\,\cos\theta\cos\phi = m\,[\dot{V}_z + p\,V_z - q\,V_x] \end{cases} \tag{3.49}$$

The moment equations in matrix form are:

$$\begin{aligned} \begin{bmatrix} \ell \\ m \\ n \end{bmatrix} = & \begin{bmatrix} \dot{I}_x & -\dot{I}_{xy} & -\dot{I}_{zx} \\ -\dot{I}_{xy} & \dot{I}_y & -\dot{I}_{yz} \\ -\dot{I}_{xy} & -\dot{I}_{yz} & \dot{I}_z \end{bmatrix} \begin{bmatrix} p \\ q \\ r \end{bmatrix} + \begin{bmatrix} I_x & -I_{xy} & -I_{zx} \\ -I_{xy} & I_y & -I_{yz} \\ -I_{xy} & -I_{yz} & I_z \end{bmatrix} \begin{bmatrix} \dot{p} \\ \dot{q} \\ \dot{r} \end{bmatrix} \\ & + \begin{bmatrix} 0 & -r & q \\ r & 0 & -p \\ -q & p & 0 \end{bmatrix} \begin{bmatrix} I_x & -I_{xy} & -I_{zx} \\ -I_{xy} & I_y & -I_{yz} \\ -I_{xy} & -I_{yz} & I_z \end{bmatrix} \begin{bmatrix} p \\ q \\ r \end{bmatrix} \end{aligned} \tag{3.50}$$

It should be noted that Equation (3.50) neglects the angular momentum due to hinged parts, elastic motion and rotating sub-systems. However, as far as aeroelasticity is concerned, the elastic motion could be kept decoupled by using the so-called 'mean-axes' formulation. Such axes are by definition a particular set of body axes for which the inertial coupling between rigid body and elastic deformation vanishes. Their use, first discussed by Milne [95], represents the classical approach for representing the dynamics of a flexible aircraft [20, 156]. The main advantage is the simplicity of dealing with basically two different dynamic systems (one being a rigid mass point representing the

aircraft, the second being the flexible structure), where the only remaining coupling is aerodynamic. Strictly speaking, this approach neglects the coupling due to gyroscopic effects, as mentioned in Section 2.2.2. If a full coupling of the equations of motion with the aeroelastic dynamics is desired, an additional set of 6 equations has to be added to identify at each instant the origin and the orientation of the body-fixed reference frame with respect to the CG, and the momentum due to elastic motion should be included in the equilibrium of Equation (3.50). However, at this stage of development, the mean-axes formulation is considered the most practical option, as it facilitates a progressive, modular implementation and validation of the flight dynamics model and of the aeroelastic model and their future coupling.

The system of equations is completed by adding the kinematics (3.51) and navigation (3.52) equations:

$$\begin{bmatrix} \dot{\phi} \\ \dot{\theta} \\ \dot{\psi} \end{bmatrix} = \begin{bmatrix} 1 & \sin\phi\tan\theta & \cos\phi\tan\theta \\ 0 & \cos\phi & -\sin\phi \\ 0 & \sin\phi\sec\theta & \cos\phi\sec\theta \end{bmatrix} \begin{bmatrix} p \\ q \\ r \end{bmatrix} \tag{3.51}$$

$$\begin{bmatrix} \dot{x}_E \\ \dot{y}_E \\ \dot{z}_E \end{bmatrix} = \boldsymbol{L}_{BE} \begin{bmatrix} V_x \\ V_y \\ V_z \end{bmatrix} \tag{3.52}$$

where the rotation matrix $\boldsymbol{L}_{BE}$ contains the Euler's angles to rotate a vector from the body to the Earth (inertial) reference frames:

$$\boldsymbol{L}_{BE} = \begin{bmatrix} (\cos\theta\cos\psi) & (-\cos\phi\sin\psi + \sin\phi\sin\theta\cos\psi) & (\sin\phi\sin\psi + \cos\phi\sin\theta\cos\psi) \\ (\cos\theta\sin\psi) & (\cos\phi\cos\psi + \sin\phi\sin\theta\sin\psi) & (-\sin\phi\cos\psi + \cos\phi\sin\theta\sin\psi) \\ \sin\theta & -\sin\phi\cos\theta & -\cos\phi\cos\theta \end{bmatrix} \tag{3.53}$$

Equations (3.49) to (3.52) are used to compute the body translational and angular accelerations, the Euler angles rates and the velocity with respect to the Earth reference frame. Those are then propagated through numerical integration to get the updated body speed, angular rate, attitude and location. The choice of the integration schemes follows the one in [158], where the 2nd-order Adams-Bashforth ([157]) is used to integrate the linear body accelerations into body speeds, the 1st-order Euler scheme is used to integrate the angular accelerations and attitude rates, and the 3rd-order Adams-Bashforth scheme to obtain the updated position in the inertial coordinates. This procedure is adopted without modifications as it complies with a well-established practice in non-linear aircraft flight simulation.

The implementation was made in Fortran language to be more easily interfaced with the VLM and UVLM solvers presented above, although the simulation code was made

independent on the aerodynamic solver. In fact, the aerodynamic forces and moments are taken from a separate function that could call any desired external computation.

The verification of the implemented model is reported in the following section.

3.5.1 Validation of the flight dynamics module

The validation of the flight dynamics module proceeded through two subsequent steps. First, only the nonlinear longitudinal dynamics was considered with no lateral coupling. Then, a pitch-and-roll manoeuvre was simulated to reproduce a full coupling between the 6-degrees-of-freedom variables.

The first test-case is for a low-speed transport aircraft from the book *Aircraft Control and Simulation* by [157]. The simulation reproduces the pitching response to elevator and throttle commands. The equations of motion employed retain all the nonlinear terms, whereas the aerodynamic model is linearized around the initial equilibrium condition. Figure 3.38 shows the perturbation in attitude and angle of attack due to an elevator doublet during steady horizontal flight. Figure 3.39 reports the response to throttle doublet. In both cases, the response matches satisfactorily with the reference.

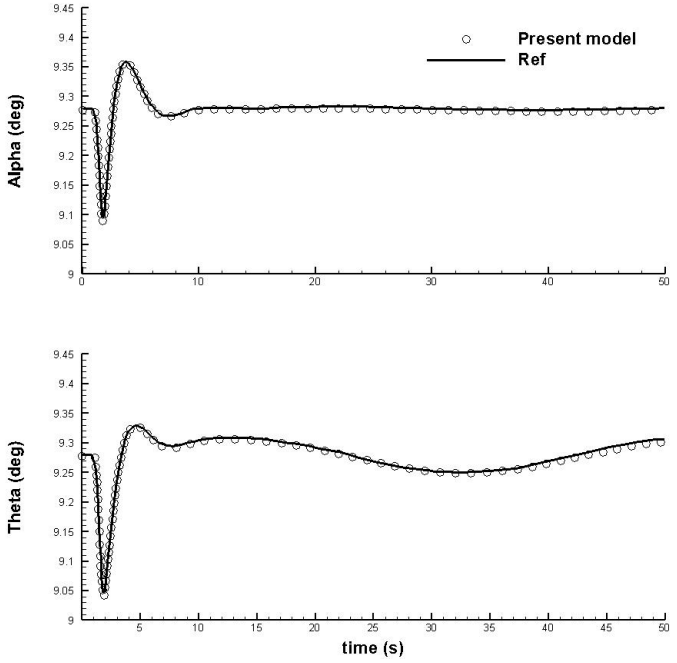

FIGURE 3.38: Evolution of angle of attack and elevation due to an elevator doublet of amplitude $\delta_e = \delta_{e_0} \pm 2.0°$, with $\delta_{e_0} = -9.2184°$ performed between 1.0 and 2.0 seconds.

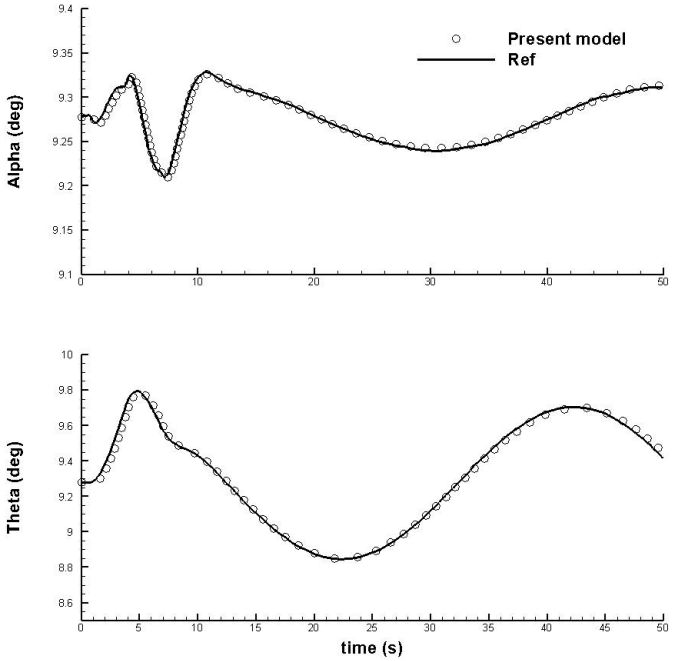

FIGURE 3.39: Evolution of angle of attack and elevation due to a throttle doublet of amplitude $\Delta T/T = \pm 0.1$ performed between 1.0 and 7.0 seconds.

The second validation case reproduces a fully coupled manoeuvre where all the nonlinear terms play a relevant role. For this purpose, the chosen test case is a small manoeuvrable airplane performing considerably fast rotational motion. The reference simulation data are from [191], and the aircraft parameters can be found in [156]. Such case is studied by the reference authors to demonstrate the relevance of the nonlinear inertial coupling terms, which can produce a consistent deviation from a steady flight and even lead to instability. The only approximations made by the authors are those of constant airspeed and small variations of angle of attack and sideslip. The validated model reproduced the constant speed approximation by forcing at each instant the thrust to exactly counterbalance drag and the eventual weight projection in the flight path direction. The aerodynamic angles were calculated with the exact trigonometrical relationships. Figures 3.40 to 3.42 respectively show the evolution of angle of attack, sideslip angle and roll rate due to a step aileron deflection starting from steady horizontal flight. Two cases are reported corresponding to aileron deflections of $\delta_a = -4.0^\circ$ and $\delta_a = -5.0^\circ$. In both cases, a pitch-down initial condition is imposed by setting the elevator to $\delta_e = 2.0^\circ$. It can be noted that divergent oscillations are experienced when the aileron deflection is $\delta_a = -5.0^\circ$, a behaviour which is exclusively due to the nonlinear inertial coupling of the equations of motion. A dynamic model linearized around the same stable initial condition would not be able to predict such behaviour.

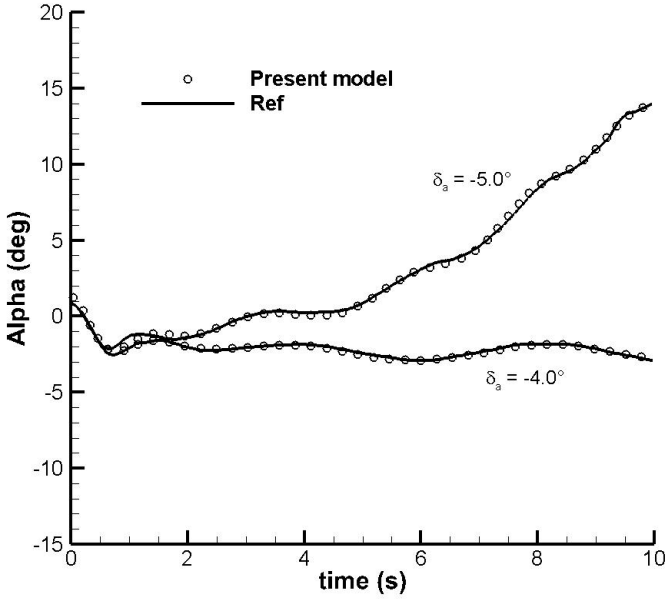

FIGURE 3.40: Evolution of angle of attack due to step aileron actuation δ_a, starting from a pitch-down initial condition with elevator deflection set to $\delta_e = 2.0°$.

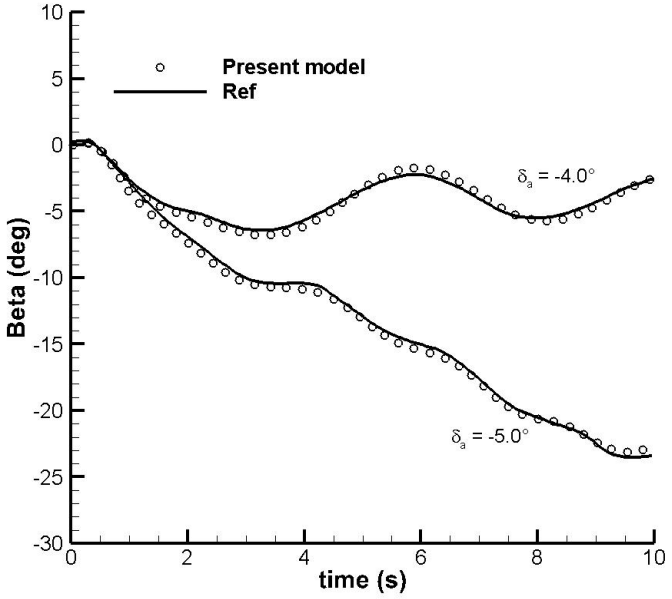

FIGURE 3.41: Evolution of sideslip angle due to step aileron actuation δ_a, starting from a pitch-down initial condition with elevator deflection set to $\delta_e = 2.0°$.

3.5.2 Coupling flight dynamics with VLM aerodynamics

Flight dynamics simulators typically rely upon simple aerodynamic models based on precomputed tables of aerodynamic coefficients. In this way the aerodynamic loads,

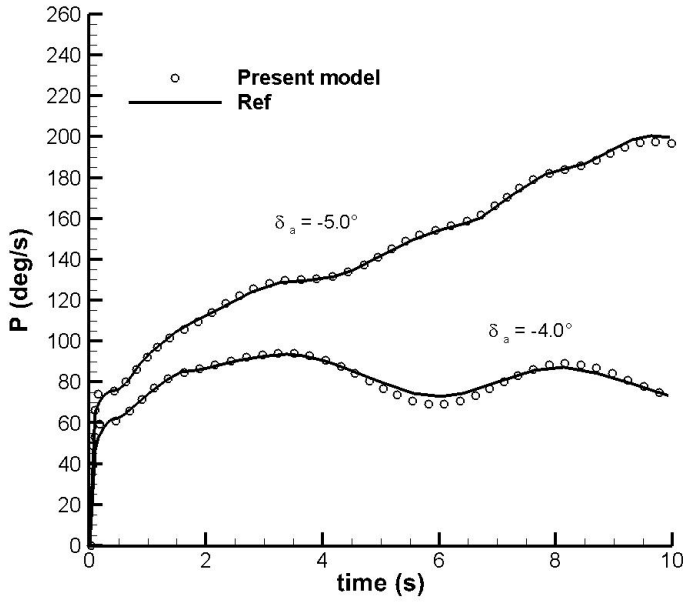

FIGURE 3.42: Evolution of roll rate due to step aileron actuation δ_a, starting from a pitch-down initial condition with elevator deflection set to $\delta_e = 2.0°$.

the most expensive to calculate, are quickly computed and the equations of motion can be integrated at high speed. The problem with this approach is that it fails when the aerodynamic database is not available. This can be the case at conceptual design phase, when several data are still missing. In this case it is still possible to set up a simplified aerodynamic model based on the limited information available describing the essential geometrical and aerodynamic parameters. When dealing with traditional aircraft design, there are several analytical or semi-empirical methods [98, 159, 192] to quickly accomplish this task. Actually such methods provide enough information on the aerodynamic performance, including stability & control characteristics, to complete the design successfully with no real necessity for a proper flight simulation tool. Things are different when designing unconventional configurations, where there is no guarantee the mentioned methods apply. The design team needs more advanced tools to at least verify whether the conventional methods are appropriate or not, and in the latter case such extra tools become the only alternative left to go forward.

The strategy here proposed is to couple the above 6-DOFs flight dynamics simulation module with the VLM-based aerodynamic module to best exploit the information available from a conceptual sizing process.

A first, simple validation case which is often run when coupling the flight equations of motion with any aerodynamic solver is that of a single wing free to oscillate around a restrained center of gravity [23, 193]. The test-case here is from [23]. A simple rectangular wing is placed downstream of a fictitious center of gravity (CG). While the CG

is fixed in space, the wing is free to rigidly rotate around it. The motion is determined by the aerodynamic loads acting on the wing due to a constant airspeed parallel to the inertial horizontal direction, as it was inside a wind tunnel. The test-case is shown in Figure 3.43, and the related parameters are reported in Table 3.9. The simulation results are compared with the reference data in Figure 3.44, showing good agreement.

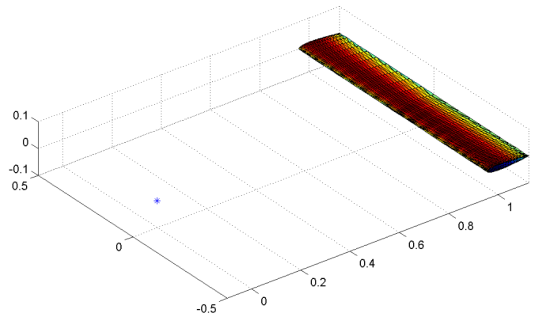

FIGURE 3.43: Single wing test-case, from [23]. The CG position is identified by the $*$ symbol. The figure has a representational purpose only, and the contour plot does not provide any relevant information.

Parameter	**Units**	**Value**
Span	m	1.0
Aspect ratio	-	6.0
Tilt angle	deg	0.0
Leading edge to CG distance	m	0.96
Chord-wise panels	-	17
Span-wise panels	-	36
Inertia moment	$kg \cdot m^2$	1.0
Airspeed	m/s	30.0
Air density	kg/m^2	1.225
Initial pitch	deg	5.0
Time step	s	0.0025

TABLE 3.9: Parameters for the free-to-pitch wing.

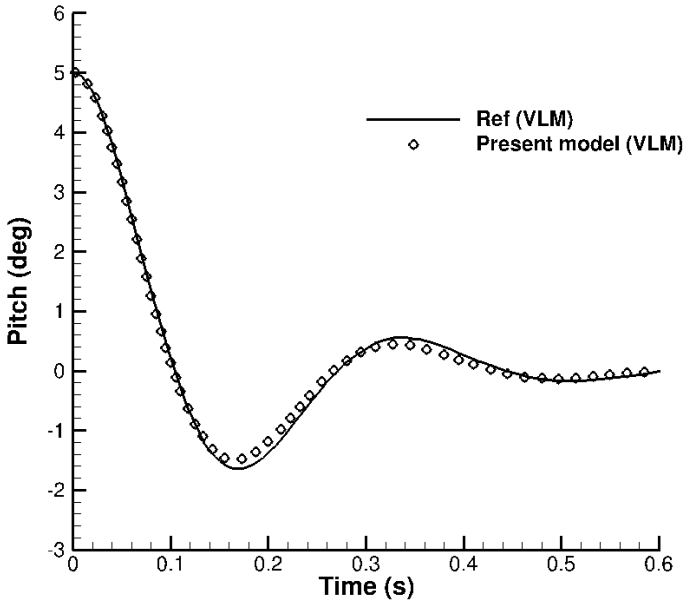

FIGURE 3.44: Evolution of pitch angle of the free-to-pitch wing due to an initial condition of $\theta = 5$ deg. Validation against data from [23].

A second validation test-case featuring a conventional wing-stabilizer configuration was run to investigate the performance of the solver for more complex geometries. In particular the interest here is to confirm that the effects of the downwash generated by the main wing upon the stabilizer are properly captured and propagated to the body dynamics. The parameters for this configuration are given in Table 3.10, and the pitch angle time evolution is compared with that from [23] in Figure 3.47. A slight mismatch is observed for this configuration, but this may be due to a different numerical setup of the simulation which cannot be exactly reproduced due to a lack of information from the reference paper. In particular, only the total number of panels is specified, and not the chord-wise and span-wise discretization schemes for the two wings. Differently from the single-wing simulation, the position of the CG is not explicitly given, and it is here guessed based on other simulations reported in the reference manuscript, but it is possible that the true value is slightly different. Also, the point around which the main wing is rotated to get the tilt angle of 3.0 deg is not specified, and it is here assumed to be the quarter chord. Nevertheless, the results give overall a very close dynamic response, without any relevant discrepancy in frequency or damping, a result which is considered satisfactory.

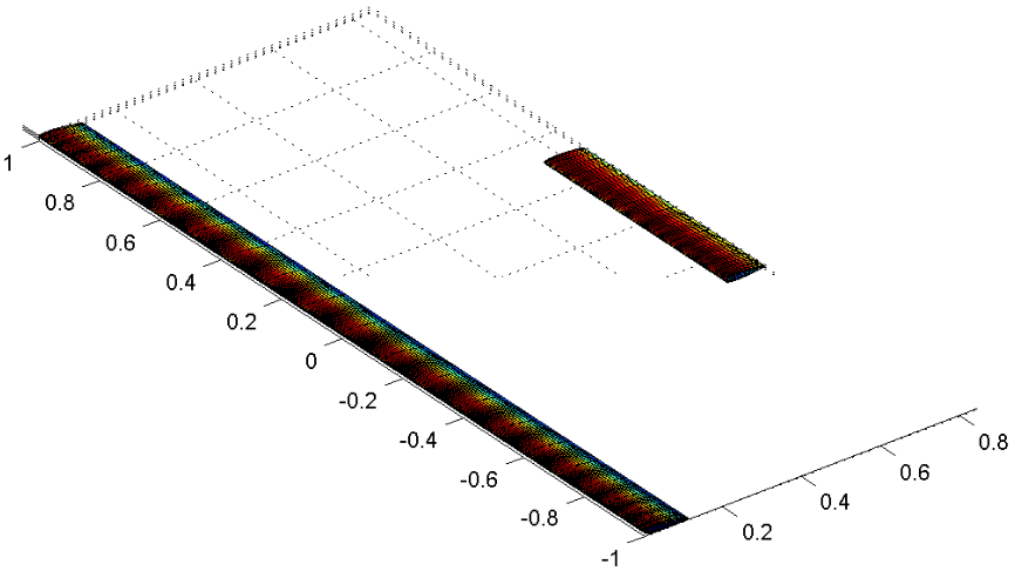

FIGURE 3.45: Two-wing conventional glider

FIGURE 3.46: Two-wing conventional glider test-case, from [23]. The figure has a representational purpose only, and the contour plot does not provide any relevant information.

Parameter	**Unit**	**Value**
Main wing		
Span	m	2.0
Aspect ratio	-	18.0
Tilt angle	deg	3.0
Leading edge to CG distance	m	0.03
Chord-wise panels	-	17
Span-wise panels	-	36
Horizontal stabilizer		
Span	m	0.6
Aspect ratio	-	6.0
Tilt angle	deg	0.0
Leading edge to CG distance	m	0.745
Chord-wise panels	-	17
Span-wise panels	-	36
Global		
Inertia moment	$kg \cdot m^2$	0.2
Airspeed	m/s	30.0
Air density	kg/m^2	1.225
Initial pitch	deg	5.0
Time step	s	0.0025

TABLE 3.10: Parameters for the free-to-pitch wing-stabilizer glider.

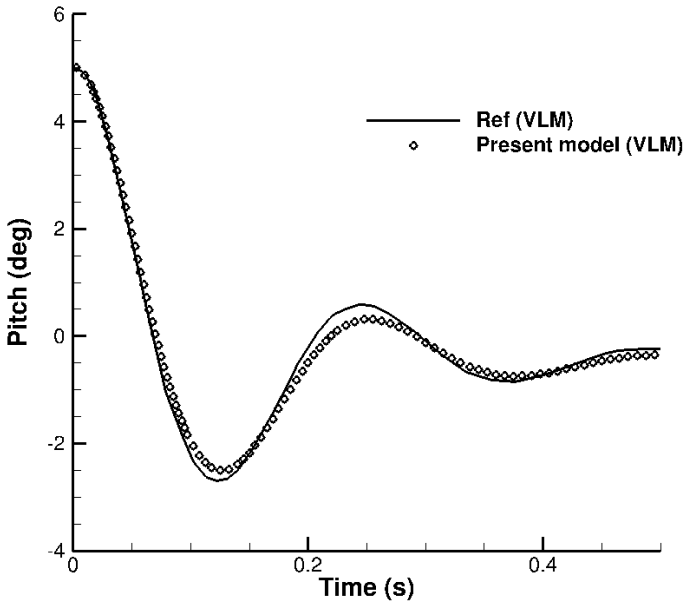

FIGURE 3.47: Evolution of pitch angle of the glider configuration due to an initial condition of $\theta = 5\,\text{deg}$. Validation against data from [23].

3.6 System identification for nonlinear systems

With the available tools presented earlier in this chapter, an useful task is the estimation of key performance indicators out of the simulation results. Some examples could be the frequencies and damping ratios of the flight modes, or similar parameters such as the Control Anticipation Parameter (CAP), often used as a flying quality indicator [83, 156], that can be used to assess specification compliance. However, the following considerations hold for other similar figures of merit, such as control derivatives, control demand, flutter speed, etc.

The quickest and easiest approach for this kind of dynamic characteristics estimation is the standard linearization of the equations of motion. In this way, the system dynamics can be expressed in state-space form (as done for example in the aeroelastic module of Section 3.4.1), in which case the Jacobian matrix can be used to compute the local dynamic characteristics by standard eigenvalue analysis. The task is even easier for conventional configurations, as analytical relationships exist ([156, 159]) to give full or approximated expressions of the linear aircraft dynamic characteristics (usually frequency, damping, time to double, time to half, CAP, [83, 156]). For example, an approximated expression for the rigid body short period natural frequency, as given in [156] is:

$$\omega_{sp}^2 = -\frac{2\,\mu\,C_{m\alpha} + C_{mq}\,(C_{L\alpha} + C_D)}{2\,\mu\,\bar{I}_y} \tag{3.54}$$

where μ is the non-dimensional mass, $\bar{I}_y$ the non-dimensional moment of inertia around the y body axis, and the remaining coefficients are the aerodynamic derivatives expressed in the conventional nomenclature.

One difficulty could be on how to compute the needed aerodynamic derivatives involved in the mentioned relationships. This could be done with conventional semi-empirical formula such as those provided in [159], or, for unconventional geometries, through the developed VLM. This is what is usually done in the literature related to aircraft dynamic characterization at conceptual design.

However, this approach may not be accurate for highly flexible unconventional aircraft, where some overlapping may occur between 'rigid-body' and structural modes. Or, some non-linear interactions may cause the behaviour to deviate from the one predicted by linear analysis. An example of such possibility is shown in Figures 3.40 to 3.42, already discussed in Section 3.5.1, where a slight difference in a control input can result in the evolution to switch from a predictable and stable behaviour to an unstable evolution that is only captured by the non-linear time-marching model. In this example, the non-linearity is only given by the non-linear terms of the rigid-body equations of motion. This reasoning can be extended to other aspects, such as dynamic loads

monitoring. In this case, the introduction of non-linear aeroelastic effects could potentially give rise to more complex behaviours. For this reason, an effort is made in this work to exploit the added information arising from nonlinear time-marching simulation. This requires some system identification or parameter identification techniques for extracting the desired quantities of interest from the simulation data.

In the context of the present work, the advantage of time-domain simulations lies in the large body of information conveyed. In particular, a valuable aspect is the capability to capture the effects of nonlinearities, which are in general lost if other methods, such as frequency-domain, are used instead. However, the richer information provided needs interpretation. When a few simulations are run, such as during human-piloted simulation campaigns, or after a very specific, one-of-a-kind evaluation, this task is often assigned to the human. When a large number of simulations need to be performed in a short time (as for example during a numerical optimization process), human interpretation is no longer a viable option. Also, even for one-of-a-kind analyses, if some parameters need to be extracted from the time history, some automatic processing technique comes in handy. In particular, it is still interesting at this design stage to have access to quantifiable figures of merit, such as frequencies or damping ratios, that are typical of linear system analysis. The estimation of such parameters would enable to assess the compliance with dynamic specification constraints, which are mostly about linear system characterization, even for design concepts that are not well represented, or at least not *a priori*, by the conventional, knowledge-based, linear characterization. Moreover, a linear Jacobian of a complex, non-linear coupled system, such as for flexible airplane dynamics, may not always be available, depending on the models employed and how their coupling is implemented. For this reason, an effort is done here to process the time domain simulation data and extract a set of figures of merits - corresponding to linear damping and frequency - that with the best approximation describe the obtained non-linear response. It should be noted that when assigning some linear descriptors (frequency, damping) to a non-linear curve, an approximation is inevitably demanded. The advantage here is that such approximation is done *a posteriori* based on the full non-linear results, and its adequacy can be verified against those.

To this purpose, different signal processing techniques have been tested, including Dynamic Mode Decomposition (DMD) [194], Empirical Modal Decomposition (EMD) [195], the Hilbert Transform [196], useful to extract damping ratios, the Fast Fourier Transform (FFT) [196], the Prony method [197] and some Least Squares fitting techniques [198]. The method to be used shall be selected according to the complexity of the problem. It is true that the applicability to more complex simulation signals is not ensured. Signal processing and system or parameter identification can often result being non-trivial tasks, as confirmed by the large amount of related literature and software libraries (such as the `Matlab Signal Processing Toolbox` and the `Scipy.signal`, [196, 199]). Some

interesting reviews of techniques specifically tailored on aerospace applications were found in [76] and [200].

When the objective of the processing module is to extract frequencies and damping ratios, the Prony method was selected as it found effective and robust enough for the applications of this work (see Chapter 4). It performs a curve fitting similar to the Fast Fourier Transform, returning a best fit function of complex exponential form:

$$\tilde{F}(t) = \sum_{i=1}^{N} A_i \, e^{\lambda_i t} \tag{3.55}$$

where A_i and λ_i are both complex coefficients, and N the number of vibration modes to retain. This can be either estimated by an FFT analysis, or fixed by the user if a certain behaviour is expected. For the initial testing of the presented framework, the category of problems investigated can be adequately described by just one or two modes, simplifying the fitting process. For example, Figure 3.48 reports the curve fitting of some random 4th-order harmonic oscillations combining both converging and diverging modes. In this case, the Prony fitting of Equation (3.55) with $N = 4$ perfectly captured the dynamics identifying the two dominant frequencies and damping ratios.

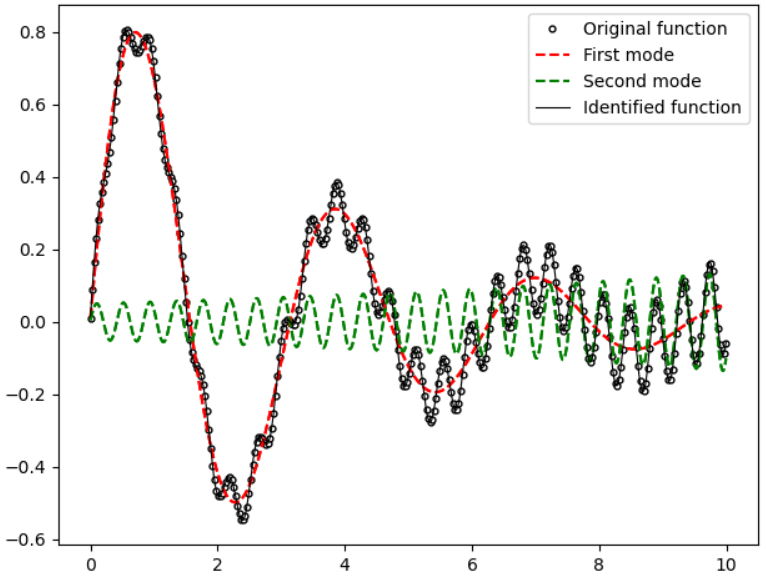

FIGURE 3.48: Example curve fitting of a 4th-order oscillator function via the Prony method.

3.7 Sensitivity analysis and uncertainty quantification approaches

3.7.1 Problem definition and tool selection

As already mentioned (see Section 2.1), early aircraft analysis is inherently affected by uncertainty, both of aleatory and epistemic kind. In this work, which focuses on aircraft flying qualities and aeroelastic performance estimation at conceptual design level, we aim to include and propagate the most relevant uncertainties onto the desired output performance indicators. The demonstrative case studies reported later in this work restrict the investigation into longitudinal dynamics, flutter speed and dynamic gust loads. The uncertainty herein considered is that arising from the approximate methods used during the sizing process. In particular, such uncertainty will involve those parameters that most influence the performance indices of interest. For example, if flying qualities are targeted as figures of merit, the uncertainty could be conveniently placed on the estimations of weight and balance characteristics (location of the center of gravity, aircraft moments of inertia). Similarly, if aeroelastic response is among the desired output, typical uncertain parameters could be the structural stiffness, mass, inertia, or the location of the elastic axis. These considerations will be further developed for each of the case studies investigated in the following Chapters.

To perform uncertainty quantification and sensitivity analysis the off-the-shelf toolbox `Uncertainpy` [137] was tested and chosen, and interfaced with the performance analysis modules. The toolbox, originally conceived mainly for computational neuroscience, is easily adaptable to any computational field in that it is a model-independent, open source, Python-based platform. The main features of the platform are here briefly summarized.

The sensitivity analysis is addressed by computation of first-order Sobol indices [139] and total Sobol indices [140, 141] when interactions between the uncertain parameters exist.

As far as uncertainty quantification is concerned, it implements both quasi-Monte Carlo methods and Polynomial Chaos Expansions (see Section 2.6) using non-intrusive methods. The quasi-Monte Carlo methods employ variance-reduction techniques to reduce the number of model evaluations needed. The samples are selected using a low-discrepancy sequence such as the Hammersley sequence [144]. As for the PCE approach, the orthogonal polynomials are found using the three-term recurrence relation [145], and the expansion coefficients can be found either through the Tikhonov regularization [201], belonging to the class of point collocation methods, or by a pseudo-spectral approach based on Leja quadrature and Smolyak sparse grids [202, 203]. The Sobol first and total order methods can be computed directly from the PCE [146]. The interested reader can find more information about this approach in the `Uncertainpy` documentation [137].

The output metrics provided are the Quantity of Interest (QoI) mean, variance, 5% and 95% percentiles and the Sobol indices. Additionally, some modifications were made to obtain the Probability Distribution Function (PDF) together with any desired percentile.

As pointed out in Section 2.6, Polynomial Chaos Expansions are much faster than (quasi-) Monte Carlo methods as long as the number of uncertain parameters is relatively low, typically smaller than about twenty [147]. As this is the case for the analyses involved in this work, the PCE method is used hereafter with the point collocation approach.

Before employing the framework for aerospace-related applications, the UQ module was tested and validated against a benchmark case to prove its functionality and effectiveness. The validation is presented in the following section.

3.7.2 Validation - mathematical example

A benchmark mathematical problem was chosen from the literature to verify the `Uncertainpy` results. The example is adopted from [24, 204] where an uncertainty quantification was performed on the following function:

$$g(x_1, x_2, x_3) = 0.25 \left(\sin(x_1 - 3)(x_2 - 1) + (x_3 - 1)^2\right) - 1 \tag{3.56}$$

with uncertainty on the three input variables as described in Table 3.11.

The main reference results are from the method proposed in [24], a dimension-adaptive PCE (DA-PCE) that proved to be quite efficient compared to other approaches (Monte Carlo, FORM, SORM, PDEM). The resulting PDF after 72 model evaluations is compared with that from [24] in Figure 3.49. Also, a comparison is reported in Table 3.12, based on the available data from the reference, on the QoI value $\bar{q}$ which is predicted to satisfy a certain probability threshold $\overline{P}$. For other methods reported in the reference paper the values of $\bar{q}$ are not directly determinable, but they do report the number of evaluations needed to complete the UQ task, and therefore this parameter is also reported in the table for comparison. The validation shows that the adopted method performs well and with good efficiency compared with other methods.

Variable	Distribution	Range
x_1	Uniform	[0.0 , 10.0]
x_2	Uniform	[6.0 , 16.0]
x_3	Uniform	[0.0 , 10.0]

TABLE 3.11: Uncertain ranges and distributions of variables for the test-case in Equation (3.56).

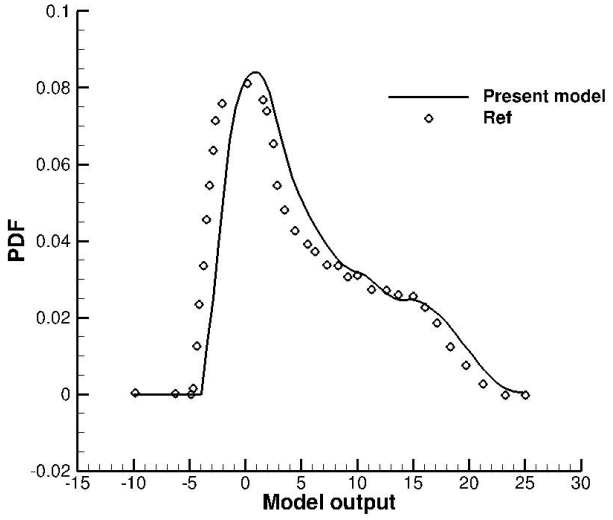

FIGURE 3.49: Comparison of the PDF obtained with the present approach against data from [24].

	$\overline{q}$ *s.t.* $P\{q(X)\} > \overline{P}$			
Method	$\overline{\mathbf{P}} = \mathbf{28.4\%}$	$\overline{\mathbf{P}} = \mathbf{77.4\%}$	$\overline{\mathbf{P}} = \mathbf{99.3\%}$	**Evaluations**
Monte Carlo ([24])	~ 0.5	~ 10.0	~ 20.0	10^6
DA-PCE ([24])	0.0	10.0	20.0	11
`Uncertainpy`	1.1	10.9	21.2	73
FORM ([24])	-	-	-	96
SORM ([24])	-	-	-	123
PDEM ([24])	-	-	-	135

TABLE 3.12: Comparison of output metrics from the UQ module for the validation test-case.

3.8 Aircraft conceptual sizing and optimization

The computational framework builds upon the aircraft design tool Fixed-wing Aircraft Sizing Tool (FAST). `FAST` has been developed by ONERA and ISAE-SUPAERO since 2015 and it is conceived as a quick conceptual design tool to be used either for quick sizing and parametric studies on conventional tube and wings transport aircraft, or in combination with advanced analysis tools for unconventional design explorations, as is the case in the current PhD project. A detailed documentation covering all the main internal processes can be found in [72] and [26]. The most recent upgrade of the tool has been renamed `FAST-OAD` (for Overall Aircraft Design) [25], and is today available open-source on GitHub[2]. In its basic formulation, the user specifies a series of Top Level Requirements and an initial geometry, and the framework estimates the overall

[2] https://github.com/fast-aircraft-design/FAST-OAD

aircraft performance (such as fuel mass, payload range, etc.) through a series of sizing loops involving modular analyses for the key disciplines. These include basic flight mechanics, aerodynamics, structures, propulsion, weight and balance. The original approach is based on a point mass approximation together with semi-empirical equations for performance and aerodynamic predictions. This allows high computational efficiency and accuracy to be achieved as long as traditional concepts are treated. The propulsion module can be based either on a dataset from the CeRAS project [160], or an analytical model that provides thrust and fuel consumption as function of altitude and flight speed [161]. The performance module gathers all the information from the disciplinary modules and performs a time marching simulation of the full mission. Sizing and positioning of components are iteratively updated during the design loops through dedicated geometry, weight and balance modules. Overall aircraft design rules from [9] are used to initially locate the main components, such as wing, tail, landing gear, etc. An overview of the multidisciplinary structure of the tool is given in Figure 3.50.

`FAST-OAD` has recently been used for more advanced studies by interfacing it with physics-based analysis tools to extend its applicability to novel aircraft concepts, such as blended wing-body, distributed propulsion, electric and hybrid propulsion [31, 39, 43, 73]. Moreover, the platform, developed in Python, can be interfaced with the Surrogate Modelling Tools `SMT` [205] and the Super Efficient Global Optimization `SEGOMOE` libraries by ONERA and ISAE-SUPAERO (see Section 2.5.2). The libraries provide several surrogate modeling methods (e.g., radial basis functions, Kriging) and sampling methods (e.g. Latin Hypercube Sampling) and allows several optimization strategies, including Bayesian optimization, to be applied to the aircraft sizing process. Some applications of aircraft multidisciplinary design and optimization using `FAST-OAD` together with `SEGOMOE` have already been demonstrated, for example in [136, 206]. In this project, a similar path is followed, where `FAST-OAD` and `SEGOOMOE` are interfaced with the discussed disciplinary tools in order to enable novel MDAO studies involving flight dynamic constraints, flexible high-aspect-ratio wings and uncertainty propagation.

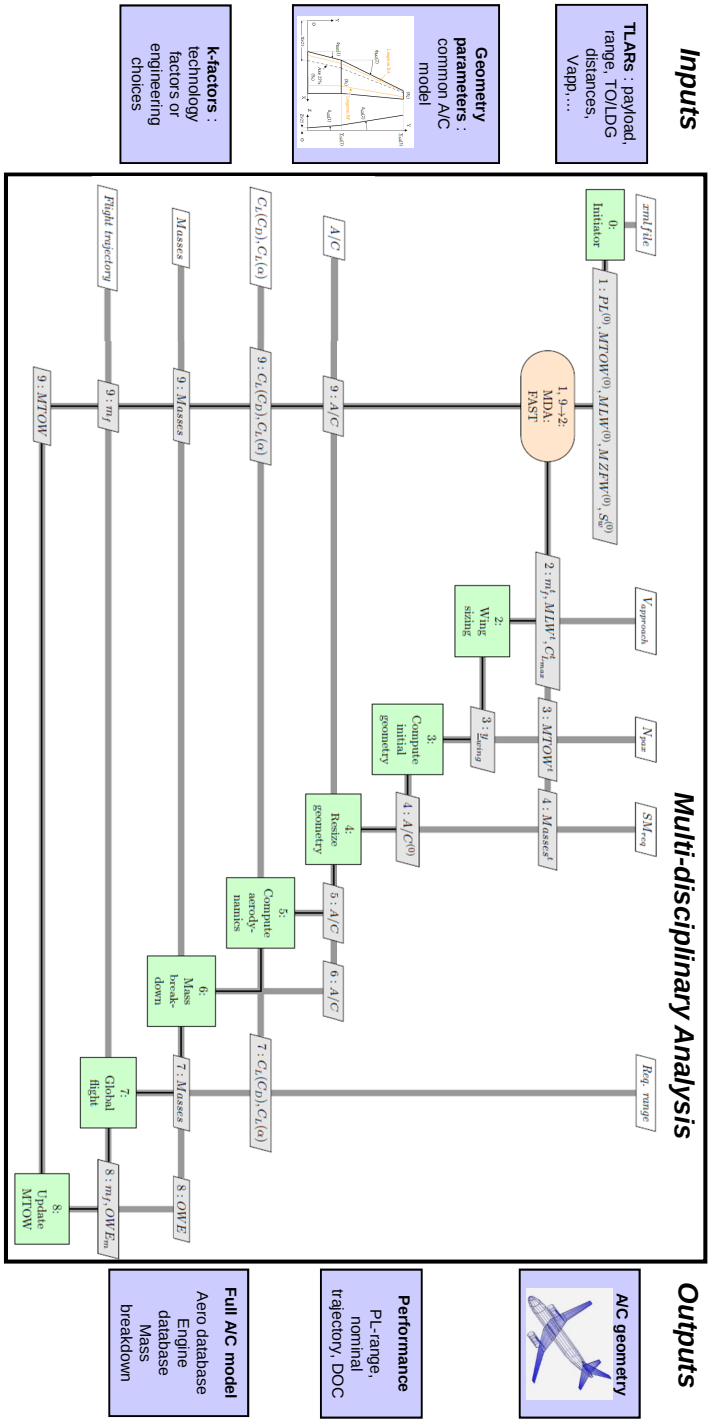

FIGURE 3.50: Structure of the FAST-OAD overall aircraft design suite, from [25].

3.9 Summary

This Chapter described the implementation, integration and validation of several analysis tools required to achieve the project's objectives. Such set of tools consists of the following models:

- A choice of aerodynamic models, including a classical analytical model based on linear aerodynamic derivatives, and a steady or unsteady implementation of the Vortex Lattice Method (VLM or UVLM);
- A nonlinear structural mechanics solver (`GEBT`, Geometrically Exact Beam Theroy)
- Two possible aeroelastic solvers: *a*) a linear solver based on potential unsteady strip theory coupled with linear beam theory, mainly required for flutter analysis; *b*) a linear/nonlinear solver coupling the `GEBT` structural solver with the VLM or UVLM aerodynamic solvers;
- A flight dynamics simulation module (FDM) implementing the 6DOFs nonlinear equations of motion;
- A post-processing module to extract the desired quantity of interest (amplitude, frequency, damping) out of the simulation history by use of a Least Square best fit technique of the time-domain data;
- An uncertainty quantification and sensitivity analysis module that wraps the above modules and propagates the uncertainty from the input parameters into the desired outputs. It returns the desired statistical metrics to be used in the reliability evaluation;
- An aircraft conceptual sizing tool (`FAST-OAD`) performing the necessary loops until convergence to a consistent configuration;
- An optimization environment (`SEGOMOE`) to be interfaced with the sizing process and with the implemented multidisciplinary deterministic or stochastic constraints (such as flying qualities constraints, flutter speed, gust loads).

The next chapters show different applications where subsets of such tools are assembled into different MDAO architectures. Each time, the overall structure and set of variables and constraints are adapted to meet the specific problem needs.

Chapter 4

Aircraft MDAO under flying qualities reliability constraints

Contents

3.1 Overview 48
3.2 Aerodynamics 52
3.2.1 Linear derivative-based aerodynamics 53
3.2.2 Linear unsteady strip theory 55
3.2.3 The steady Vortex Lattice Method 57
3.2.4 The Unsteady Vortex Lattice Method 67
3.2.5 Compressibility corrections 75
3.3 Structural dynamics 78
3.3.1 Linear beam Finite Element Model 78
3.3.2 Nonlinear Geometrically-Exact Beam Theory (GEBT) 80
3.4 Aeroelasticity 82
3.4.1 Linear aeroelasticity by 1D-beam FEM and unsteady strip aerodynamics 82
3.4.2 Nonlinear aeroelasticity 88
3.5 Flight dynamics 97
3.5.1 Validation of the flight dynamics module 99
3.5.2 Coupling flight dynamics with VLM aerodynamics 101
3.6 System identification for nonlinear systems 107
3.7 Sensitivity analysis and uncertainty quantification approaches 110
3.7.1 Problem definition and tool selection 110
3.7.2 Validation - mathematical example 111
3.8 Aircraft conceptual sizing and optimization 112
3.9 Summary 115

4.1 Overview

A first application of the discussed framework is here presented. The case study aims to optimize the planform of an A320-like configuration with respect to the fuel mass required for a representative flight, under reliability constraints on the short period dynamics. The reference configuration is the CeRAS baseline [160] (see Figure 4.1), a public database from the University of Aachen that provides an approximation of the A320 aircraft. Its main characteristics are summarized in Table 4.1. Four geometric parameters were chosen as optimization variables: the taper ratio and the quarter-chord sweep of the main wing and horizontal tail. Although previous studies [31] showed that aspect ratio may play a key role in fuel mass optimization, it was decided here not to include it among the optimization variables. In fact, highly elongated wings would require further aeroelastic verification, which is not available at the current state of the presented framework. It was assumed instead that the baseline aspect ratio is already the best trade-off between aerodynamic efficiency and structural mass. Uncertainty is associated to the estimation of the center of gravity location x_{CG} and to the longitudinal moment of inertia I_{yy}. The propagation of this uncertainty through the MDA is handled by the uncertainty quantification module, which ultimately returns the probabilities of constraint violations. Four flying qualities constraints were applied: the upper and lower bounds of short period damping ξ_{sp} and natural frequency $\omega_{n\,\text{sp}}$. This choice arises from the fact that short period characteristics in particular have critical influence on manoeuvrability. The overall optimization task is summarized in Tab 4.2. Of course this study does not aim at a complete treatment of flying qualities requirements, which would require a prohibitive effort for the collection and codification of the certification specifications. Instead, we want to present a proof of concept of the proposed framework, showing the capability to handle multidisciplinary aircraft design and optimization under uncertainty, with reliability constraints on aerodynamic and/or dynamic performances. The aim is to demonstrate the ability of the framework to handle this optimization problem on any kind of aircraft configuration, possibly disruptive ones where the verification of FQ requirements from the early design stage would be of primary importance. Similarly, the Bayesian Optimization tool `SEGOMOE` was selected to demonstrate the feasibility of the proposed MDAO approach, although in effect this method is not strictly required for the low dimension and relatively limited space of the specific problem here addressed.

The global framework architecture is summarized in Figure 4.2. The optimizer requires to define the optimization variables, their bounds, the constraints and the objective function. In this case the optimization variables are denoted as V_g. For each candidate evaluation the uncertainty quantification module takes into account the prescribed distributions of the uncertain parameters and runs an adequate number of calls to the multidisciplinary analysis (MDA) in order to compute the statistical metrics associated

FIGURE 4.1: CeRAS baseline planform, from [26].

Top Level Aircraft Requirements	
Number of passengers	150
Passenger weight [lbs]	200
Design Range [NM]	2750
Operational Range [NM]	800
Cruise Mach number	0.78
Approach speed [kts]	132
Planform parameters	
Wing area [m^2]	122.4
Mean aerodynamic chord (MAC) [m]	4.2
Aspect ratio	9.48
Wing break	0.40
Wing sweep angle at 25% chord [deg]	24.5
Wing taper ratio	0.313
Horizontal tail sweep angle at 25% chord [deg]	28.0
Horizontal tail taper ratio	0.300
Propulsion	
Max thrust at sea level [N]	117880
Weight & balance	
Max take-off weight [N]	7.55×10^5
Selected nominal CG location	45%MAC
Pitching moment of inertia [kg$\times$ m^2]	3.6×10^6

TABLE 4.1: CeRAS baseline parameters, from [26].

to one or more QoIs. In the present study the chosen metrics are the 5% and 95% percentiles of the short period damping and natural frequency, indicated as $P_5\left(\hat{\xi}_{sp}, \hat{\omega}_{nsp}\right)$ and $P_{95}\left(\hat{\xi}_{sp}, \hat{\omega}_{nsp}\right)$. These values are compared by the optimizer with the required boundaries to enforce the reliability constraints. The MDA starts with the `FAST-OAD` sizing process, which receives the design variables V_g and returns a converged configuration, meaning that TLARs are always satisfied when changing the design variables, by means of a full resizing of the aircraft. This is characterized by additional

	Function/quantity	Range/distribution
Minimize	Fuel mass	
with respect to	Main wing taper ratio	[0.25, 0.37]
	Main wing sweep at 25% chord	[20° , 29°]
	Horizontal tail taper ratio	[0.24, 0.36]
	Horizontal tail sweep at 25% chord	[23° , 34°]
with uncertainty on	CG location	Normal ($\mathbb{E} = \overline{x}_{CG}$, $\mathbb{V} = 0.1\,\overline{x}_{CG}$)
	Longitudinal inertia moment	Uniform ($0.8\,I_{yy}$, $1.2\,I_{yy}$)
subject to	$\mathbb{P}\,[\xi_{\text{sp}} > 0.45] > 95\%$	
	$\mathbb{P}\,[\xi_{\text{sp}} < 1.35] > 95\%$	
	$\mathbb{P}\,[\omega_{n\,\text{sp}} > 2.4\ ] > 95\%$	
	$\mathbb{P}\,[\omega_{n\,\text{sp}} < 3.4\ ] > 95\%$	

TABLE 4.2: Definition of the MDAO problem under flying qualities reliability constraints.

geometric parameters P_g, an estimation of the CG location x_{CG}, and other indicators such as the mission fuel mass, which is here used as objective function. The configuration returned by `FAST-OAD` is subsequently given to the UVLM module, with a CG position altered by $\Delta\,x_{CG}$, representing its uncertainty. The unsteady solver simulates some pitching oscillations at the frequency ω_0, which is assumed a representative short period frequency for the particular class of aircraft considered. The time response in terms of aerodynamic loads is then processed to extrapolate an equivalent, derivative-based aerodynamic model characterized by a set of coefficients C_{L_i}, C_{m_i} (defined later in Section 4.2). The assumption here is that even if each candidate has a slightly different frequency, this variation adds a negligible aerodynamic contribution compared to the model obtained at ω_0. The assumption is reasonable because, given the relatively high flight speed, a small variation of ω produces a negligible variation of the reduced frequency $k = \omega\,\bar{c}/2\,V$, which is the parameter that really affects the unsteady aerodynamics. Once the aerodynamic derivatives are identified, they are fed to the flight dynamics module, together with the other aircraft parameters P_g and the longitudinal moment of inertia I_{yy}, given by the uncertainty quantification module. Here the time response (in this case the longitudinal short period response) is computed following a disturbance, and the time domain results are then processed to get the desired QoI, in this case the short period damping ξ_{sp} and natural frequency $\omega_{n\,\text{sp}}$. More details on the single disciplinary modules mentioned above are given in the following sections.

This Chapter continues in Section 4.2 with a detailed description of how the aerodynamic and flight dynamics disciplines are taken into account. Then, Section 4.3 shows how the computational cost of the proposed MDAO architecture can be considerably reduced by introducing a surrogate model of the most expensive calculation blocks. Subsequently, Section 4.4 discusses more in details how the flying qualities reliability constraints are defined and implemented. The results of the overall optimization study

are then presented and discussed in Section 4.5. Finally, conclusions are drawn in Section 4.6.

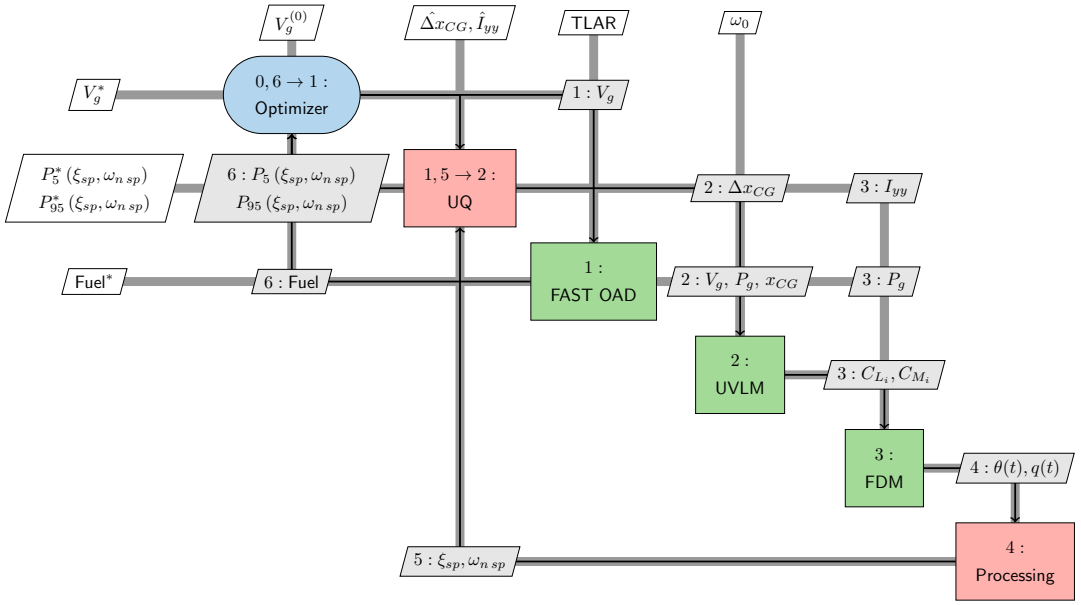

FIGURE 4.2: Framework for aircraft multidisciplinary design and optimization under reliability constraints.

4.2 Aerodynamics and flight dynamics

To demonstrate the versatility of the developed framework, offering the user different disciplinary tools to be selected and combined according to the specific study, it was chosen to adopt a quasi-steady aerodynamic model that combines a linear derivative-based approach with more complex unsteady simulations.

The quasi-steady aerodynamic model expresses the global aerodynamic coefficients as in Equation (4.1).

$$\Delta C_i = C_{i\alpha}\,\Delta\alpha + C_{iq}\left(\frac{\bar{c}}{2V}\right) q + C_{i\dot{\alpha}}\left(\frac{\bar{c}}{2V}\right)\dot{\alpha} + C_{i\ddot{\alpha}}\left(\frac{\bar{c}}{2V}\right)^2 \ddot{\alpha} \qquad (i = D, L, m) \tag{4.1}$$

Such a model requires the knowledge of some unconventional derivatives, namely $C_{i\dot{\alpha}}$, $C_{i\ddot{\alpha}}$, which are not generally provided by standard analytical conceptual design methods. However, they can be obtained by means of higher-fidelity unsteady solvers. A possible approach for their derivation is described in [207], which requires that first

some unsteady aerodynamic simulations are performed for a forced oscillating motion. Enough oscillation cycles must be run in order to let the transient response vanish, achieving the periodic evolution. This could take two or three cycles at high frequency, but in the present case it was found that the initial transient decays in a small fraction of a period.

For a sinusoidal pitch oscillation with $\alpha(t) = \alpha_0 \sin(\omega t)$ the aerodynamic variables of interest are:

$$\dot{\alpha} = q = \alpha_0 \omega \cos(\omega t) \tag{4.2}$$

$$\ddot{\alpha} = \dot{q} = -\alpha_0 \omega^2 \sin(\omega t) \tag{4.3}$$

Equation (4.1) then becomes:

$$\Delta C_i = \overline{C}_{i\alpha} \alpha_0 \sin(\omega t) + \overline{C}_{iq} \alpha_0 \cos(\omega t) \tag{4.4}$$

with:

$$\overline{C}_{i\alpha} = (C_{i\alpha} - k^2 C_{i\ddot{\alpha}}) \tag{4.5}$$

$$\overline{C}_{iq} = (C_{iq} + C_{i\dot{\alpha}}) \tag{4.6}$$

where $k = \omega \bar{c}/(2V)$ is the reduced frequency. Equation (4.4) represents a truncated Fourier series for $C_i(wt)$, and therefore the coefficients (4.5) and (4.6) can be obtained as:

$$\overline{C}_{i\alpha} = \frac{2}{\alpha_0 n T} \int_0^{n T} \Delta C_i(t) \sin(\omega t)\, dt \tag{4.7}$$

$$\overline{C}_{iq} = \frac{2}{\alpha_0 k n T} \int_0^{n T} \Delta C_i(t) \cos(\omega t)\, dt \tag{4.8}$$

These coefficients can be computed by numerical integration of the $C_L(t)$ and $C_m(t)$ curves obtained with the UVLM. The $C_{i\alpha}$ and C_{iq} coefficients can be calculated through the steady VLM. Ultimately, with these quantities known, the remaining terms $C_{i\dot{\alpha}}$ and $C_{i\ddot{\alpha}}$ are obtained from (4.5) and (4.6).

To provide an example, the unsteady aerodynamics module based on the UVLM (see Section 3.2.4) and its steady version are here employed to compute the full set of derivatives needed for longitudinal flight simulation. A snapshot from a UVLM simulation of the CeRAS baseline is reported in Figure 4.4. These simulations impose a sinusoidal pitching oscillation and return the time history of the force and moment coefficients. As the short period is not really affected by drag, only lift and moment coefficients are

taken into account. The imposed pitching motion is of the form:

$$\alpha(t) = \alpha_M + \alpha_0 \sin(\omega t) \tag{4.9}$$

with $\alpha_M = 5.0°$ and $\alpha_0 = 3.0°$.

The effectiveness of the approach is demonstrated in Figure 4.3, where the lift and moment coefficients obtained with the steady and unsteady derivatives are compared with the output curves from the UVLM. It can be seen that the linear model based on the identified unsteady derivatives matches satisfactorily the reference curve, except for the initial transient due to the start of motion. An appreciable difference is found with respect to the prediction based on static derivatives only.

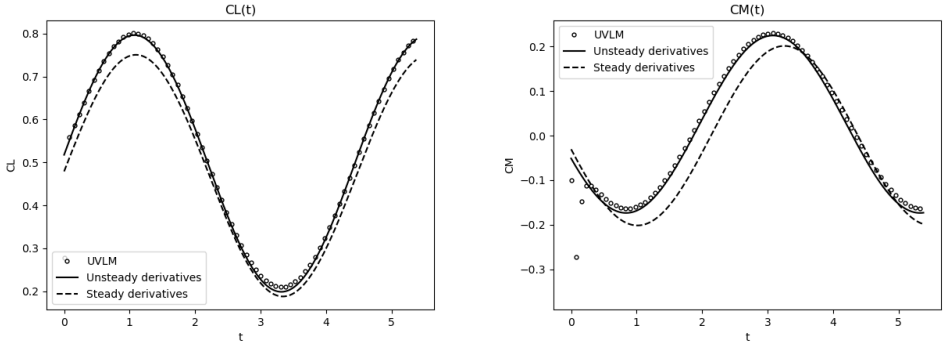

(a) Lift coefficient

(b) Moment coefficient

FIGURE 4.3: Identification of lift coefficient time history under forced pitch oscillations.

The choice of oscillations around a non-zero angle of attack is mainly due to the fact that it is of no interest to include negative angles of attack for an airliner configuration. It is preferable instead to span a larger portion of the positive, linear range of angles of attack. An example of the lift and moment responses is reported in Figure 4.5. It can be seen that the unsteady aerodynamics captures two main differences with respect to the steady model. The first is an amplitude gap, especially visible in the lift coefficient curve, producing a higher lift for the unsteady case. This translates into a slightly steeper slope of the $C_L - \alpha$ ellipse, and therefore an increased aerodynamic stiffness. The second effect, mainly affecting the pitching moment, is a phase anticipation of the unsteady moment with respect to the steady one. That appears clearly in the time-domain curve and it is even more evident from the larger $C_L - \alpha$ ellipse. These effects are to be attributed to the interaction between main wing and tail, and in particular to tail downwash delay, whose effect is to let the main wing lift coefficient grow bigger and the main wing moment coefficient grow earlier than the steady prediction, where the tail effect is considered immediate. Note that some points related to the initial transient may be visible in the curves, but as it vanishes quite fast, this does not prevent from capturing the stationary periodic behaviour via the linear unsteady derivatives.

The aerodynamic calculations were carried out around a trimmed climb configuration with $\alpha = \theta = \alpha_M$, where θ is the pitch angle. The trim is achieved by a Newton algorithm to find the nonlinear equilibrium with the steady VLM. The nonlinearity comes from the fact that a change in the tail tilt angle also changes loads and loads distribution, so that an iterative process is required to achieve balance. The UVLM is then run from the trimmed geometry. This allows to be consistent with the following flight dynamics simulation, which is then started from an equilibrium condition at $\alpha = \alpha_M$. The flight dynamics module, taking as input the configuration file including the computed derivatives, returns the response to a step pitch control. The output is then processed as described in Section 3.6 to extract the damping and frequency of the short period mode.

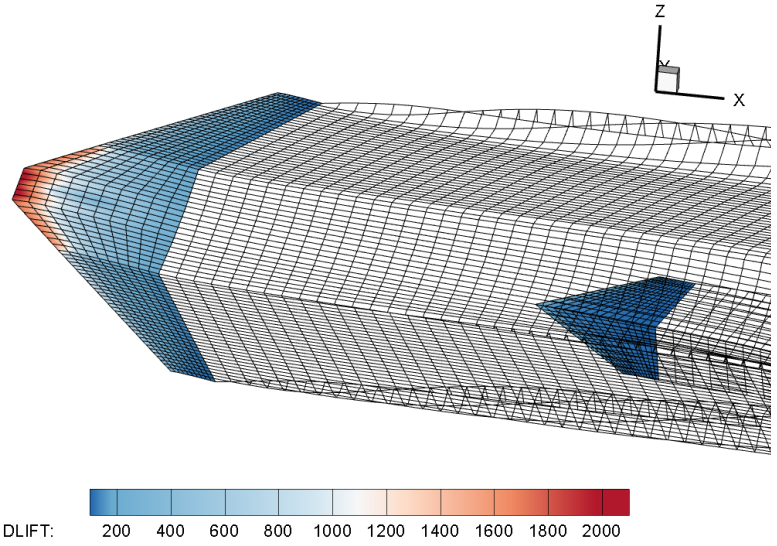

FIGURE 4.4: Snapshot during unsteady simulation of the CeRAS A320 baseline, run with the present UVLM solver.

4.3 Surrogate modelling of the aircraft sizing process and aerodynamic characterization

The aircraft sizing process and the aerodynamic characterization of the converged configuration are the most expensive tasks in the present MDAO chain. Running the optimization and uncertainty quantification loops with the full architecture showed in Figure 4.2 would reach prohibitive costs for conceptual exploration and design (the study presented herein would require several days as one single run of the UVLM analysis

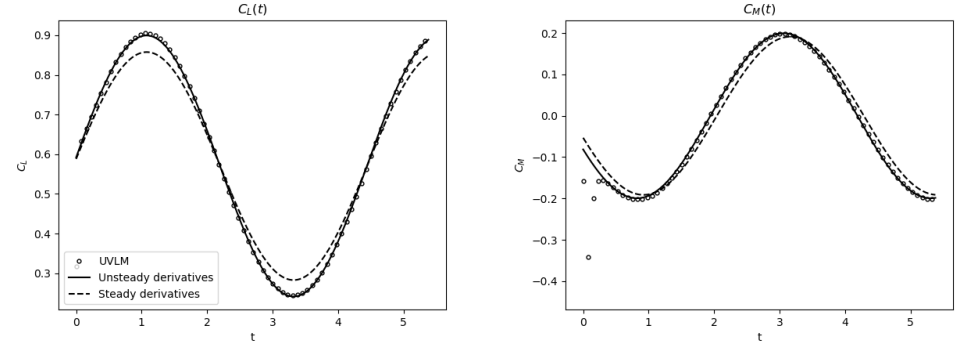

(a) Lift coefficient vs time

(b) Moment coefficient vs time

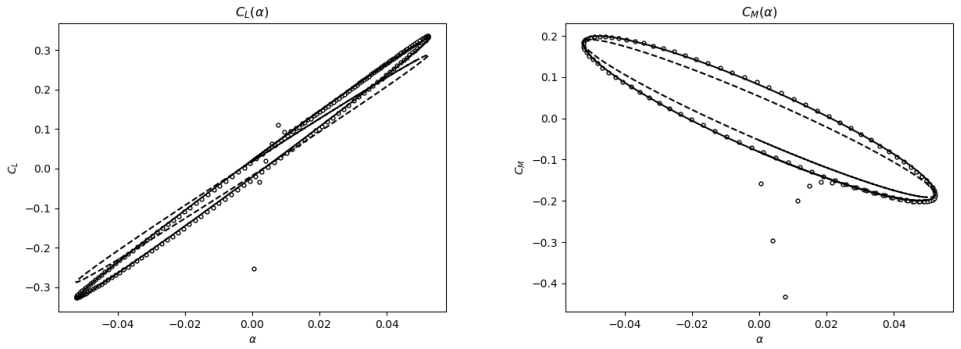

(c) Lift coefficient vs angle of attack

(d) Moment coefficient vs angle of attack

FIGURE 4.5: Example of aerodynamic responses to pitch oscillations and their identification via linear derivatives.

takes around one hour). For this reason it was chosen to build a surrogate model of sizing and aerodynamic characterization of the design candidates. The `FAST-OAD` output depends only on the geometrical optimization variables V_g. The UVLM solver requires as input, in addition to V_g, a complementary set of geometrical outputs from `FAST-OAD`, P_{g1} (root chords, distance between main wing and tail, nominal center of gravity location, etc) and the uncertainty on the center of gravity location Δx_{CG}, and its ultimate output, after the derivative identification process, is the set of aerodynamic derivatives to be fed to the flight dynamics module. Therefore the block `FAST-OAD`+UVLM takes five inputs (the four optimization variables V_g plus the uncertain parameter Δx_{CG}) and outputs the fuel mass objective function, the eight aerodynamic derivatives (C_{L_α}, C_{L_q},$C_{L_{\dot{\alpha}}}$,$C_{L_{\ddot{\alpha}}}$,C_{m_α}, C_{m_q},$C_{m_{\dot{\alpha}}}$,$C_{m_{\ddot{\alpha}}}$) and the remaining aircraft parameters P_{g2} needed by the flight dynamics module (wing area and mean aerodynamic chord). Overall, the block takes five inputs and returns ten outputs. The structure of this updated version of the MDAO framework is summarized in Figure 4.6. A Gaussian process was chosen as kernel for the surrogate model. This generally requires around $10\times N_{\text{dim}}$ sample points to reach adequate precision. As in this case $N_{\text{dim}} = 5$, a DOE of 65 samples was set up via Latin Hypercube Sampling (LHS), accounting for about 20% extra points to be used for validation. The training points and the test points were selected through a nested LHS

algorithm from the `ScikitLearn` toolbox [208]. With this set up the surrogate model gave satisfactory results for all the outputs, with a root mean square error always below the 0.3%. The validation is reported in Appendix B.

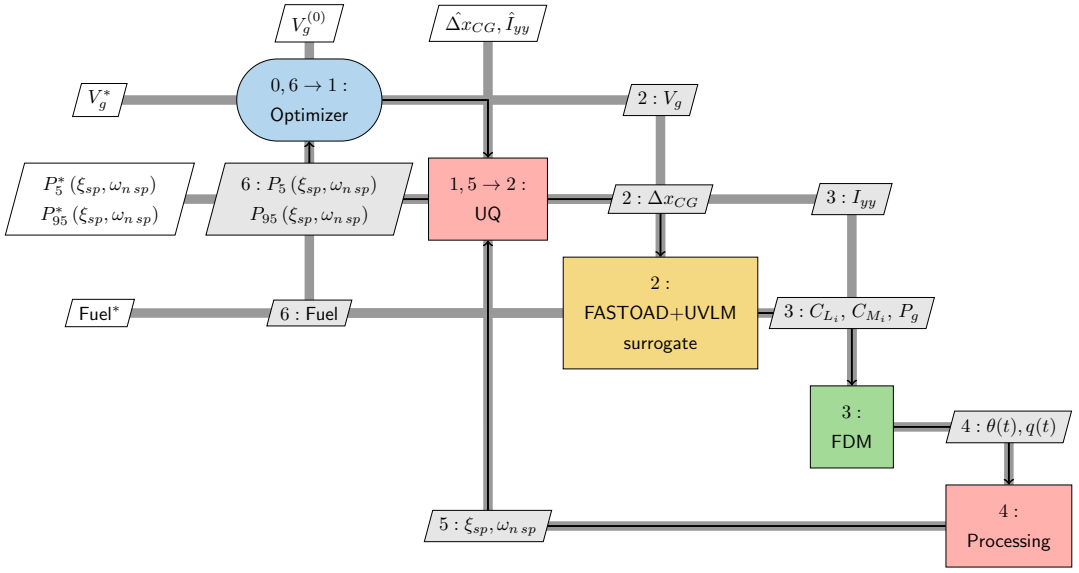

FIGURE 4.6: Framework for robust design and optimization under reliability constraints, where the aircraft sizing, aerodynamic and flight dynamic modules are replaced by a surrogate model.

4.4 Reliability constraints

As mentioned above, the dynamic constraints here adopted are on the short period damping and natural frequency. A wide set of possibilities is available from the literature for flying qualities specifications or recommendations, including qualitative and quantitative guidance, in frequency and time domain. In this work the quantitative definition of the constraints was made starting from the so-called longitudinal short period *thumb print* criterion. It defines some regions in the $\xi_{\text{sp}} - \omega_{n\,\text{sp}}$ plane corresponding to different pilot ratings such as satisfactory, acceptable, poor, unacceptable. The diagram is reported in Figure 4.7. The figure also shows four lines defining the scalar values adopted here as upper and lower bounds for the two parameters. It is worth pointing out that as ξ_{sp} is expected to stay close to the lower bound, the upper bound on $\omega_{n\,\text{sp}}$ was fixed close to the satisfactory limit corresponding to $\xi_{\text{sp, min}}$. The values for each bound are given in Table 4.4.

With these scalar bounds fixed, the reliability problem is based on the probability of those bounds to be violated: acceptable configurations are considered those for which the probability to fall within the bounds is greater than 95%. Before running the optimization task, the capability of the uncertainty quantification module to well predict

the statistics for the quantities of interest was tested with a single, random combination of the design variables V_g. An uncertainty quantification with the PCE method introduced in Section 3.7 was run on this configuration assigning the following uncertainty distributions reported in Table 4.3. The choice of these different distributions is due to the fact that `FAST-OAD` gives an estimation for the CG location but not for the moment of inertia. In lack of enough supporting data, the amount of uncertainty (variance, bounds) injected was decided somewhat arbitrarily. The results were validated against a distribution obtained via a Monte Carlo simulation with 10^4 samples. A probability distribution function was extrapolated from the PCE evaluating it at 10^5 samples, and this is compared in Figures 4.8(a) and 4.8(b) with a histogram chart built from the Monte Carlo results. The outcome demonstrated that the PCE approach is able to reproduce the model with satisfactory accuracy. It was found that a polynomial order of 4, using point collocation method and the Hammersley sampling with 32 function calls was sufficient as no appreciable improvement was obtained by increasing the order up to 6 and the function calls up to 80. The main statistical metrics are reported in Figures 4.8(c) and 4.8(d). It also confirms that the sensitivity analysis is consistent as the first Sobol indices correctly sum to 1. It is worth pointing out that the obtained distributions are wide enough to approach the constraint boundaries of Table 4.4, which justifies the search for optimal constrained configuration.

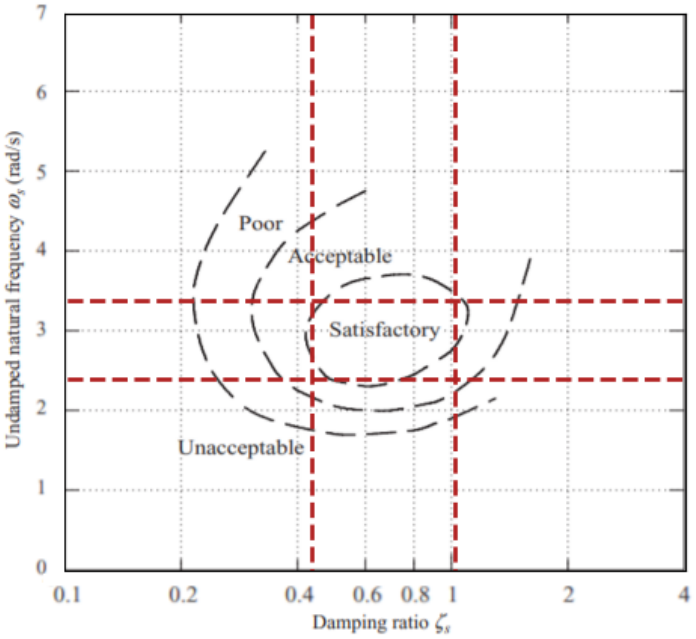

FIGURE 4.7: Thumb print criterion reporting the pilot opinion contours related to the short period characteristics. The dashed red lines show the bounds used in this work.

Parameter	Distribution	Descriptors
Δx_{CG}	Normal	$\mathbb{E} = \overline{x}_{CG}, \quad \mathbb{V} = 0.1\,\overline{x}_{CG}$
I_{yy}	Uniform	$I_{\min} = 0.8\,I_{yyB}, \quad I_{\max} = 1.2\,I_{yyB}$

TABLE 4.3: Uncertainty distributions on the input parameters. $\overline{x}_{CG}$ is the CG location for a prescribed load case defined in `FAST-OAD`. I_{yyB} is the moment of inertia of the baseline configuration.

Parameter	Lower bound	Upper bound
ξ_{sp}	0.45	1.35
$\omega_{n\,\text{sp}}$	2.4	3.4

TABLE 4.4: Short period damping and natural frequency constraints adopted for the present case study.

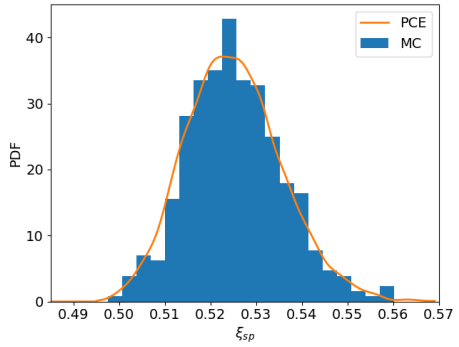

(a) Short period damping - PDF

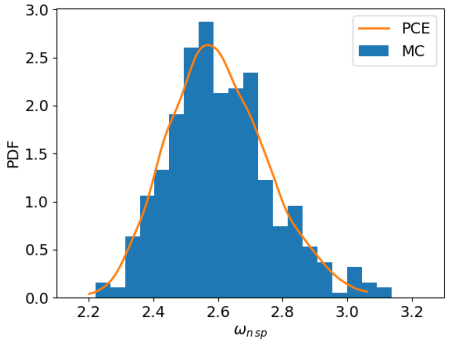

(b) Short period natural frequency - PDF

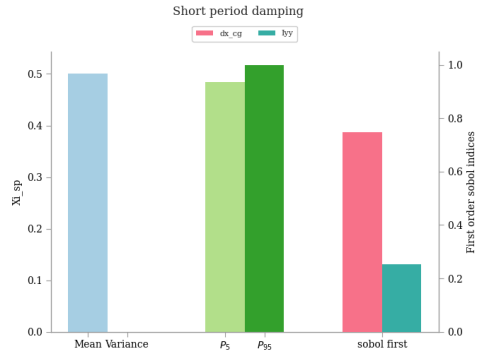

(c) Short period damping - statistical metrics

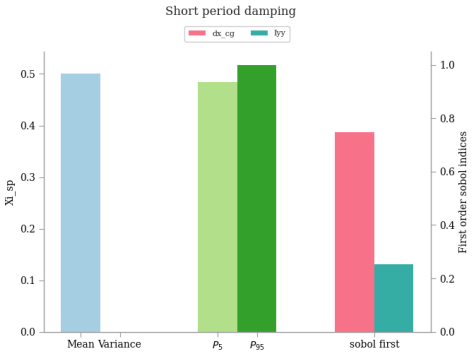

(d) Short period frequency - statistical metrics

FIGURE 4.8: Validation of the PCE approach for a reference configuration ($t_{r\,W} = 0.3$, $\Lambda_W = 25°$, $t_{r\,T} = 0.28$, , $\Lambda_T = 28°$).

4.5 Optimization results

In order to perform the optimization with the `SEGOMOE` tool it is required to define a learning DOE, which is used to build a Gaussian process for the black-box function to optimize. A DOE size of 60 points was given, and additional 100 calls were allowed to the optimizer as exploration iterations. Such values are quite high for a 4-dimension

space, but it was decided to keep this setup to produce more data and test the stability of the framework over a large number of iterations. At each iteration, the optimizer updates the surrogate with the added knowledge and maximizes the WB2 acquisition function (see Section 2.5.2). to choose the next candidate to evaluate. The learning and optimization history is reported in Figure 4.9. It can be seen that the optimizer rapidly converges to candidates very close to the optimum in few iterations after running the DOE, demonstrating that the learning was sufficient to identify the most promising design regions. The 100 iterations were also enough to explore the design space, as no relevant changes in the objective function were found after the first iterations. In a few cases the expected improvement moved towards worse candidates, sometimes giving a very high value of the objective function. It was found that the best configurations in terms of fuel burn always have satisfactory short period characteristics with respect to the given constraints. In particular, the only constraint which is sometimes violated is the lower bound on natural frequency, whereas the others are matched in all cases. This could be explained by recalling, from classical notions of flight dynamics [156, 209] that a low short period frequency could arise mainly from a low absolute value of the aerodynamic stiffness in pitch C_{m_α} (the sign is always negative), or from a high moment of inertia, or both. As the inertia is here distributed in the same way for every configuration, the correlation between higher fuel consumption and lower short period frequency is to be found on the aerodynamic pitch stiffness. In effect, the module of C_{m_α} is reduced with a backward shift of the CG but also with a lower slope C_{L_α}, and the latter decreases with a decrease on efficiency. Moreover, a very low pitch stiffness due to wing shape is automatically compensated in the sizing process with a more effective (larger) tail plane, which translates into a heavier and consequently less efficient configuration. For this reasons the most aerodynamically efficient configurations also provide good short period characteristics, and conversely the worst shapes promoting inefficient load distributions also determine a deterioration of the short period response. It is also interesting to note, from Figure 4.10, that low sweep angles Λ_W never comply with the constraints. The reason is linked with the above discussion: low sweep angles have here the effect of moving the aerodynamic center forward, reducing the static margin and the absolute value of the pitch stiffness C_{m_α}, producing lower short period frequencies.

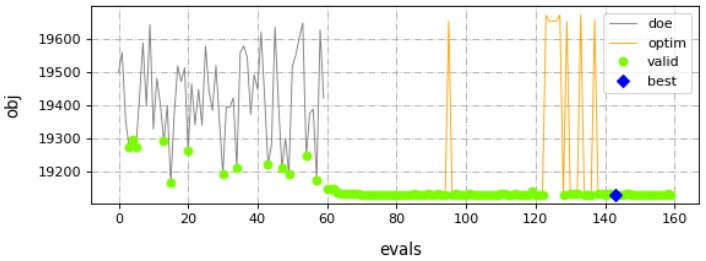

FIGURE 4.9: Monitor plot of the DOE runs and optimization history.

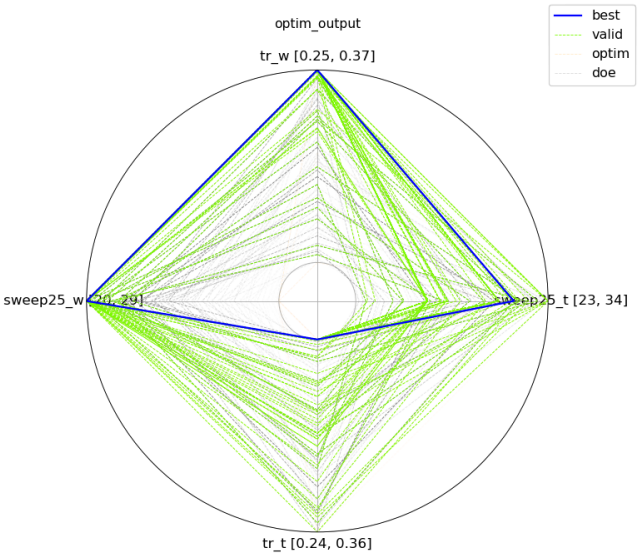

FIGURE 4.10: Radar plot summarizing all the evaluations during the DOE and the optimization iterations.

Source	t_{rW}	Λ_W	t_{rT}	Λ_T	Fuel mass
CeRAS	0.31	24.5°	0.3	28.0°	19406 kg
Optimizer	0.37	29.0°	0.24	32.0°	19137 kg

TABLE 4.5: Fuel mass optimization results compared with baseline data. The optimized configuration offers an improvement of 1.4%.

4.6 Conclusions

This work introduced a MDAO framework for aircraft design applications capable to deal with optimization under uncertainty. The framework is composed by a combination of existing tools for aircraft sizing, optimization and uncertainty quantification, and some more recent tools for aerodynamic and flight performance analysis developed, validated and assembled during this PhD project. The framework was tested on a demonstrative case study: a transport aircraft fuel mass optimization with respect to planform variables, with uncertainty on the center of gravity location and on the longitudinal moment of inertia, and under reliability constraints on the short period damping and natural frequency. The unsteady aerodynamics module was used to run a series of oscillating simulations, which were processed to identify a set of aerodynamic derivatives. These were used to set up a much faster aerodynamic function to be called by the flight dynamics module. This enabled a very fast computation of the dynamic response of the aircraft, which can then be processed to get the desired figures of merit, in this case the short period damping and natural frequency. Further improvement on computational speed (by a factor of 10) was obtained by a surrogate modelling approach replacing the aircraft design and unsteady aerodynamics modules, with negligible error. The above process is automatically handled by the uncertainty

quantification module, that computes the stochastic output, given the distributions of the uncertain input parameters. Such outputs are ultimately passed to the optimizer, which verifies the reliability of the candidate against the required boundaries. The bayesian optimization converged to an optimum satisfying all the given constraints. It was found that the most stringent constraint is the lower bound on the natural frequency, but for the type of vehicle considered all the best candidates in terms of fuel burn also comply with the present short period requirements. The reason for this was recognized to be the fact that aerodynamic efficiency also translates into increased aerodynamic pitch stiffness, and this relationship is favourable at least for the category of aircraft studied herein.

The framework proved capable to successfully address the multidisciplinary optimization task, with an architecture conceived to be flexible with respect to the problem. In fact, although a reduced set of variables and constraints was here adopted, the same approach and tools are applicable to more complex problems, with increased number of variables or constraints or uncertain parameters. The same kind of analysis could be performed for example to include robust control design, provided that the aerodynamic function is enriched with the needed control laws. In that case more stringent constraints could be applied, and additional dynamic responses could be studied, including lateral dynamics or the complete coupled set of the equations of motion. Moreover, as the aerodynamic tools here employed have already been coupled with a structural dynamic solver of aeroelastic calculations, the next studies will extend the framework to include aeroelastic constraints. This would allow to broaden the exploration to larger aspect ratios and more efficient and innovative configurations. Further work can also include comparisons against lower or higher fidelity methods, and additional investigations involving other parameters uncertainties and their impact on the aeroelastic safety of the candidate vehicles.

4.7 Summary

This Chapter provides a first demonstration of a robust multidisciplinary analysis and optimization task under uncertainty performed using some of the tools presented in Chapter 3. The application involves a transport aircraft planform optimization under short period reliability constraints, targeting the best aerodynamic configuration to minimize the fuel mass for a given reference mission. The Chapter is structured as follows:

- An overview of the problem is given, defining the optimization objective (fuel minimization), variables (wing planform parameters), uncertain inputs (longitudinal balance), dynamic constraints (short period characteristics). The proposed framework architecture for this particular task is also presented and discussed.

- A detailed description is given about how the aerodynamics and flight dynamics modules are employed to calculate the required quantities of interest;
- Given the cost of the aircraft design loops combined with the unsteady aerodynamic evaluations, an alternative approach based on a surrogate model of these processes is introduced, allowing to significantly speed up the overall optimization;
- The implementation of the flying qualities reliability constraints is detailed, covering also how the uncertainty propagation from the input parameters to the output dynamic characteristics is performed.
- The optimization results are presented and discussed, and some conclusive remarks are drawn.

No effort is made at this stage to take static or dynamic aeroelastic issues into account. These aspects are left as the main objects of the next chapters.

Chapter 5

MDAO framework for flexible transport aircraft

Contents

4.1 Overview 118
4.2 Aerodynamics and flight dynamics 121
4.3 Surrogate modelling of the aircraft sizing process and aerodynamic characterization 124
4.4 Reliability constraints 126
4.5 Optimization results 128
4.6 Conclusions 130
4.7 Summary 131

5.1 Overview

Robust analysis and optimization for flexible aircraft is a wide and challenging problem. This is still true at the conceptual design phase, which is the focus of this work. In fact, although conceptual design involves simplified methods and faster tools compared to the more advanced design phases, on the other hand the task is complicated by the need to guess several parameters or to make certain assumptions, with the responsibility that choices made at this stage may prove decisive for the success of the next development. Moreover, as most assumptions and guesses are made based on statistical and semi-empirical data, if a disruptive concept is to be achieved, those data may simply be missing, or unreliable. This calls for new methods that not only can predict the effects of relevant disciplinary interactions - such as fluid-structure interaction - but that are also capable to provide information about the sensitivity of the analysis to some key, uncertain parameters and about the robustness of the design outcome with respect to those uncertainties.

Due to the variety of domains involved - static and dynamic structural mechanics, steady and unsteady aerodynamics, aircraft performance, optimization, sensitivity analysis, uncertainty quantification, etc. - and of methods available, there is no unique approach to the problem. The different methods and tools could be combined in a variety of ways, and the approach to be preferred is case-specific, depending on what knowledge is available and on the exact problem definition, that is, what objective, what variables, which constraints, which uncertainties.

Hereafter an approach to the design and optimization of a high aspect ratio transport aircraft is presented making use of the tools previously introduced in this manuscript. The idea is to demonstrate the applicability of those tools to a complex research case, showing the ability to custom the framework according to some prescribed research needs. It is shown how the different available modules are combined into an adaptable architecture to be tailored on different problem definitions. The core ideas of the proposed approach are briefly outlined in the present section. Additional details with quantitative information, results and discussion are given in the following sections.

The aim is to use the developed tools to extend the design capabilities of the existing FAST-OAD aircraft design tool, in order to take into account the main aeroelastic problems of high aspect ratio wings, and the effect of uncertainties in the wing structural model. More in detail, the objective is to find a configuration with minimal fuel consumption, with respect to some wing planform parameters, including aspect ratio, ensuring that:

- The wing structure is properly sized using static loads arising from the flexible wing;

- The weight of the sized wing is optimal with respect to an identified set of structural parameters;
- The overall aircraft design process takes into account the eventual corrections on wing weight due to the aeroelastic sizing;
- The wing does not undergo plastic deformation or structural failure under gust loads, computed on the flexible wing;
- The wing is flutter-free within the prescribed fight envelope;
- Compliance with gust loads and aeroelastic flutter requirements can be granted not only in a deterministic way, but also in a robust way, propagating some key structural model uncertainty.

To meet these targets, a MDAO framework was developed, integrating the disciplinary tools in a set of functional blocks designed to respond to the points above. A better understanding of the architecture can be achieved with the aid of Figure 5.1. The overall optimization process calls the Multi-Disciplinary Analysis with input variables V_g, which refer to a desired set of aircraft geometry parameters. The MDA is handled by an aeroelastic sizing routine, which is aimed at ensuring that the overall aircraft sizing process run by `FAST-OAD` is consistent with the aeroelastic sizing of the wing, which is done outside `FAST-OAD`. In fact, the latter does not take into account any effect of structural flexibility, nor does it build any structural model to predict stress. It only adopts traditional rigid-body equations and semi-empirical regressions based on existing conventional aircraft to estimate performance and weight and balance characteristics. The tool only allows for some technological correction factors to be applied as inputs in link with some components. For example, one correction factor could be applied, if known, to the drag build-up accounting for the effect of winglets. In the present case, the factor k_w is employed to correct the estimation of the flexible wing's structural weight. This is done as follows. First, `FAST-OAD` is launched, with no correction applied ($k_w = 1$), based on the input geometric variables V_g, and some Top Level Aircraft Requirements (TLAR). The sizing process terminates with a sized rigid aircraft with a certain amount of fuel burn required, and a wing structure weighing W_{w1}. This value is collected and stored by the aeroelastic sizing routine. It is worth pointing out here that the fuel burn, which is used as objective for the overall optimization, is the one calculated for the rigid aircraft. It is assumed here that structural deformation adds a negligible effect to the overall aircraft drag polar, so no effort is made to apply such a correction. The main interest in including aeroelastic analyses is to capture the more important effects on structural integrity, which have a strong impact on weight and safety. Based on the sized rigid body wing geometry, completely identified by the parameters W_g, an approximated wing-box structural model is initialized, depending on the three variables t_w, t_s, A_s, defining the web thickness, skin thickness and stringers

cross section area, respectively. After initializing the wing-box model with a rigid body, analytical approach, providing the initial guess t_{w0}, t_{s0}, A_{s0}, a structural optimization is performed in a neighborhood of $[t_{w0}, t_{s0}, A_{s0}]$, aimed at minimizing the wing structural weight W_{w2} with the constraints that the static direct and shear stresses $\sigma_{s,\max}$ and $\tau_{s,\max}$ on the structure do not exceed the material - aluminium - yield strength. This time, loads are computed on the elastic wing, requiring an aeroelastic model has to be generated. This is done through a beam generation module that computes the needed elastic properties from the wing box geometry and condensates them into an equivalent finite element beam model. The beam properties (`FEM data`) are passed to the aeroelastic solver, which couples the nonlinear beam solver with the VLM aerodynamics to compute the structural loads on the deformable wing. This analysis has to be run at a prescribed load factor L/W. As the structural flexibility introduces a nonlinearity in the lift slope of the wing, the angle of attack providing the required load factor cannot be determined directly, and has to be calculated iteratively. Once the load factor is matched, the structural stresses are stored and used to constrain the structural optimization process. After the latter has converged to the best structural weight W^*_{w2}, this value is compared with the wing structural weight W_{w1} estimated by `FAST-OAD`. If $W_{w1} \approx W^*_{w2}$, then the design is consistent and the sizing process is terminated. If $W_{w1} \neq W^*_{w2}$, a correction factor k_w is generated to make `FAST-OAD` size a new airplane with a different wing weight. This in general ends up with a different configuration W_g, and therefore a different wing-box, and different aeroelastic behaviour. The aeroelastic sizing and optimization on the new wing is repeated until a new W^*_{w2} is computed. The process is iterated until a consistent design is found with $W_{w1} \approx W^*_{w2}$. Once this is achieved, the dynamic aeroelastic behaviour of the candidate is investigated. At this point, the dynamic aeroelastic solvers are called to evaluate either the flutter speed, or the gust loads, or both. The outputs (V_f, $\sigma_{d,\max}$ and $\tau_{d,\max}$) are used as constraints for the overall MDAO. The process described this far is repeated for each design candidate corresponding to different values of the V_g vector.

The above workflow stands for the deterministic case. The robust case has the same structure, but the deterministic dynamic aeroelastic constraints are replaced by reliability constraints. In this case, illustrated in Figure 5.2, uncertainty is attributed for example to the elastic axis location a and to the center of gravity axis location d of the wing. Prescribed distributions $\hat{a}$ and $\hat{d}$ are given to the uncertainty quantification module, that propagates the uncertainty into the needed quantities of interest, producing the output distributions $\hat{V}_f$, $\hat{\sigma}_{d,\max}$ and $\hat{\tau}_{d,\max}$. At this point, the constraints are translated into probabilistic inequalities, requiring that the probability of failure is lower than a prescribed acceptable probability threshold.

This description only aimed at providing an overview of the framework and of the main ideas behind the developed approach. Further details are given in the following Sections. In particular, Section 5.2 describes in deep the sizing process for the flexible

wing, including quantitative example applications. Then, Section 5.3 describes how the dynamic aeroelastic constraints are defined and enforced, both for the deterministic and the probabilistic approaches. Quantitative examples are given as well, both for the flutter analysis and the dynamic gust loads evaluations. These include sensitivity analyses aimed at selecting what uncertainty parameters should be considered for the robust optimization problem.

The content of this Chapter covers in details the whole proposed framework architecture. Some example applications will be demonstrated later in Chapter 6

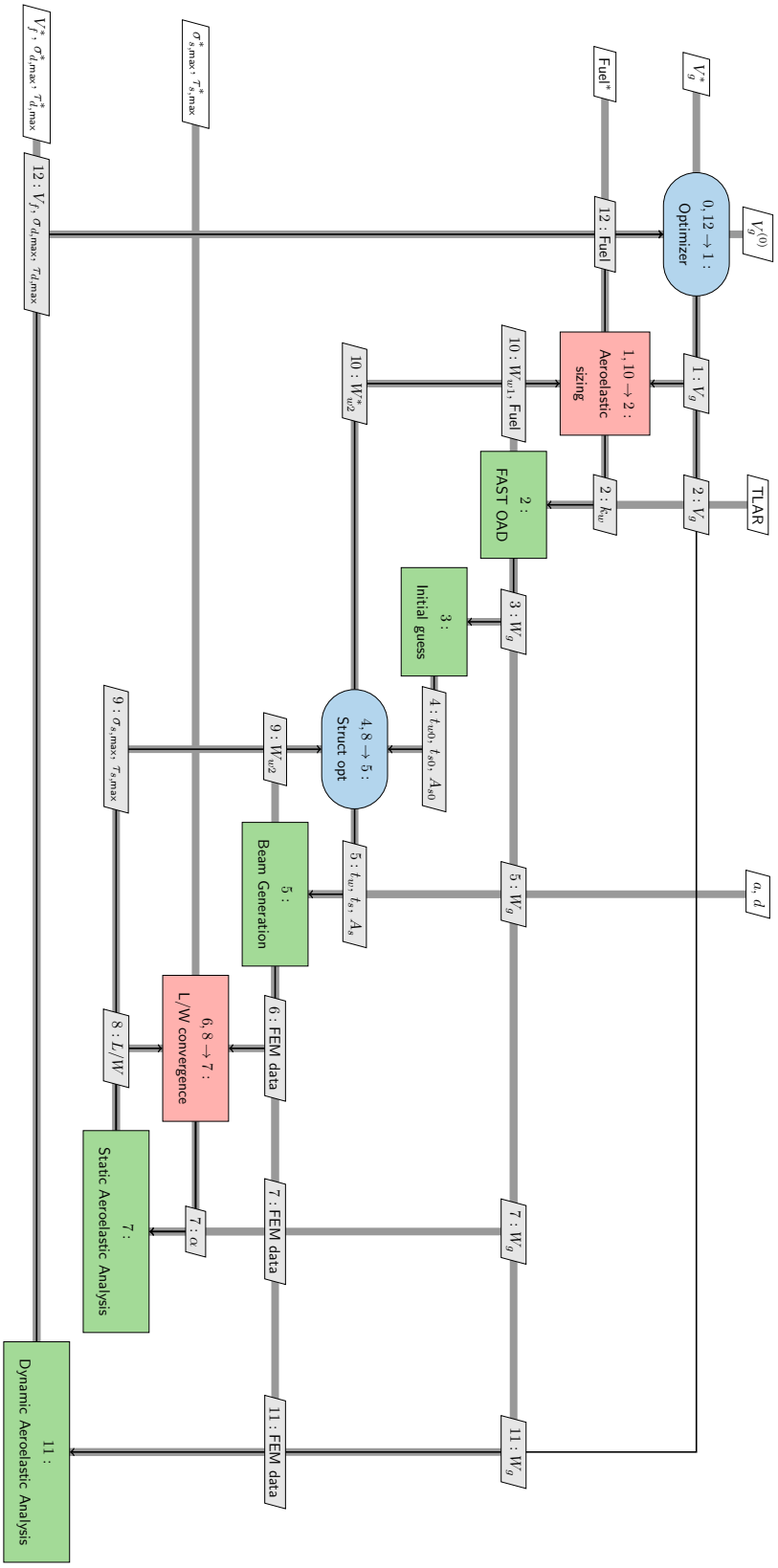

FIGURE 5.1: Extended design structure matrix of the present MDAO framework for aeroelastic sizing and fuel burn optimization of a transport aircraft. Deterministic approach.

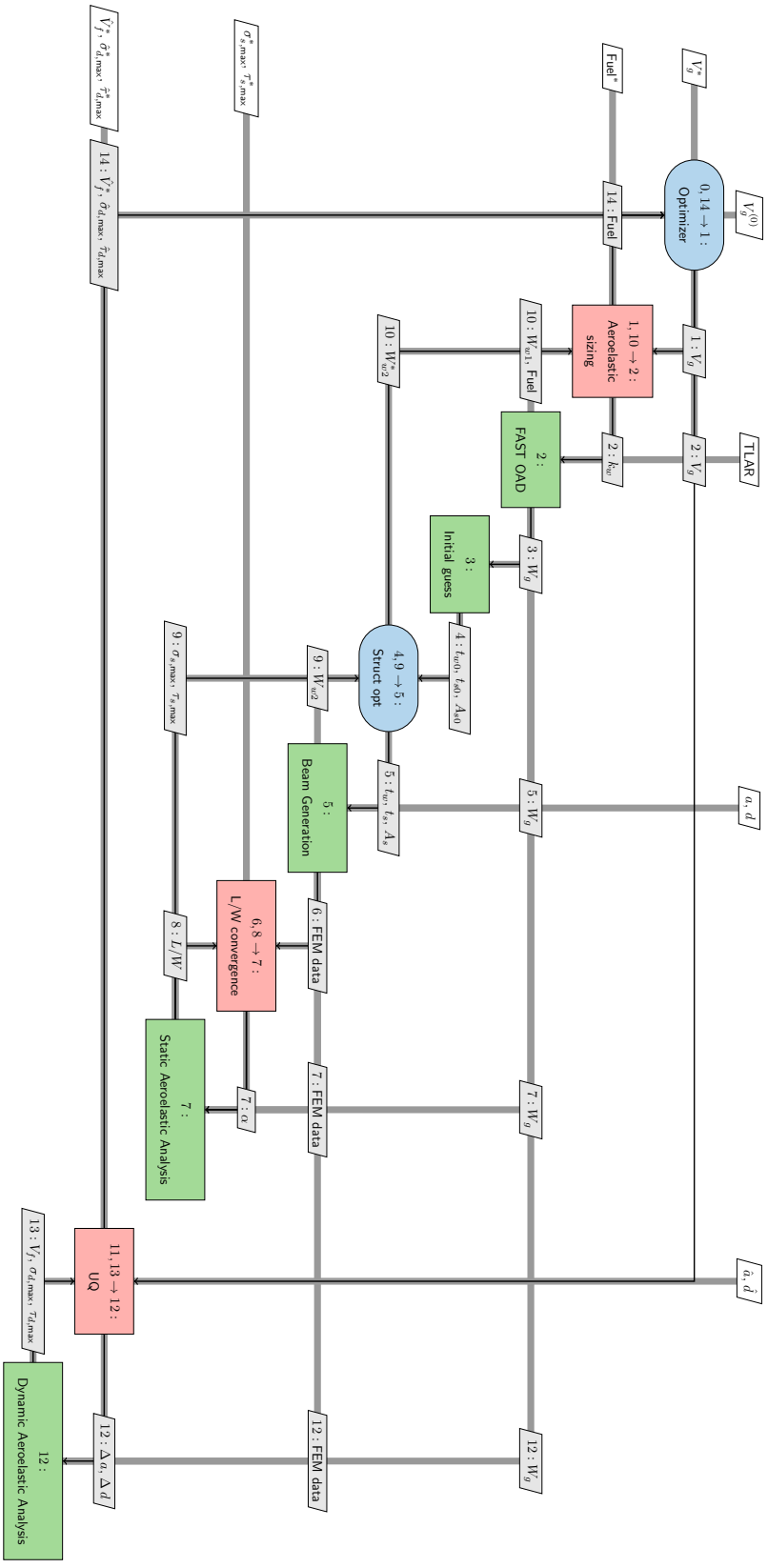

FIGURE 5.2: Extended design structure matrix of the present MDAO framework for aeroelastic sizing and fuel burn optimization of a transport aircraft. Probabilistic approach.

5.2 Flexible wing sizing

This Section describes in detail the structural sizing and optimization process for flexible wings and how this is merged with the overall aircraft sizing process. First, the approach for the initialization of the wing structure is introduced in Section 5.2.1. The outcome of this initial guess is a simplified three-dimensional wing-box structure. In order to enable the assessment of the aeroelastic performance of the resulting wing, the 3D wing-box model is first reduced into an equivalent beam model. This process is explained in Section 5.2.2. Once the aeroelastic model is ready, with both the beam model and the VLM aerodynamic model correctly generated and interfaced, the static aeroelastic analysis can be launched to finalize the wing structural sizing, now with taking into account the effects of flexibility. The numerical setup for this analysis and the definition of the sizing load case are detailed in Section 5.2.3. Once the static aeroelastic analysis for the wing structural sizing is clearly defined, Section 5.2.4 describes how the optimization process is put in place in order to produce the best structural layout, in terms of structural mass, that satisfies the imposed static safety requirements. Two sample optimization cases are also provided. Finally, Section 5.2.5 explains how the result of the wing structural optimization is combined with the overall aircraft sizing process, ensuring that the rest of the aircraft is consistently designed with respect to the optimal wing shape and weight.

5.2.1 Initial sizing of a wing-box structure

The overall aircraft design tool `FAST-OAD`, following a common conventional approach, was not designed to encapsulate stress analysis or aeroelastic analysis during the sizing loops. It rather relies on semi-empirical formulations that relate the wing weight to the main planform parameters. Therefore, it does not handle sufficient information about the structural layout to allow for these types of studies. This fact translated into a gap between the existing design process and the desired extension leveraging on the developed aeroelastic tools. For instance, the aeroelastic models in question need input quantities such as bending rigidity, torsional rigidity, moments of inertia, mass distribution, shear center location. This information is unnecessary, and therefore unavailable, within the `FAST-OAD` routines. The problem was then to fill this gap by somehow estimating the required data, starting from the available quantities. The issue was addressed by estimating a simplified wing-box structure, initially sized using simple analytical expressions for loads and stress calculation.

The use of wing-box models with simplified geometry and parameterization is a common approach in literature when addressing wing aeroelastic sizing and optimization (see for instance [8, 101]). Here follows a detailed description of the model adopted in this work.

The sizing process is adapted from [27]. Aeronautical aluminium properties, summarized in Table 5.1, are assigned to all components. The wing-box geometry is assumed having a rectangular cross section, composed by the three main functional elements: two (identical) spars carrying the shear loads, the skin absorbing the twisting loads and a set of stringers resisting bending loads. A schematic representation is given in Figure 5.3. It can be noted that the adopted cross section idealization lays somewhere between the one of [27] (reported in Figure 5.5) and the one of [8] (see Figure 5.4). In addition, ribs are also considered, but only for mass estimation, based on data from the same category of aircraft, and they do not share any load. The breakdown into the three main functional elements means that the three different kind of loads - vertical shear, torsional shear and bending stress - are totally assigned to the corresponding structural components: the spars are sized to sustain the total vertical force, the skin to carry the total twisting moment, the stringers to withstand the total bending moment. This separation allows the structure to be quickly sized analytically. A three-dimensional representation of such a structural idealization is given in Figure 5.6, borrowed from [27], which highlights the described loads breakdown. As far as the two-dimensional cross-section is concerned, the outer rectangle dimensions are fixed by three outputs from `FAST-OAD`: the two chordwise locations of the front and rear spars, and the average thickness ratio of the aerodynamic profile. The resulting wing-box planform is represented in Figure 5.7, which refers to the CeRAS baseline wing planform. As the rectangular cross-section is assumed to be perfectly symmetrical, its shear center is considered located at the rectangle's centroid, and therefore the elastic axis is located exactly in the middle of the two spar lines.

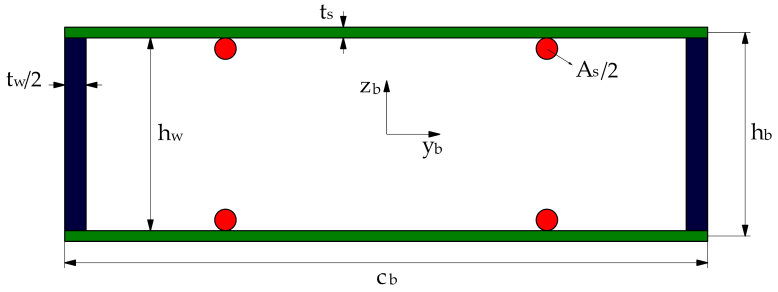

FIGURE 5.3: Cross section idealization adopted in this work.

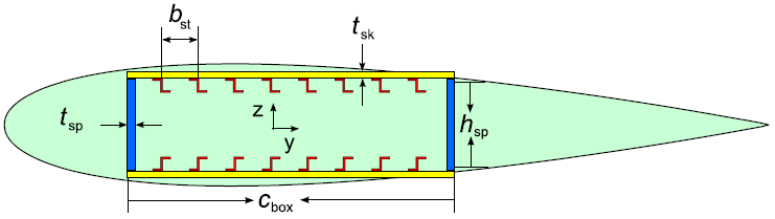

FIGURE 5.4: Cross section idealization used in [8].

Once the cross-section perimeter is fixed, its layout can be completely defined by the three additional parameters t_s, t_w, A_s indicating, respectively, the skin thickness, the

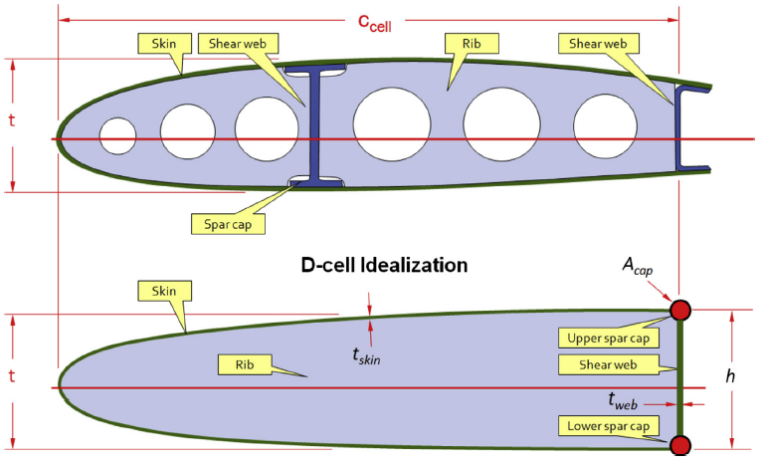

FIGURE 5.5: Cross section idealization used in [27].

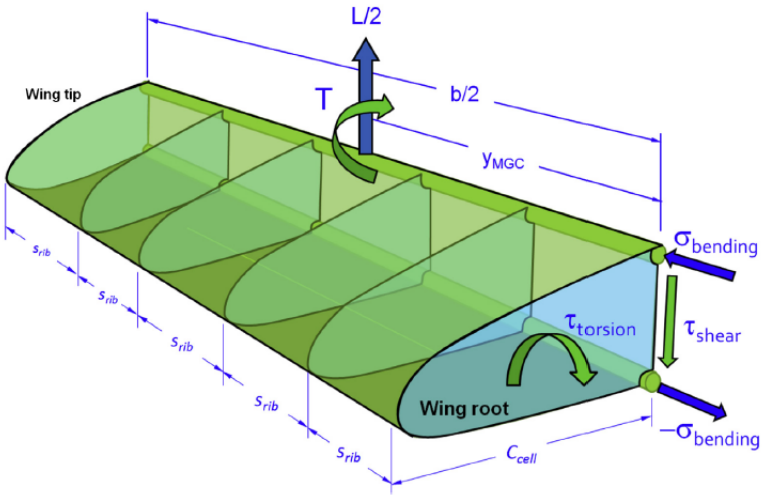

FIGURE 5.6: Wing primary structure idealization and loads partitioning, as proposed in [27].

total web thickness (twice the thickness of one spar) and the stringers cross section, as indicated in Figure 5.3. The stringers are considered equally distributed in the lower and upper surface and chord-wise, and they are regarded as longitudinal rods located along the skin, supposed to react the direct stress needed to counteract bending. Therefore, the only parameter that needs to be sized is their total area. Their actual number and shape are not relevant at this scale. The parameter A_s refers to the sum of all cross section areas of the stringers located on the upper (or lower) surface, so that the total available area equals $2\,A_s$. We found that this functional partitioning approach is more conservative than evaluating an equivalent Von Mises stress at the most stressed point of the cross section, and, despite approximated, it matches satisfactorily with the semi-empirical correlations used in `FAST-OAD`, as it will be shown later. Therefore, it was chosen to keep this idealization not only for the initial guess of the three variables, but also during the wing mass optimization iterations.

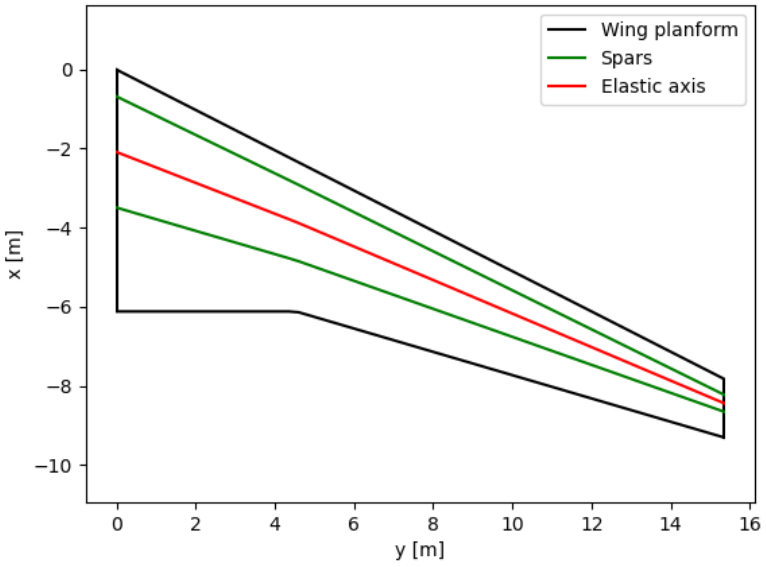

FIGURE 5.7: Spars and elastic axis location on the baseline wing planform.

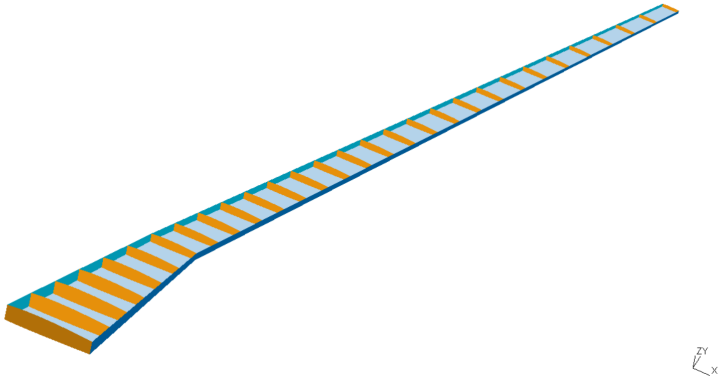

FIGURE 5.8: View of the 3D wing-box idealization adopted in this work. The particular example is from a kinked $\mathcal{AR}$ 15 wing configuration.

Property	Symbol	Unit	Value
Density	ρ_m	kg/m^3	2900
Young's modulus	E	GPa	68.9
Shear modulus	G	GPa	24.0
Yield strength	σ_m	MPa	276
Shear strength	τ_m	MPa	207

TABLE 5.1: Material properties for the wing-box components. Values typical of aeronautical aluminium alloy.

The span-wise parameterization is again kept simple, following [27]: the three variables t_s, t_w, A_s are linearly scaled from root in order to reach the minimum technologically feasible values at the wing tip. In this way, the structural optimization problem is reduced to three dimensions, corresponding to the three cross section parameters at the wing root, which is assumed to be the most solicited section. A view of the adopted

wing-box idealization is given in Figure 5.8.

It should be noted that only the three main structural responses above are taken into account for sizing the structure and for constraining the optimization by comparison with the material allowable stress. Other types of failure, such as stringer buckling, panel compression and shear buckling, stringer-panel buckling or crippling are not considered here. Instead, secondary failure modes are considered prevented by summing to the primary structure mass an additional weight fraction, estimated by `FAST-OAD`, accounting for appropriate reinforcements and other secondary masses. The main reason for this simplifying choice is that the increased level of detail would require several additional optimization variables, such as stringers' shape, stringers' spacing, ribs number, ribs spacing. This would turn into a much higher computational cost, and a level of detail more appropriate to preliminary than conceptual design. As the present approach is already conservative, the added cost of the extended design space would be of marginal use, and would add unnecessary complexity with respect to this first, demonstrative application to robust aeroelastic MDAO. Also, the introduction of one or more additional structural variables and constraints represents a fairly simple modification to the code architecture, and would not bring any substantial change in the philosophy of the approach. Moreover, it should be noted that the main focus here is the wing structural weight, because of its impact on the mission fuel burn. In this perspective, it is assumed here that the additional constraints would mainly impact the structural layout, in terms of ribs ans stringers distribution, with little influence on the overall wing mass. Finally, as it will be shown later, some effects linked to fluctuations in the nominal section properties, due to the remaining uncertainty on the structural configuration, are still accounted for, at least in the evaluation of the aeroelastic reliability constraints. For these reasons, the implementation of additional structural constraints is left to future developments - which should be eased by the modularity of the proposed framework - and is not included in the present work.

The initial sizing and weight estimation of the wing-box is achieved by four separate steps, corresponding to skin, web, stringers and ribs sizing. Loads are estimated based on a limit load factor $n_L = L/W = 2.5$. Neglecting the contributions of fuselage and horizontal tail, all the lift is supposed to be carried by the wing, and considered acting at the 25% of the mean aerodynamic chord (see again Figure 5.6). Reference [27] evaluates its length and location by finding the mean geometric chord of a straight-tapered unswept wing. Here, as the wing is in general swept and kinked, these quantities are directly available among the wing parameters W_g from `FAST-OAD`, where they are computed with the appropriate relationships. The overall force and moments are applied to the wing root section, supposed to be the most loaded one, and once its parameters are sized, they are scaled linearly along the span to reach their minimum technological limit at the wing tip. The analytical procedure is outlined in Appendix C.

5.2.2 Beam model generation for aeroelastic analysis

So far, the process of overall aircraft sizing and wing-box initial sizing have been detailed. But a wing-box model, albeit simplified, still demands a relatively high computational cost if some aero-structural analysis is to be carried out for conceptual design purposes. This can become especially prohibitive in the present case, where not only multiple optimization and sizing loops are required, but also dynamic analysis and uncertainty quantification are to be performed. Therefore, one further simplifying step is taken here, which is the reduction of the generated wing-box model into an equivalent, three-dimensional beam model. To give an overview of such a model, it is worth recalling the main underlying assumptions, already discussed in Section 5.2.1:

- The same homogeneous, isotropic aluminium is adopted for all the components;
- Linear elastic behaviour of the material is assumed;
- The wing-box has a regular rectangular cross section with two axes of symmetry;
- The wing-box is the only structural part of the wing to play an active role: no loads or inertia are transferred to or from other parts of the wing;
- The structure is slender, so that vertical and horizontal shear deformations are negligible with respect to the effect of rotation;
- All cross sections rotate and translate rigidly.

These assumptions allow stating the following:

- Only one elastic modulus E and one shear modulus G are needed, and they are set equal to the standard values available for aeronautical aluminium, reported in Table 5.1;
- The shear center of each cross section is located at the centroid of the wing-box rectangle;
- The center of gravity of each cross section with and without fuel is located at the centroid of the wing-box rectangle;
- Only three main sectional moments of inertia need to be calculated, the products of inertia being zero due to the section symmetry;
- Only the wing-box geometry is needed to completely define the elastic and inertial properties of the equivalent beam;
- The equivalent beam can be conveniently placed along the locus of all centroids of the wing-box.

With these considerations in mind, it is possible to derive all the needed parameters to define the beam model. As discussed in Section 3.3.2, this requires to define one flexibility matrix $\boldsymbol{S}$ and one mass matrix $\boldsymbol{M}$ for each beam element. By enforcing the above assumptions, the former shall have the following form:

$$\boldsymbol{S} = \begin{bmatrix} \frac{1}{EA} & 0 & 0 & 0 & 0 & 0 \\ 0 & \frac{1}{GK_{xy}} & 0 & 0 & 0 & 0 \\ 0 & 0 & \frac{1}{GK_{xz}} & 0 & 0 & 0 \\ 0 & 0 & 0 & \frac{1}{GJ} & 0 & 0 \\ 0 & 0 & 0 & 0 & \frac{1}{EI^{\mathrm{A}}_{yy}} & 0 \\ 0 & 0 & 0 & 0 & 0 & \frac{1}{EI^{\mathrm{A}}_{zz}} \end{bmatrix} \tag{5.1}$$

Here, EA is the cross-section axial rigidity, with A denoting the cross-section area, and GK_{xy} and GK_{xz} are the shearing rigidity in the horizontal and vertical planes. Note that the assumption of negligible vertical and horizontal shear deformation is enforced by considering infinite shearing rigidity ($1/GK_{xy} = 1/GK_{xz} = 0$), so K_{xy} and K_{xz} do not need to be computed. GJ is the torsional rigidity, with J being the cross-section torsion constant. I^{A}_{yy} and I^{A}_{zz} are the two section area moments of inertia, and their product with the Young's modulus E gives the bending rigidity around the structural y_s and z_s axes. Note that all quantities are here referred to the local right-handed cross-sectional reference frame, with x_s denoting the normal direction, and y_s and z_s indicating respectively the horizontal and vertical Cartesian coordinates.

Within the same reference frame, the local mass matrix is as follows:

$$\boldsymbol{M} = \begin{bmatrix} \mu & 0 & 0 & 0 & \mu\, z_{\mathrm{CG}} & -\mu\, y_{\mathrm{CG}} \\ 0 & \mu & 0 & -\mu\, z_{\mathrm{CG}} & 0 & 0 \\ 0 & 0 & \mu & \mu\, y_{\mathrm{CG}} & 0 & 0 \\ 0 & -\mu\, z_{\mathrm{CG}} & \mu\, y_{\mathrm{CG}} & I_p & 0 & 0 \\ \mu\, z_{\mathrm{CG}} & 0 & 0 & 0 & I_{yy} & 0 \\ -\mu\, y_{\mathrm{CG}} & 0 & 0 & 0 & 0 & I_{zz} \end{bmatrix} \tag{5.2}$$

The local mass per unit length is here denoted by μ, and is given by the product of the material density ρ_m by the cross-sectional area A. The shift of the local center of gravity from the beam axis is indicated by y_{CG} and z_{CG}. Evidently, if the two quantities are not equally zero, the structure would feature inertial coupling in bending and torsion dynamics. According to what stated above, in the present nominal configuration the mass center, the shear center and the beam axis are all coincident, located at the centroid of the wing-box cross-section, and therefore y_{CG} and z_{CG} are set equal to zero. The effect of uncertainty on this assumption, and more precisely the effect of $y_{\mathrm{CG}} \neq 0$, is investigated and discussed in Section 5.3, and a robust MDAO approach where the

impact of this uncertainty is taken into account is described in Section 6.4. The terms I_{yy}, I_{zz} and I_p denote the two mass moments of inertia and the polar moment of inertia, respectively.

According to the assumed wing-box geometry and to the associated material properties, the structural parameters needed in Equations (5.1) and(5.2) are calculated as follows.

The cross-sectional area A is simply given by summing the area of all the wing-box components. With reference to the wing-box parameters illustrated in Figure 5.3, that gives:

$$A = c_b\,(h_w + 2\,t_s) - h_w\,(c_b - t_w) + 2\,A_s \tag{5.3}$$

The torsion constant J required in Equation (5.1) must be derived from the part of the structure that actually reacts torsion. Therefore, it only depends on the rectangle walls composed by skin and spars, and no contribution arises from the stringers. The torsion constant of a rectangular thin-walled cross-section does not have an analytically exact expression, which is only available for circular shapes. Any other shape would undergo a certain amount of warping, that prevents the derivation of simple analytical expressions and requires numerical methods for precise calculations. With the approximation of thin walls and constant shear flow across the thickness of shell and spars, the torsion constant can be expressed as:

$$J = \frac{4\,\Omega_{wb}^2}{\oint \frac{ds}{t}} \tag{5.4}$$

where ds represents an increment of curvilinear coordinate defining the thin wall perimeter, and t is the local thickness. Applied to the present rectangular cross-section, Equation (5.4) gives:

$$J = \frac{t_s\,t_w\,h_b^2\,(c_b - t_w/2)^2}{c_b\,t_s + h_b\,t_w/2 - t_s^2 - t_w^2/4} \tag{5.5}$$

Considering that the stringers have the overall arms of $h_w/2$ and $c_b/4$ with respect to the symmetry axes, the two area moments of inertia of the wing-box cross section are given by:

$$I_{yy}^b = \frac{1}{12}\left[c_b\,(h_w + 2\,t_s)^3 - (c_b - 2\,t_s)\,h_w^3\right] + A_s\,(h_w/2)^2 \tag{5.6}$$

$$I_{zz}^b = \frac{1}{12}\left[(2\,t_s + h_w)\,c_b^3 - h_w\,(c_b - 2\,t_s)^3\right] + A_s\,(c_b/4)^2 \tag{5.7}$$

The wing-box polar moment of inertia is simply obtained by:

$$I_p^b = I_{yy}^b + I_{zz}^b \tag{5.8}$$

To give an idea of how the computed beam properties would be distributed along the wing, the stiffness distributions calculated for the CeRAS baseline wing are plotted in Figure 5.9. Also, in confirmation of the correctness of the presented approach, the bending stiffness distributions were derived for an aspect ratio 18 wing, and compared to those reported from [8] for a very similar configuration. The curves are shown in Figure 5.10. As neither the aircraft configuration, nor the models employed are exactly the same, there is no expectation of a perfect match, and therefore the comparison is intended only to be qualitative.

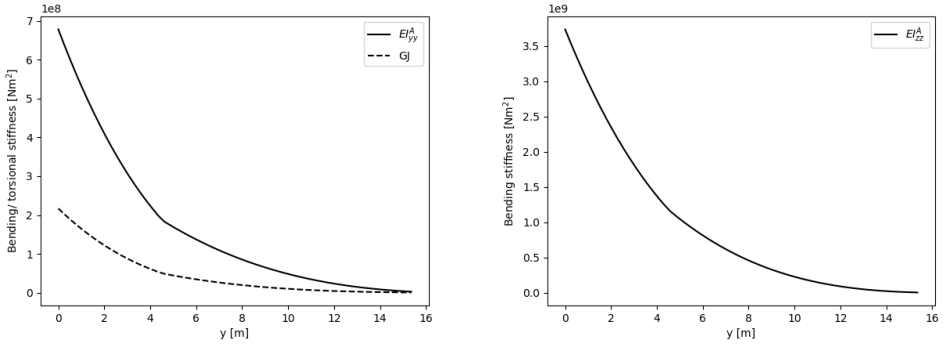

(a) (b)

FIGURE 5.9: Span-wise distributions of the beam stiffness properties derived for the CeRAS baseline wing. The out-of-plane bending stiffness EI_{yy}^{A} and torsional stiffness GJ are plotted in (a), whereas the in-plane bending stiffness EI_{zz}^{A} is shown in (b).

As far as mass properties are concerned, it should be noted that these vary according to whether fuel is included or not. The empty weight configuration would only be characterized by the wing-box parameters above. On the other hand, the heavy configuration should include the additional inertia of the fuel. In this case, the fuel contributions are:

$$\mu_f = \rho_f \left(c_b - t_w\right) h_w \tag{5.9}$$

$$I_{yy}^f = \rho_f \frac{\left(c_b - t_w\right) h_w^3}{12} \tag{5.10}$$

$$I_{zz}^f = \rho_f \frac{\left(c_b - t_w\right)^3 h_w}{12} \tag{5.11}$$

$$I_p^f = \rho_f \left(I_{yy}^f \; I_{zz}^f\right) \tag{5.12}$$

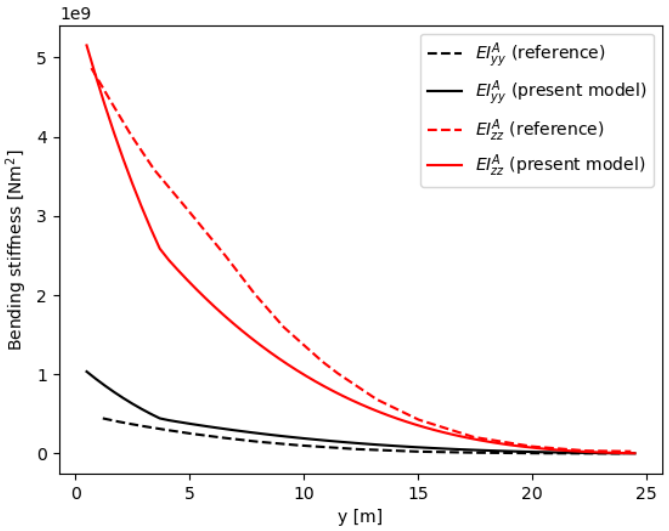

FIGURE 5.10: Verification of the computed span-wise distributions of the out-of-plane and in-plane bending stiffness (EI^{A}_{yy} and EI^{A}_{zz}, respectively) for an $\mathcal{AR}$ -18 wing. The comparison is against data from [8].

Therefore, for the empty weight configuration, the parameters needed by the mass matrix of Equation (5.2) would be:

$$\mu = \rho_m A \tag{5.13}$$
$$I_{yy} = I^b_{yy} \tag{5.14}$$
$$I_{zz} = I^b_{zz} \tag{5.15}$$
$$I_p = I^b_p \tag{5.16}$$

Whereas, for the heavy configuration:

$$\mu = \rho_m A + \mu_f \tag{5.17}$$
$$I_{yy} = I^b_{yy} + I^f_{yy} \tag{5.18}$$
$$I_{zz} = I^b_{zz} + I^f_{zz} \tag{5.19}$$
$$I_p = I^b_p + I^f_p \tag{5.20}$$

All of the above quantities are calculated at each beam node location, according to the local wing-box dimensions. The `GEBT` structural module assumes a linear variation of those nodal values along each beam element.

Once all the wing-box properties are defined, the primary structure mass is estimated by simply summing the mass of each structural element:

$$W'_{w2} = \sum_{i=1}^{N_{el}} 0.5 \left(\mu^{(i)} + \mu^{(i+1)}\right) l_e \tag{5.21}$$

where N_{el} is the number of beam elements, $\mu^{(i)}$ is the cross-section mass per unit length at the i-th node, and l_e is the element length. Note that W'_{w2} is the primary structure mass as calculated from the FEM model, in contrast with W'_{w1}, which is the `FAST-OAD` estimation for the same quantity.

With all the structural and geometrical properties defined, the model is ready for the needed aeroelastic studies. A graphical representation of what such a model looks like is given in Figure 5.11, showing some details of the aerodynamic and structural discretizations, as well as the resulting aerodynamic loads distribution on the deformed wing.

5.2.3 Sizing load case definition

Once the aeroelastic model is completely defined, the sizing process for the elastic wing can be addressed. Wings must generally be sized in order to withstand manoeuvre loads and gust loads. Manoeuvre loads are treated as steady loads, so that a few static load conditions are selected and applied to the wing. In a preliminary design context, this translates into the selection of one positive and one negative load factor, and several flow conditions determined by the different flight altitudes. Here, in the context of conceptual design, although 'enriched', the static load case scenario is restricted to a single condition. This is defined by a limit load factor of 2.5, and a flight speed corresponding to the dive speed referred to sea-level (EAS). As regulations specify that "the structure must be able to support limit loads without detrimental permanent deformation" [210], the sizing process here has to insure that the material yield strength is not exceeded at the prescribed load case. It is important to underline that this condition is here verified only at the wing root, which is assumed to be the most solicited section.

A few considerations are needed to understand how the aeroelastic analysis is carried out to get the loads at the required load factor. It is clear that at any fixed dynamic pressure, the loads acting on a flexible wing, unlike a rigid wing, depend non-linearly on the reference angle of attack. In fact, different increments of the angle of attack generate increments of loads that are not proportional, because larger non-linear local deformations have to be superimposed to the nominal angle of attack. Therefore, to get the desired load factor, the correct angle of attack must be found iteratively. However, a complex non-linear behaviour is excluded, because there are no expected sources of discontinuities or drastic changes - such as stall, shock waves, buckling - within the flow conditions and angles of attack expected in the simulations. The only possible mechanism of marked non-linearity would be aeroelastic divergence, and in that case

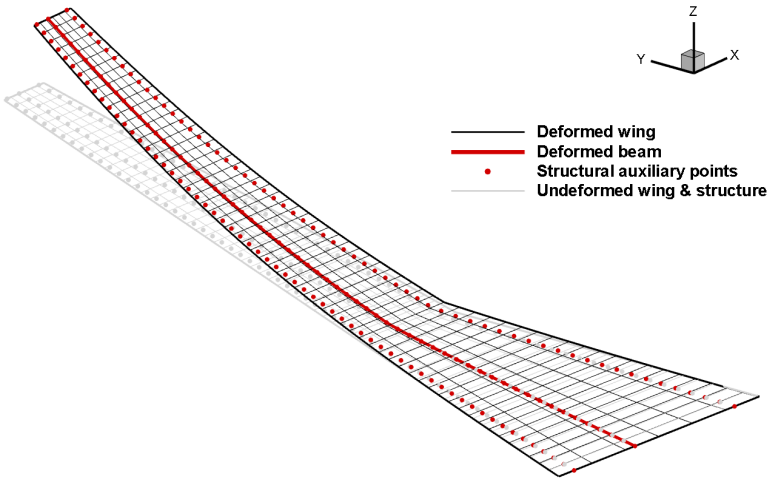

(a) Details of the aerodynamic and structural discretizations

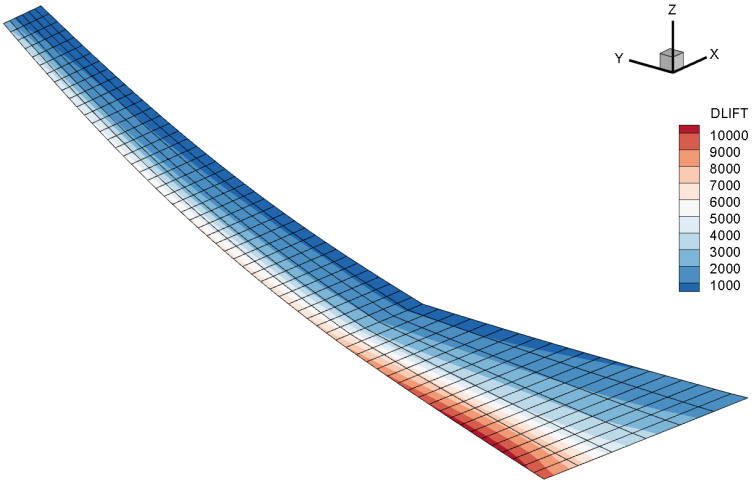

(b) Contour plot for the lift distribution

FIGURE 5.11: 3D views of the aeroelastic model employed, showing both the VLM discretization and the beam model, including the auxiliary structural points needed for the fluid-structure interpolation.

there is no reason to search for a sizing point: the candidate structure is not adequately strong, and it shall be discarded for the next one to be analyzed.

For these reasons, a couple of first-order methods were implemented and tested to find the correct angle of attack producing the required load factor: the *classic chord* and the *regula falsi* methods [28, 211] (see Appendix D). While the former occasionally did not converge due to subsequent iterations too close to each other, the latter was found to behave remarkably well: most cases converge to the prescribed load factor, with an error of less than 1%, in three or four iterations, which is practically the minimum number attainable for the numerical solution of non-linear equations. Other methods, such as the common second-order *Newton-Raphson* method were not considered, first

because of the satisfactory performance of the *regula falsi* method, second because they would require the computation of derivatives.

5.2.4 Static structural optimization of flexible wings

As introduced at the beginning of this Section, a simplified approach is proposed in this work to address the sizing of a flexible wing structure, which is a necessary step in order to be able to investigate some relevant aeroelastic performance of the aircraft design candidate. The objective function to minimize here is the mass of the wing-box structure W'_{w2}, also referred to as the primary structure, which does not include reinforcements or secondary parts. The strategy adopted is to start with an initial guess of the structural layout, already discussed in Section 5.2.1, and then to run an optimization to minimize the structural weight within a design space surrounding the initial guess configuration. This is intended to reduce the search space and therefore speed-up the convergence. In fact, it is expected that high aspect ratio wings require a stronger structure compared to low aspect ratio ones, and therefore it is detrimental to use a unique, wide design space in the two situations.

Consistently with the above initial guess approach, the optimization cost is kept as low as possible by relying only on the three variables t_s, t_w and A_s already defined, referring to the root section of the wing-box (see again Figure 5.3). Again, to eliminate possible additional variables, the lower technological bounds of these three parameters are assigned to the wing tip, and a linear decrease is assumed to define their distribution along the span. Such an hypothesis is believed to be conservative, as in other, more detailed studies on similar aircraft (as in [212]) the slope of this decrease is allowed to change in order to reach the minimum parameters' bounds before the wing tip, with the effect to further decrease weight. In other cases (such as in [8]) the wing-box parameters at multiple stations are even treated as independent variables. These approaches are powerful and effective for a single wing optimization case, but would require prohibitive costs for the purpose of this work, where many optimization cases are to be addressed. In line with the choice of the three optimization variables, the only constraints employed are the bending and shear stresses at root. Monitoring many stress values all over the beam as additional constraints would represent an increased burden for the structural optimizer, and it is not considered an essential task at this stage. A more detailed optimization approach and a comparison of the computational costs may be the object of future studies.

In the present case, three root loads are considered to constrain the optimization: the torsion shear on the skin τ_t, the vertical shear on the webs τ_v and the bending stress on the stringers σ_b. They are calculated by the expressions given in Sections C.1 to C.3, retaining the same underlying assumptions. The constraints provide that the material

shear strength τ_m is not exceeded in the skin and spars at root, and that the material yield strength σ_m is not exceeded in the stringers.

As mentioned above, the three-dimensional design space is adaptively bounded for each aircraft configuration depending on the pre-calculated initial guess $[t_{s0},\, t_{w0},\, A_{s0}]$. The upper bounds for all the three variables are set (arbitrarily) to 1.5 times the initial guess values. For the lower bounds, a factor of 0.5 is applied, but for the skin and web thicknesses a comparison with the corresponding minimum technological value is made, and the biggest is retained. The minimum skin thickness is set equal to 2.7 mm, a value commonly assumed for lightning strike requirements [212]. For the spars thickness, the minimum aluminum sheet thickness of 1.2 mm is selected [27]. No technological bounds are applied for the stringers' area.

The wing structural optimization problem is summarized in Table 5.2. An example of the sizing and optimization process is given in the following Section, where the wing of the CeRAS baseline configuration is adopted as a first test case, so that it will serve both to clarify and to validate the approach.

	Function/quantity	**Lower bound**	**Upper bound**
Minimize	Wing structural mass W'_{w2}		
with respect to	Root skin thickness t_s	$\max(0.5\, t_{s0},\, t_{s\mathrm{L}})$	$1.5\, t_{s0}$
	Root spar thickness t_w	$\max(0.5\, t_{w0},\, t_{w\mathrm{L}})$	$1.5\, t_{w0}$
	Root stringers area A_s	$0.5\, A_{s0}$	$1.5\, A_{s0}$
subject to	$\tau_t < \tau_m$	(material shear strength not exceeded)	
	$\tau_v < \tau_m$	(material shear strength not exceeded)	
	$\sigma_b < \sigma_m$	(material yield strength not exceeded)	

TABLE 5.2: Definition of the simplified structural optimization problem for the flexible wing.

5.2.4.1 Application and verification on the baseline test case

The results of a sample wing structural optimization case is here presented, applied on the CeRAS baseline configuration. The initial guess is obtained with the approach already discussed in Section 5.2.1.

The optimization process consists of a Design of Experiment (DOE) of 15 points, followed by 30 optimization iterations, for a total of 45 evaluations. As previously mentioned, the optimization is run through `SEGOMOE` using a GP with the WB2 acquisition function (see Section 2.5.2). The evolution of the best objective function over the optimization iterations is reported in Figure 5.12(a). The first 15 iterations are dedicated to exploration, and this is why the current best is initially quite far from the final one. The corresponding constraint and variable values are reported in Figures 5.12(b) and 5.13. Note that the current best only stores the best value in the optimization history

that complies with the constraints. It should also be noted that the initial guess configuration is added as the last point (15th) of the DOE, and it considerably contributes to reduce the current best and enables a quick convergence to the optimum, which in this case is quite close to it. This can be seen clearly from Figure 5.12(a), where the current best gets substantially close to the optimum, both in terms of objective and variables, right after the 15th iteration. This can also be seen from Figures 5.14(a) to 5.14(b). The first shows the objective function values of each iteration in chronological order. The other two, similarly, plot the evolution of the three constraints and the three variables, respectively. They show that, despite a certain exploration is still carried out, the best valid points are always close to the initial guess and the optimal, which is found very soon. Note that the constraints have been normalized with respect to the material limits according to the following expressions:

$$c(\sigma_b) = \frac{(\sigma_m - \sigma_b)}{\sigma_m} > 0 \tag{5.22}$$

$$c(\tau_t) = \frac{(\tau_m - \tau_t)}{\tau_m} > 0 \tag{5.23}$$

$$c(\tau_v) = \frac{(\tau_m - \tau_v)}{\tau_m} > 0 \tag{5.24}$$

It is interesting to point out here that despite the simplified and separated expressions for the loads on the three functional components of the wing box, the optimization task is not trivial: a violation of the bending stress, evaluated on stringers, does not necessarily translate into an increase of the stringers area variable A_s. In fact, any change of each design variable will affect all the section properties assigned to the equivalent beam. This means that, for example, an increase of the skin or web thickness will increase the area moment of inertia, the torsion constant, etc., resulting in a stiffer beam, less sensible to deformation-induced loads, possibly to the point that the bending loads on the stringers are no longer above the allowable ones. This could happen without any increase of the A_s variable. Therefore, different combinations of the three parameters can provide constraints compliance, and the non-trivial optimization task is to find the one that minimizes mass. This is exactly what happens in the present case: looking at Table 5.3, where the results are summarized, it can be seen that the optimal configuration is lighter and safer than the initial guess even though the stringers area A_s is actually reduced with respect to the initial guess. The best configuration turns out to correspond to one where sufficient strength is achieved by a slightly thicker skin, and a mass saving is obtained with thinner spars and stringers.

Another aspect that emerges from Figures 5.12(b) and 5.14(b) is that in this case the torsion constraint is always largely satisfied. This indicates that the lighting strike requirement, imposing a skin thickness no lower than 2.7 mm, is more stringent than the torsional strength constraint. This fact is here accepted as a confirmation that the

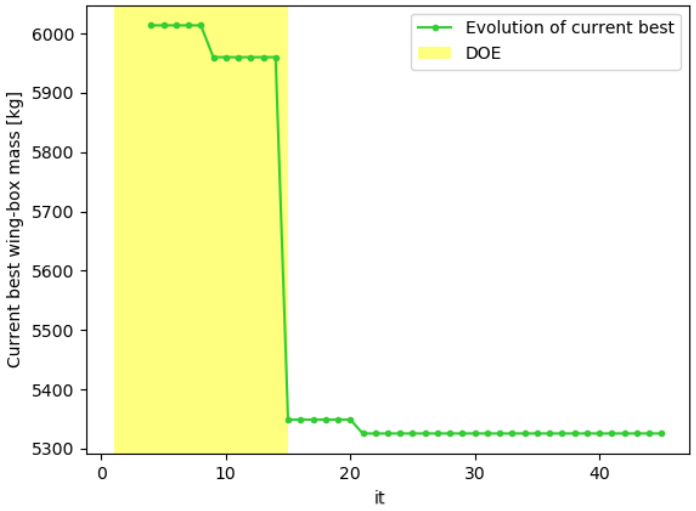

(a) Structural mass objective

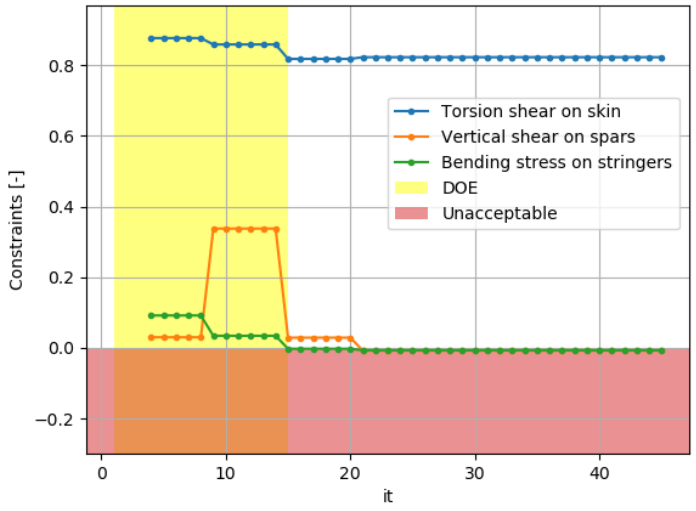

(b) Static loads constraints

FIGURE 5.12: Flexible wing structural optimization process under static loads constraints over the CeRAS baseline configuration. Evolution of the current best wing mass objective function (a) and the corresponding static loads constraints (b) through the `SEGOMOE` optimization iterations.

adopted approach is conservative. Although the case could be further optimized by allowing the skin to share part of the vertical or bending loads, permitting in turn the other parts to be lightened, this solution is undesirable because it could underestimate the overall mass. Therefore, the 'excessive' safety in torsion is retained here as a conservative solution, that provides margin against other constraints, such as buckling, which are ignored.

This choice is further sustained by the fact that the results obtained are satisfactorily

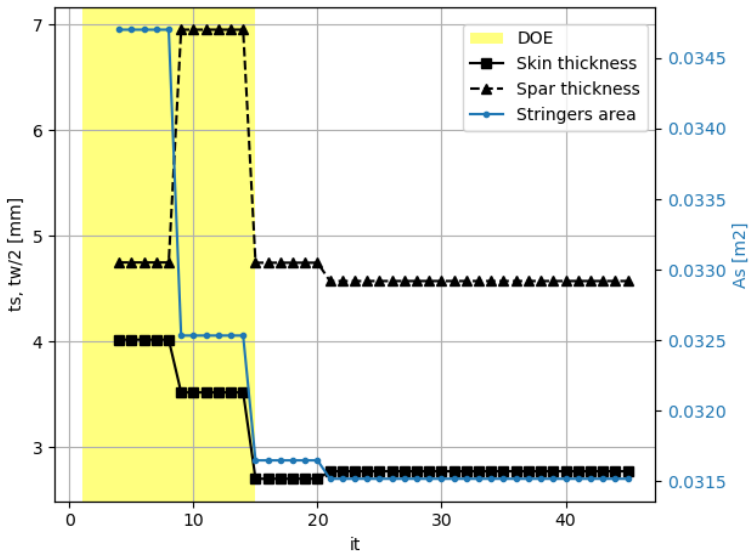

FIGURE 5.13: Flexible wing structural optimization process under static loads constraints over the CeRAS baseline configuration. Evolution of the current best variables through the SEGOMOE optimization iterations.

close to the data available from FAST-OAD, which can be considered, as far as the baseline is concerned, a reliable reference. For instance, the empty-weight wing mass of 8200 kg provided by the initial guess exceeds by less than 1% the value of 8120 kg of FAST-OAD. The mass predictions for the overall structure as well as its different components are detailed in Figure 5.16. Here, the mass fraction corresponding to stringers and spar caps, which mainly sustain bending loads, is labeled as 'bending' mass. The mass of skin and spars, whose main function is to react shearing loads, are not separated in FAST-OAD, so they are grouped in 'shear' mass. It is worth recalling that the difference between the total empty weight mass W_w and the primary structure mass W'_w, composed by the skin, spars, stringers and ribs, is the mass of landing gear reinforcements and secondary masses, which is set equal to the value given by FAST-OAD. It can be seen that a good match is achieved for all the sub-parts.

Configuration	t_s (mm)	t_w (mm)	A_s (m^2)	W'_w (kg)	W_w (kg)
Initial guess	2.7	9.5	0.0316	5,349	8,200
Optimal	2.8	9.1	0.0315	5,326	8,178
FAST-OAD	-	-	-	5,267	8,120

TABLE 5.3: Optimization results for the flexible wing structural optimization process over the CeRAS baseline configuration. The data for the initial guess structure, as well as from the corresponding rigid configuration sized by FAST-OAD are reported for comparison.

Given this already accurate initial estimation, the optimization barely influences the result, giving an optimum wing mass of 8178 kg, reducing the initial guess of only about 20 kg. Despite the contribution of the optimization looks here irrelevant, these results are indeed desired, because they confirm the consistency of both the initial guess

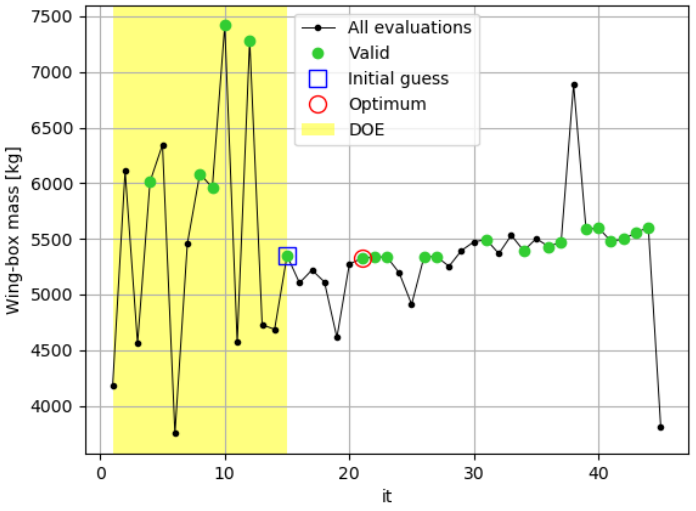

(a) Structural mass objective

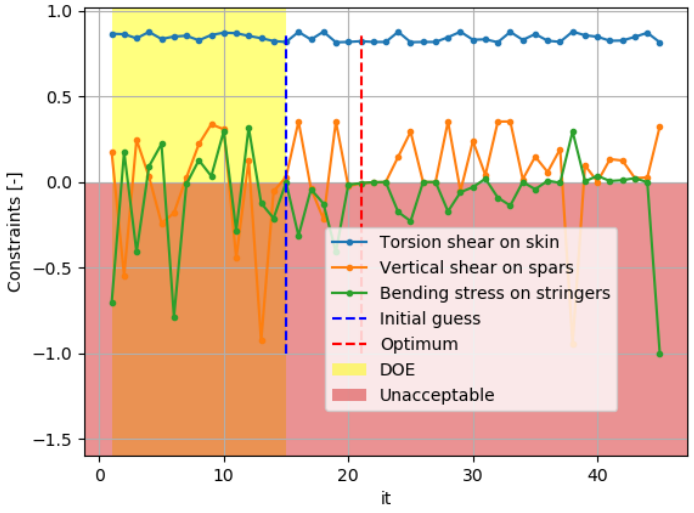

(b) Static loads constraints

FIGURE 5.14: Flexible wing structural optimization process under static loads constraints over the CeRAS baseline configuration. Monitor plot of the wing mass objective function (a) and the corresponding static loads constraint (b) through the SEGOMOE optimization iterations.

and the optimization approach with respect to known data (the baseline is expected to be quite an optimized configuration!). Also, it should be noted that the optimizer converges to a configuration that not only features a lower objective function, but that is also valid with respect to the structural constraints, while the initial guess is not.

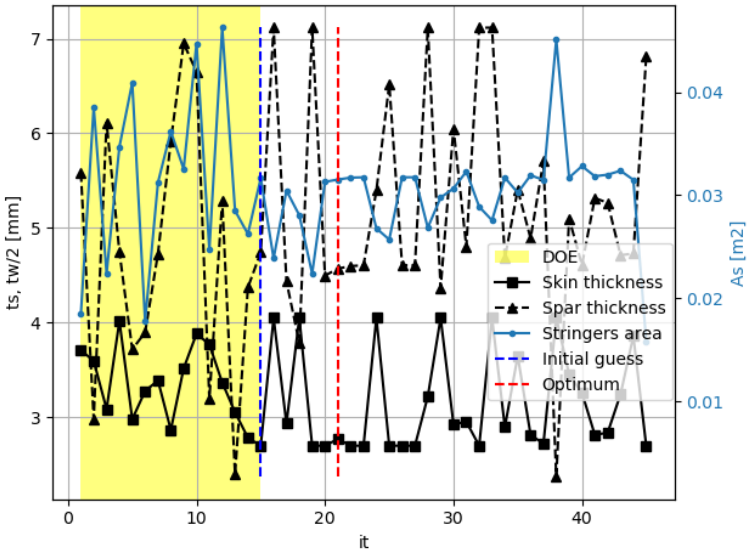

FIGURE 5.15: Flexible wing structural optimization process under static loads constraints over the CeRAS baseline configuration. Monitor plot of the design variables through the SEGOMOE optimization iterations.

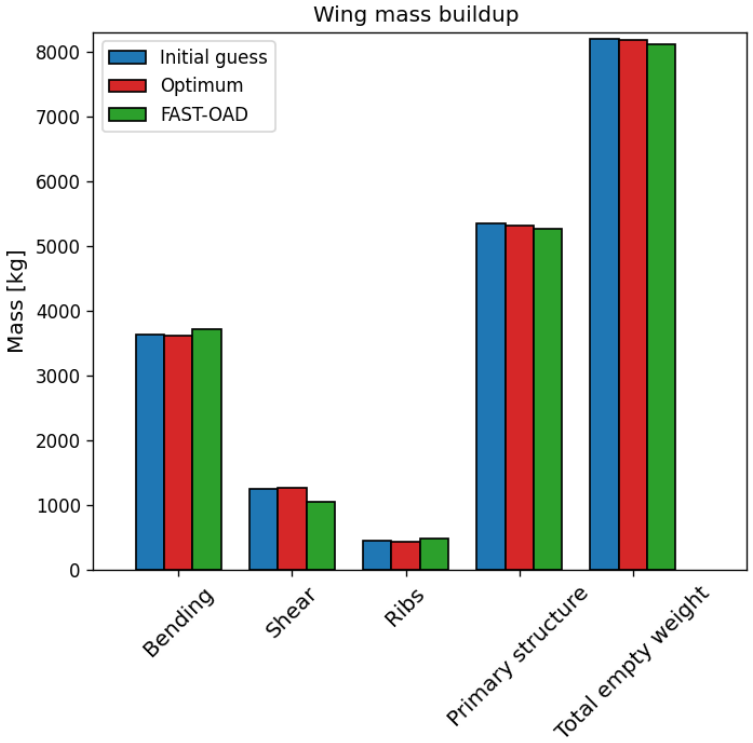

FIGURE 5.16: Wing structural mass buildup for the CeRAS baseline. Three sets of data are compared: the FEM data for the initial guess structural layout (blue), the FEM data for the optimal structural layout (red) and the estimation for the rigid aircraft by FAST-OAD (green).

5.2.4.2 Application on high aspect ratio wing

An analogous structural optimization task to the one of Section 5.2.4.1 is presented here, but applied on a wing of aspect ratio 15, quite higher than the 9.5 of the CeRAS baseline. Qualitatively, the same kind of plots and data are reported (Figures 5.17 to 5.20). Quantitatively, there are a few details worth to be noted.

First, the convergence to the optimum is slower (32 evaluations were needed instead of 21). One reason for that is that less points in the DOE comply with the constraints, including the initial guess, that this time violates the bending strength condition. It takes 17 iterations after the DOE for the optimizer to progressively converge to a candidate fulfilling all the conditions. This ends up with the selection of a heavier configuration compared to the initial guess, with the mass increase resulting from thicker skin and stringers (see Table 5.4).

Another interesting and reassuring aspect, emerging from Figure 5.21, is the remarkably accurate match between the initial guess and the `FAST-OAD` predictions, which further confirms the validity of the implemented initial guess approach.

Finally, and most importantly, this high-aspect-ratio example shows that, differently from the baseline case, the aeroelastic module is predicting an appreciable difference with respect to the conventional `FAST-OAD` approach, suggesting that the latter may not be totally accurate for flexible wings. In particular, the aeroelastic optimization gives a wing-box mass and a total empty-weight wing mass around 11% and 8% higher than the respective values from `FAST-OAD`. Therefore, the mismatch confirms that the conventional approach may underestimate the structural weight of high aspect ratio wings, confirming that the adoption of the proposed aeroelastic approach is a desirable enhancement. This conclusion was expected, because the semi-empirical relationships are fine-tuned on pretty rigid wings with $\mathcal{AR} \approx 10$, and therefore their validity and conservativeness were indeed questionable.

Configuration	t_s (mm)	t_w (mm)	A_s (m^2)	$W_w^{'}$ (kg)	W_w (kg)
Initial guess	2.7	10.7	0.0462	8,786	12,086
Optimal	2.9	10.4	0.0534	9,894	13,194
`FAST-OAD`	-	-	-	8,898	12,198

TABLE 5.4: Optimization results for the flexible wing structural optimization process over the $\mathcal{AR}$ 15 configuration. The data for the initial guess structure, as well as from the corresponding rigid configuration sized by `FAST-OAD`, are reported for comparison.

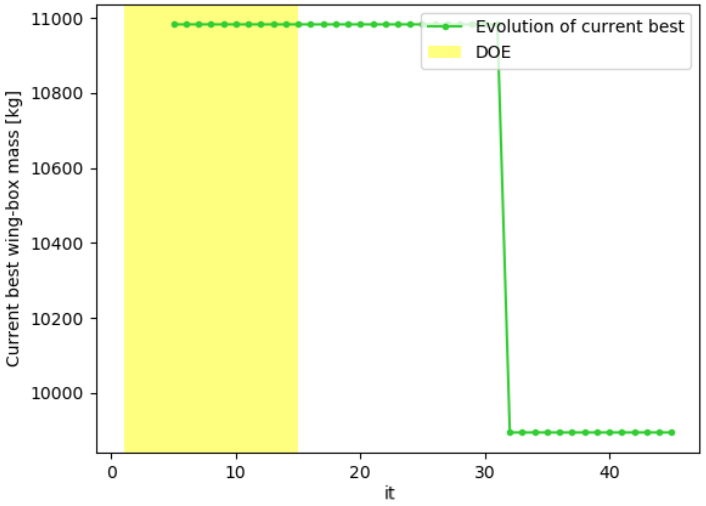

(a) Structural mass objective

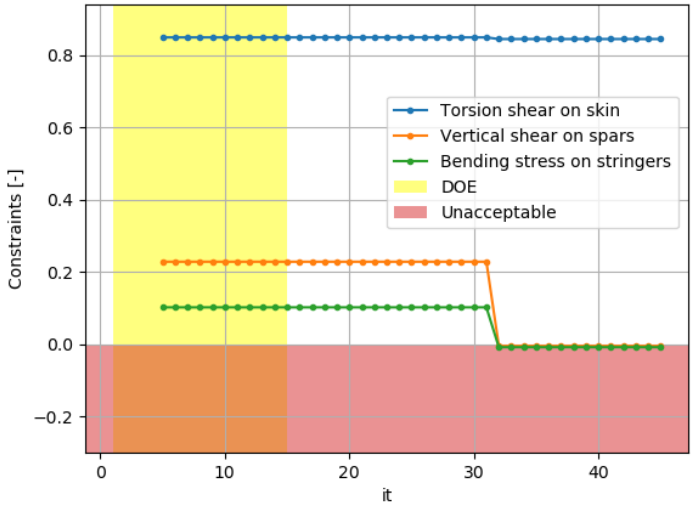

(b) Static loads constraints

FIGURE 5.17: Flexible wing structural optimization process under static loads constraints over the '$\mathcal{AR}$ 15' configuration. Evolution of the current best wing mass objective function (a) and the corresponding static loads constraints (b) through the SEGOMOE optimization iterations.

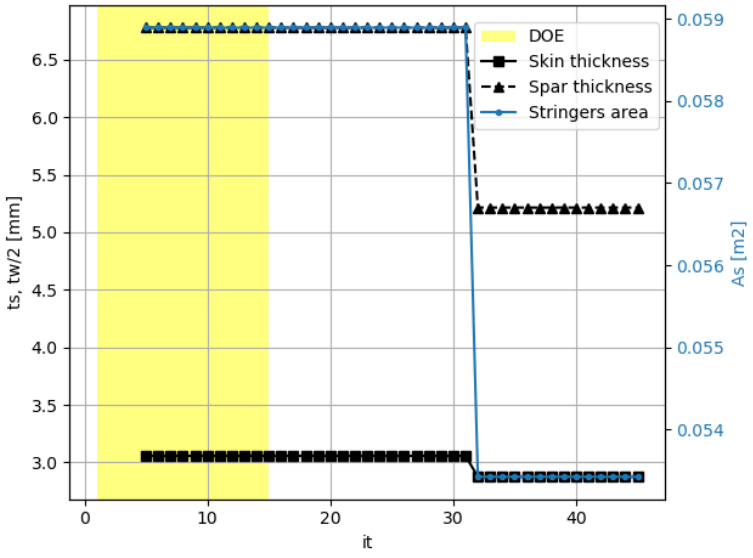

FIGURE 5.18: Flexible wing structural optimization process under static loads constraints over the $\mathcal{AR}$ 15 configuration. Evolution of the current best variables through the SEGOMOE optimization iterations.

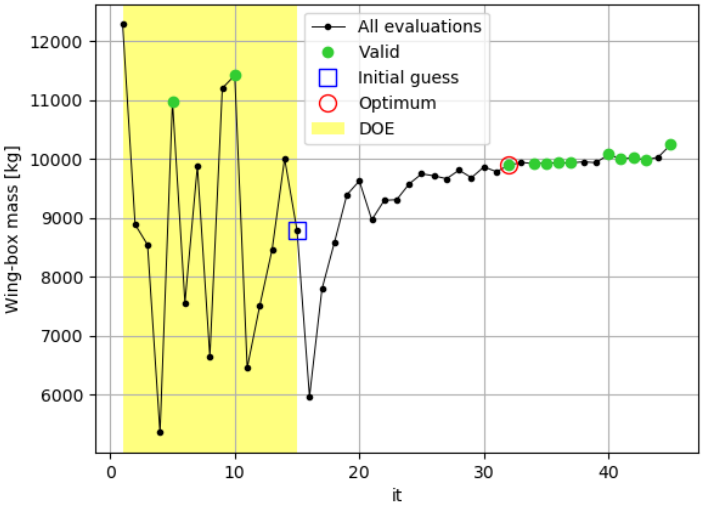

(a) Structural mass objective

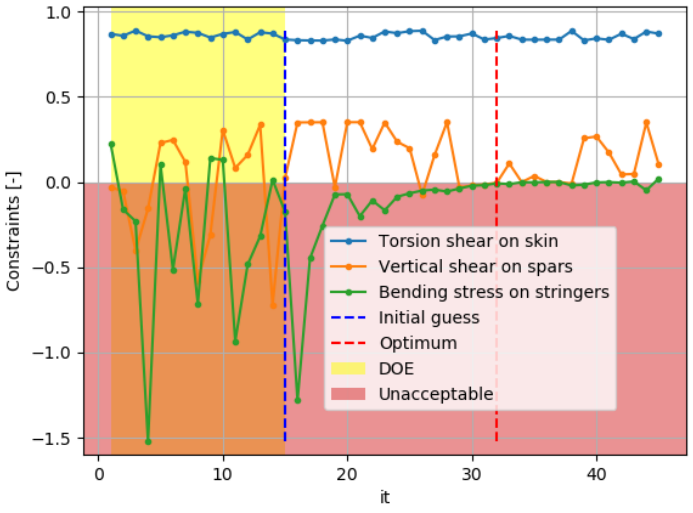

(b) Static loads constraints

FIGURE 5.19: Flexible wing structural optimization process under static loads constraints over the $\mathcal{AR}$ 15 configuration. Monitor plot of the wing mass objective function (a) and the corresponding static loads constraint (b) through the SEGOMOE optimization iterations.

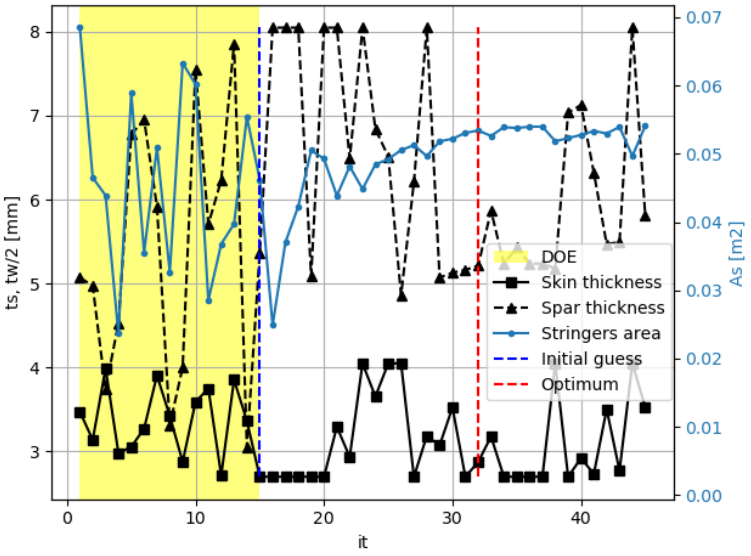

FIGURE 5.20: Flexible wing structural optimization process under static loads constraints over the $\mathcal{AR}$ 15 configuration. Monitor plot of the design variables through the SEGOMOE optimization iterations.

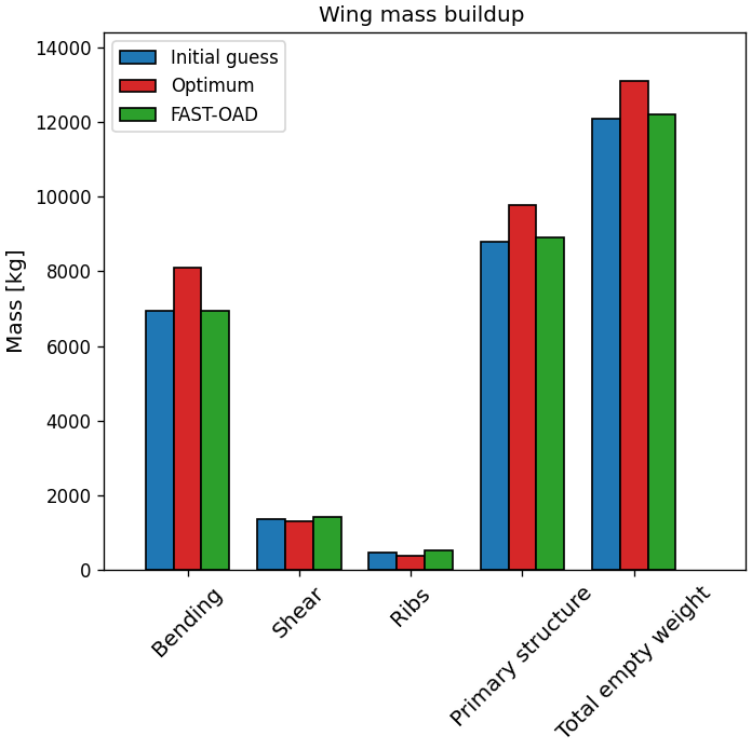

FIGURE 5.21: Wing structural mass buildup for the $\mathcal{AR}$ 15 configuration. Three sets of data are compared: the FEM data for the initial guess structural layout (blue), the FEM data for the optimal structural layout (red) and the estimation for the rigid aircraft by FAST-OAD (green).

5.2.5 Consistency against overall aircraft sizing

Section 5.2.4 described the structural optimization process for a flexible wing aimed at minimizing the wing structural mass while ensuring safety against the main failure modes. The process implies a fixed wing planform geometry and mean thickness, resulting from the initial FAST-OAD overall aircraft sizing, and selects the best wing-box structure fitting that geometry. It was shown that the optimization may end up with an optimal mass which is higher than the one initially predicted by the overall aircraft sizing. The mismatch is expected to be accentuated when dealing with elongated wings, where the structural flexibility can affect loads in a way that the traditional semi-empirical relations of FAST-OAD are not guaranteed to capture properly. When the mismatch between the wing mass from FAST-OAD, here denoted as W_{w1}, and the one from the aeroelastic optimization W_{w2}, is significant, then the consistency between the overall aircraft sizing and the wing sizing is lost. In other words, the aircraft would be sized with respect to a wing which has a wrong, unsafe weight. To enforce consistency, an iterative approach has been implemented, and it is here briefly described.

The basic idea is to feed the optimal wing weight W_{w2} back to the aircraft sizing process, which in turn elaborates a correction factor that is passed to FAST-OAD, so that a new overall sizing process is run with the updated wing mass. The result will be an updated aircraft configuration consistently sized in order not only to meet the fixed top-level requirements, but also to carry an appropriate wing structure.

Although this core idea is relatively simple, its implementation is in practice slightly complicated by the way the correction is conveyed within FAST-OAD. The program is indeed conceived to allow several technological correction factors to be defined. For instance, some of them are employed to account for secondary aerodynamic effects on trim, shape or lift-induced drag due to specific devices such as winglets. Others, such as the one which is of interest in this case, provide for weight corrections of the different parts, taking into account for example the weight save and balance changes due to the employment of composite materials in the fuselage, or in the wings, or in the tails, etc. In this specific case, a wing weight correction factor, referred to as k_w, is used to introduce a weight penalty if the structural optimization gives W_{w2} significantly greater than W_{w1}. In particular, the correction is triggered by a discrepancy of more than 2%. The problem at this point is the choice of the appropriate factor k_w. In fact, its value only applies when the FAST-OAD analysis is initialized, but then the aircraft sizing process starts a series of iterations to make the whole configuration converge into a consistent, feasible concept. Over these inner iterations, the wing geometry, mass and all the other aircraft parameters progressively change and adapt. This means that, if the initial wing weight estimate, without correction, is denoted as $W_{w1}^{(0)}$, at the end of the next call to FAST-OAD, the final corrected wing weight, denoted as $W_{w1}^{(1)}$ is going to be different from $k_w W_{w1}^{(0)}$. Therefore, the choice to set $k_w = W_{w2}/W_{w1}^{(0)}$, that could initially seem

straightforward, does not bring to the desired result. What happens instead is that the resulting wing mass of the updated configuration is an unknown nonlinear function of k_w:

$$W_{w1}^{(i+1)} = f(k_w) \neq k_w W_{w1}^{(0)} \tag{5.25}$$

For this reason, it is necessary to solve numerically for k_w in order to get the desired configuration where $W_{w1} \approx W_{w2}$. As the nonlinear problem is still relatively simple and depending on a single variable, the same numerical strategy already discussed in other parts of this manuscript, the *ragula falsi* method (see Appendix D), was successfully applied. The initial `FAST-OAD` sizing provides a first point, corresponding to $k_w = 1$. A second point is evaluated at $k_w = W_{w2}/W_{w1}^{(0)}$. With two known points, the algorithm starts converging quickly, and generally finds a solution in about 4 function calls.

In addition, another issue has to be addressed in order to ensure the consistency between the overall aircraft sizing and the wing structural sizing. In fact, even if a new aircraft configuration is found where the wing mass matches the mass provided by the optimizer, that new wing planform is in general expected to be different, and in particular larger, than the one used during the optimization. This means that there is no guarantee that the optimized structure still complies with the constraints, now that the loads arise from a different wing. On the contrary, it is rather possible that a new, larger wing requires an adapted, reinforced structure. Therefore, at each time the aircraft configuration is updated, a new wing-box sizing and optimization should be carried out. For example, let us consider that an aircraft configuration has been updated after n_k iterations - needed to find the adequate correction factor k_w - so that $W_{w1}^{(n_k)} \approx W_{w2}$. At this point a new guess wing-box structure is produced and a new optimization cycle is launched. At the end, the new optimal wing structure is obtained, with its mass being denoted by $W_{w2}^{(1)}$ ($\neq W_{w2}^{(0)}$). Note that the two different apexes indicate that the two estimates have been obtained by two different, subsequent optimization loops. The new optimal wing mass $W_{w2}^{(1)}$ is then checked against the last prediction from `FASTOAD`, $W_{w1}^{(n_k,1)}$, where the second apex $^{(1)}$ was added for the reason just explained. Again, if the two new mass values $W_{w2}^{(1)}$ and $W_{w1}^{(n_k,1)}$ still differ by more than 2%, the process above is repeated. Eventually, in a few iterations a final configuration will be produced where the wing mass is consistent with a structure optimized to safely comply with the static limit loads. This condition is achieved when $W_{w2}^{(n_o)} \approx W_{w1}^{(n_k,n_o)}$, with n_o denoting the number of outer iterations (that is the number of structural optimization cycles that were carried out).

To sum up, the iterative process starts with `FASTOAD` producing an aircraft configuration with a wing of mass $W_{w1}^{(0,0)}$. The wing structure is optimized using the described methods and tools, resulting on a best structure of weight $W_{w2}^{(0)}$. If $W_{w2}^{(0)} > 1.02 \cdot W_{w1}^{(0,0)}$,

a correction factor is found in n_k iterations with the *regula falsi* method and is applied to FASTOAD to get an updated configuration with $W_{w1}^{(n_k,1)} \approx W_{w2}^{(0)}$. Once this is obtained, a second structural optimization is performed on the new wing to get a new best, $W_{w2}^{(1)}$. This process is reiterated n_o times until $W_{w2}^{(n_o)} \approx W_{w1}^{(n_k,n_o)}$. For further clarification, an extract from Figure 5.1 is given in Figure 5.22, providing a graphical overview of the procedure just discussed.

It was found that up to an aspect ratio of about 15, only one or two iterations are in general sufficient to ensure design consistency. For higher aspect ratios, more iterations may be required, depending on the other wing shape parameters. For instance, higher taper ratios tend to shift the aerodynamic loads toward the wing tip, increasing bending loads at root, and therefore demanding a heavier structure that could require more design iterations to achieve a consistent aircraft configuration. Similarly, a low kink span ratio reduces the room available for the structure around the root, demanding thicker structural components in order to sustain loads, and likely resulting in a structure quite heavier than predicted by the rigid wing sizing approach of FASTOAD. This can also contribute to an increase in the number of iterations required to attain consistency.

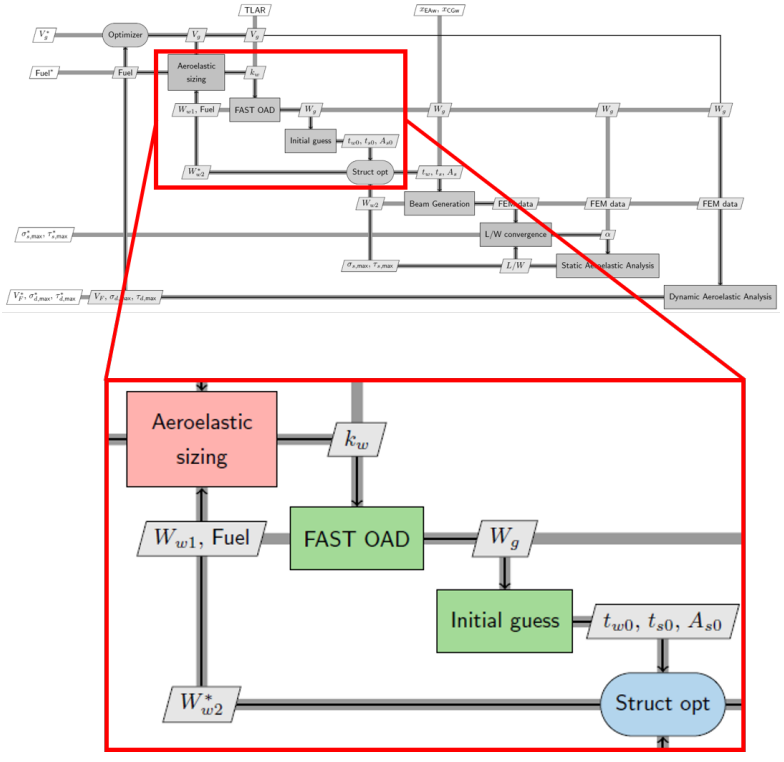

FIGURE 5.22: Highlight from the overall XDSM scheme of Figure 5.1. Detail of the iterative aeroelastic sizing approach, designed to ensure consistency between the wing mass W_{w1}, considered in the overall aircraft sizing, and the wing mass optimized to sustain the prescribed aeroelastic loads, W_{w2}. The design is considered consistent when the two values differ by less than 2%.

Just to provide a few visual examples of what the discussed iterative approach looks like, three cases are reported in Figures 5.23 to 5.25. The first one corresponds to an aspect ratio $\mathcal{AR} = 17.6$, taper ratio $t_r = 0.34$ and a kink span ratio $k_{sr} = 0.33$. Despite the wing is quite slender, two iterations were sufficient to converge to a consistent aircraft. The second case corresponds to an aspect ratio $\mathcal{AR} = 19.1$, taper ratio $t_r = 0.30$ and a kink span ratio $k_{sr} = 0.26$. This higher aspect ratio case turned out to be more challenging than the previous one, requiring three design and optimization iterations to converge. Finally, an even higher aspect ratio configuration, with $\mathcal{AR} = 19.6$, taper ratio $t_r = 0.32$ and a kink span ratio $k_{sr} = 0.27$, is shown to have demanded four iterations before convergence. Note that each iteration represented on these figures requires about 2 to 5 minutes of serial computation on a modern computer.

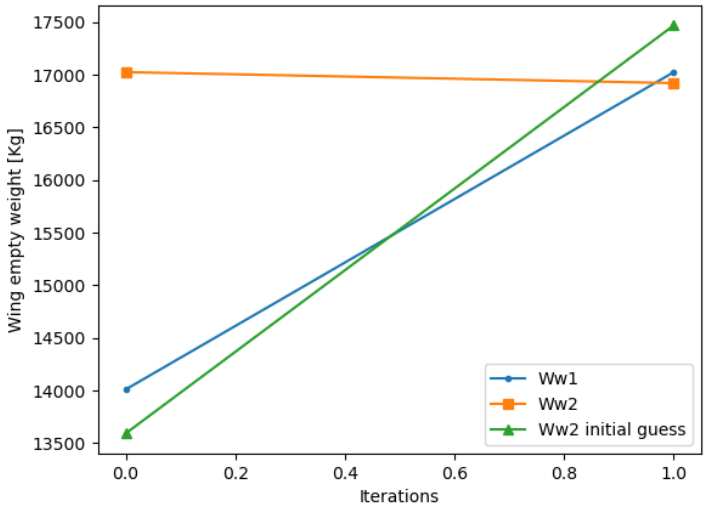

FIGURE 5.23: Sizing and optimization iterations for an aircraft configuration with $\mathcal{AR} = 17.6$, $t_r = 0.34$ and $k_{sr} = 0.33$. The traced quantities correspond to the wing empty weight estimated by `FAST-OAD` (W_{w1}), by the initial guess, and by the aeroelastic structural optimization (W_{w2}).

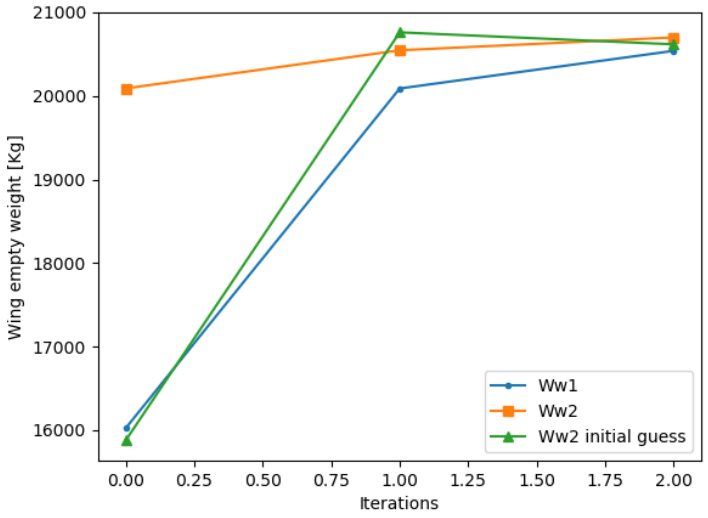

FIGURE 5.24: Sizing and optimization iterations for an aircraft configuration with $\mathcal{AR} = 19.1$, $t_r = 0.30$ and $k_{sr} = 0.26$. The traced quantities correspond to the wing empty weight estimated by FAST-OAD (W_{w1}), by the initial guess, and by the aeroelastic structural optimization (W_{w1}).

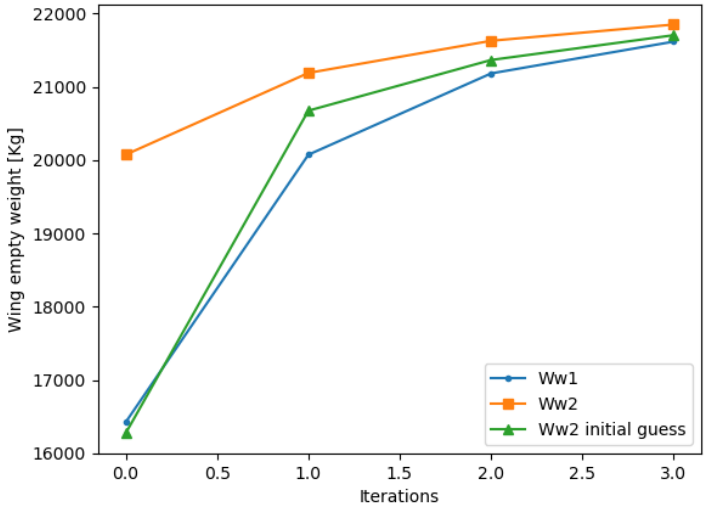

FIGURE 5.25: Sizing and optimization iterations for an aircraft configuration with $\mathcal{AR} = 19.6$, $t_r = 0.32$ and $k_{sr} = 0.27$. The traced quantities correspond to the wing empty weight estimated by FAST-OAD (W_{w1}), by the initial guess, and by the aeroelastic structural optimization (W_{w1}).

5.3 Dynamic aeroelastic constraints under uncertainty

The process described until now is intended to size each aircraft configuration with respect to static limit loads taking into account the static aeroelastic behaviour of the wing. Dynamic aeroelastic behaviour is in general more complex and expensive to investigate, and therefore a retrofit approach, where structural changes are updated in

order to improve their dynamic aeroelastic characteristics, would require a substantial increase of the computational burden, with respect to the proposed one, where only static behaviour is considered. This additional cost would be sharply increased if some kind of robustness has to be granted, as it is the case in this work, because the uncertainty propagation inevitably multiplies the cost of deterministic analyses. On the other hand, dynamic aeroelastic phenomena remain of undeniable importance for the safety of any flying vehicle, especially where slender lifting surfaces are involved. This is why dynamic aeroelasticity is kept as a key target area to be explored in this research. Therefore, one main challenge of this project was to conciliate the need to minimize the computational time for conceptual design exploration with the contrasting requirement of addressing at least the main safety issues related with dynamic aeroelasticity. The solution proposed in this work results from a compromise between these demands.

First, two main dynamic aeroelastic phenomena are identified and included in the analysis framework: flutter and open-loop gust response. Other aspects, such as closed-loop gust response, tail aeroelastic dynamics, the impact of flexibility on the overall flight dynamics, etc., are not considered here. It is believed that they can still be better addressed in a successive, more detailed phase after that the overall aircraft conceptual design has been accomplished, and the primary geometry has been fixed. Otherwise, future developments could be addressed at improving and broadening the actual capabilities to cover these other challenges.

Second, it was decided to exclude the dynamic aeroelastic analyses from the sizing and structural optimization phases. Instead, these are carried out only after the configuration has converged and been fixed, and they just act as constraints for the outer optimization, which aims at minimizing the fuel burn with respect to wing planform geometry. Hence, any configuration proving non-compliant with the flutter or gust response requirements is simply rejected, and no retrofit is addressed.

Third, as far as robustness is concerned, although the list of uncertain parameters at this stage could potentially be very large, it has been repeatedly underlined in the previous sections that an effort is made here to keep the number of parameters and variables limited as far as possible. This is true for the overall MDAO problem, as well as for inner structural optimization task and the dynamic aeroelastic constraints. For this reason, as far as the latter are concerned, an initial conceptual screening of those parameters that could relevantly affect the wings' aeroelastic response was carried out, bringing to the selection of only six quantities. Then, some sensitivity analyses were carried out in order to further restrict the set of uncertain parameters to be actually employed in the overall MDAO.

Finally, as already mentioned at the beginning of this chapter, the choice was made to only investigate uncertainty propagation when evaluating the dynamic aeroelastic constraints. Therefore, the proposed robust MDAO problem takes more specifically

the form of a reliability-constrained optimization. The inner sizing and structural optimization cycles are all run in a deterministic way on the nominal configurations.

The following sections give more details about how exactly the constraints are put in place, and what kind of analyses they involve. In particular, Section 5.3.1 introduces the deterministic flutter analysis and the implementation of the corresponding constraint within the MDAO, and Section 5.3.2 describes the sensitivity studies made on flutter and the consequent definition of the flutter speed reliability constraint. Then, similarly, Section 5.3.3 discusses how the deterministic gust response simulations are set up and how deterministic gust constraints are defined, whereas the sensitivity analyses and the implementation of the probabilistic gust loads constraints are subsequently treated in Section 5.3.4.

5.3.1 Deterministic flutter speed on low and high aspect ratio configurations

One of the dynamic aeroelastic constraints that have been enforced in this case study is the wing flutter speed. The deterministic constraint is simply formulated by requiring that flutter must not happen below a fixed speed threshold. This follows the indications given by airworthiness regulations. For example, the EASA Certification Specifications for large aeroplanes (CS25) originally imposed that the airplane must be free from aeroelastic instability within an envelope enlarged up to 20% in terms of Mach and air speed at all altitudes. Today, as from the latest amendment (see [213]), this value has been harmonized with the U.S. FAA regulations [214], putting that value at 15%. Here, one single condition is imposed to constrain the optimization, corresponding to the speed threshold of $1.15\,V_D$ EAS, and to a Mach number of 0.6, based on the sea-level speed of sound of 340 m/s. No other conditions, such as different altitudes and Mach numbers are studied. This is motivated on one hand by the need for minimizing the computational costs, and on the other hand by the fact that the adopted tools would not capture more complex phenomena such as dynamic shock waves or buffeting that could be involved at high altitude, transonic conditions. Therefore it would be of little use to repeat the same analysis with different, less reliable flow conditions. Moreover, this work offers a first proof of concept of a proposed approach, and the number of flight conditions and their physical complexity can be increased in future work.

The tools adopted for flutter analysis are different from those employed for the static aeroelastic studies. From the aerodynamic side, the unsteady strip theory presented in Section 3.2.2 is used instead of the steady VLM. This choice was motivated in Section 2.4.3. The structural model is still a finite element beam model, sharing the same properties as the static aeroelastic case, but the beam degrees of freedom are restricted to three, namely vertical translation, bending rotation and twist (see Section 3.3.1). Also, as flutter is a matter of stability in the immediate surrounding of a static equilibrium,

the model is kept linear, differently from the static approach, where geometric nonlinearity is taken into account. This is in line with most of the literature relating to similar studies at conceptual design (see again Section 2.4.3). As a consequence, the effect of initial static deformation is neglected. More technical details about the aerodynamics, structural dynamics and their coupling have been given in Section 3.4.1.

Nonetheless, it is worth resuming here some key aspects of the approach adopted. The flutter problem consists in finding the speed at which the aeroelastic system turns unstable. Different numerical approaches are possible to solve this problem, depending also on how the physics is modeled. In most cases the problem is complicated by the intrinsic dependence of the unsteady aerodynamic loads not only on the flow speed, but also on the reduced frequency. Nevertheless, in the present model this dependency is removed by relying on Wagner's indicial function, which constitutes an approximation of the indicial unsteady aerodynamic response to a step change in the angle of attack. In the domain of strip theory, the exact analytical response was only formulated by employing the Theodorsen function, which is a complex function of the reduced oscillation frequency. But Wagner's indicial function, and the use of convolution to extend its applicability to arbitrary motion, offers a valid and practical alternative to frequency-based methods. This allowed, after the manipulations explained in Section 3.4.1, the present aeroelastic model to be expressed as a linear system in the canonical form:

$$\dot{\boldsymbol{x}} = \boldsymbol{A}\,\boldsymbol{x} \tag{5.26}$$

where $\boldsymbol{x}$ is a state vector, containing structural and aerodynamic variables, and $\boldsymbol{A}$ is the dynamic matrix, which is assembled from the structural and aerodynamic mass, stiffness and damping matrices, plus additional coupling matrices relating to some aerodynamic variables deriving from the unsteady formulation. Now, it is well known that the stability of any such system as in Equation (5.26) is completely characterized by the eigenspectrum of the dynamic matrix: its stability can easily be inferred by examining its eigenvalues. In this specific aeroelastic system, once the structural model, with its parameters, and the wing planform geometry are fixed, the remaining quantity that shapes the model, and therefore the dynamic matrix, is the dynamic pressure, or, if the density is kept constant, the speed. Therefore, it is possible to trace the change in the system eigenvalues with respect to the flow speed, until the first one crosses the imaginary axis, or, equivalently, until the first mode exhibits a negative damping.

With this formulation, where the system matrix and eigenvalues depend only on the speed, this method falls into the category of what are called p methods, in contrast with the other widely diffused category of $p-k$ methods, where the dependency on the reduced frequency k is maintained (see Section 2.4).

With these considerations, finding the flutter speed reduces to solving a nonlinear one-dimensional problem. The unknown is the speed at which the first eigenvalue has its

real part approaching zero. As for other problems discussed previously in this work, the *regula falsi* method (see Appendix D) proved effective also in this case. The main difference here is that there is no initial guess available, so the first iterations just evaluate the system stability at the arbitrary value of 150 m/s, and then at increments of 100 m/s, until a first unstable speed is found. At this point, the algorithm starts to converge. However, the eigenvalue analysis of the present dynamic matrix is a rather cheap task, compared to other nonlinear problems previously discussed, such as the search for the correct angle of attack matching the required load factor, or for the `FAST-OAD` correction factor to get the desired wing mass. Therefore, a slightly higher number of iterations does not add sensible computational burden. Moreover, the initial system size, deriving from the number of finite elements, is consistently reduced by means of a simple modal projection. More specifically, the beam structure made of 60 elements, having 3×60 degrees of freedom, was found to be adequately modeled by retaining only the first 10 modes (ordered per ascending frequency). This amounts to a reduction of 95% of the structural system size, and allows the solution for the flutter speed to be found in a couple of seconds, with an error of less than 1% with respect to the full-order model.

An interesting aspect of the adopted method, and in general of any p method, is that the stability analysis holds the same degree of accuracy at any speed. In contrast, the $p - k$ method is accurate only in the immediate neighborhood of the stability limit, where damping is almost zero and the behaviour can be approximated as purely harmonic. Therefore the p method is more suited to study the change in stability with varying speed. Frequencies and damping ratios can be easily evaluated at different speeds and plotted to have a better understanding of the system behaviour and its evolution.

An example, run on the baseline test-case, is reported in Figures 5.26 and 5.27. The first one shows the shift of the modal frequencies with respect to speed. In particular, it can be seen that appreciable changes arise above 100 m/s, where the third mode, corresponding to the first torsional mode, starts to experience a progressive decrease in frequency. On the other hand, the first mode, of pure bending, shifts to higher frequencies, approaching the second bending and the first torsional modes. As it is well known in aeroelasticity, this approach leads to a coupling between the modes that at some point turns to amplifying, unstable oscillations. A red line indicates the actual speed of 255 m/s where instability is reached. At this point, the first bending and torsion mode have the frequency of 4.5 and 7.5 Hz, respectively. The phenomenon is graphically more evident from the damping ratios plot of Figure 5.27. The flutter speed is clearly identified by the point at which the first mode's damping crosses the zero axis, after a sudden shift from its initial trend of increasing stability. At the same time, also the first torsion mode experiences a sudden change in damping, in this case towards higher values. The second bending mode, although its frequency overlaps with the first torsion mode, does not show any appreciable shift in frequency or damping,

suggesting it does not participate in the flutter mechanism. The first six modal shapes are represented in Figure 5.30.

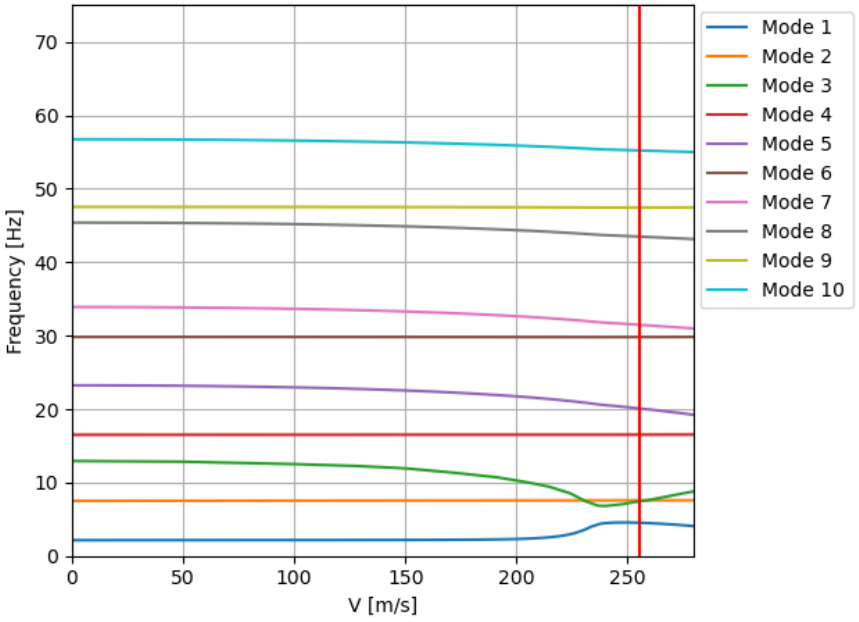

FIGURE 5.26: Evolution of the first 10 modal frequencies with air speed for the CeRAS wing model. A red vertical line marks the speed at which the flutter instability is reached.

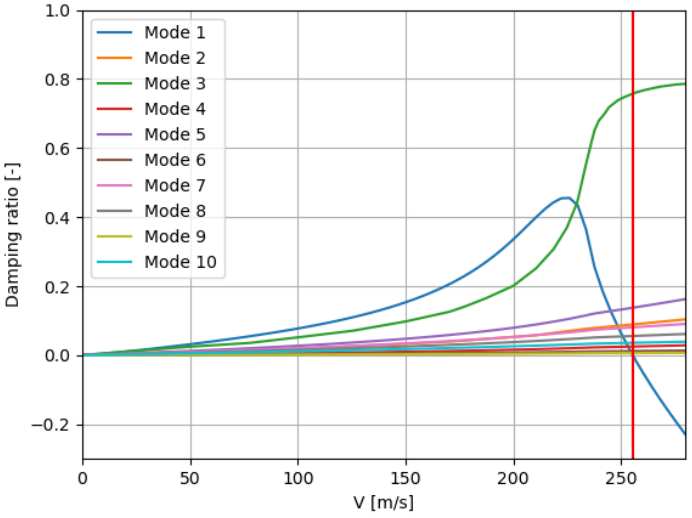

FIGURE 5.27: Evolution of the first 10 modal damping ratios with air speed for the CeRAS wing model. A red vertical line marks the speed at which the flutter instability is reached.

To provide another example, the same plots are reported for a higher aspect ratio wing. The configuration is the same as the one treated in Section 5.2.4.2, with the same taper ratio and kink span ratio as the baseline, and an aspect ratio of 15. A few differences

can be noted in comparison to the previous case. First of all, as it could be expected from a more elongated structure, the wing shows a reduced aeroelastic stability, with a flutter speed of 215 m/s, 40 m/s lower than the baseline. Also, the increased bending inertia, resulting from a mass distribution that is moved further from the wing root, determines lower bending frequencies. The torsional frequencies do not show a similar shift from the corresponding baseline frequencies. As a result, three bending modes initially appear in Figure 5.28 below the first torsion mode. Then, the first torsional frequency progressively drops from 13.5 Hz down to 6.6 Hz, while the first bending frequency increases from 1.5 to 3.7 Hz. Here, the coupling with the first bending mode finally brings instability. The damping ratio trends, illustrated in 5.29, do not show particular differences, at least qualitatively, from the baseline case. Similarly, the modal shapes, represented in Figure 5.31, are almost identical to those of the baseline, as it can be seen by comparison with Figure 5.30. It is worth noting that the '$\mathcal{AR}$ 15' wing shows an evident mode switching with increasing speed. For example, the 1st torsion mode is the 4th mode in the order of ascending frequencies at zero speed, but its frequency reduces with increasing speed and just before flutter it goes below the 3rd bending mode, which is why it is plotted as the 3rd mode ($f = 6.6$ Hz) in Figure 5.31. Also, comparing Figures 5.30 and 5.31, it can be seen that the 5th and 6th modes are inverted for the two wings. Such observations demonstrate that mode switching is a common phenomenon in flutter analysis, which can be easily triggered during parametric studies, uncertainty quantification, design exploration and optimization. Therefore, in order to have a correct understanding of the causes of the instability, it is important that the tools employed are adequately precise to capture and show such modes evolution.

It is worth pointing out that all the discussed results, as well as all the following flutter analyses launched during the MDAO process, are based on the heavy weight wing configuration, that is, the wing with all fuel onboard. The reason for this choice is that the increased mass and inertia anticipate the bending-torsional coupling and the speed of flutter. In fact, all tests that were done with empty weight wings, with various geometries, revealed a great increase in stability, due to the prevalence of the stiffening elastic forces over the aerodynamic and inertial loads. This resulted in very high flutter speeds, in most cases well above Mach 0.7, which is considered the limit of validity of the adopted models. Such results, from a qualitative perspective, simply reveal that those configurations are not critical at all for flutter constraints. From a quantitative point of view, they are meaningless because they violate the validity of the physical models, and therefore they are not reported in this manuscript.

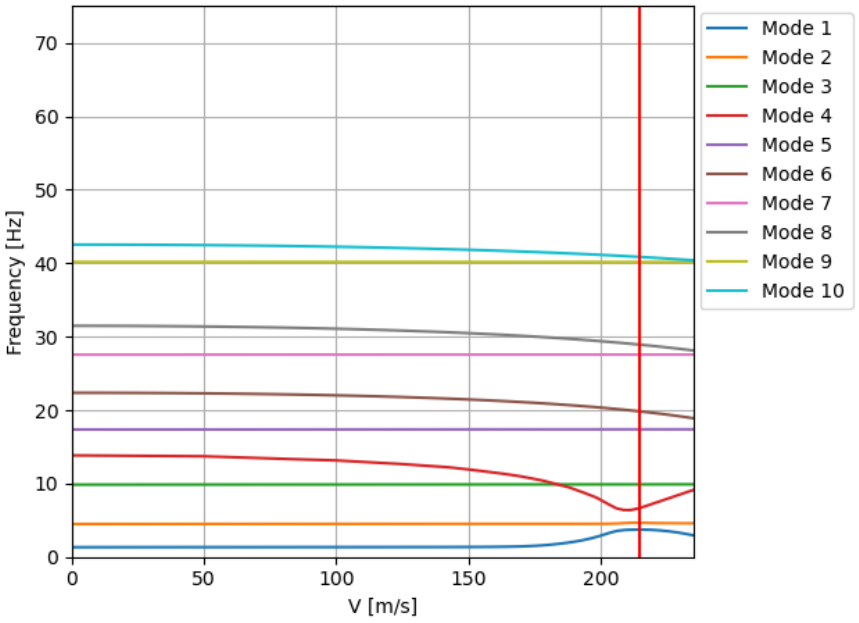

FIGURE 5.28: Evolution of the first 10 modal frequencies with air speed for the '$\mathcal{AR}$ 15' wing model. A red vertical line marks the speed at which the flutter instability is reached.

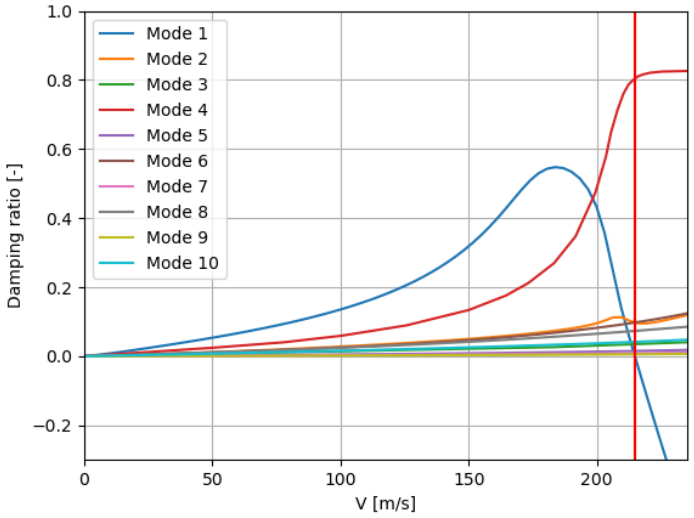

FIGURE 5.29: Evolution of the first 10 modal damping ratios with air speed for the '$\mathcal{AR}$ 15' wing model. A red vertical line marks the speed at which the flutter instability is reached.

5.3.2 Sensitivity of flutter speed with respect to aeroelastic parameters

The examples provided in Section 5.3.1 refer to nominal configurations, both for the baseline and for the '$\mathcal{AR}$ 15' cases. The nominal parameters are derived from the aeroelastic sizing process discussed previously in this Chapter: a first guess of the wing-box

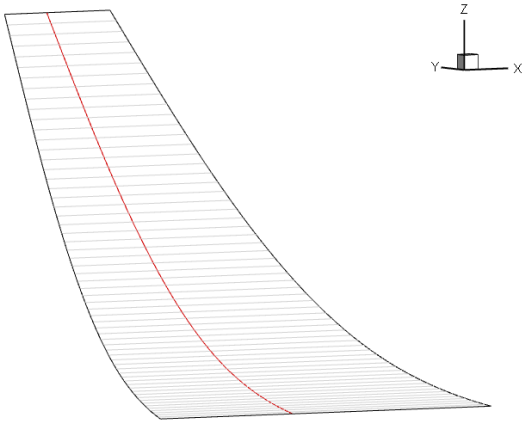

(a) Mode 1 (1st bending, $f = 4.5$ Hz).

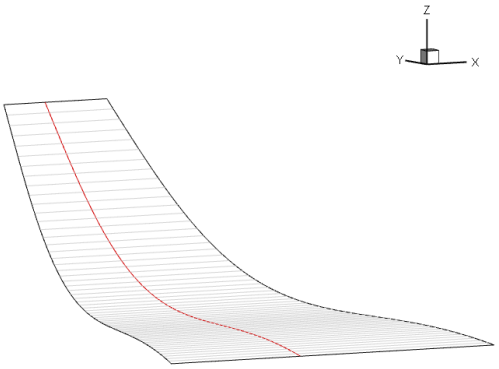

(b) Mode 2 (2nd bending, $f = 7.3$ Hz).

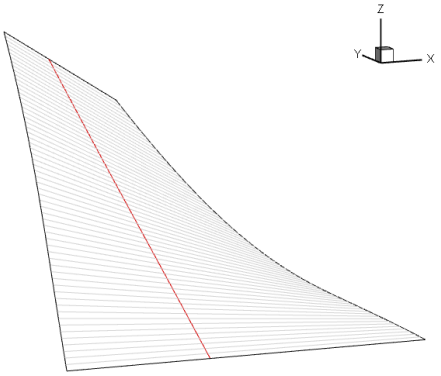

(c) Mode 3 (1st torsion, $f = 7.5$ Hz).

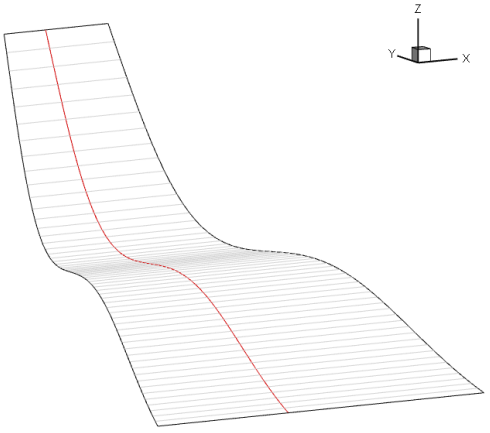

(d) Mode 4 (3rd bending, $f = 15.5$ Hz).

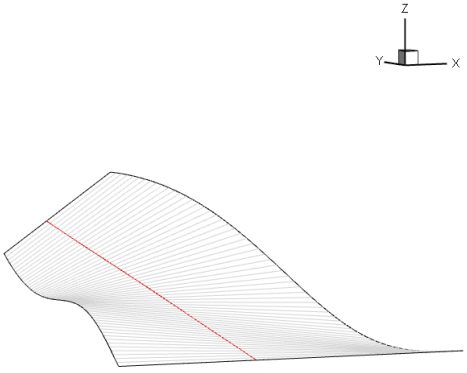

(e) Mode 5 (2nd torsion, $f = 20.1$ Hz).

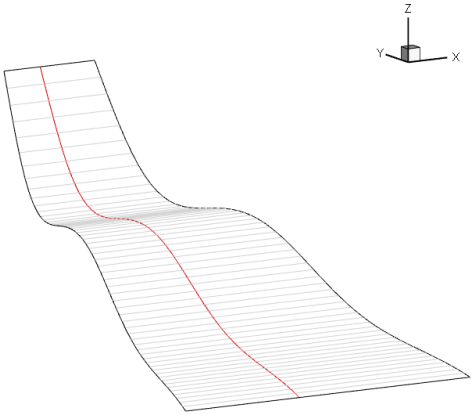

(f) Mode 6 (4th bending, $f = 29.8$ Hz).

FIGURE 5.30: First six wing structural modes of the baseline configuration. The red line identifies the elastic axis. The reported frequencies correspond to flutter speed. Each shape is scaled freely in order to give a better visual understanding.

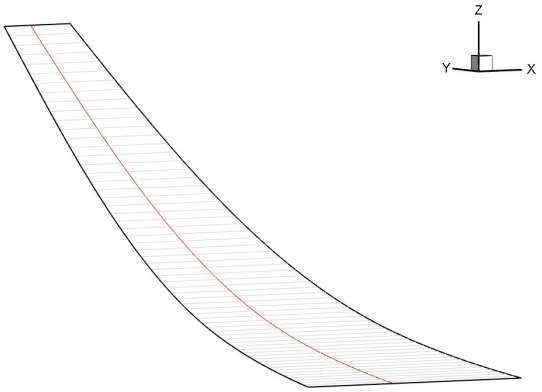

(a) Mode 1 (1st bending, $f = 3.7$ Hz).

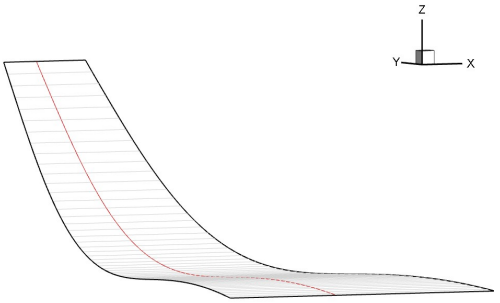

(b) Mode 2 (2nd bending, $f = 4.7$ Hz).

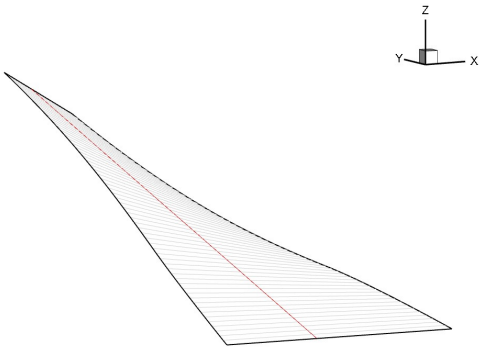

(c) Mode 3 (1st torsion, $f = 6.6$ Hz).

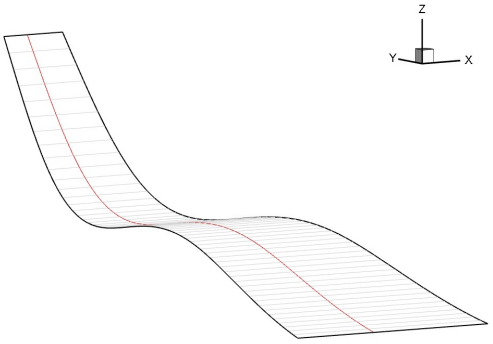

(d) Mode 4 (3rd bending, $f = 9.8$ Hz).

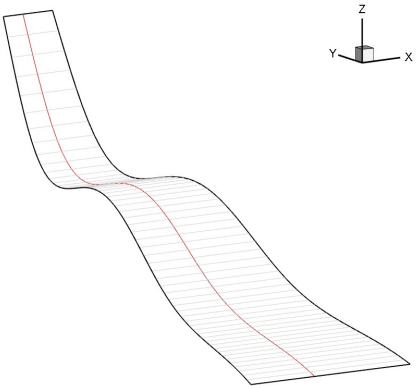

(e) Mode 5 (4th bending, $f = 17.4$ Hz).

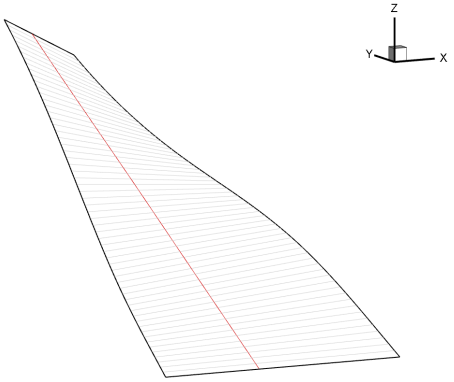

(f) Mode 6 (2nd torsion, $f = 19.8$ Hz).

FIGURE 5.31: First six wing structural modes of the '$\mathcal{AR}$ 15' configuration. The red line identifies the elastic axis. The reported frequencies correspond to flutter speed. Each shape is scaled freely in order to give a better visual understanding.

structure and its equivalent beam model are produced, then optimized with respect to the structural safety constraints, and the process is repeated iteratively, if needed, until the wing mass is consistent with the overall aircraft configuration. It has already been discussed how the structural parameters are directly computed from the assumed wing-box geometry. Given the different simplifying assumptions, it is clear that such predictions provide only an approximation of a realistic, definitive structure. Moreover, throughout successive, more advanced design phases, it is likely that several features, including geometry and material properties, will be adjusted. For these reasons, it is of interest at this stage to evaluate how errors in the underlying assumptions, or changes during forthcoming design phases, could impact the outcome of the optimization, and in particular how they would impact the structural safety and the fuel mass, the latter being the final objective of this optimization. To this aim, some sensitivity analyses have been preliminary conducted, in order to identify the most relevant parameters affecting the aeroelastic stability of the main wing. The identified parameters will be considered as the uncertainty sources to be taken into account when enforcing the reliability constraint on flutter speed.

The definition of the flutter sensitivity analysis problem is given in Section 5.3.2.1, whereas two sensitivity analysis applications are reported in Section 5.3.2.2, applied to the baseline and the '$\mathcal{AR}$ 15' configuration.

5.3.2.1 Problem definition

When choosing what parameters should be considered as uncertain in the present model, two possible approaches were weighed.

The first one is to look at the variables that define the wing-box model, i.e. the thicknesses of spars and skin and the stringers area. Once these are fixed, all the beam characteristics follow. So assigning uncertainty to this limited group of independent variables would result in a propagation of uncertainty affecting all of the derived properties. However, the physical meaning of this approach, in this case, is that a simplified wing-box with rectangular cross sections is allowed to change into other simplified wing-boxes with equally simple rectangular cross sections. Therefore, any sample analyzed during the uncertainty quantification would still represent another unrealistic sample, just as for the nominal case, with a high risk of not covering any plausible variations of the structure properties.

In reality, the final design would be characterized by more complex geometries, with each section following the local aerodynamic profile, components made of slightly different aluminium alloys, thickness and mass distributions adjusted due to reinforcements, secondary components and to a large number of additional requirements that can only be treated in more advanced design phases.

The second way to address the definition of the uncertainty quantification problem is to start from the derived beam model, characterized by a certain number of 'condensed' properties, and to assign uncertainty to those derived parameters. This approach would cover a wider domain of structural changes, without need to trace the uncertainty propagation from a highly detailed model. Any property change in the beam model could then represent the effect of different changes of the real, detailed configuration. In this way, the study would be more general, and not restricted to a small family of simplified, unrealistic structures, as it would be with the first approach. Therefore, this second strategy was preferred.

Considering the relative simplicity of a beam model, like the one here adopted, it was not difficult to select a restricted set of key parameters that may relevantly affect the wing aeroelastic performances.

One of them is the chord-wise position of the elastic axis. It primarily determines the intensity of aerodynamic twisting moment on the structure: the further the elastic axis is from the aerodynamic center of pressure, the stronger the twisting moment would be. The nominal position of the elastic axis is at the center of the rectangular wing-box cross section, which is fixed from `FAST-OAD`. The uncertainty on this quantity can derive from different factors and their combination, for example a change in the front and/or rear spar position or thickness, the asymmetry of the actual cross section, a chord-wise shift of the real center of pressure from the theoretical quarter-chord position assumed in VLM and strip theory models.

Some of the above factors would also cause another important parameter to change: the location of the center of gravity. However, rather than the absolute CG location, the relevant parameter, as far as the aeroelastic behaviour of the wing is concerned, is the relative distance between the CG and the elastic axis, because it affects the inertial coupling between bending and torsional dynamics. This shift could arise from different factors: asymmetric fuel distribution inside the actual wing, asymmetric use of components of different densities, position of reinforcements, actuators and other secondary elements. Although some factors can affect at the same time both the elastic axis and the center of gravity, others would mainly affect only one of the two. Therefore, the two parameters will be allowed to vary independently from one another.

Other key factors that define a beam model are the equivalent elastic properties. As far as the flutter analysis is concerned, the elastic properties of the simple linear beam model are represented by the two quantities EI^A_{yy} and GJ. On the one hand, a first source of uncertainty lies in the definition of the two elastic moduli E and G. The nominal values are assigned by assuming that all the active components of the structure are made of exactly the same alloy. This is not actually true, because in general not only different components are made of different alloys, but also they are manufactured via different processes - lamination, forming, etc - that alter the metallic grain structure

and as a consequence also the macroscopic characteristics such as the elastic moduli. In addition, geometry changes can also affect the elastic properties of the equivalent beam, in particular via the area moments of inertia I_{yy} and the torsion constant J. Therefore, assigning uncertainty to the two quantities EI_{yy}^{A} and GJ would encompass all of these effects.

Finally, important changes on the beam dynamics can arise from its inertia properties. In fact, any changes in geometry and mass distribution would affect structural modal shapes and frequencies, and therefore its stability and dynamic characteristics. The condensed beam parameters that convey such information are the linear mass distribution and the different moments of inertia. More specifically, the linear beam model employed for the flutter analysis only requires two inertial parameters to be defined: the local mass per unit length μ and the polar moment of inertia I_p (see Table 5.5). The slightly more complex non-linear beam model adopted for the gust response analysis additionally requires the two inertia moments EI_{yy} and EI_{zz}. The products of inertia continue to be neglected.

In consequence of these considerations, six parameters have been selected to perform a sensitivity analysis on the flutter speed: the elastic axis location a, the offset between the elastic axis and the center of gravity d, the beam average mass per unit length μ, the bending and torsional stiffnesses EI_{yy}^{A} and GJ and the moment of inertia I_p. These are all the parameters needed to completely define the stiffness and mass matrices of the finite element model used for flutter analysis. It is worth noting that an important assumption still holds: all these quantities are defined at the wing root, and they change over the wing span according to the same distribution obtained from the nominal wing-box. This means that, for example, if the root value for the mass μ is increased by 5% with respect to the nominal one, then all the nodal mass values along the span are increased by 5% with respect to the nominal ones at the corresponding nodes. Therefore the spanwise distributions are only scaled with respect to the nominal ones, keeping the same shapes (some examples were plotted in Figures 5.9 and 5.10). However, adding some additional uncertainty to these distributions would not be a difficult implementation, if needed.

Quantitatively, it is hard to estimate how all the discussed uncertainty sources would affect the six selected parameters, in terms of statistical distributions. It is already hard to evaluate how all the above design changes could impact the characteristics of one single, well-known aircraft configuration such as the baseline. Especially if there is no detailed model available, which is the case at this early design phase. It would be even harder to quantify or justify the choice of any uncertainty distribution regarding unconventionally high aspect ratio configurations. Nor is it the scope of this work to provide evaluations at high technological readiness and industrial-level reliability. Instead, the primary interest here is to provide a proof of concept of the capabilities of the developed framework. The quantity and quality of data available to accurately define

the sensitivity and uncertainty quantification problems are of secondary importance. Therefore, uncertainty has here been assigned based on simple reasonable assumptions, rather than opting for questionable quantitative approaches requiring extensive data collection and detailed evaluations, or industrial expert judgement.

The assumptions are that: *a*) all quantities feature normal uncertainty distributions, centered around their nominal values; *b*) all distributions are assigned such that the 99.7% of the cases fall within an interval of $\pm$ 10% of their nominal values, except for the center of gravity to elastic axis distance, for which the interval is restricted to $\pm$ 5% because there are less reasons why these two points should move away from each other.

The chosen uncertain parameters and their distributions to be used in the flutter sensitivity analysis are reported in Table 5.5.

Property	**Mean**	**Standard deviation**
Elastic axis location	$\overline{a}$	$3\,\varsigma = 10\%$ chord
CG shift from EA	$\overline{d}$	$3\,\varsigma = 5\%$ chord
Mass per unit length	$\overline{\mu}$	$3\,\varsigma = 10\%\,\overline{\mu}$
Bending stiffness	$\overline{EI}^A_{yy}$	$3\,\varsigma = 10\%\,\overline{EI}^A_{yy}$
Torsional stiffness	$\overline{GJ}$	$3\,\varsigma = 10\%\,\overline{GJ}$
Polar moment of inertia	$\overline{I}_p$	$3\,\varsigma = 10\%\,\overline{I}_p$

TABLE 5.5: Uncertain parameters and corresponding distributions adopted for the flutter sensitivity analysis. All distributions are Gaussian. Symbols denoted with a bar $\bar{(\,)}$ represent the nominal values produced by the sizing and optimization process. The symbol ς indicates the standard deviation.

5.3.2.2 Application to the baseline and the high aspect ratio test-cases

A first sensitivity analysis was carried out on the baseline configuration using the `Uncertainpy` toolbox introduced in Section 3.7. A polynomial order of 4 was found adequate to generate the polynomial chaos expansion, after comparing results from order 2 up to 6. The generation of the PCE required 422 function calls - a number calculated automatically by the PCE library. Then, the statistical characterization of the response, including mean, variance, 1st order and total Sobol's indices, was obtained after a Monte Carlo sampling of the PCE, with a DOE size of 10^6. The nominal values of the 6 uncertain parameters are reported in Table 5.6, which also includes the data for the second test case, the '$\mathcal{AR}$ 15' wing.

The output probability density function for the flutter speed is reported in Figure 5.32. The distribution peak is reached slightly before the deterministic flutter speed of 255

Property	Symbol	Baseline	$\mathcal{AR}$ 15
Elastic axis location	$\overline{a}$	38%chord	38%chord
CG shift from EA	$\overline{d}$	0.0	0.0
Mass per unit length	$\overline{\mu}$	1.8e3 kg/m	1.9e3 kg/m
Bending stiffness	$\overline{EI}^A_{yy}$	6.9e8 N·m^2	9.3e8 N·m^2
Torsional stiffness	$\overline{GJ}$	2.1e8 N·m^2	2.4e8 N·m^2
Polar moment of inertia	$\overline{I}_p$	1.0e3 kg·m	1.1e3 kg·m

TABLE 5.6: Mean (nominal) values of the 6 selected uncertain parameters for the flutter speed sensitivity studies on the CeRAS baseline and the '$\mathcal{AR}$ 15' wings.

m/s. The mean is at 264 m/s, just above the deterministic value, and the standard deviation is of 39 m/s. As the reader could see from the Figure, the output is not a perfectly symmetric distribution as a Gaussian curve would be, although the asymmetry is subtle. This is attributed to the substantial 'asymmetry' of the physical problem: as the speed is increased, compressibility increasingly affects the results through the Prandtl-Glauert correction, which is a nonlinear function of the Mach number. Therefore, the samples falling into the right half of the curve cannot be expected to be distributed exactly specularly with respect to those on the left side. Also, it is important to remember that results of flutter speeds above Mach 0.7, corresponding to 240 m/s, are not trustworthy, because the Prandtl-Glauert compressibility correction loses its validity. Results around Mach 1 (V = 340 m/s) and above are simply meaningless, they just represent the numerical output of a model which is not physically consistent anymore. But this right portion (high speed) of the distribution is not of concern at all in the purpose of this work, as the samples will anyway lie above the minimum threshold. The interest here is to have a fair understanding on the left part (low speed) of the distribution, where the model is valid, to evaluate the probability of flutter happening below the safety threshold. The safety region, where this probability has to be negligible, is set to be up to 200 m/s, consistently with what discussed in Section 5.3.1, and is highlighted in Figure 5.32 by a red shade. That indicates the region where flutter should occur with the least probability (ideally zero probability).

The first important result that this analysis provides is not the whole distribution in itself, but the distribution at dangerous speeds. In this case, the baseline appears to be adequately safe, with almost zero probability of having flutter below 200 m/s. The definition of 'safe' in probabilistic terms, as far as flutter speed is concerned, is not given by regulations, and clearly the early design phase cannot give an accurate assessment of sensitivity and uncertainty. The definition is rather arbitrary and would depend much on the specific design task and needs. The acceptable probability is driven by the risk that the designer is ready to accept. Here, as this work is purely demonstrative, and no immediate industrial interests are at stake, a free choice was made to consider

safe any design candidate whose probability to experience flutter below 200 m/s is less than 5%. This translates into the condition that the 5th percentile of the flutter speed PDF must be greater than 200 m/s.

The second fundamental outcome of this study is the assessment of the sensitivity of the flutter speed to the selected uncertain parameters. The sensitivity analysis here consists on the evaluation of the 1st order and total Sobol indices. These are graphically given in Figure 5.33, together with a few other statistical metrics. What emerges is that out of the six uncertain parameters, only two of them, namely the elastic axis position a and its distance from the center of gravity d, have a major impact on the flutter speed, at least with the assumed input distributions (see Table 5.5). In physical terms, the former determines the intensity of the aerodynamic twisting moment on the structure, and the latter affects the arm of the inertial forces, and therefore their moment around the elastic axis. The results indicate that these effects have much larger importance than the assumed variations in mass and stiffness. In effect, stiffness has a more direct impact on deformations, but not necessarily on stresses. The sum of all the 1st order Sobol indices amounts to 0.94. When this sum approaches 1, it means that no relevant effects arise from the interaction between the uncertain parameters. Higher order indices would give the sensitivity due to these interactions. Here only the total Sobol indices are additionally computed. Their sum amounts to 1.06, confirming that there is little sensitivity to parameter's interaction, and however such little interaction effects, again, come only from the two parameters a and d, as the total indices of the remaining parameters are negligible. All the main statistical figures are summarized in Table 5.7.

The net dominance of the two parameters a and d suggests that the robust MDAO process can be addressed by only assigning uncertainty to these two quantities, whereas the remaining four can be kept fixed to their deterministic estimation. This would significantly reduce the computational cost of evaluating the flutter reliability constraint.

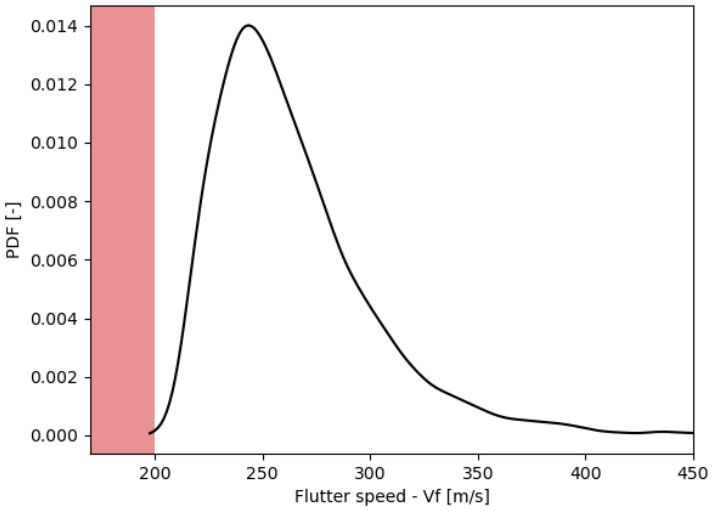

FIGURE 5.32: Flutter speed Probability Distribution Function following the uncertainty propagation on the baseline test-case. The area shed in red indicates the imposed flutter-safe region: the probability of flutter occurring within this region should be lower than 5%. The baseline results robust enough with respect to such condition.

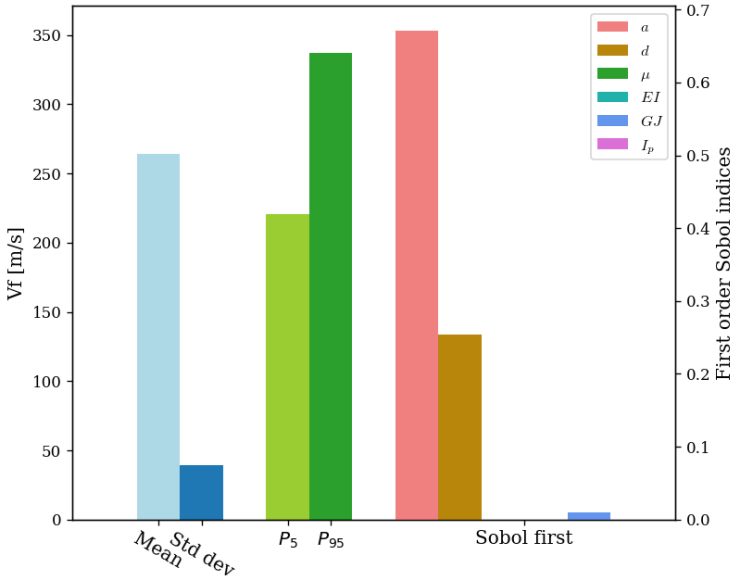

FIGURE 5.33: Main statistical and sensitivity indices from the flutter sensitivity analysis on the baseline configuration.

To gain some further insights on the problem of uncertain flutter characteristics, the same analysis was repeated on the '$\mathcal{R}$ 15' configuration that has already been used as a comparative use case in previous Sections of this Chapter. The output distribution of the flutter speed of this second wing is reproduced in Figure 5.34. The response does not present relevant qualitative differences from the baseline case. The distribution

Distribution properties							
Mean	264 m/s						
Standard deviation	39 m/s						
5th percentile (P_5)	221 m/s						
Sensitivity indices							
	a	d	μ	EI	GJ	I_p	**Sum**
Sobol first	**0.67**	**0.25**	1.4e-5	1.9e-5	1.0e-2	1.6e-4	0.93
Sobol total	**0.73**	**0.32**	8.6e-4	7.2e-4	1.2e-2	1.0e-3	1.06

TABLE 5.7: Main statistical figures from the sensitivity analysis and uncertainty quantification on the flutter speed for the baseline configuration.

features the same light asymmetry, with a peak almost coincident with the nominal flutter speed of 215 m/s, a mean shifted slightly upwards, to 230 m/s, and a standard deviation of 35 m/s. This time, the higher flexibility of the wing translates into a less robust design: despite the nominal flutter speed is above the minimum allowable of 200 m/s, the 5th percentile $P_5 = 193$ m/s makes it not sufficiently reliable, according to the above statement that P_5 must be greater than 200 m/s. Therefore, while the deterministic optimization would keep this as a valid configuration, the probabilistic approach, that as already explained relies on reliability constraints, would dismiss this candidate as inadequate, because it is insufficiently robust to uncertainties.

The sensitivity analysis reveals almost identical characteristics with respect to the baseline: the response is dominated by the elastic axis location a and its distance from the center of gravity d. The Sobol indices mirror those obtained from the baseline. The statistical results are graphically summarized in Figure 5.35, and are also collected in Table 5.8.

Considering the close sensitivity results between the two significantly different configurations, it was decided that during the overall MDAO the reliability constraint on flutter speed shall be based only on the uncertainty on the two parameters a and d, with their distributions kept the same as in Table 5.5.

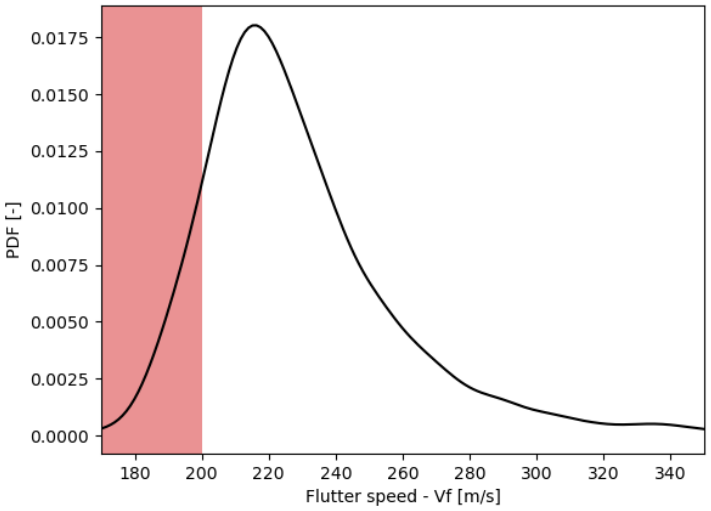

FIGURE 5.34: Flutter speed distribution following uncertainty propagation on the '$\mathcal{AR}$ 15' test case. The area shed in red indicates the imposed flutter-safe region: the probability of flutter occurring within this region should be lower than 5%. This configuration does not appear to be robust enough with respect to such condition.

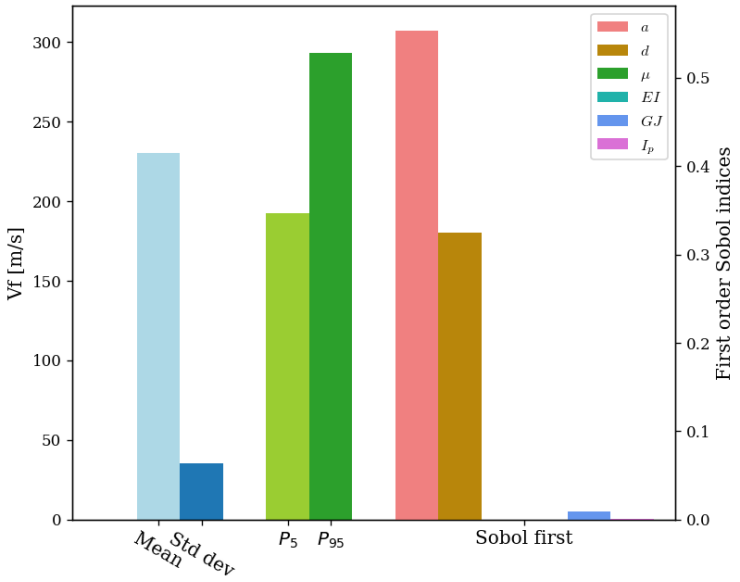

FIGURE 5.35: Main statistical and sensitivity indices from the flutter sensitivity analysis on the aspect ratio 15 configuration.

Distribution properties							
Mean	230 m/s						
Standard deviation	35 m/s						
5th percentile (P_5)	192 m/s						
Sensitivity indices							
	a	***d***	***μ***	***EI***	***GJ***	***I_p***	**Sum**
Sobol first	**0.55**	**0.32**	8.3e-5	9.7e-5	9.7e-3	6.6e-4	0.88
Sobol total	**0.65**	**0.43**	6.4e-3	5.9e-3	2.0e-2	8.3e-3	1.12

TABLE 5.8: Main statistical figures from the sensitivity analysis and uncertainty quantification on the flutter speed for the aspect ratio 15 configuration.

5.3.3 Dynamic gust response

Gust response is a critical aeroelastic issue in aircraft sizing. The static manoeuvre loads are never considered sufficient in any sizing approach, even in traditional conceptual design. Specifications always impose to combine the static manoeuvre flight envelope with the gust envelope, and pick the most critical conditions among the two. In simplified approaches, such as the one of `FAST-OAD`, this translates into additional semi-empirical relationships to estimate the worst gust loads. Such relationships are in general expressed in terms of flow conditions (speed, density, Mach number), wing geometry and mass, and are tuned according to empirical studies on a given class of aircraft (as mentioned in Section 2.4.2). Therefore, the predictions can be considered quite accurate when dealing with conventional designs, but there is no guarantee they hold valid for unconventional configurations. Especially when flexible high aspect ratio wings are involved, the subject becomes risky, as these wings are more prone to high gust-induced aeroelastic loads, and no parameter exists in the semi-empirical formulation to account for flexibility. For this reason, gust loads were introduced, together with flutter, as additional aeroelastic constraints to be enforced in the proposed aircraft MDAO framework.

Again, a compromise was needed when selecting the tools to be used. The model adopted for flutter predictions was discarded for different reasons. First, the structural model would neglect any nonlinear effect in terms of deformation and pre-stress due to static loads before gust encounter. Also, the implemented unsteady strip theory would not capture three dimensional flow effects around the wing tip. This is not a major concern when addressing flutter, because the phenomenon depends on the entire wing, rather than on local effects confined at wing tip. Even more so if considering that the higher the aspect ratio, the more these effects are localised and the less they are relevant. On the other hand, the outboard wing region is the most critical when evaluating gust loads, because the airloads on that region have greater impact on the bending loads, and because structural twist is accentuated towards the far end of the wing, with a relevant impact on those tip loads. Finally, discrete gust calculations will be limited to

the first wing structural peak frequency, corresponding to a reduced frequency of approximately 0.02, as it will be explained later. Such value is well within the range of 0.0 - 0.05 that is commonly accepted as quasi-steady. Under such conditions, it is assumed that unsteady aerodynamic effects can be neglected. For these reasons, it is preferred to use a three-dimensional aerodynamic solver, such as the VLM, despite quasi-static, rather than a two-dimensional strip theory. In effect, unsteady aerodynamics is more important when studying the flutter phenomenon, where the involved frequencies are at least twice as high as the critical gust frequencies, as the following sections will show.

For these reasons, it was chosen to adopt the same models used for the static aeroelastic sizing: the beam model adapted from `GEBT`, coupled with the developed VLM. In particular, the initial static equilibrium is found exactly as discussed in Section 5.2 at sea level, searching the nonlinear structural solution. Then, the dynamic analysis is carried out from that nonlinear equilibrium, but this time, at each time step, the structural states are updated according to the linear dynamic incremental solution, derived from the instantaneous aerodynamic, inertial and internal loads.

The next Sections give details on how the gust loads constraints are implemented according to regulations (Section 5.3.3.1) and show some examples of the deterministic responses obtained from the baseline configuration, as well as from a higher aspect ratio one (Section 5.3.3.2).

5.3.3.1 Implementation of specifications requirements

The constraints on dynamic gust loads are here introduced following the certification specifications discussed in Section 2.4.2.

The design conditions for encounters with gusts are to be evaluated with respect to steady, 1-g level flight. Here, cruise conditions are used, expressed in equivalent sea-level conditions. This translates into a density of ρ = 1.225 kg/m^3, a flight speed of 135 m/s and a Mach number of 0.4. Because of the assumption of symmetric wingbox made in the structural model, and the flat-plate approximation used for the VLM analysis, only positive (upwards) gust profiles are taken into account. Negative gusts would not add any relevant information.

Before setting up the dynamic gust constraints to be enforced within the MDAO, a preliminary assessment was carried out in order to determine whether there are certain gust conditions, in terms of amplitudes and frequencies, that are worth including and others that can reasonably be excluded to reduce the computational burden. Regulations require that a sufficient number of gust gradient distances in the range 9 m to 107 m must be investigated to find the most critical case. This range was here explored with 10 samples. For each gradient distance H, the corresponding design gust velocity U_{ds} is found by Equation 2.5. The 10 profiles, which can slightly change for each particular

aircraft because of Equations (2.6) to (2.11), would look like those in Figure 5.36. The desired simulation output is the time history of the same three structural loads that are employed as constraints during the static structural optimization. These are the direct stress on the stringers due to bending, σ_b, the vertical shear stress on the spars due to vertical shearing forces, τ_v, and the shear stress on the skin due to twist, τ_t. Consistently with the static structural optimization approach, discussed in Section 5.2.4, the quantities monitored are only those at the wing root.

Strictly speaking, it is also recommended to study all appropriate combinations of airplane configuration, weight, center of gravity, payload, fuel load, thrust, speed, and altitude. As already stated in Section 2.4.2, a full verification of all these combinations is out of the scope of this research. Nevertheless, to gain a wider understanding of the problem, the preliminary study involved not only 10 different gust gradients, but also the two limit fuel conditions of full and empty tanks, with updated aircraft mass and static equilibrium. The outcome of such preliminary assessment is reported and discussed in the following Section.

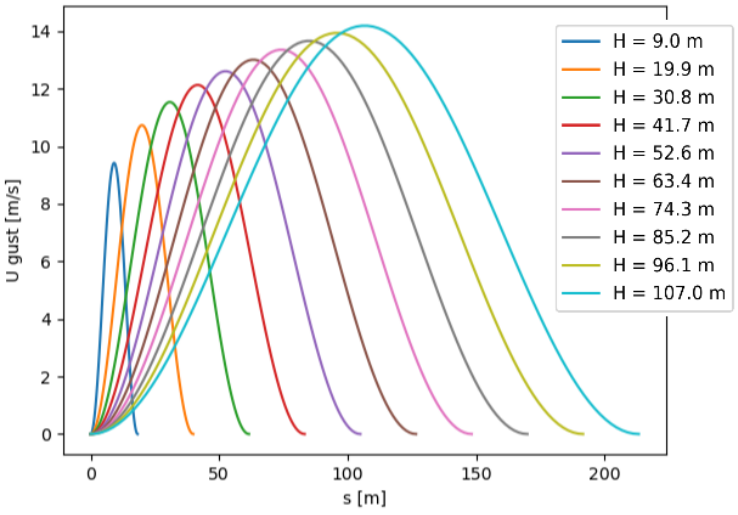

FIGURE 5.36: Example of gust profiles used for preliminary studies on dynamic gust response.

5.3.3.2 Deterministic loads on low and high aspect ratio configurations

A first investigation was carried out on the baseline test case. Dynamic gust response simulations were performed for each of the 10 gust inputs shown in Figure 5.36, initially for the heavy weight configuration (full fuel tanks). The dynamic simulation starts from the nonlinear static equilibrium at load factor 1, which is iteratively obtained as described in Section 5.2.3. The time step and simulation time were adjusted according to each particular gust frequency, with each gust input discretized in 80 steps. The outputs of the structural stresses at root are shown in Figure 5.37 to 5.39.

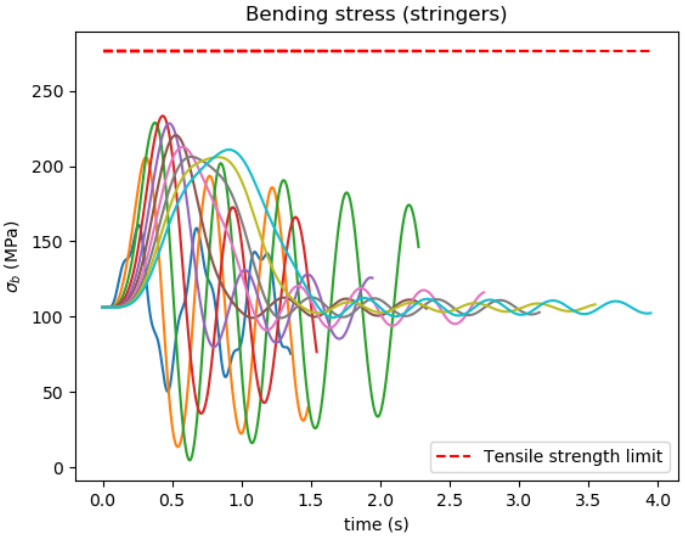

FIGURE 5.37: Bending stress responses to discrete gusts from the baseline test case.

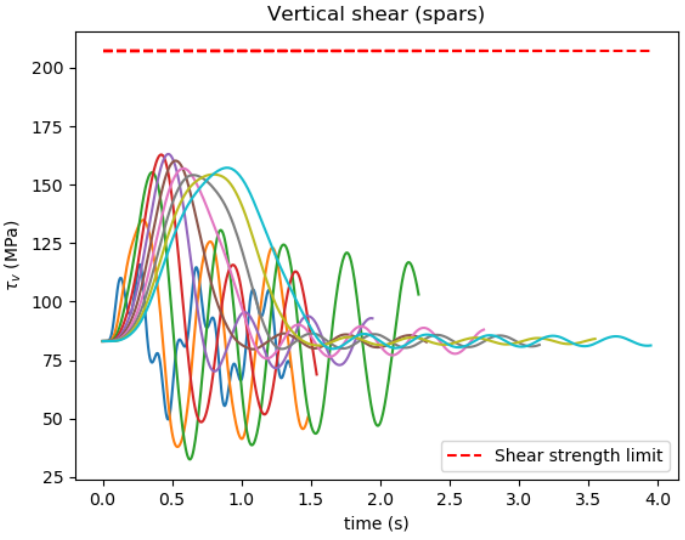

FIGURE 5.38: Vertical shear stress responses to discrete gusts from the baseline test case.

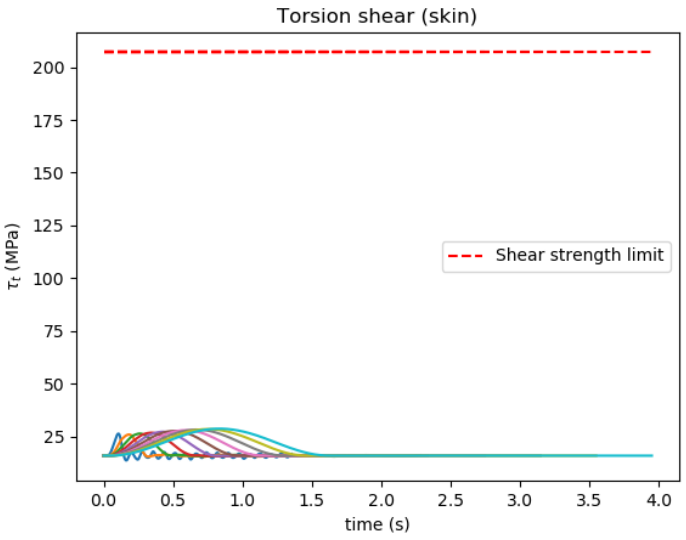

FIGURE 5.39: Torsional shear stress responses to discrete gusts from the baseline test case.

The first observation that emerge by comparing the three outputs is that the loads on the stringers and spars are largely more significant than the torsional shear on the skin. This is an expected result, in line with the static analysis results and with the considerations discussed in Section 5.2.4. The minor importance of the twisting shear stress allows focusing the attention on the other two stress quantities.

From Figures 5.37 and 5.38 it is possible to identify one single worst case, corresponding to a gust gradient of 42 m, or a frequency of 3.2 Hz (reduced frequency $k = 0.049$). The most severe load, when compared with the allowable limits, appear to be the bending stress on the stringers, which in the worst case attains the 85% of the material tensile strength. For the same gust input, the corresponding vertical shear on the spars achieves the 80% of the material shear strength.

The second set of simulations was performed on the '$\mathcal{AR}$ 15' wing, already adopted for other demonstrations previously in this Chapter, still in heavy weight configuration. The responses are reported in Figures 5.40 to 5.42. Again, the only relevant stresses are those arising from bending and vertical shear loads. This time, the worst cases arise from gust gradients between 63 and 74 m, corresponding to around 1.8 and 2.1 Hz (reduced frequency $k = 0.026$ - 0.031). The sensitivity is therefore higher for lower gust frequencies. This is consistent with the fact that the natural frequencies of this high aspect ratio configuration are lower than the baseline ones, as already shown comparing Figures 5.26 and 5.28.

It is also interesting to note that here the structural stresses are higher than for the baseline, despite both cases are safely sized to withstand static loads. This confirms that high aspect ratios bring an increased risk in terms of aeroelastic loads. It can be

seen, in fact, that this time the bending and vertical shear loads reach respectively about 92% and 90% of the material strength in the worst gust cases.

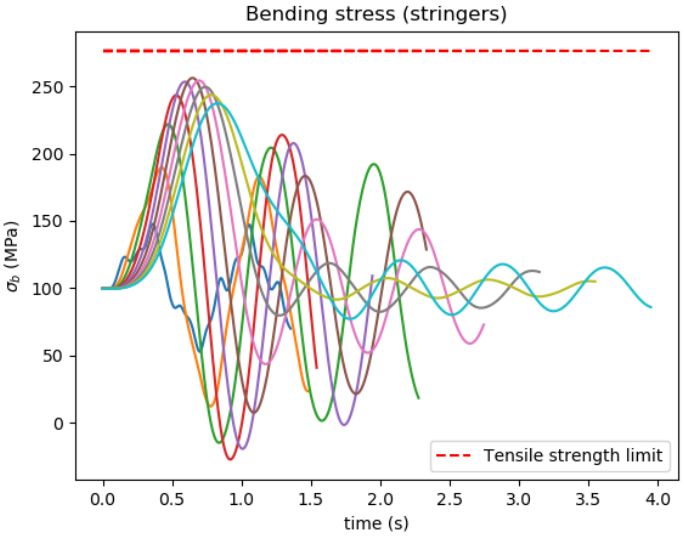

FIGURE 5.40: Bending stress responses to discrete gusts from the aspect ratio 15 test case.

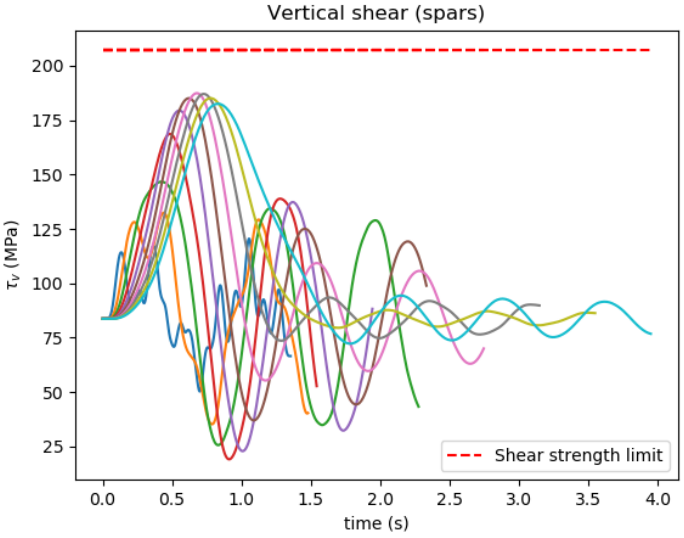

FIGURE 5.41: Vertical shear stress responses to discrete gusts from the aspect ratio 15 test case.

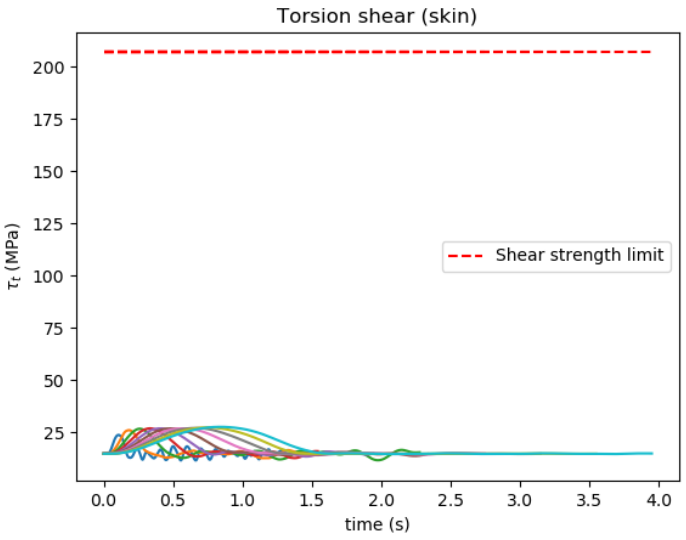

FIGURE 5.42: Torsional shear stress responses to discrete gusts from the aspect ratio 15 test case.

The responses for the empty weight configurations (zero fuel) are reported in Figures 5.43 to 5.45 for the baseline wing and in Figures 5.46 to 5.48 for the '$\mathcal{AR}$ 15' wing. These cases revealed that the reduction of inertia associated to the absence of fuel determines an increase of the modal frequencies, and a reduction in the structural loads. The higher natural frequencies are expected, since it is a well-known physical notion that in any system frequency is proportional to stiffness and inversely proportional to mass or inertia. The loads reduction indicates that inertial loads have a penalising effect, making the structure more sensitive to low frequencies, closer to the range where the most of the turbulence energy is statistically more concentrated. These considerations led to the choice of excluding the empty-weight case from the definition of the gust loads constraints to be enforced during the global MDAO. Only the heavy weight configurations will be considered hereafter.

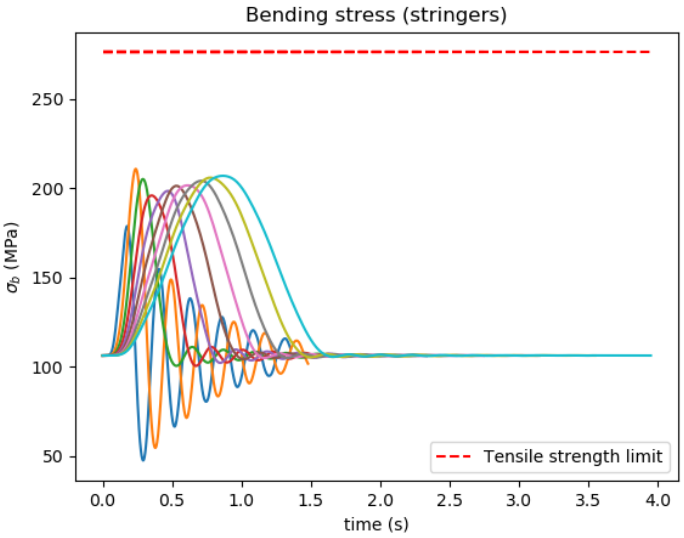

FIGURE 5.43: Bending stress responses to discrete gusts from the empty weight baseline test case.

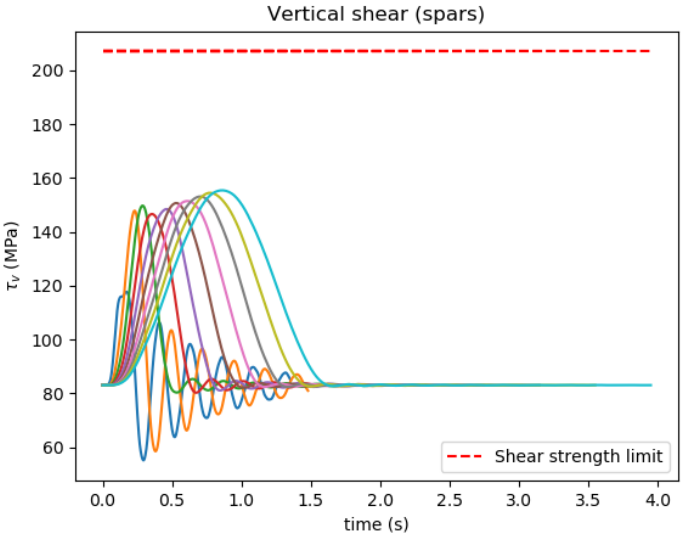

FIGURE 5.44: Vertical shear stress responses to discrete gusts from the empty weight baseline test case.

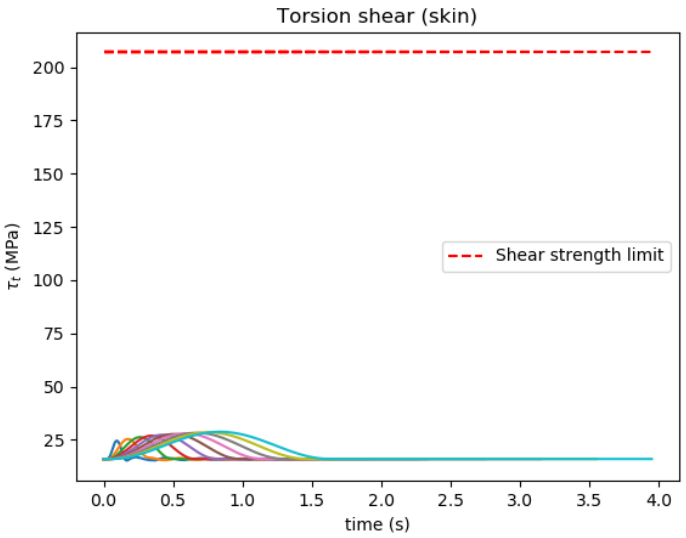

FIGURE 5.45: Torsional shear stress responses to discrete gusts from the empty weight baseline test case.

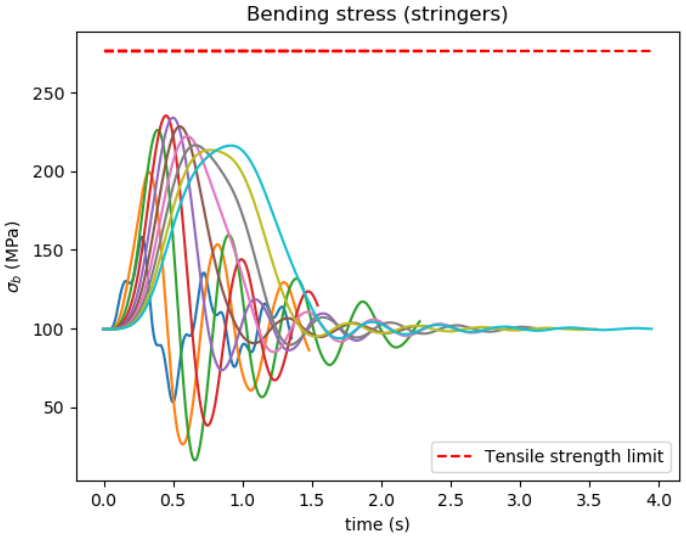

FIGURE 5.46: Bending stress responses to discrete gusts from the empty weight aspect ratio 15 test case.

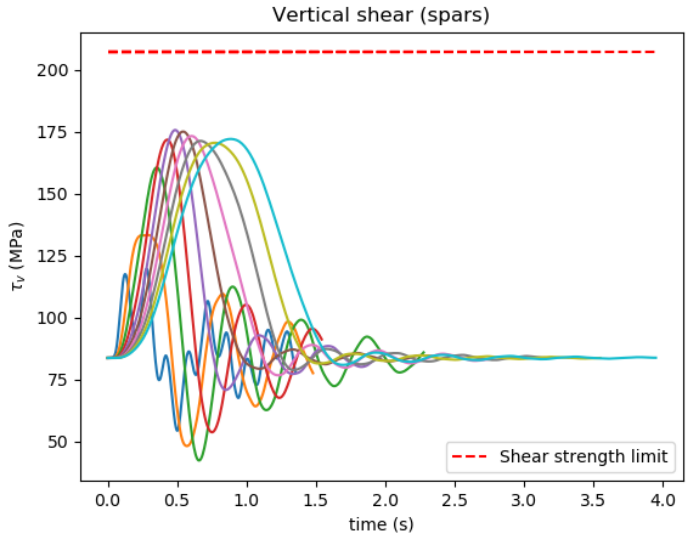

FIGURE 5.47: Vertical shear stress responses to discrete gusts from the empty weight aspect ratio 15 test case.

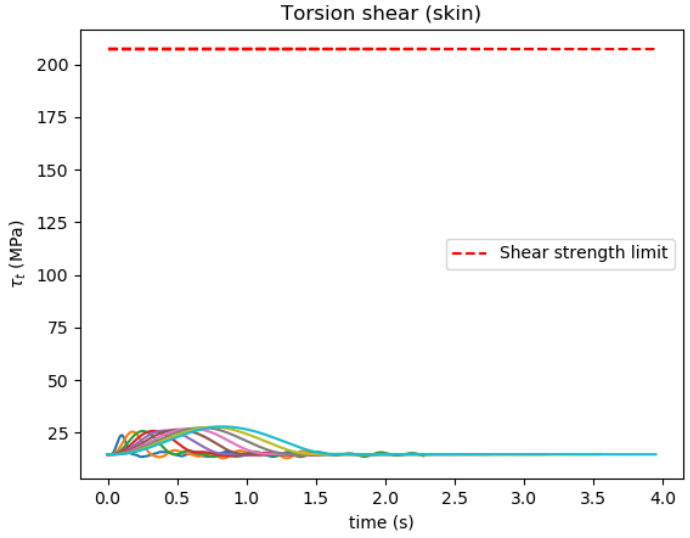

FIGURE 5.48: Torsional shear stress responses to discrete gusts from the empty weight aspect ratio 15 test case.

Overall, two main conclusions are to be drawn out of this preliminary study. The first is the confirmation that high aspect ratio configurations, although statically sized with the same approach and constraints than the low aspect ratio ones, are expected to be less safe with respect to gust loads. The second, which follows, is that the most critical conditions arise when a high aspect ratio wing encounters a gust disturbance of low frequency (around 2 Hz). Although low aspect ratio wings may have a peak response at slightly higher frequencies (around 3 Hz), its impact would not be as severe as for the high aspect ratio wings. Therefore, if the number of analyses has to be minimized

during the conceptual design exploration, it is preferable to focus on low frequency gust inputs, and then verify safety against the entire range only for the final best candidate. Or, a frequency analysis on the linear beam could be run on each candidate to estimate its specific dominant frequency, and then select the most appropriate worst-case gust input. However, even frequency analysis leaves some room for uncertainty, as it only captures the steady state response, without providing information about the transient response. This step was not taken here for simplicity, although it would not require much effort to be implemented in future developments. Instead, it was decided to base the gust loads constraints on one single gust input of frequency 1.8 Hz, leaving the complete verification of safety at the end of the optimization process.

5.3.4 Sensitivity of gust loads to aeroelastic parameters

The same considerations outlined in Section 5.3.2 about the interest for sensitivity of flutter speed to the main aeroelastic parameters apply also for gust loads. The relevant lack of knowledge due to the early design phase, especially in the case of unconventional design exploration, and the unavoidable presence of simplifying assumptions, which limit the accuracy of the aeroelastic predictions, motivate the quest for a robust approach when dealing with aeroelastic constraints. To gain a deeper understanding on the most critical parameters impacting the dynamic gust response, and therefore being able to efficiently and effectively set up the gust reliability constraints, a sensitivity study was performed similarly to what has been done with respect to the flutter speed.

The details, some of which differ from the flutter sensitivity analysis due to the different tools employed, are given in Section 5.3.2.1. Then, as for the flutter case, two studies are reported and compared in Section 5.3.4.2.

5.3.4.1 Problem definition

The sensitivity analysis performed on gust loads was kept basically specular to the one done on flutter speed. The only difference arises from the fact that the beam model used in the gust loads analysis is more detailed than the one used for flutter, as already discussed (see Section 5.3.3). For this reason, a further selection had to be made. More in detail, the flutter sensitivity analysis was run with respect to the following six parameters: the elastic axis location a, its offset d from the center of gravity, the mass per unit length μ, the bending and torsional stiffnesses EI_{yy}^{A} and GJ, the polar moment of inertia I_p. Each of the two bending and torsional stiffnesses is defined by the product of two different parameters. Whereas the beam model used for the flutter analysis only needs their products, making irrelevant whether the uncertainty comes from the elastic modulus or from the section geometry, the beam model adopted for gust analysis treats the four parameters (E, I_{yy}^{A}, G and J) independently when building the stiffness

and mass matrices. Therefore, if one wants to replicate the same sensitivity analysis problem as the one presented in Section 5.3.2.1, a choice has to be made on which of the four parameters carries the uncertainty. A choice was made based on the simple assumption that the aluminium elastic moduli cannot vary to the same extent as the wing-box geometry may do. Therefore, it was decided to fix them to their nominal values, and assign the uncertainty only to the geometry-governed parameters: the inertia moment I_{yy}^A and the torsion constant J. All the other parameters are treated exactly the same way as done for the flutter sensitivity analysis. The uncertainty distributions are summarized in Table 5.9. The following Section presents and discusses the results of two sensitivity analyses on the two usual wing configurations.

Property	**Mean**	**Standard deviation**
Elastic axis location	$\overline{a}$	$3\varsigma = 10\%$ chord
CG shift from EA	$\overline{d}$	$3\varsigma = 5\%$ chord
Mass per unit length	$\overline{\mu}$	$3\varsigma = 10\%\,\overline{\mu}$
Bending stiffness	$\overline{I}_{yy}^A$	$3\varsigma = 10\%\,\overline{I}_{yy}^A$
Torsional stiffness	$\overline{J}$	$3\varsigma = 10\%\,\overline{J}$
Polar moment of inertia	$\overline{I}_p$	$3\varsigma = 10\%\,\overline{I}_p$

TABLE 5.9: Uncertain parameters and corresponding distributions adopted for the gust loads sensitivity analysis. All distributions are Gaussian. Symbols denoted with a bar $\bar{(\,)}$ represent the nominal values produced by the sizing and optimization process. The symbol ς indicates the standard deviation.

5.3.4.2 Application to the baseline and the high aspect ratio test-cases

The two studies here presented refer to the same two test cases used previously in this Chapter, the baseline and the aspect ratio 15 configuration. The three quantities of interest monitored are those already discussed when defining the static and dynamic load constraints: the direct bending stress on the stringers σ_b, the vertical shear stress on the spars τ_v, and the torsional shear on the skin τ_t. As before, these are only the loads at the wing root. Similarly to what was done for the flutter speed constraint, it was decided to consider 'robust' any configuration whose probability of resulting safe is at least 95%. This is equivalent to saying that the 95th percentile P_{95} of the output distribution must be lower than the material strength.

As far as the baseline is concerned, the output distributions of the three loads are reported in Figure 5.49. The unsafe zones are again highlighted with a red shade. The three Figures qualitatively show that the baseline is quite robust with respect to the injected uncertainty. They also confirm that the most critical constraint is the bending one, for which P_{95} = 226 MPa, amounting to 82% of the material yield strength. It is immediately followed by the vertical shear, with P_{95} = 163 MPa, at 80% of the material

shear strength. As expected, considering the results from the deterministic analysis, the torsional loads are significantly lower, with a P_{95} of just 40 MPa.

The sensitivity analysis results for the three types of loads are graphically summarized in Figure 5.50, and numerically reported in Tables 5.10 to 5.12. The most important result to be drawn out from the three Figures is the net prevalence of one single parameter: the elastic axis location a. In all the three loads its first-order Sobol indices of 0.74, 0.81 and 1.0 largely exceed the indices of the other five parameters. For the bending and vertical loads, a secondary role is played by the mass per unit length μ, with first order indices of 0.12 and 0.09, respectively. A slightly lower sensitivity is exhibited with respect to the inertia moments and the CG to EA distance d. In the case of twisting loads, almost zero sensitivity is found to all parameters except the elastic axis location. Finally, it should be noted that in the three cases the sum of the first-order Sobol indices is exactly one, revealing no relevant sensitivity to the interactions among the different parameters.

These results are somehow in line with what was found for the flutter sensitivity analysis: also in that case the most important parameter was the elastic axis location. Differently from that case, though, the CG to EA distance is much less relevant. This can be explained by considering that the main physical effect of this parameter is to introduce an inertial coupling between bending and torsional dynamics. Now, since flutter usually arises from the aeroelastic coupling between bending and torsional modes, with their frequencies moving close to each other, it is easily understood that the speed at which this instability phenomenon appears may be relevantly impacted by the bending-torsion inertial coupling introduced by the offset d. This coupling results of minor importance in the case of gust encounters, because the speed is low enough to have bending and torsional frequencies well separated, so that the gust input excites essentially only one type of response (bending in most cases). It can be added that mass and inertia have a lower impact at the simulated gust conditions because the frequency is not high enough to trigger strong inertial loads. The elastic axis location, on the other hand, remains of primary importance because it affects the aerodynamic pitching moment acting on the structure both in the static and in the dynamic cases.

When moving to the high aspect ratio test case, only a few differences can be observed. First, if one looks at the three output distributions in Figure 5.51, they are shifted towards higher loads values compared to the baseline case. This is an expected outcome, reflecting what was already observed with the deterministic tests. The distributions are also wider, as also indicated by the higher standard deviations, confirming that flexible wings involve not only higher levels of structural stress, but also higher uncertainty with respect to model errors or future design changes. In fact, this precise configuration does not meet all the reliability requirements: the 95th percentile of the bending stress distribution, $P_{95}(\hat{\sigma}_b)$, which amounts to 279 MPa, is higher than the material yield

strength, which means that the probability of encountering bending stress at root above the allowable limit is higher than 5%.

A second main difference with respect to the baseline results is in the sensitivity analysis. Here, the importance of the elastic axis location is even higher than for the baseline, with the respective Sobol indices equal almost to one in the three load types (see Figure 5.52 and Tables 5.13 to 5.15). The difference can be explained by the fact that the dominating frequencies are even lower, so that a gust encounter is even closer to a static phenomenon, where the elastic axis location plays the most important role.

Despite these quantitative differences, a common, qualitative result of these two sensitivity studies is that one single parameter, the EA location, dominates the output distributions. For this reason, in order to minimize the computational cost of the probabilistic approach to the global MDAO process, it was decided that the uncertainty will only be attributed to this parameter when evaluating the robustness against the gust loads constraints.

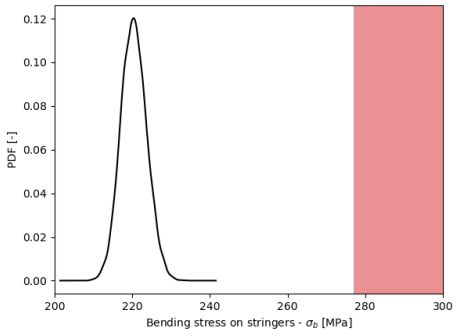

(a) Bending stress - σ_b

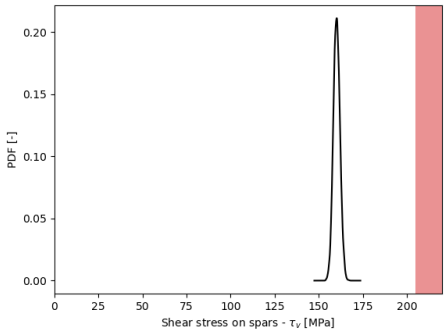

(b) Vertical shear - τ_v

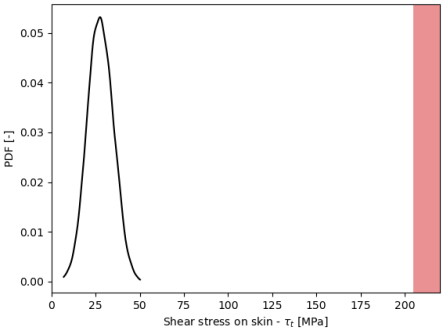

(c) Torsional shear - τ_t

FIGURE 5.49: Gust loads distributions following uncertainty propagation on the CeRAS baseline wing. The area shed in red indicates the imposed safe region: the probability of loads occurring within this region should be lower than 5%. The baseline results robust enough with respect to all constraints.

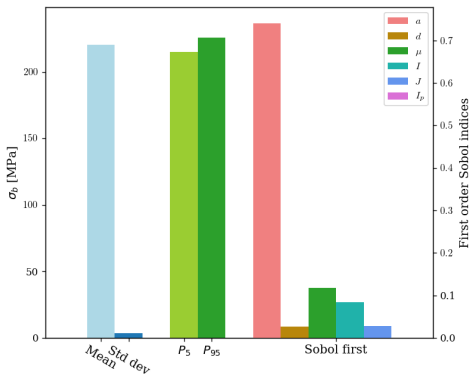

(a) Bending stress on stringers - σ_b

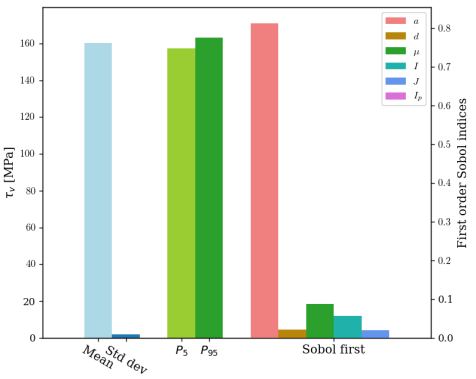

(b) Vertical shear on spars - τ_v

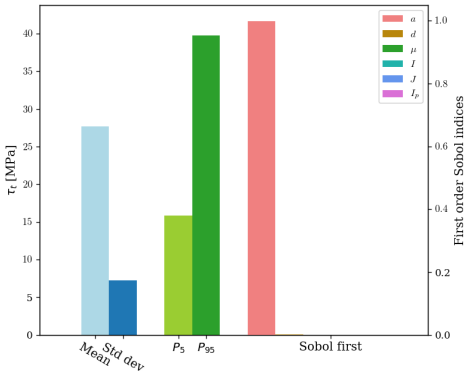

(c) Torsional shear on skin - τ_t

FIGURE 5.50: Main statistical figures from the sensitivity analysis and uncertainty quantification on the gust-induced loads at wing root for the CeRAS baseline wing.

Distribution properties							
Mean	220 MPa						
Standard deviation	3 MPa						
95th percentile (P_{95})	226 MPa						
Sensitivity indices							
	a	***d***	***μ***	***I***	***J***	***I_p***	**Sum**
Sobol first	**0.74**	0.03	0.12	0.08	0.03	7.8e-6	1.0
Sobol total	**0.74**	0.03	0.12	0.08	0.03	3.0e-5	1.0

TABLE 5.10: Main statistical figures from the sensitivity analysis and uncertainty quantification on the gust-induced bending loads at wing root for the baseline configuration.

Distribution properties							
Mean	160 MPa						
Standard deviation	2 MPa						
95th percentile (P_{95})	163 MPa						
Sensitivity indices							
	a	***d***	***μ***	***I***	***J***	***I_p***	**Sum**
Sobol first	**0.81**	0.02	0.09	0.06	0.02	1.2e-5	1.0
Sobol total	**0.81**	0.02	0.09	0.06	0.02	3.0e-5	1.0

TABLE 5.11: Main statistical figures from the sensitivity analysis and uncertainty quantification on the gust-induced vertical shear loads at wing root for the baseline configuration.

Distribution properties							
Mean	28 MPa						
Standard deviation	7 MPa						
95th percentile (P_{95})	40 MPa						
Sensitivity indices							
	a	***d***	***μ***	***I***	***J***	***I_p***	**Sum**
Sobol first	**1.0**	1.0e-3	4.0e-7	2.2e-6	1.1e-6	6.7e-8	1.0
Sobol total	**1.0**	1.0e-3	4.0e-7	2.0e-6	6.3e-6	4.0e-8	1.0

TABLE 5.12: Main statistical figures from the sensitivity analysis and uncertainty quantification on the gust-induced torsional shear loads at wing root for the baseline configuration.

Distribution properties							
Mean	256 MPa						
Standard deviation	13 MPa						
95th percentile (P_{95})	279 MPa						
Sensitivity indices							
	a	***d***	***μ***	***I***	***J***	***I_p***	**Sum**
Sobol first	**0.98**	7.7e-4	1.4e-3	2.3e-3	0.01	4.2e-6	1.0
Sobol total	**0.98**	9.8e-4	1.4e-3	2.6e-3	0.01	1.8e-5	1.0

TABLE 5.13: Main statistical figures from the sensitivity analysis and uncertainty quantification on the gust-induced bending loads at wing root for the '$\mathcal{AR}$ -15' configuration.

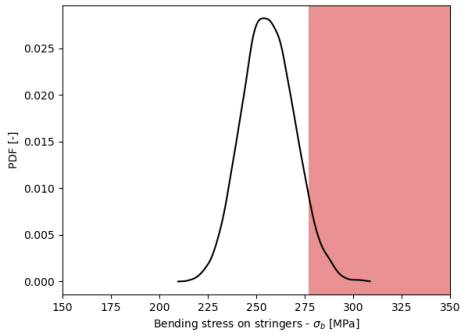

(a) Bending stress on stringers - σ_b

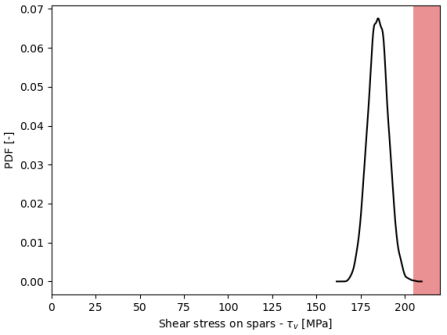

(b) Vertical shear on spars - τ_v

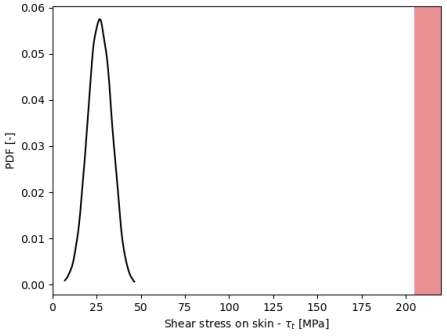

(c) Torsional shear on skin - τ_t

FIGURE 5.51: Gust loads distributions following uncertainty propagation on the '$\mathcal{AR}$ 15' wing. The area shed in red indicates the imposed safe region: the probability of loads occurring within this region should be lower than 5%. This configuration does not result robust enough with respect to the bending loads.

Distribution properties							
Mean	184 MPa						
Standard deviation	6 MPa						
95th percentile (P_{95})	194 MPa						
Sensitivity indices							
	a	***d***	***μ***	***I***	***J***	***I_p***	**Sum**
Sobol first	**0.95**	0.01	4.6e-5	0.02	0.01	1.3e-5	1.0
Sobol total	**0.95**	0.01	9.1e-4	0.02	0.01	6.2e-5	1.0

TABLE 5.14: Main statistical figures from the sensitivity analysis and uncertainty quantification on the gust-induced vertical shear loads at wing root for the '$\mathcal{AR}$ -15' configuration.

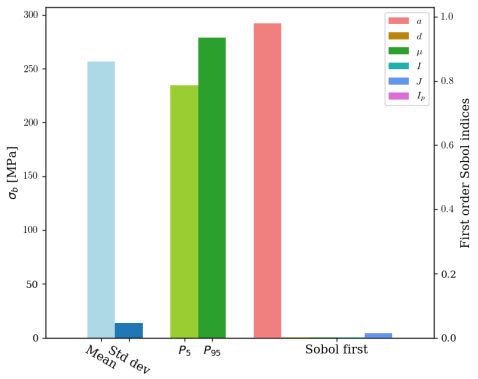

(a) Bending stress on stringers - σ_b

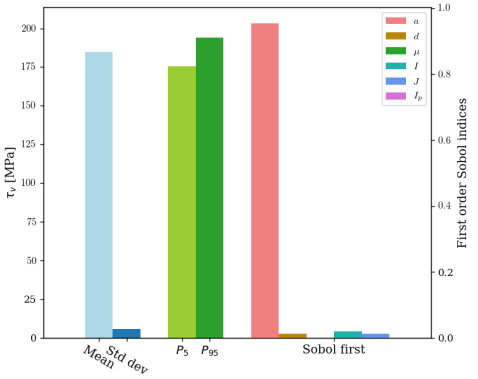

(b) Vertical shear on spars - τ_v

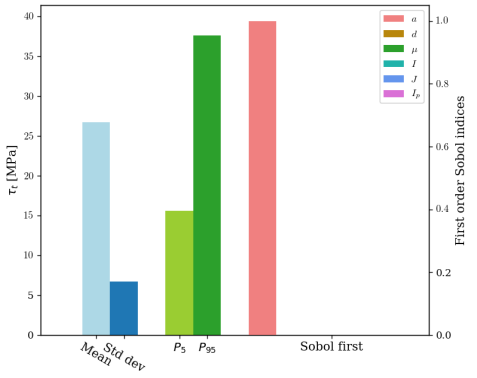

(c) Torsional shear on skin - τ_t

FIGURE 5.52: Main statistical figures from the sensitivity analysis and uncertainty quantification on the gust-induced loads at wing root for the '$\mathcal{AR}$ 15' wing.

Distribution properties							
Mean	27 MPa						
Standard deviation	7 MPa						
95th percentile (P_{95})	38 MPa						
Sensitivity indices							
	a	***d***	***μ***	***I***	***J***	***I_p***	**Sum**
Sobol first	**1.0**	4.9e-6	3.0e-5	2.4e-5	1.1e-4	2.1e-7	1.0
Sobol total	**1.0**	4.9e-6	6.0e-5	5.0e-5	1.5e-4	1.5e-7	1.0

TABLE 5.15: Main statistical figures from the sensitivity analysis and uncertainty quantification on the gust-induced torsional shear loads at wing root for the '$\mathcal{AR}$ -15' configuration.

5.4 Summary

This Chapter proposes an MDAO architecture to enable the overall design and optimization of flexible aircraft, taking into account nonlinear static aeroelasticity during the wing sizing process, and allowing to propagate input uncertainty into some dynamic aeroelastic constraints, including flutter speed and gust loads. The Chapter is structured as follows:

- An overview of the problem is given, and two proposed architectures are described, corresponding to the deterministic and to the robust approaches.
- One of the main added values of this development is the sizing and optimization of flexible wings and its implementation within the overall aircraft sizing process. These aspects are thoroughly discussed, and some examples are presented, serving also as validation cases for such newly-introduced capabilities.
- Considerable space is also given to the implementation of the dynamic aeroelastic constraints. Dedicated sections describe how the flutter and gust constraints are defined, explain how flutter analysis and gust response simulations are carried out, and provide numerical examples.
- As robustness in the optimization represents another key contribution of this work, this Chapter also details how uncertainty can be propagated into the flutter and gust loads constraints.
- Some sensitivity analyses and uncertainty quantification examples are performed to achieve a better understanding of the parameter dependencies, enabling to select only the most relevant input uncertainty and therefore reduce the computational burden of the overall robust MDAO.

Demonstrative applications of the deterministic and robust MDAO process using the above architectures are presented in the next chapter.

Chapter 6

Robust MDAO studies

Contents

5.1 Overview 134

5.2 Flexible wing sizing 140

5.2.1 Initial sizing of a wing-box structure 140

5.2.2 Beam model generation for aeroelastic analysis 145

5.2.3 Sizing load case definition 150

5.2.4 Static structural optimization of flexible wings 152

5.2.5 Consistency against overall aircraft sizing 164

5.3 Dynamic aeroelastic constraints under uncertainty 168

5.3.1 Deterministic flutter speed on low and high aspect ratio configurations 170

5.3.2 Sensitivity of flutter speed with respect to aeroelastic parameters 175

5.3.3 Dynamic gust response 187

5.3.4 Sensitivity of gust loads to aeroelastic parameters 197

5.4 Summary 205

6.1 Overview

The previous Chapter presented the different building blocks of the developed MDAO framework, covering not only the overall structure, but also the details of numerical methods, inner processes such as coupled analyses, optimization and uncertainty quantification, and of how the information is exchanged among the different modules. Several demonstrative test cases were also given to better illustrate the main functionalities.

With all these aspects being clarified, it is now possible to show some applications of the whole MDAO process. In all cases, the definition of the optimization problem is kept relatively simple, as the work represents the first application of the proposed approach. Applications to higher dimension design spaces, or to more complex configurations, such as strut-braced wings, are interesting perspectives for a future evolution of the present research work.

The overall MDAO process was given for the deterministic and robust approach in Figures 5.1 and 5.2, respectively. Also, the aircraft baseline and the mission definition are the same as in Figure 4.1 and Table 4.1. The design space is limited to three dimensions, selected among some wing shape variables that have a relevant physical impact either on the objective function or on the constraints, or both. The first and most important one is the wing aspect ratio, for the obvious reason that it greatly influences both the aerodynamic efficiency - and therefore the fuel consumption - and the aeroelastic characteristics of the wing. This was already seen in Chapter 5 when comparing the aeroelastic behaviour of the '$\mathscr{R}$ 15' test case against that of the baseline configuration. The second selected variable is the taper ratio. This parameter influences the span-wise lift distribution, which in turn impacts on the one hand the aerodynamic efficiency and on the other the aerodynamic and inertial loads transferred to the structure - a high taper ratio moves those loads outboard - impacting both the static and the dynamic aeroelastic response. Finally, the kink span ratio is selected as the third and last wing planform variable. It has a secondary effect on the aerodynamic efficiency in comparison to the two previous variables, but it is expected to have an impact on the aeroelastic behaviour of the wing, because it changes its structural layout, especially towards the root sections where loads are higher. Modifying the structural shape also impacts the amount of material to be added to reach adequate structural strength. For example, from a structural point of view it is in principle desirable to have a large chord - and therefore a larger profile thickness - at the wing root, because the larger wing box would better absorb bending and twisting loads with employing less structural mass. Also, a wing which is larger at root would have loads more concentrated inboard, producing lower bending loads and therefore allowing a lighter structure. As a consequence, because it impacts the airframe mass, this quantity would also have an indirect, secondary effect on the fuel consumption.

Other important parameters, that it would be interesting to add in future studies, would be for example the sweep angle and the twist. Both of them contribute considerably to the aerodynamic efficiency and the wing aeroelastic performance, both static and dynamic. Nevertheless, the former is not touched here because a credible assessment of its aeroelastic effects would require some analysis at the transonic conditions experienced at cruise, possibly involving localised shock waves and buffeting, which remains a challenging task to be addressed at such an early design phase. Regarding twist, the main reason why it is not included as a variable is because its effect on the drag polar and therefore on the fuel consumption is not accounted for in `FAST-OAD`, which assumes the twist is already optimized to provide an almost elliptical span-wise lift distribution. Taking into account the effects of twist in the computation of the flexible wing polar would require an expensive coupling with the aeroelastic module. This is something feasible with the tools and interfaces already available at this stage of the development, and the only reason why such coupling was not put in place was to reduce the computational burden of each configuration analysis, with the priority given to the evaluation of the dynamic aeroelastic constraints. Therefore, for the following analyses a fixed linear twist distribution was assigned, culminating with a 5.0° nose down at the wing tip, with respect to the root chord. Finally, it is worth noting that the wing area is not a degree of freedom of the problem because it is sized by the OAD process to match low-speed performance and tank volume requirements. Therefore the optimization can only concentrate on the variables that influence the planform at iso-area.

This choice of design variables and fixed parameters applies to all the following optimization cases, which differ only by what aeroelastic constraints are adopted and whether they are treated as deterministic or probabilistic.

This Chapter continues with an optimization task carried out using only the conventional aircraft sizing tool `FAST-OAD`, based on traditional design rules assuming rigid airframe. The results are reported in Section 6.2. This will serve as a reference for comparison against some MDAO studies on flexible aircraft. These are presented in the subsequent Sections, where different combinations of the dynamic aeroelastic constraints were enforced, following both the deterministic (Sections 6.3.1 to 6.3.3) and the robust approaches (Sections 6.4.1 to 6.4.3).

6.2 Rigid aircraft optimization

The optimization task here presented is aimed at providing a reference from a conventional rigid aircraft design approach for comparison with the proposed flexible aircraft design approach. As stated above, the objective function to be minimized is the fuel

mass, and the design variables are the wing aspect ratio, taper ratio and kink span location. The aspect ratio, which is believed to play the main role, is allowed to vary in a large range, between 8.0 and 20.0, with the CeRAS baseline placed close to the lower bound, at $\mathcal{AR} = 9.5$. The remaining two variables change in a smaller range around the baseline values, because large deviations from it would appear quite unrealistic.

As the involved methods only apply to rigid aircraft design, no aeroelastic constraints can be enforced. The optimization is therefore unconstrained. All the top level aircraft requirements are automatically satisfied with the internal `FAST-OAD` sizing loops. The problem definition is summarized in Table 6.1.

	Function/variable	**Lower bound**	**Upper bound**
Minimize	Fuel mass		
with respect to	Aspect ratio	8.0	20.0
	Taper ratio	0.25	0.35
	Kink span ratio	0.2	0.4
subject to	No aeroelastic constraints applicable		

TABLE 6.1: Definition of the fuel mass optimization problem for a rigid aircraft.

A description of the optimization process and its outcome is provided in Figures 6.1 to 6.4. The first part of the optimization is the learning phase, where the optimizer performs a design exploration according to a Design of Experiment (DOE) of a prescribed size. The DOE is automatically created by `SEGOMOE` following a Latin Hypercube Sampling scheme. Once the DOE is analyzed, the optimizer starts the actual optimization iterations based on a Gaussian process, in a balance between exploitation of the acquired information and exploration of new candidates selected according to the best expected improvement. The purely exploratory part where the DOE is evaluated is shaded in yellow in all the following images. The size for the DOE was set equal to 13, and its last point is imposed to be the baseline configuration, corresponding to an aspect ratio of 9.5, taper ratio 0.31 and kink span ratio 0.375. Then, the optimization is allowed running for 30 additional iterations, for a total number of 43 candidates evaluated.

Figures 6.1 and 6.2 report the monitor plots of the objective function and the design variables, respectively. These plots show the chronological evolution of the optimization process, including the initial DOE evaluation. It can be seen that immediately after the DOE, the optimizer starts converging towards the optimal region. The design variables slightly fluctuate towards their optimal combination, which is practically found already at the 20th iteration. The remaining evaluations only involve imperceptible changes, except the very last ones, where some additional exploration is attempted, somehow forcibly, without delivering any improvement.

The convergence to the optimum is better shown in Figures 6.3 and 6.4, where only the current best objective and variables are traced. In particular, Figure 6.3 gives an idea of how quickly and in what measure the fuel mass is reduced in comparison with the baseline value. The improvement is of about 700 kg of fuel, which represents a reduction of almost 4%, a quantity not huge but nonetheless considerable. The variable plots, both in Figure 6.2 and 6.4, clearly indicate that the best configuration is reached in correspondence of an aspect ratio of about 15, taper ratio 0.35 and kink span ratio 0.4. The first value is remarkable, as it shows a clear trend towards a very high aspect ratio wing compared to the baseline. This figure alone confirms the need to pursue the optimization study with the added aeroelastic capabilities. Moreover, the slightly increased taper ratio involves some shift of the aerodynamic loads towards the wing tips, making it interesting to study how this change would impact the aeroelastic behaviour of the wing, and whether it would comply with the dynamic aeroelastic constraints or not. The kink position at 40% of the wing span is quite close to the baseline value of 37.5%, suggesting that this quantity is already close to the real optimum. This value should have a positive influence from an aeroelastic point of view, as it implies that the inboard section of the wing is quite large, so that there is room for a strong structure in the most critical region of the wing.

The optimal wing planform is represented in Figure 6.5, together with the baseline one for comparison.

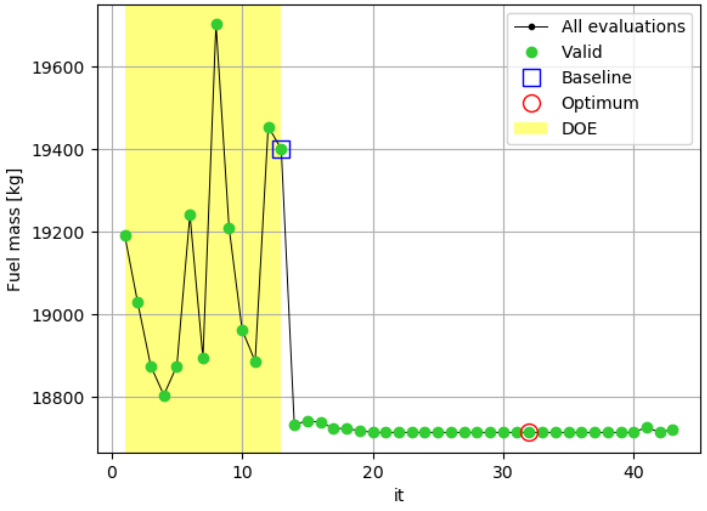

FIGURE 6.1: Optimization process using the conventional FAST-OAD approach. Monitor plot of the fuel mass objective function through the SEGOMOE optimization iterations.

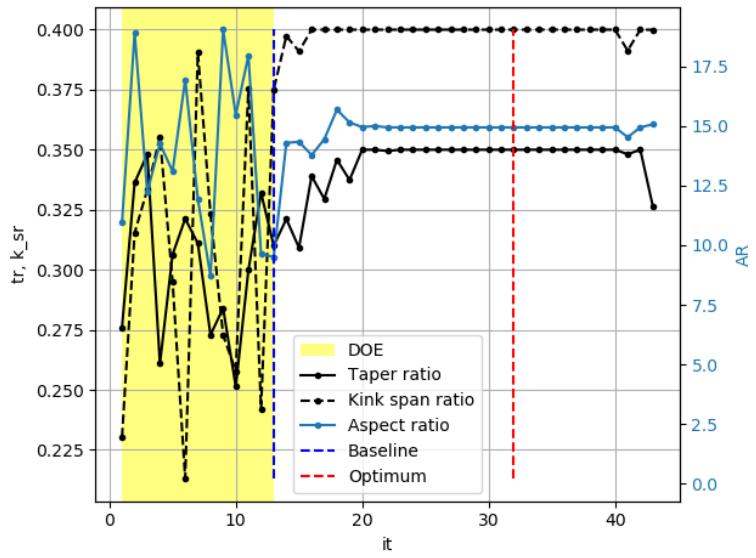

FIGURE 6.2: Optimization process using the conventional FAST-OAD approach. Monitor plot of the three design variables through the SEGOMOE optimization iterations.

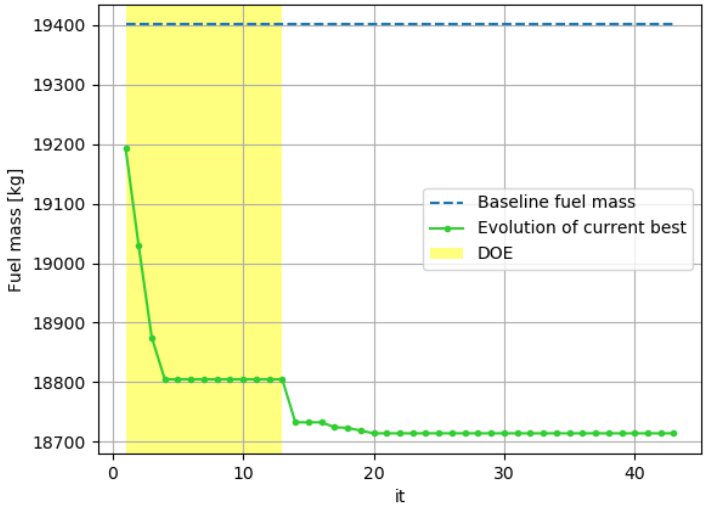

FIGURE 6.3: Optimization process using the conventional FAST-OAD approach. Evolution of the current best fuel mass through the SEGOMOE optimization iterations.

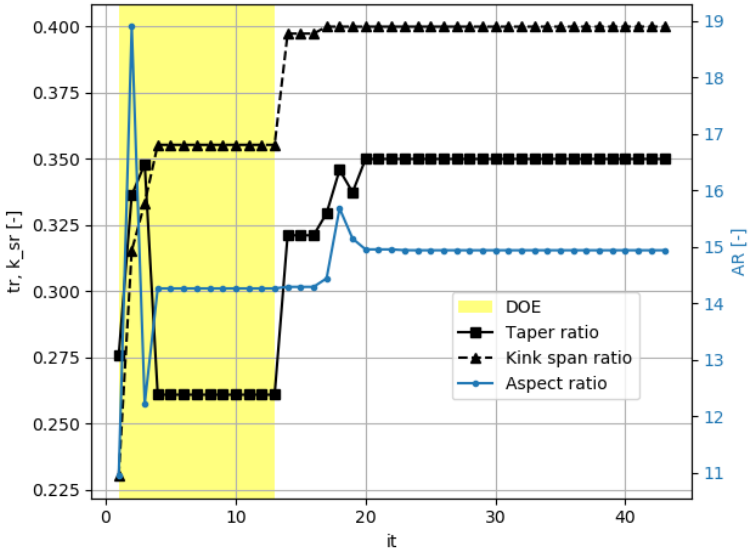

FIGURE 6.4: Optimization process using the conventional FAST-OAD approach. Evolution of the current best design variables through the SEGOMOE optimization iterations.

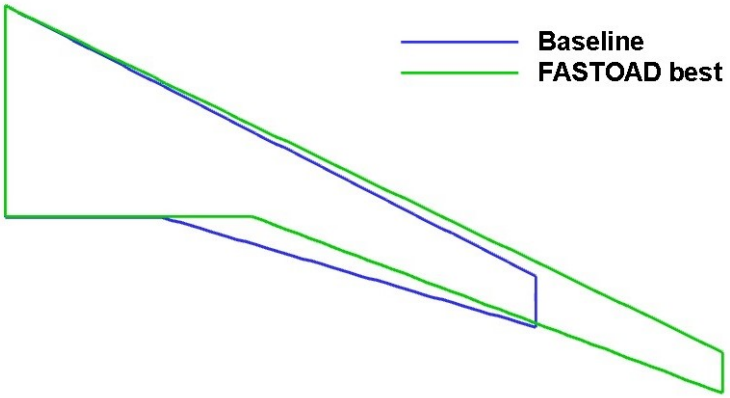

FIGURE 6.5: Best wing planform from the unconstrained rigid aircraft optimization. The baseline wing planform is also reported for comparison.

6.3 Deterministic MDAO results

The first application of the MDAO framework for flexible aircraft design was aimed at addressing the optimization problem introduced earlier in this Section with enforcing the discussed aeroelastic constraints in a deterministic way. In this case, the framework architecture corresponds to the one outlined in Figure 5.1. Three possible combinations for the constraints' setup were tested separately: flutter constraint only, gust loads constraints only, flutter and gust constraints together. These three cases are presented in Sections 6.3.1, 6.3.2 and 6.3.3, respectively.

6.3.1 Optimization under flutter constraint only

The first proposed application of a MDAO using the developed framework involves the enforcement of one dynamic aeroelastic constraint targeting the flutter speed. It was imposed that acceptable configurations are those with a flutter speed above 200 m/s. The choice of this value was justified in Section 5.3.1.

Because a constrained optimization is more challenging than an unconstrained one, the initial DOE size was slightly increased with respect to the previous unconstrained, rigid aircraft optimization, going from 13 to 15. Among these points, the last two were imposed to be the baseline configuration and the optimal configuration obtained in the previous optimization, which relied exclusively on the original `FAST-OAD` modules. The number of subsequent optimization iterations was also increased to 35, bringing the total number of evaluations to 50.

It should be noted that for ease of representation, all constraints are plotted after being normalized and translated to be referred to zero. In the case of flutter, the normalized constraint value is defined as:

$$c(V_f) = \frac{(V_f - 200)}{200} \tag{6.1}$$

In this way, negative values correspond to constraint violations. Also, for instance, a constraint value of 0.2 would mean that the flutter speed is 20 % higher than the defined minimum threshold of 200 m/s, i.e. $V_f = 240$ m/s. The problem definition is summarized in Table 6.2.

The monitor plots of the optimization process are given in Figures 6.6 and 6.7. In particular, the first one presents the evolution of both the objective function and the flutter constraint over the iterations. The second one reports the corresponding trajectories of the three design variables. Note that the unacceptable region, where constraints are violated, is shaded in red in Figure 6.6(b). The same is done for all the following constraint plots of this Chapter.

	Function/variable	Lower bound	Upper bound
Minimize	Fuel mass		
with respect to	Aspect ratio	8.0	20.0
	Taper ratio	0.25	0.35
	Kink span ratio	0.2	0.4
subject to	$V_f > 200$ m/s $\Rightarrow$ $c(V_f) > 0$		

TABLE 6.2: Definition of the MDAO problem for the flexible aircraft with a deterministic constraint on flutter speed.

A few aspects are worth to be commented. To begin with, at a first glance it is quite evident that the optimizer is efficient at approaching the optimal region, as the fuel mass values in Figure 6.6(a) drops close to the optimum immediately after the computation of the DOE. Second, Figure 6.6(b) reveals that the deterministic flutter constraint is rarely violated, and this happens only in correspondence of the highest aspect ratios. An interesting point to focus the attention on is the candidate that scored best in the rigid aircraft optimization based on `FAST-OAD`. It is identified by a green diamond in Figure 6.6(a), and by a green dashed line in Figures 6.6(b) and 6.7. In fact, under the new approach where aeroelasticity is taken into account, this configuration not only turns out to be unsafe by violating the flutter constraint, but it does not even appear as efficient as predicted from the basic `FAST-OAD` analysis in terms of fuel consumption. Indeed, its fuel mass is increased to above 18,900 kg, around 1.3% higher than what estimated with the rigid aircraft approach. This is due to the static flexible wing sizing, that required a stronger and heavier wing structure in order to resist the high loads. For this reason, the candidate no longer results optimal. The best configuration, instead, was found in correspondence of the lower aspect ratio of 13.2 (the numerical optimization results are collected in Table 6.3). Its figure of merit amounts to 18,800 kg, just above the 18,700 kg of the best configuration from the rigid aircraft approach of `FAST-OAD`. It is interesting to note that together with the aspect ratio, also the optimal taper ratio changed with respect to the rigid aircraft optimization, shifting from 0.35 to 0.25. This drop is another effect of the aeroelastic sizing, which penalizes the shift outboard of the aerodynamic loads caused by high taper ratios. In fact, at a lower taper ratio the reduction of bending loads, which translates into a lighter structure, compensates the loss in aerodynamic efficiency. As far as the kink span location is concerned, it was already anticipated that the `FAST-OAD` optimum at 0.4 would have likely benefited to the aeroelastic behaviour of the wing, because it concentrates a larger fraction of the wing area closer inboard, contributing to loosen bending loads and thus reducing the required airframe weight. Such considerations are confirmed by these new results, as the optimal kink span ratio remains unchanged.

A clearer view of the fuel minimization process is given in Figures 6.8 and 6.9, plotting

the evolution of the current best fuel mass and the corresponding constraint and variables. Additionally, the optimal wing configuration is shown in Figure 6.10, together with the baseline and the optimal wing found with the rigid airframe approach.

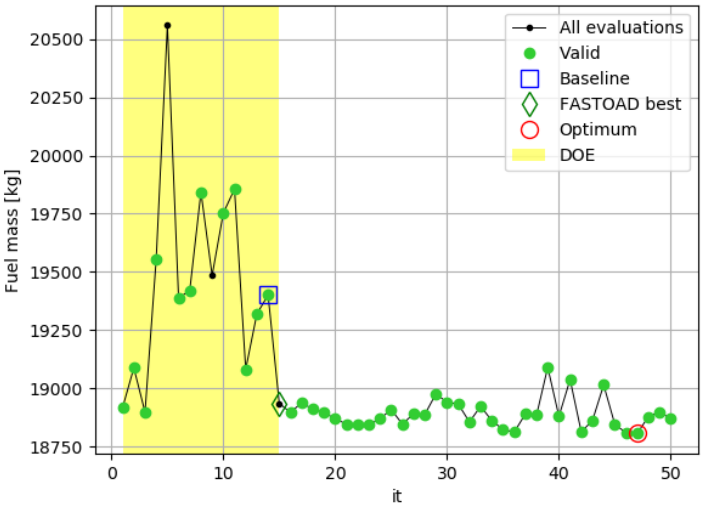

(a) Fuel mass objective

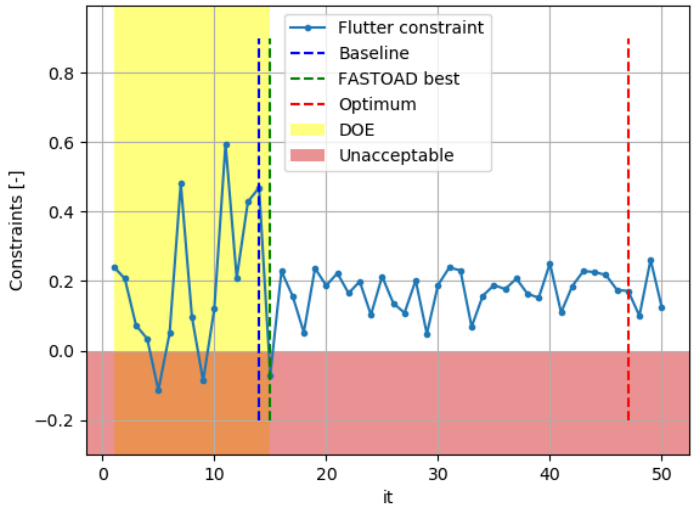

(b) Flutter speed constraint

FIGURE 6.6: MDAO process for flexible aircraft under deterministic constraint on flutter speed. Monitor plot of the fuel mass objective function (a) and the flutter constraint (b) through the SEGOMOE optimization iterations.

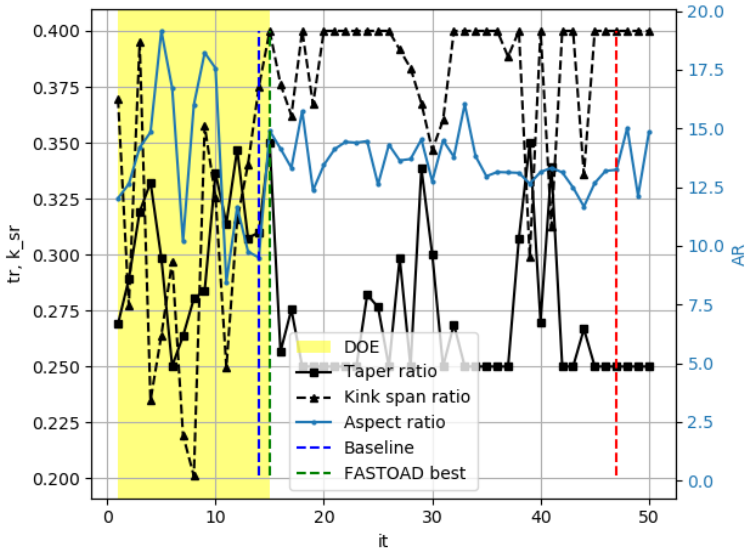

FIGURE 6.7: MDAO process for flexible aircraft under deterministic constraint on flutter speed. Monitor plot of the three design variables through the SEGOMOE optimization iterations.

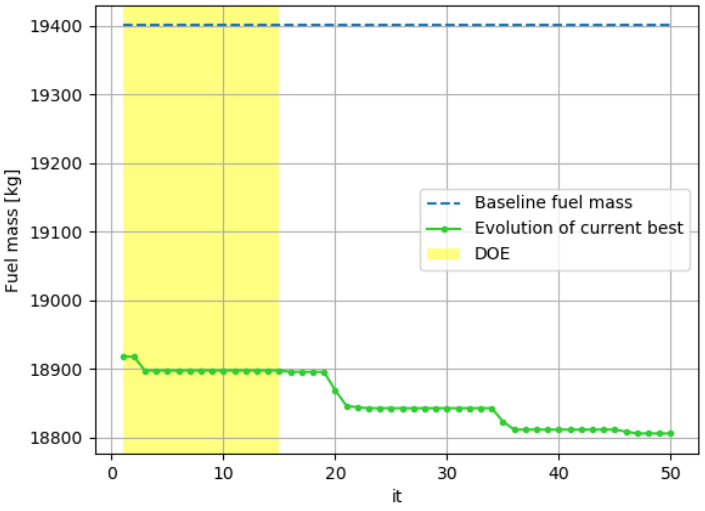

(a) Fuel mass objective

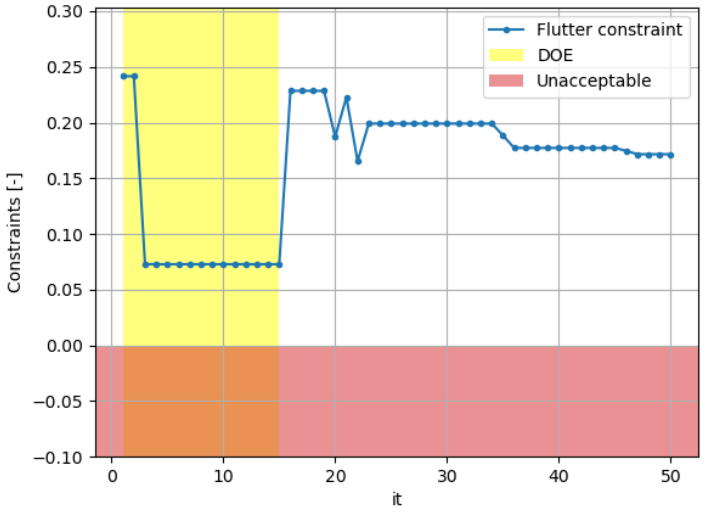

(b) Flutter speed constraint

FIGURE 6.8: MDAO process for flexible aircraft under deterministic constraint on flutter speed. Evolution of the current best fuel mass (a) and the corresponding flutter constraint (b) through the `SEGOMOE` optimization iterations.

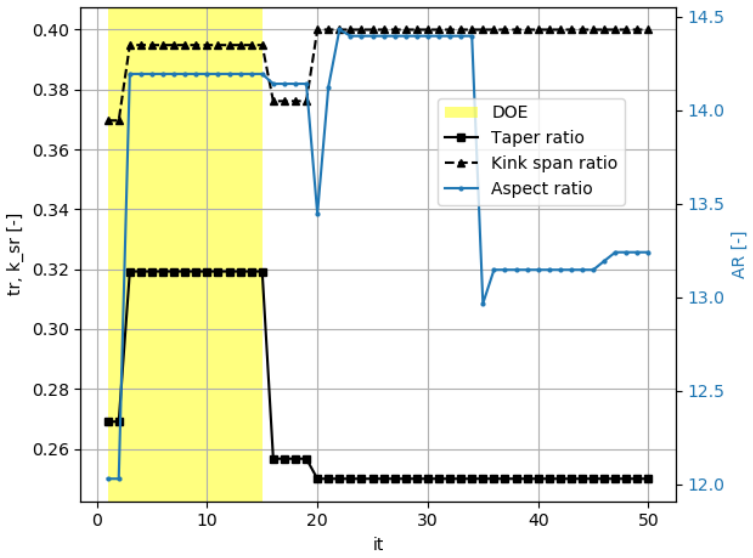

FIGURE 6.9: MDAO process for flexible aircraft under deterministic constraint on flutter speed. Evolution of the current best design variables through the SEGOMOE optimization iterations.

$\mathcal{AR}$	t_r	k_{sr}	**Fuel mass**
13.2	0.25	0.4	18,806 kg

TABLE 6.3: Best point from the MDAO results under flutter deterministic constraint.

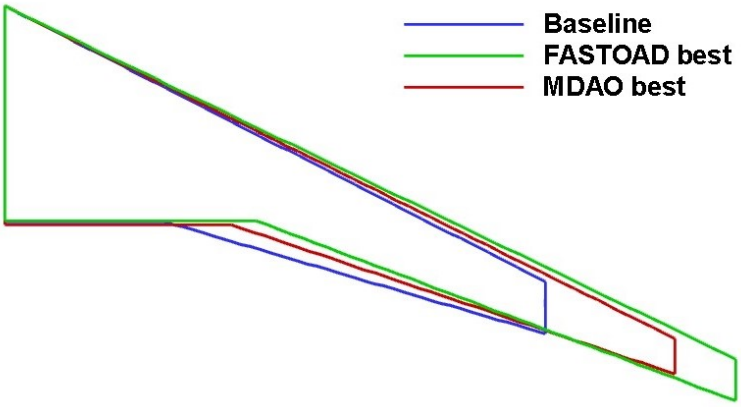

FIGURE 6.10: Best wing planform from the MDAO results under flutter deterministic constraint. The baseline and the best planform from the FAST-OAD rigid aircraft optimization are also reported for comparison.

6.3.2 Optimization under gust loads constraints only

The second MDAO application is analogous to the first one, except the dynamic aeroelastic constraints: the flutter constraint is now replaced by the gust loads constraints.

As already anticipated in Section 5.3.3, these consist of the three loads at wing root: direct stress on the stringers (σ_b), vertical shear on the spars (τ_v) and torsional shear on the skin (τ_t). The optimizer setup is kept identical, with an imposed total of 50 evaluations, divided into 15 DOE and 35 optimization iterations. Again, the last two points of the DOE correspond to the baseline configuration and the best configuration given by the rigid aircraft optimization. The problem definition is given in Table 6.4.

Similarly to what was done for the flutter constraint, also the gust loads constraints were conveniently represented in normalized form. These are defined in Equations (6.2) to (6.4).

$$c(\sigma_b) = \frac{\sigma_m - \sigma_b}{\sigma_m} \tag{6.2}$$

$$c(\tau_v) = \frac{\tau_m - \tau_v}{\tau_m} \tag{6.3}$$

$$c(\tau_t) = \frac{\tau_m - \tau_t}{\tau_m} \tag{6.4}$$

where $\sigma_m = 276$ MPa and $\tau_m = 207$ MPa are the material yield and shear strengths. In this way, negative values correspond to violated constraints, with loads higher than the allowable material limits. All values are reduced in such a way that they can be more easily plotted together. For example, a value of 0.2 indicates a 20% of safety with respect to the material limit, no matter its absolute value.

	Function/variable	**Lower bound**	**Upper bound**
Minimize	Fuel mass		
with respect to	Aspect ratio	8.0	20.0
	Taper ratio	0.25	0.35
	Kink span ratio	0.2	0.4
subject to	$\sigma_b^{\text{gust}} < \sigma_m \Rightarrow c(\sigma_b) > 0$		
	$\tau_v^{\text{gust}} < \tau_m \Rightarrow c(\tau_v) > 0$		
	$\tau_t^{\text{gust}} < \tau_m \Rightarrow c(\tau_t) > 0$		

TABLE 6.4: Definition of the MDAO problem for the flexible aircraft with deterministic constraints on dynamic gust loads.

The same types of plots as the previous optimization case are reported. Figure 6.11 shows the monitor plot of the fuel mass objective function and the corresponding constraints. Figure 6.12 contains the history of the three design variables. The numerical results are reported in Table 6.5, whereas their graphical representation is drawn in Figure 6.15.

As noted in the previous optimizations, the Figures show that the optimizer was quite fast at identifying the most promising design region right after the DOE evaluations. This time, there are no occurrences of constraint violations all over the process. Only a couple of candidates, within the DOE, featured a very limited safety margin, although it never goes negative (see Figure 6.11(b)). This reveals that the adopted gust constraints are less restrictive than the static structural sizing. In fact, it should be reminded that before evaluating the dynamic aeroelastic constraints, any configuration has first undergone the static aeroelastic sizing loops to ensure that the static limit loads are safely sustained. A second observation can be made about the significant difference between the shearing stress constraints and the other two: whereas the direct and vertical stress safety margin oscillate between 0% and 30%, with the optimum featuring around 10% for both of them, the torsion shear stress is always largely safe, with margins above 80%. This is an expected outcome, considering what discussed in Section 5.2.4.1, confirming that the estimations done with the proposed method can be considered conservative in terms of structural mass allocation.

The fact that these constraints are less restrictive than the flutter one apparently allows the aspect ratio to be slightly increased (up to 14.1, see Table 6.5). Nevertheless, this does not bring any significant change in the fuel burn, which in this case amounts to 18,850 kg, just 50 kg above the previous optimum - a difference of just 0.2%. It is important to point out here that a certain sensitivity limit in terms of mass estimations exists with the present approach. In fact, the reader should recall (see Section 5.2.5) that a 2% tolerance is allowed during the inner sizing loops, when imposing that the sized wing box weight must equal the weight considered by `FAST-OAD`. Now, 50 kg of fuel is close to that sensitivity limit, as it will be shown in the final results discussion (Section 6.5). Therefore, it would make no sense, technically but also practically, to search or compare candidates that differ of less than this quantity. Thus, it can be concluded that a same optimum is found in terms of objective function, but at slightly different coordinates, suggesting the existence of a plateau.

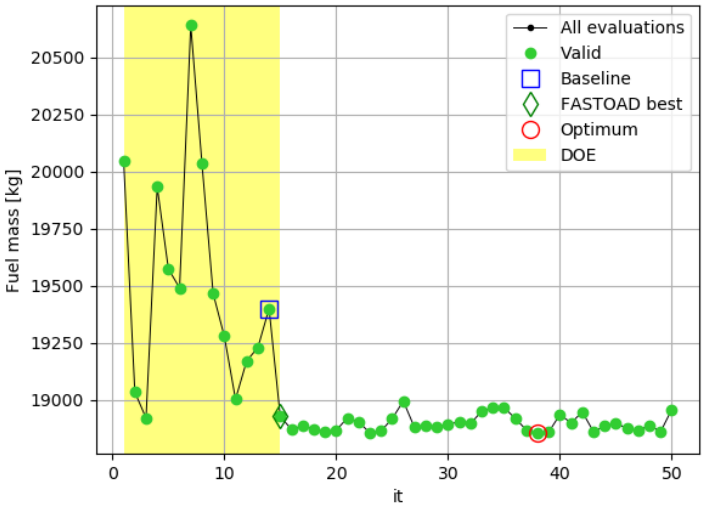

(a) Fuel mass objective

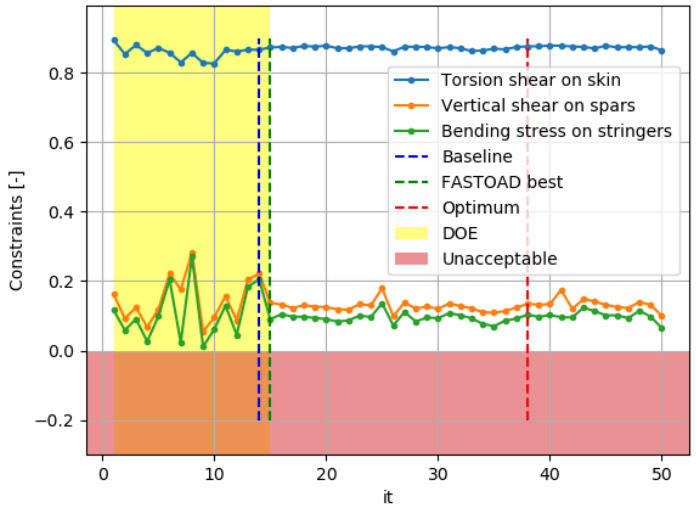

(b) Flutter speed constraint

FIGURE 6.11: MDAO process for flexible aircraft under deterministic constraints on gust loads. Monitor plot of the fuel mass objective function (a) and the gust loads constraints (b) through the SEGOMOE optimization iterations.

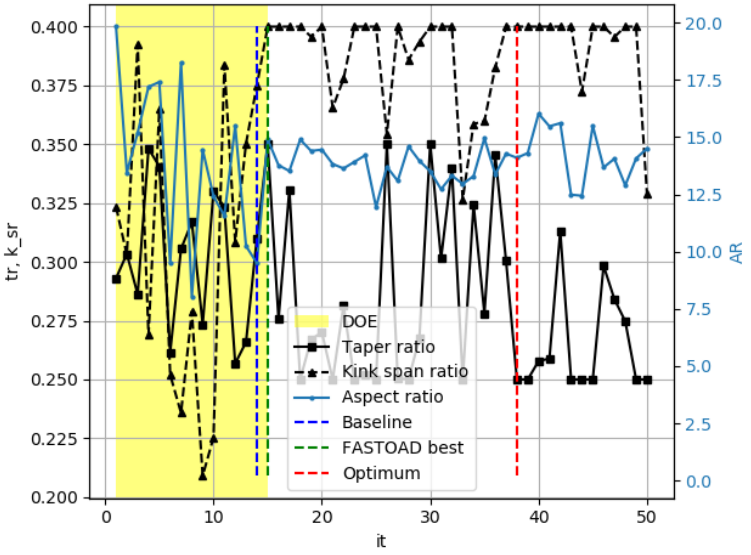

FIGURE 6.12: MDAO process for flexible aircraft under deterministic constraints on gust loads. Monitor plot of the three design variables through the SEGOMOE optimization iterations.

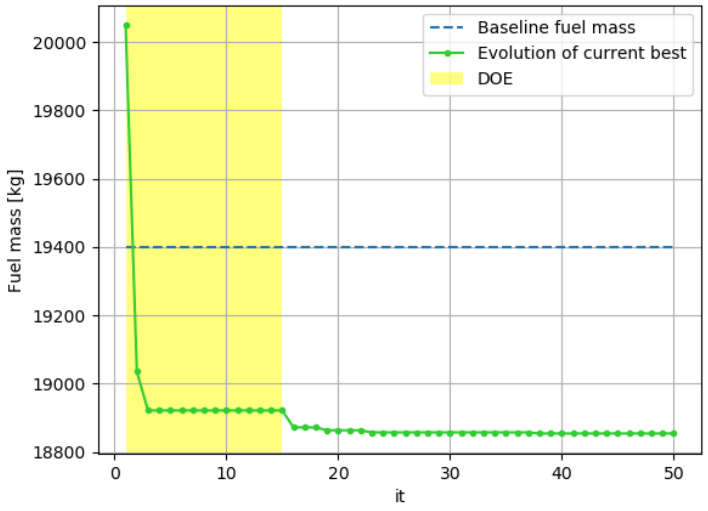

(a) Fuel mass objective

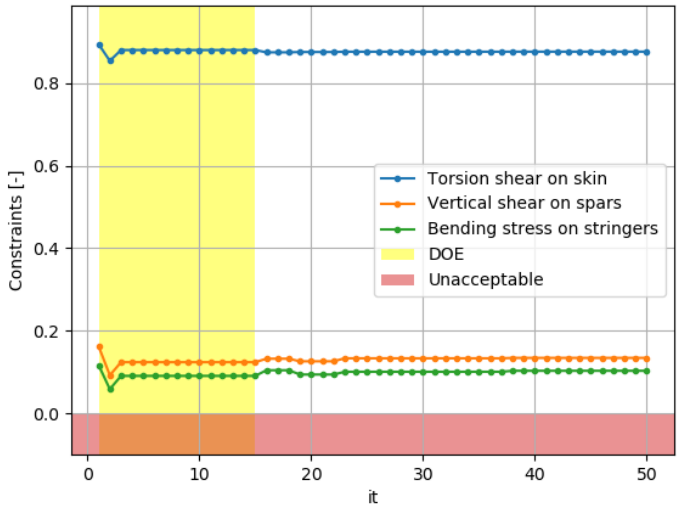

(b) Flutter speed constraint

FIGURE 6.13: MDAO process for flexible aircraft under deterministic constraints on gust loads. Evolution of the current best fuel mass (a) and the corresponding gust loads constraints (b) through the SEGOMOE optimization iterations.

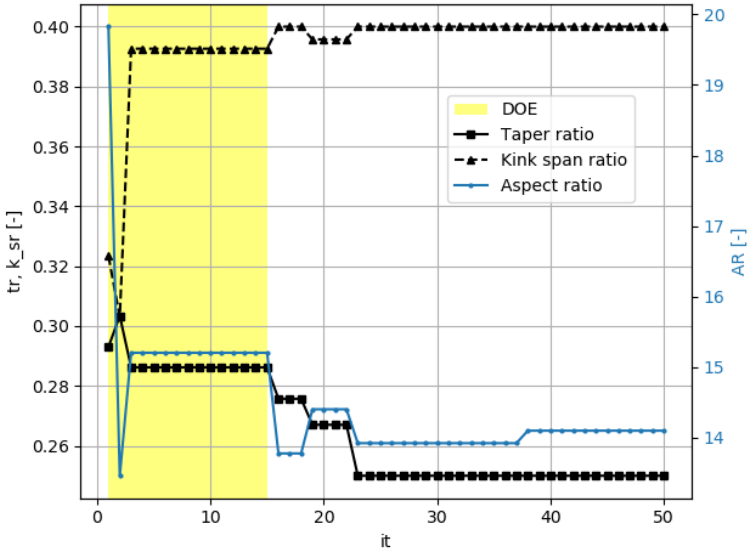

FIGURE 6.14: MDAO process for flexible aircraft under deterministic constraints on gust loads. Evolution of the current best design variables through the SEGOMOE optimization iterations.

$\mathcal{AR}$	t_r	k_{sr}	**Fuel mass**
14.1	0.25	0.4	18,854 kg

TABLE 6.5: Best point from the MDAO results under gust loads deterministic constraints.

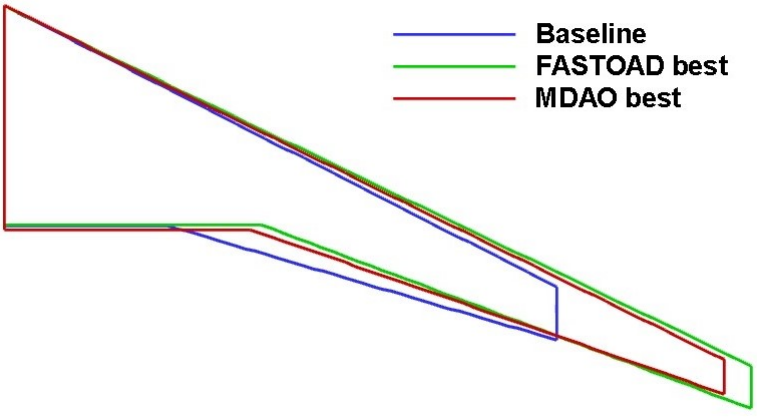

FIGURE 6.15: Best wing planform from the MDAO results under gust loads deterministic constraints. The baseline and the best planform from the FAST-OAD rigid aircraft optimization are also reported for comparison.

6.3.3 Optimization under flutter and gust loads constraints

The last proposed case of MDAO under deterministic aeroelastic constraints is the combination of the two former cases: the same optimization task is performed, this time

including all the aeroelastic constraints on flutter and gust loads (see Table 6.6). The reason to set up this case is mainly to test the ability of the framework and the optimizer to perform a more complex task and reach a result that is consistent with the two previous cases. The outcome confirmed such consistency. As summarized in Table 6.7, the optimal fuel mass was found at 18,814 kg, close to the previous values, at an aspect ratio of 13.1, taper ratio of 0.25 and kink span ratio of 0.4. The point matches almost exactly the optimal point obtained with the flutter constraint only, confirming that flutter has a dominating effect in the present case. However, as already stated, its effect impacts only the aspect ratio, which is kept one unit lower than the optimal one given by the gust-constrained case, and almost 2 units lower than the best one given by the rigid aircraft optimization.

A graphical representation of the best planform is given in Figure 6.16. The monitor plots describing the optimization iterations are provided in Figures 6.17 and 6.18, whereas the evolution of the best candidate is reported in Figures 6.19 to 6.20.

It is worth mentioning at this point that comparative remarks about all the optimization cases discussed in this Chapter, including those for robust MDAO presented in the next Section, are given later in Section 6.5.

	Function/variable	**Lower bound**	**Upper bound**
Minimize	Fuel mass		
with respect to	Aspect ratio	8.0	20.0
	Taper ratio	0.25	0.35
	Kink span ratio	0.2	0.4
subject to	$V_f > 200$ m/s $\Rightarrow$ $c(V_f) > 0$		
	$\sigma_b^{\text{gust}} < \sigma_m \Rightarrow c(\sigma_b) > 0$		
	$\tau_v^{\text{gust}} < \tau_m \Rightarrow c(\tau_v) > 0$		
	$\tau_t^{\text{gust}} < \tau_m \Rightarrow c(\tau_t) > 0$		

TABLE 6.6: Definition of the MDAO problem for the flexible aircraft with deterministic aeroelastic constraints on flutter and gust loads.

$\mathcal{AR}$	t_r	k_{sr}	**Fuel mass**
13.1	0.25	0.4	18,814 kg

TABLE 6.7: Best point from the MDAO results under flutter and gust loads deterministic constraints.

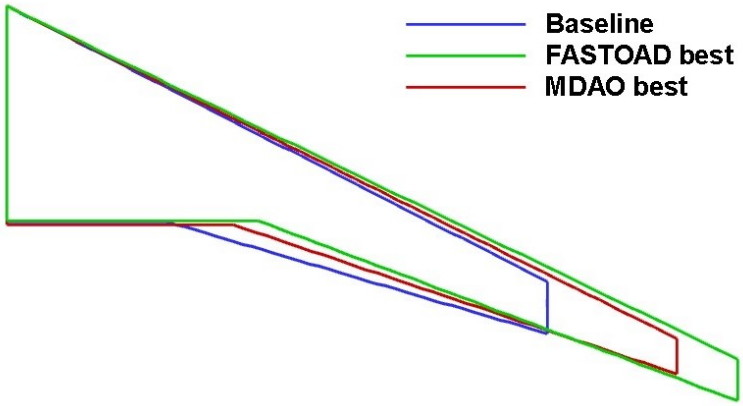

FIGURE 6.16: Best wing planform from the MDAO results under flutter and gust loads deterministic constraints. The baseline and the best planform from the FAST-OAD rigid aircraft optimization are also reported for comparison.

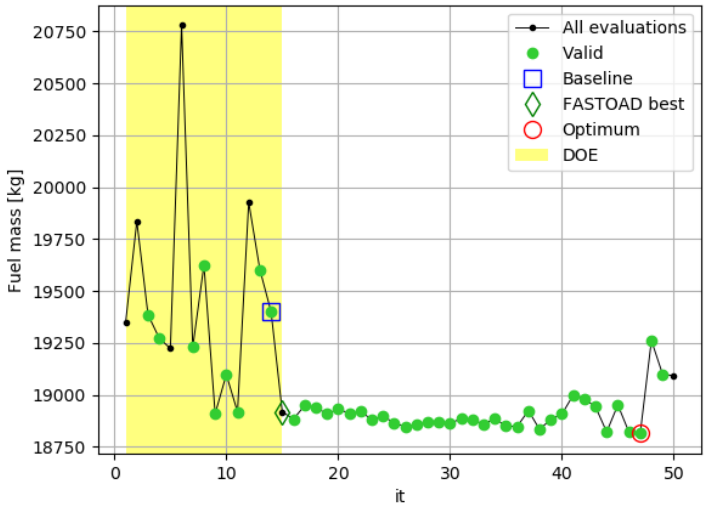

(a) Fuel mass objective

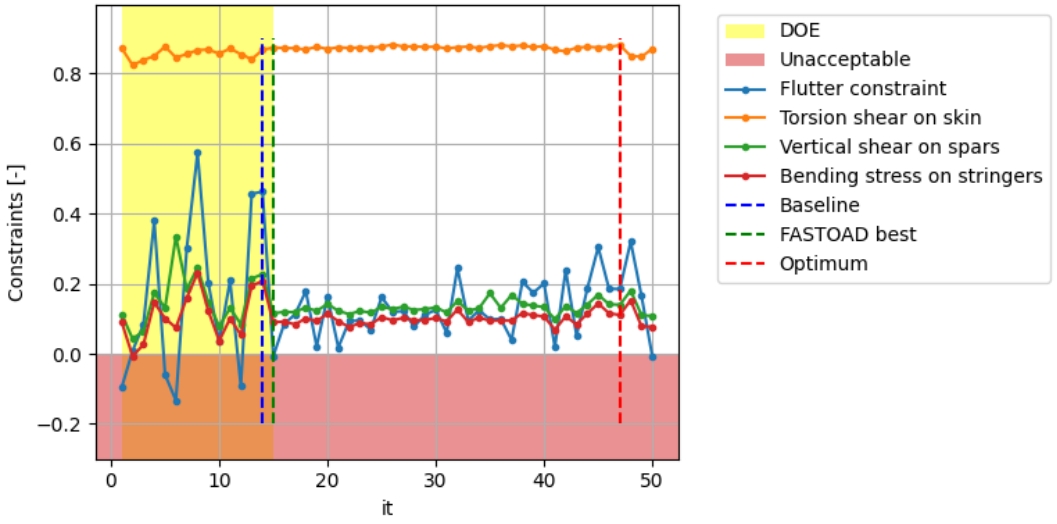

(b) Flutter speed constraint

FIGURE 6.17: MDAO process for flexible aircraft under deterministic constraints on flutter speed and gust loads. Monitor plot of the fuel mass objective function (a) and the flutter and gust loads constraints (b) through the SEGOMOE optimization iterations.

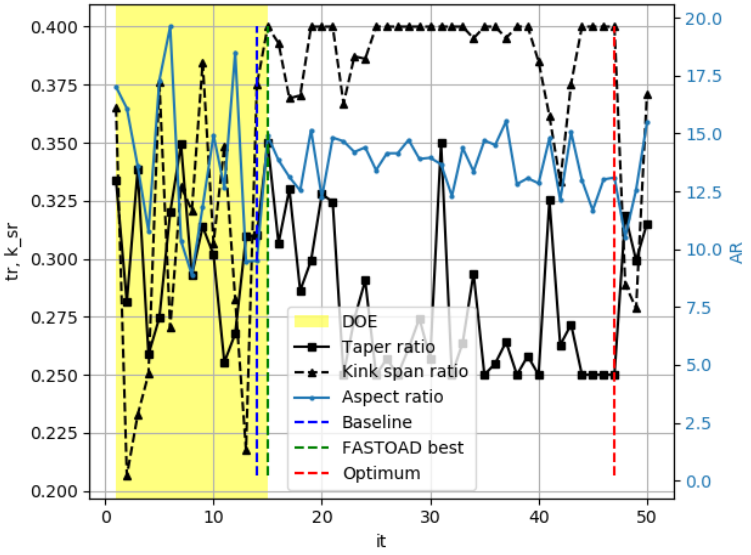

FIGURE 6.18: MDAO process for flexible aircraft under deterministic constraints on flutter speed and gust loads. Monitor plot of the three design variables through the SEGOMOE optimization iterations.

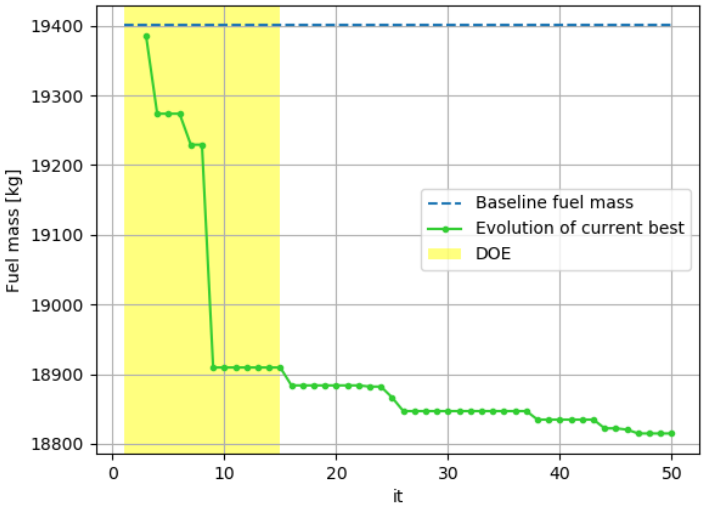

(a) Fuel mass objective

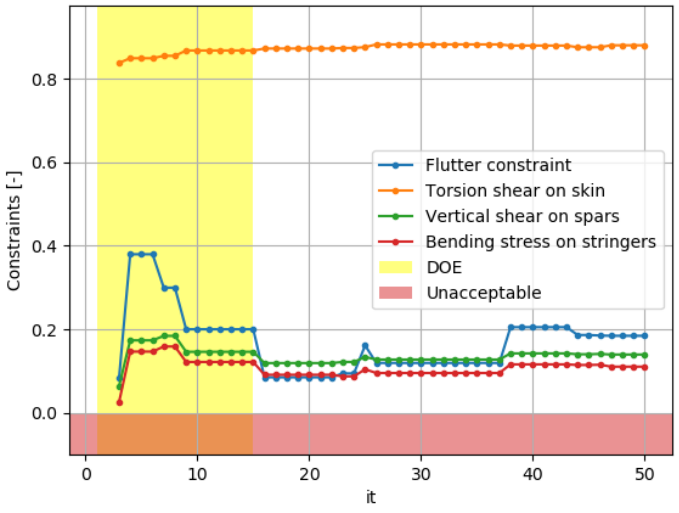

(b) Flutter speed constraint

FIGURE 6.19: MDAO process for flexible aircraft under deterministic constraints on flutter speed and gust loads. Evolution of the current best fuel mass (a) and the corresponding flutter and gust loads constraints (b) through the SEGOMOE optimization iterations.

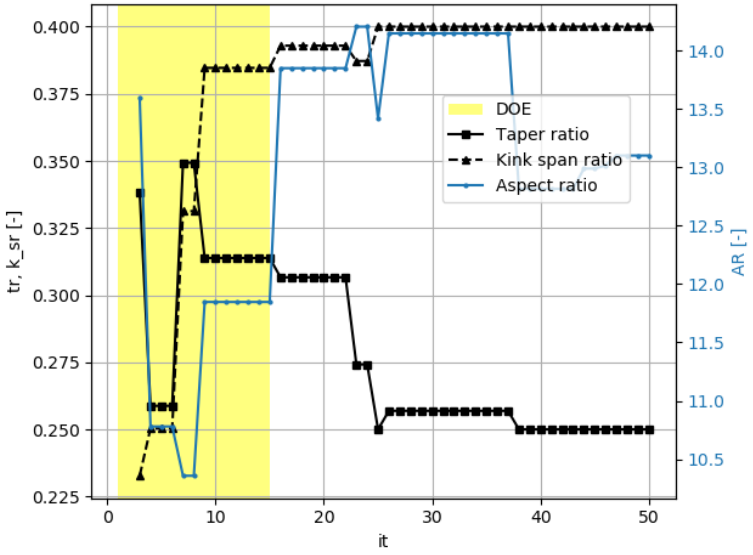

FIGURE 6.20: MDAO process for flexible aircraft under deterministic constraints on flutter speed and gust loads. Evolution of the current best design variables through the SEGOMOE optimization iterations.

6.4 Robust MDAO results

The last step to demonstrate the framework capabilities is to repeat the optimization studies presented above with the additional complexity of introducing reliability aeroelastic constraints, in order to asses the impact of uncertainty on some key parameters. The choices about what the parameters to be treated as uncertain and what uncertainty distributions to be assigned were discussed in Sections 5.3.2.2 and 5.3.4.2, with the support of some sensitivity studies. Just to remind the main conclusions from those Sections, it was established that the flutter constraint shall be analyzed considering uncertainty on two parameters: the location of the wing elastic axis a, and its offset from the wing center of gravity axis, d. Both those quantities are normalized with respect to the local chord, and are assumed constant all over the span. To evaluate the reliability constraints on gust loads, it was assessed that considering only the uncertainty on the elastic axis location a is sufficient, as the sensitivity to the other selected parameters proved to be much less relevant.

Again, the same three combinations for the constraints setup were tested, as done for the deterministic studies: flutter constraint only, gust loads constraints only, flutter and gust constraints together. These three cases are presented in Sections 6.4.1, 6.4.2 and 6.4.3, respectively.

6.4.1 Optimization under flutter reliability constraint only

The first presented case of MDAO under uncertainty involves the enforcement of one reliability constraint on flutter speed. The uncertainty is attributed to the wing's elastic axis location a and its distance from the center of gravity axis d. This uncertainty is propagated to the flutter speed prediction, and the constraint imposes that flutter must occur above the limit of 200 m/s with a probability of at least 95%. In other words, for a candidate to be acceptable, less than 5% of the cases shall feature a flutter speed below that limit. The constraint can therefore be expressed by the inequality $P_5(\hat{V}_f) > 200$ m/s, where $P_5()$ indicates the 5th percentile, in this case of the output flutter speed distribution $\hat{V}_f$. Consistently with what was done previously, the constraint is translated and normalized to ease its graphical representation, especially for comparison with other cases and other constraints. The represented quantity, which must result positive, is the one defined in Equation (6.5).

$$c(\hat{V}_f) = \frac{P_5(\hat{V}_f) - 200}{200} \tag{6.5}$$

The case description is summarized in Table 6.8. The usual plots to follow the optimization process and outcome are reported. In particular the monitor plots of the objective function, constraints and variables are given in Figures 6.22 and 6.23, and the evolution of the current best is portrayed by Figures 6.24 and 6.25.

Compared to the corresponding deterministic case, it can be clearly seen from Figure 6.22 that much more constraint violations occurred. Nevertheless, the optimum reached is very close to the one found in the deterministic optimization, both in terms of variables and objective function. The quantitative results are summarized in Table 6.9, and the best candidate is represented in Figure 6.21. The closeness with the deterministic results suggests that the imposed uncertainty is not very penalising. Indeed, it is seen on the deterministic case that the constraint is not active at the optimum. The slight mismatch in the results - about 60 kg in the optimal fuel mass (18,865 kg here, 18,806 kg in the deterministic case) and 0.5 in the optimal AR (13.7 here vs 13.2 in the deterministic case) - suggests that some impact may be caused by the underlying sensitivity limit mentioned in Section 6.3.2. However, any significant increase of the search efforts would be hardly justified, considering that the variations in the objective function are very small and close to the tool sensitivity. A more comprehensive, comparative discussion and explanation of the different results is given a dedicated space in Section 6.5.

Before moving to the next case, it is worth observing the results of the propagation of uncertainty on the flutter speed during the optimization iterations. The output distributions, in form of PDFs, are collected in Figure 6.26. These help gaining a better

understanding of the reliability constraint mechanism. As already said, any acceptable configuration must have less than 5% probability of experiencing flutter below 200 m/s. Now, the Figure highlights in particular three interesting candidates. The first one is the baseline (in blue): its distribution is quite far above the limit, showing, as expected, practically zero probability of developing flutter below the imposed threshold. Conversely, the best rigid configuration found with `FAST-OAD` alone (in green) evidently violates the constraint, with its distribution laying mostly below the 200 m/s limit, featuring more than 60% probability of developing low-speed flutter. Therefore, while the baseline could be labelled as 'excessively' safe, the other would be excessively unsafe. Consistently with this reasoning, the optimum is found in between the two excesses: its distribution, highlighted in red, is closer to the dangerous region, but with only around 4% probability of having an unacceptable flutter speed, proving therefore to be safe 'enough' with respect to the prescribed constraint. Another interesting fact emerging from those plots is that low aspect ratio configurations, whose PDFs are located on the right side with higher flutter speeds, show wider distributions compared to high aspect ratio configurations, concentrated on the left side. This outcome, not completely intuitive, demonstrates that despite having in general a greater aeroelastic stability, low aspect ratio wings appear to be more sensitive to structural changes. On the other hand, slender wings are less stable in terms of flutter, but their behaviour seems somewhat more predictable. This is likely due to the fact that the uncertainty is given in percentage of the root chord, which translates into higher absolute values for low-aspect-ratio wings (low span and large root chord) compared to high-aspect-ratio ones (long span and small root chord).

	Function/quantity	**Range/distribution**
Minimize	Fuel mass	
with respect to	Aspect ratio	[8.0 , 20.0]
	Taper ratio	[0.25, 0.35]
	Kink span ratio	[0.2 , 0.4]
with uncertainty on	Wing EA location (a)	Normal ($\mathbb{E} = \overline{a}$, $3\varsigma = 10\%$ chord)
	Wing CG to EA offset (d)	Normal ($\mathbb{E} = 0$, $3\varsigma = 5\%$ chord)
subject to	$\mathbb{P}\,(V_f > 200\text{m/s}) > 95\% \quad \Rightarrow \quad c(\hat{V}_f) > 0$	

TABLE 6.8: Definition of the MDAO problem for the flexible aircraft with reliability constraint on flutter speed.

$\mathcal{AR}$	t_r	k_{sr}	**Fuel mass**
13.7	0.25	0.4	18,865 kg

TABLE 6.9: Best point from the MDAO results under flutter reliability constraint.

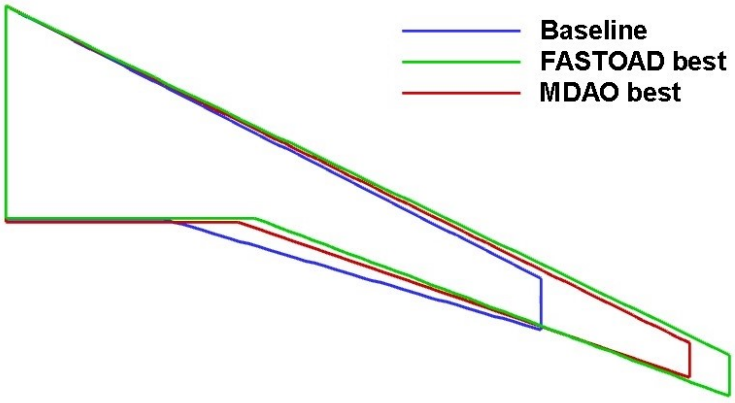

FIGURE 6.21: Best wing planform from the MDAO results under flutter reliability constraints. The baseline and the best planform from the FAST-OAD rigid aircraft optimization are also reported for comparison.

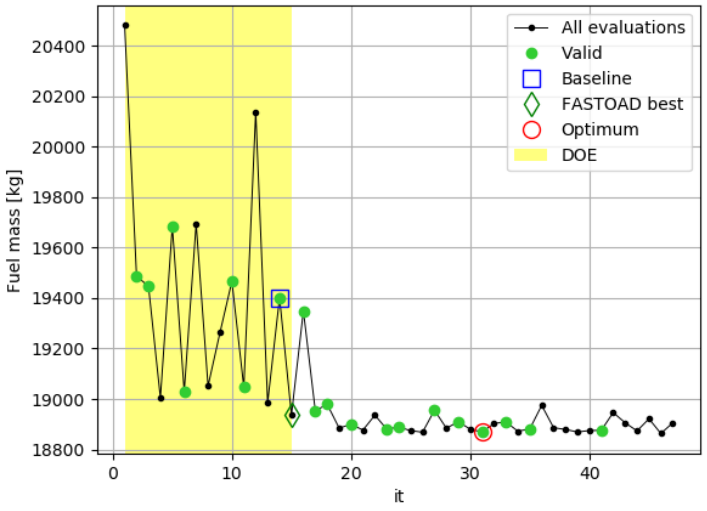

(a) Fuel mass objective

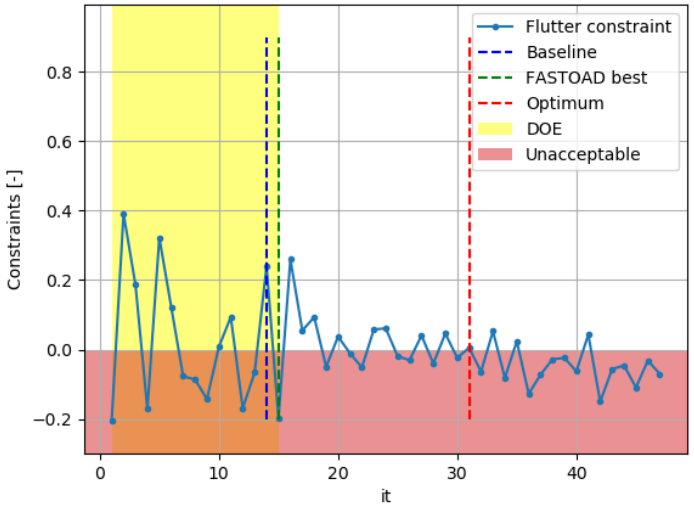

(b) Flutter speed constraint

FIGURE 6.22: MDAO process for flexible aircraft under reliability constraint on flutter speed. Monitor plot of the fuel mass objective function (a) and the flutter constraint (b) through the SEGOMOE optimization iterations.

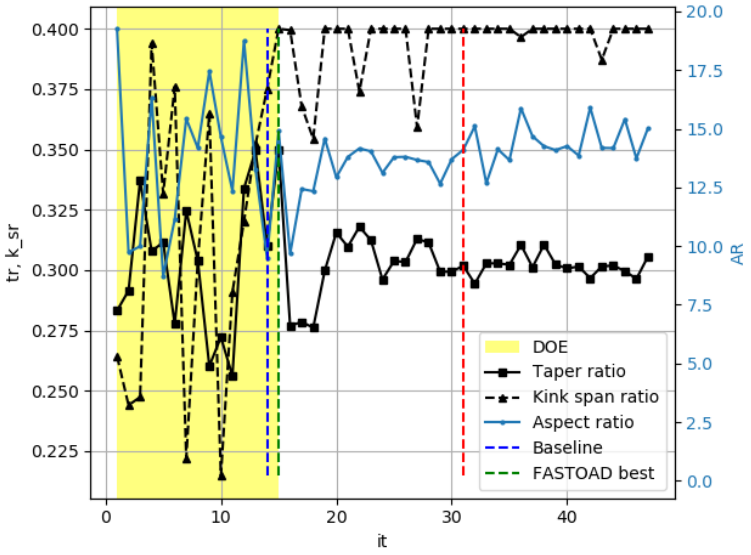

FIGURE 6.23: MDAO process for flexible aircraft under reliability constraint on flutter speed. Monitor plot of the three design variables through the `SEGOMOE` optimization iterations.

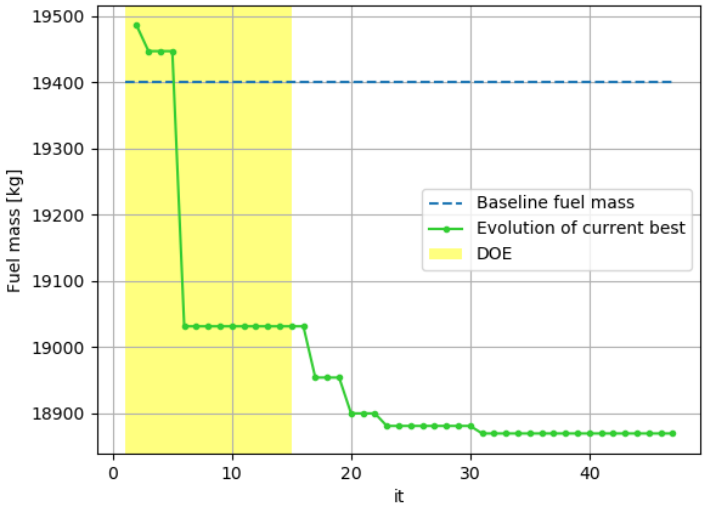

(a) Fuel mass objective

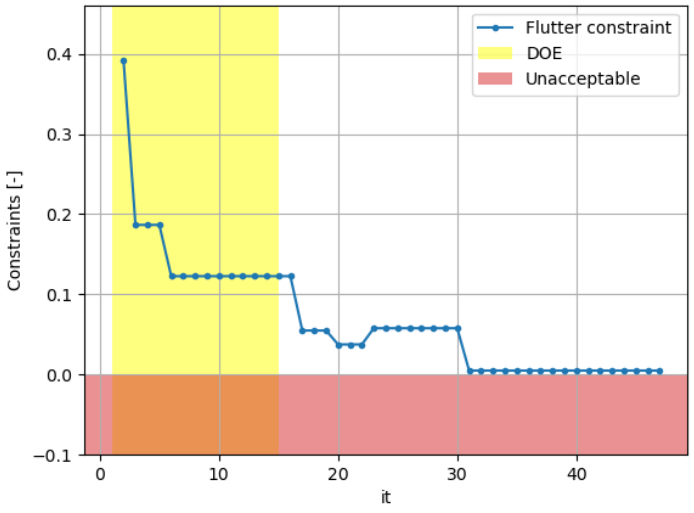

(b) Flutter speed constraint

FIGURE 6.24: MDAO process for flexible aircraft under reliability constraint on flutter speed. Evolution of the current best fuel mass (a) and the corresponding flutter constraint (b) through the `SEGOMOE` optimization iterations.

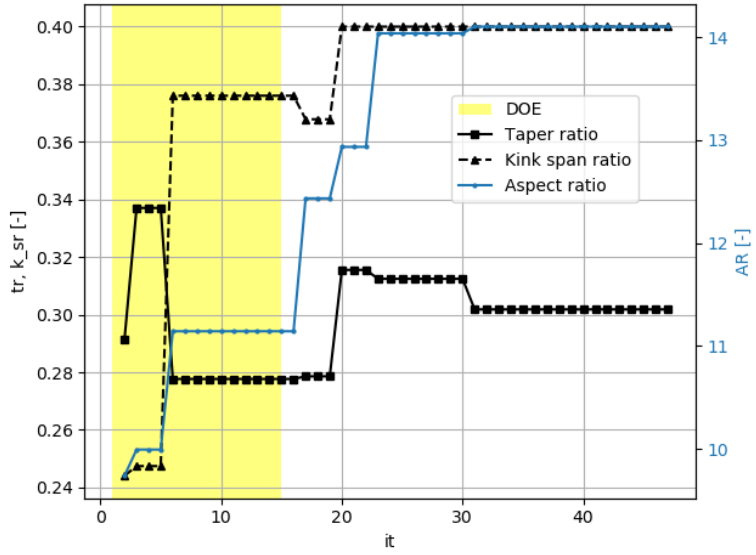

FIGURE 6.25: MDAO process for flexible aircraft under reliability constraint on flutter speed. Evolution of the current best design variables through the SEGOMOE optimization iterations.

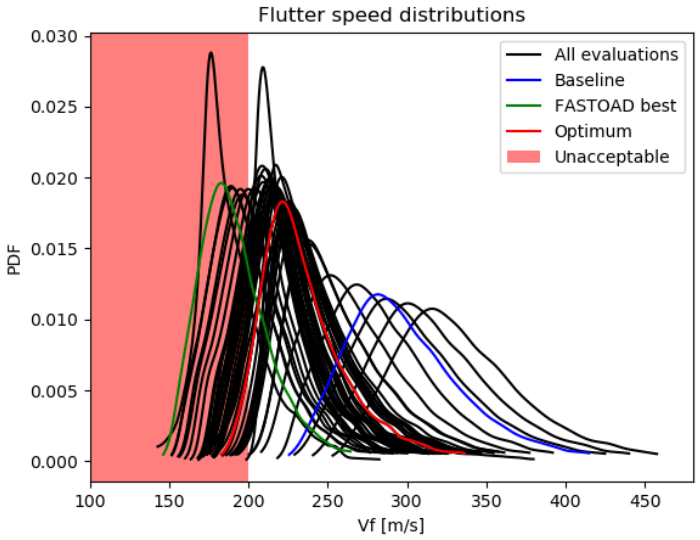

FIGURE 6.26: MDAO process for flexible aircraft under reliability constraint on flutter speed. Juxtaposition of all evaluated flutter speed distributions during the optimization process.

6.4.2 Optimization under gust loads reliability constraints only

Following the approach used with the deterministic optimization studies, the second robust MDAO task takes into account only the dynamic gust loads constraints, this time under uncertainty. As motivated in Section 5.3.4.2 after a sensitivity study, only the wing elastic axis location (denoted by a) is considered uncertain and propagated

to evaluate the reliability constraints. The aim of such constraints is to ensure that the probability of the material strength not being exceeded during a gust encounter is greater than a certain threshold, which in this case has been fixed to 95%. This condition can be reformulated by imposing that the 95th percentile of the output distributions for the gust loads must be lower than the material allowable limit. This must hold simultaneously for all the three gust loads already identified, namely the bending stress on the stringers, the maximum vertical shear on the spars and the torsional shear on the skin, all the three evaluated at the wing root. Therefore, the corresponding expressions to Equations (6.2) to (6.4) for the normalized reliability constraints are those in Equations (6.6) to (6.8). The problem definition is summarized in Table 6.10.

$$c(\hat{\sigma}_b) = \frac{\sigma_m - P_{95}(\hat{\sigma}_b)}{\sigma_m} \tag{6.6}$$

$$c(\hat{\tau}_v) = \frac{\tau_m - P_{95}(\hat{\tau}_v)}{\tau_m} \tag{6.7}$$

$$c(\hat{\tau}_t) = \frac{\tau_m - P_{95}(\hat{\tau}_t)}{\tau_m} \tag{6.8}$$

The usual plots for the monitoring of the optimization process and the evolution of the current best are given in Figures 6.28 to 6.31. In particular, looking at Figure 6.28, a similar trend as the deterministic case is evident, with the bending loads being the most important in all cases. Moreover, although the constraints are rarely violated, this time the safety margin is considerably lower. For instance, the safety margin of the deterministic optimum for the bending load constraint was around 12%, whereas the same margin under uncertainty falls to about 4%. However, it appears that even the reliability constraint, at least under the specified uncertainty and the chosen approximated definition, does not have a relevant impact on the optimization outcome. In fact, the best configuration found does not deviate considerably from the deterministic case (see Table 6.11 and Figure 6.27). This means that what mainly penalizes the fuel minimization is the inner static sizing, and not the gust loads constraints.

As for the flutter-constrained case, it is still worth observing the output distributions of the gust loads during the optimization evaluations. In particular, the PDFs of the bending and vertical shear loads, the most relevant ones, are reported in Figures 6.32(a) and 6.32(b). As seen in the previous case with the flutter reliability constraint, the baseline configuration is confirmed to be largely away from the dangerous region (its distribution is highlighted in blue). On the other hand, both the robust optimum and the rigid optimum, with their higher aspect ratios, are much closer to the unacceptable region, although none of them demonstrates any significant probability of structural failure. Contrary to the flutter constraint, it can be noted that this time the high aspect ratio

configurations, whose distributions are located on the right part of the plots (towards higher loads), prove to be also the most sensible to the structural variations: the more slender the wing, the wider its distribution and therefore the larger the uncertainty and the risk of structural failure.

	Function/quantity	**Range/distribution**
Minimize	Fuel mass	
with respect to	Aspect ratio	[8.0 , 20.0]
	Taper ratio	[0.25, 0.35]
	Kink span ratio	[0.2 , 0.4]
with uncertainty on	Wing EA location (a)	Normal ($\mathbb{E} = \bar{a}$, $3\varsigma = 10\%$ chord)
subject to	$\mathbb{P}\left(\sigma_b^{\text{gust}} < \sigma_m\right) > 95\% \Rightarrow c(\hat{\sigma}_b) > 0$	
	$\mathbb{P}\left(\tau_v^{\text{gust}} < \tau_m\right) > 95\% \Rightarrow c(\hat{\tau}_v) > 0$	
	$\mathbb{P}\left(\tau_t^{\text{gust}} < \tau_m\right) > 95\% \Rightarrow c(\hat{\tau}_t) > 0$	

TABLE 6.10: Definition of the MDAO problem for the flexible aircraft with reliability constraint on flutter speed.

$\mathcal{AR}$	t_r	k_{sr}	**Fuel mass**
13.7	0.25	0.4	18,858 kg

TABLE 6.11: Best point from the MDAO results under gust loads reliability constraints.

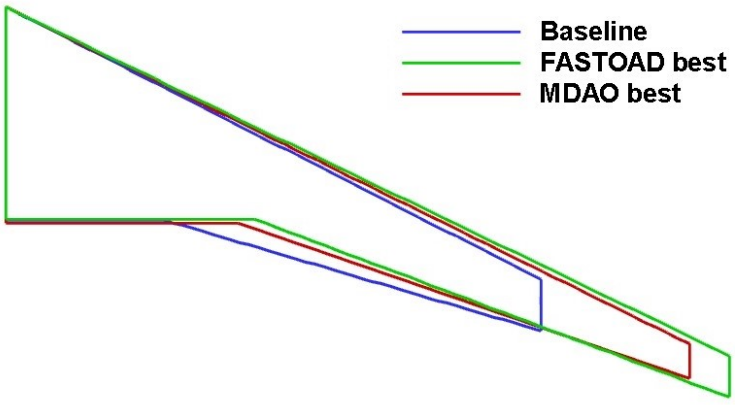

FIGURE 6.27: Best wing planform from the MDAO results under gust loads reliability constraints. The baseline and the best planform from the FAST-OAD rigid aircraft optimization are also reported for comparison.

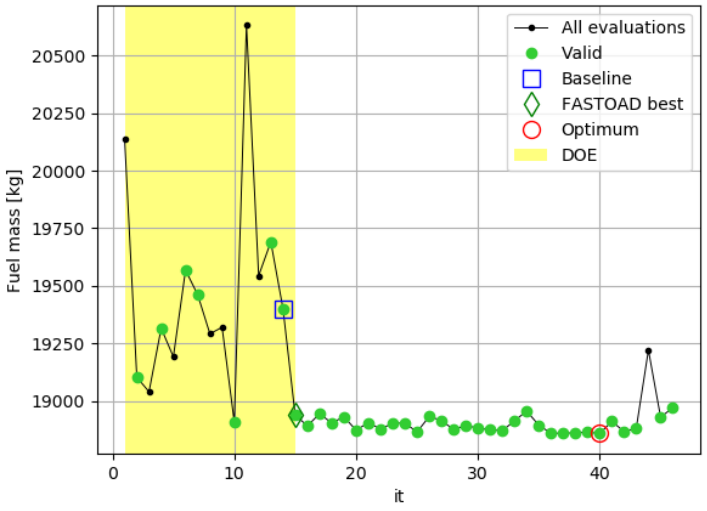

(a) Fuel mass objective

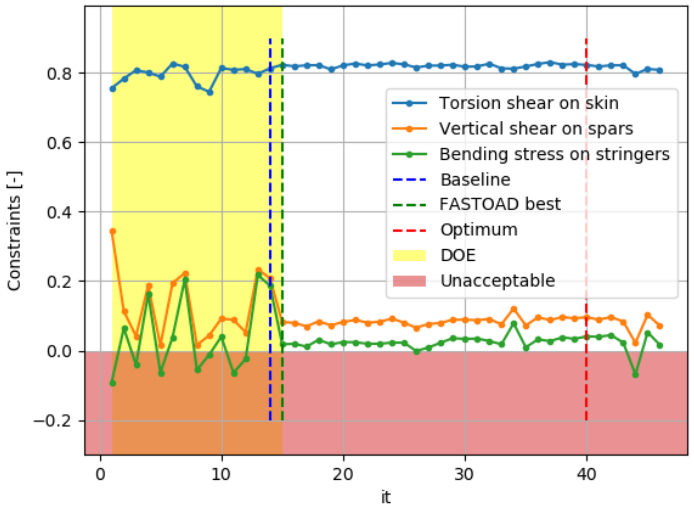

(b) Gust loads constraints

FIGURE 6.28: MDAO process for flexible aircraft under reliability constraints on gust loads. Monitor plot of the fuel mass objective function (a) and the gust loads constraints (b) through the SEGOMOE optimization iterations.

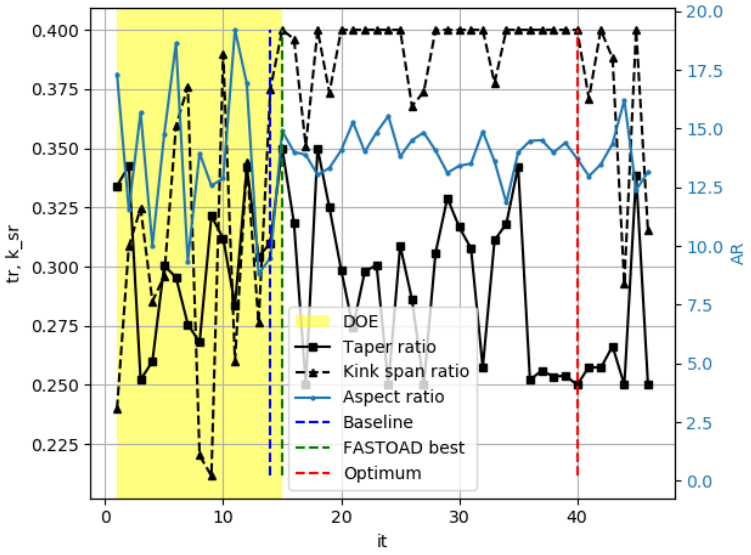

FIGURE 6.29: MDAO process for flexible aircraft under reliability constraints on gust loads. Monitor plot of the three design variables through the SEGOMOE optimization iterations.

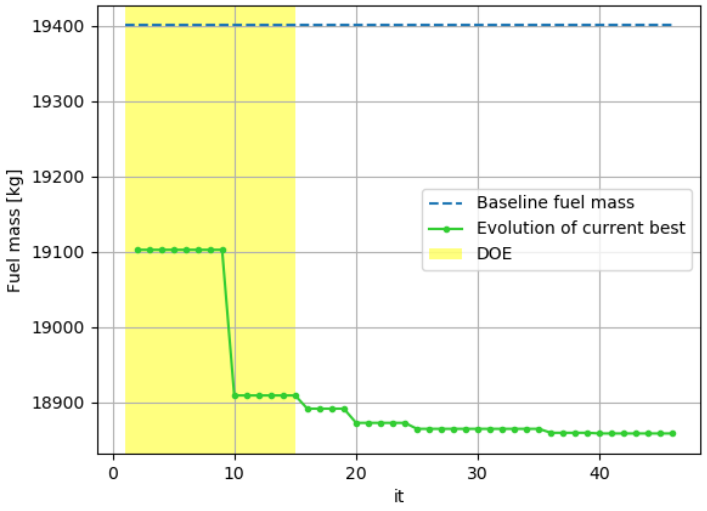

(a) Fuel mass objective

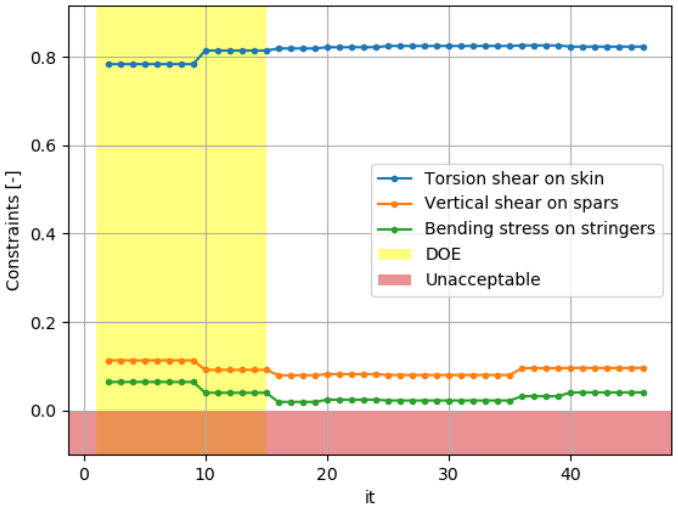

(b) Gust loads constraints

FIGURE 6.30: MDAO process for flexible aircraft under reliability constraints on gust loads. Evolution of the current best fuel mass (a) and the corresponding gust loads constraints (b) through the SEGOMOE optimization iterations.

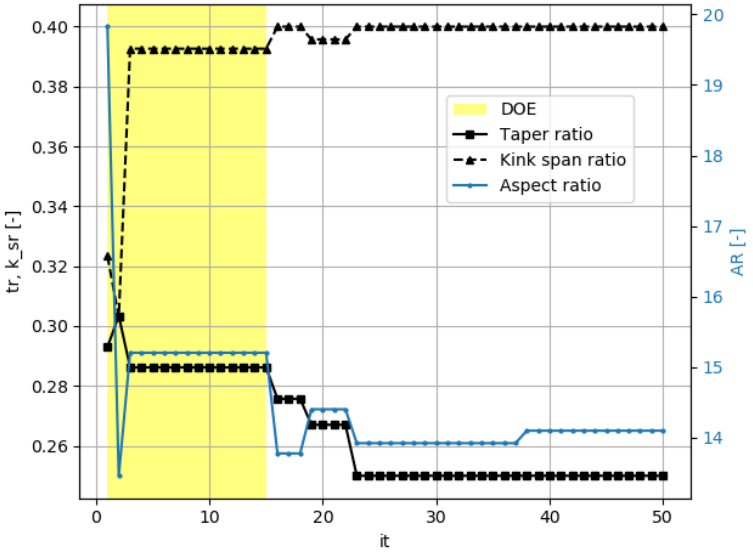

FIGURE 6.31: MDAO process for flexible aircraft under reliability constraints on gust loads. Evolution of the current best design variables through the SEGOMOE optimization iterations.

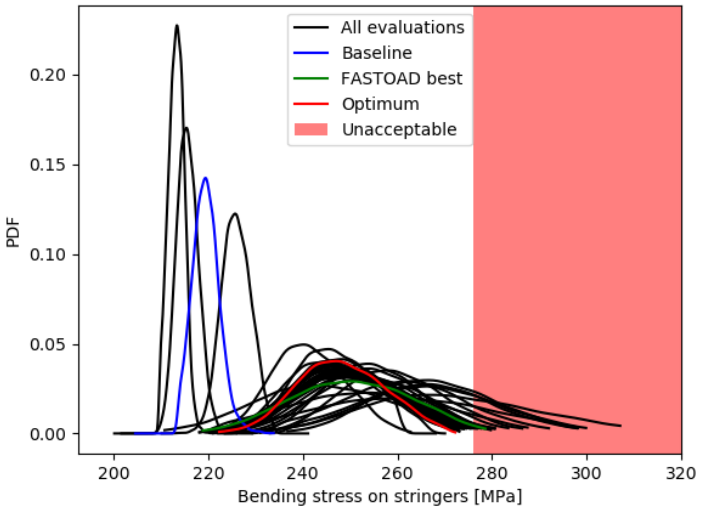

(a)

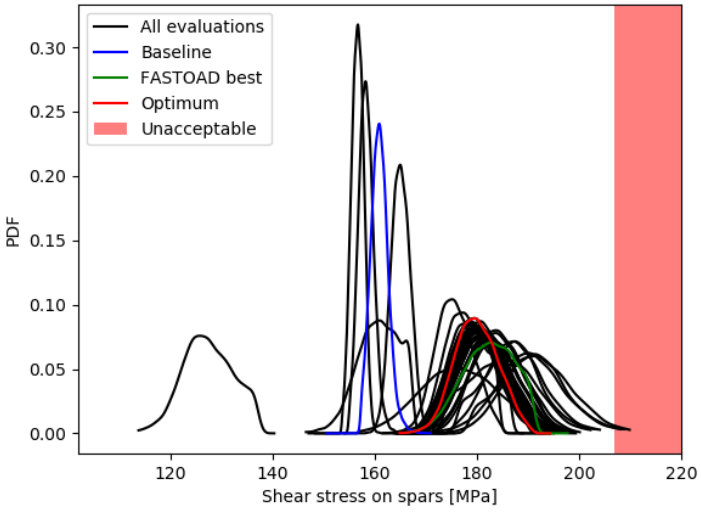

(b)

FIGURE 6.32: MDAO process for flexible aircraft under reliability constraints on gust loads. Juxtaposition of all evaluated bending loads distributions (a) and vertical shear loads (b) during the optimization process.

6.4.3 Optimization under flutter and gust loads reliability constraints

The last optimization example to demonstrate the framework capabilities is the most complex, where the uncertainty is propagated to all the available dynamic aeroelastic constraints. As already stated, the output flutter speed distribution $\hat{V}_f$ is computed after assigning uncertainty to two parameters, namely the elastic axis location a and its distance from the center of gravity axis d. Instead, the gust loads distributions are

derived by considering only the first input uncertainty. The problem definition is summarized in Table 6.12. The tracking of the optimization process is given in Figures 6.34 to 6.37. The plotted constraint values are the normalized ones, defined in Equations (6.5) and (6.6) to (6.8). The optimal candidate is represented in Figure 6.33, and its numerical details are given in Table 6.13. No relevant changes are observed with respect to the previous case, neither on the best coordinates nor on the objective function. Also, consistently with the previous cases, the most stringent constraint is again the flutter one, and a large number of constraint violations can be observed both during DOE evaluation and the optimization process. A final, comparative discussion of these and all the other results presented above is provided in Section 6.5.

	Function/quantity	**Range/distribution**	**Propagated to**
Minimize	Fuel mass		
with respect to	Aspect ratio	[8.0 , 20.0]	
	Taper ratio	[0.25, 0.35]	
	Kink span ratio	[0.2 , 0.4]	
with uncertainty on	EA location a	Normal ($\mathbb{E} = \bar{a}$, $3\varsigma = 10\%$ chord)	Flutter, gust
	CG to EA offset d	Normal ($\mathbb{E} = 0$, $3\varsigma = 5\%$ chord)	Flutter
subject to	$\mathbb{P}\left(V_f > 200\,\mathrm{m/s}\right) > 95\% \Rightarrow c(\hat{V}_f) > 0$		
	$\mathbb{P}\left(\sigma_b^{\mathrm{gust}} < \sigma_m\right) > 95\% \Rightarrow c(\hat{\sigma}_b) > 0$		
	$\mathbb{P}\left(\tau_v^{\mathrm{gust}} < \tau_m\right) > 95\% \Rightarrow c(\hat{\tau}_v) > 0$		
	$\mathbb{P}\left(\tau_t^{\mathrm{gust}} < \tau_m\right) > 95\% \Rightarrow c(\hat{\tau}_t) > 0$		

TABLE 6.12: Definition of the MDAO problem for the flexible aircraft with reliability constraint on flutter speed and gust loads.

$\mathcal{AR}$	t_r	k_{sr}	**Fuel mass**
13.0	0.25	0.4	18,821 kg

TABLE 6.13: Best point from the MDAO results under flutter speed and gust loads reliability constraints.

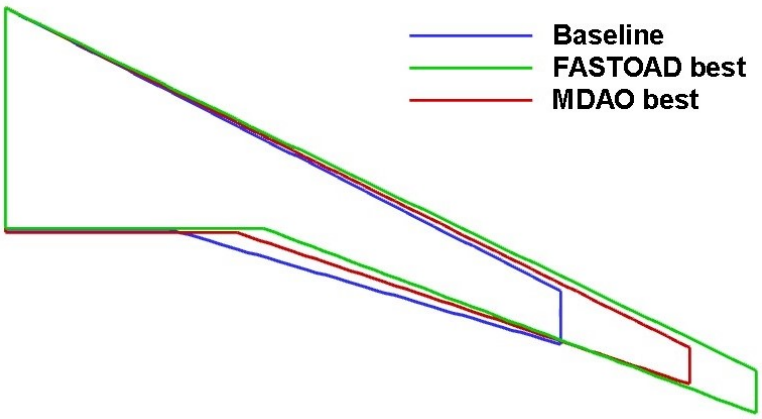

FIGURE 6.33: Best wing planform from the MDAO results under flutter speed and gust loads reliability constraints. The baseline and the best planform from the FAST-OAD rigid aircraft optimization are also reported for comparison.

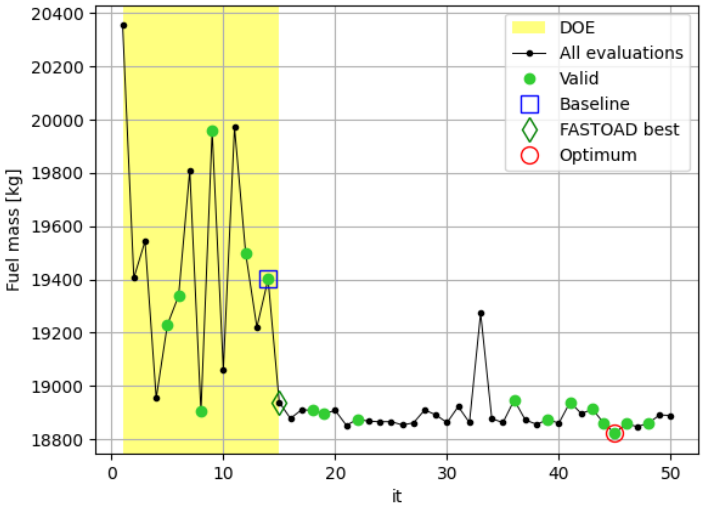

(a) Fuel mass objective

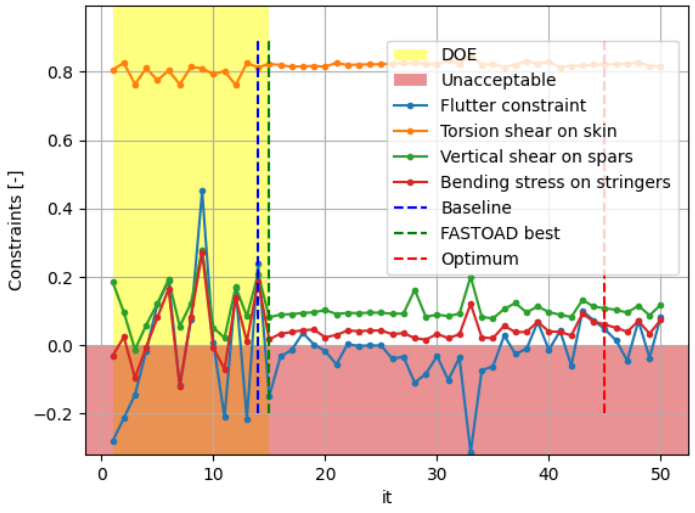

(b) Flutter and gust loads constraints

FIGURE 6.34: MDAO process for flexible aircraft under reliability constraints on flutter speed and gust loads. Monitor plot of the fuel mass objective function (a) and the flutter and gust loads constraints (b) through the SEGOMOE optimization iterations.

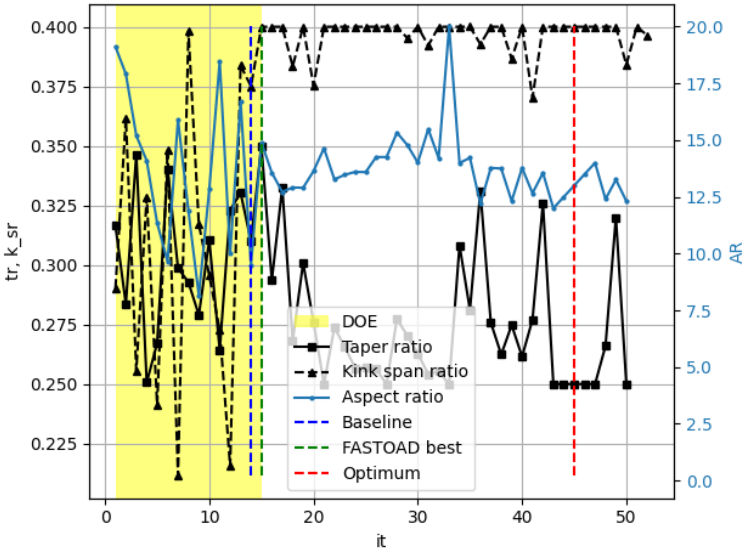

FIGURE 6.35: MDAO process for flexible aircraft under reliability constraints on flutter speed and gust loads. Monitor plot of the three design variables through the SEGOMOE optimization iterations.

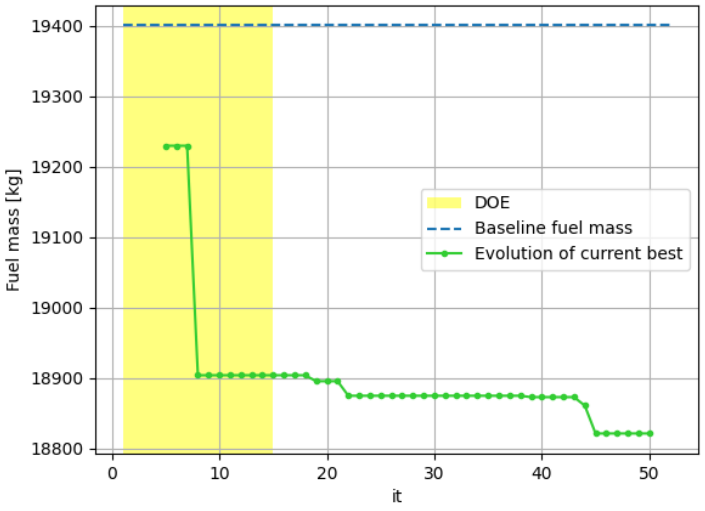

(a) Fuel mass objective

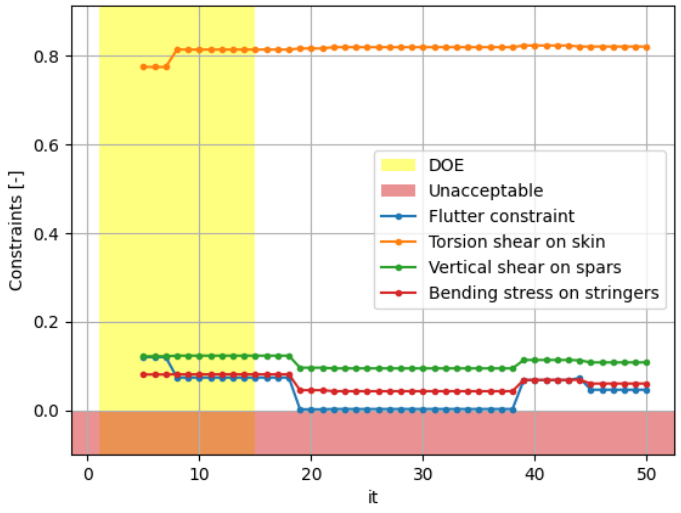

(b) Flutter speed constraint

FIGURE 6.36: MDAO process for flexible aircraft under reliability constraints on flutter speed and gust loads. Evolution of the current best fuel mass (a) and the corresponding flutter and gust loads constraints (b) through the SEGOMOE optimization iterations.

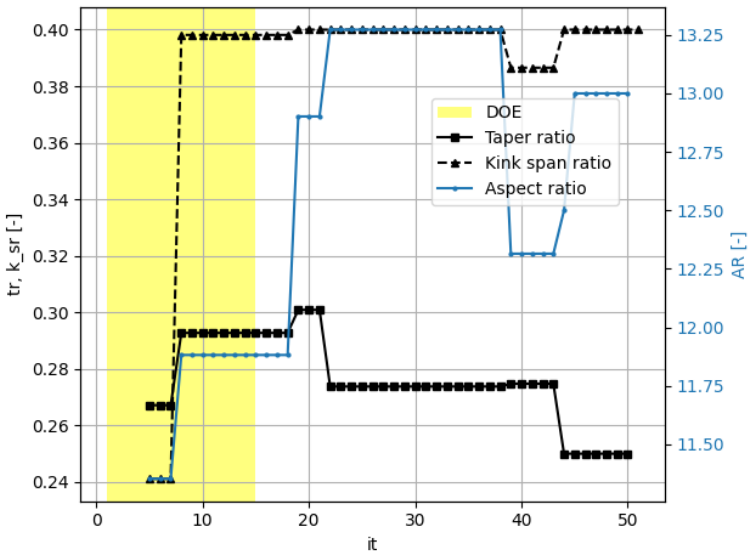

FIGURE 6.37: MDAO process for flexible aircraft under reliability constraints on flutter speed and gust loads. Evolution of the current best design variables through the SEGOMOE optimization iterations.

6.5 Results review and discussion

As several optimization cases have been presented one after another, it is worth collecting the results and discussing the main outcomes in a comprehensive and comparative way, which is the purpose of this Section. In fact, it was already observed that some mismatches emerged from the different studies, some of which did not appear to allow perfectly consistent conclusions.

First of all, it is useful to gather all the optimal points obtained from the different optimization applications. This is done in Table 6.14, reporting the best coordinates and objective functions obtained over the 7 different cases. Also, the corresponding wing configurations are represented and compared in Figure 6.38.

ID	Case description	$\mathcal{AR}$	t_r	k_{sr}	Fuel mass (kg)
0	Rigid aircraft	14.9	0.35	0.4	18,714
1	Deterministic flutter constraint	13.2	0.25	0.4	18,806
2	Deterministic gust constraints	14.1	0.25	0.4	18,854
3	Deterministic flutter & gust constraints	13.1	0.25	0.4	18,814
4	Reliability flutter constraint	13.7	0.25	0.4	18,865
5	Reliability gust constraints	13.7	0.25	0.4	18,858
6	Reliability flutter & gust constraints	13.0	0.25	0.4	18,821

TABLE 6.14: Summary of the optimization results from the different cases previously presented.

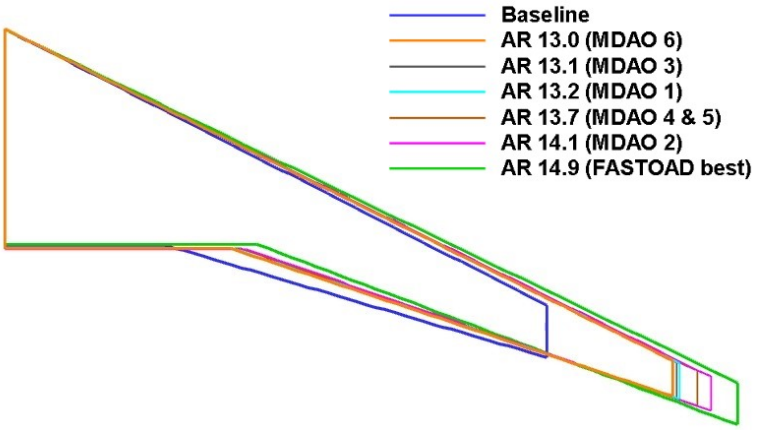

FIGURE 6.38: Best wing planforms from the different optimization cases previously presented. The baseline and the best planform from the `FAST-OAD` rigid aircraft optimization are also reported for comparison.

One clear outcome is that the rigid aircraft optimization is always optimistic compared to the flexible aircraft MDAOs, with the former giving a fuel burn prediction around 100-150 kg lower than the flexible aircraft process. Also, the best coordinates for the rigid aircraft [$\mathcal{AR}$, t_r] = [14.9, 0.35] are never reached with the aeroelastic approach.

A second general observation is that appreciable variations of the aspect ratio (between 13 and 14.1) produce small variations of the fuel mass, indicating, as already suggested, a possible plateau in the fuel-vs-$\mathcal{AR}$ relationship.

A good overview of the problem is obtained by looking at the plots showing the scatter of the objective function with respect to the three optimization variables over all the different analyses that have been carried out (including feasible and unfeasible evaluations). These are given in Figure 6.39. The first interesting information conveyed by these plots is the kind of relationship that links the fuel mass to the three variables. The evidence is that only the aspect ratio and the kink span ratio have a clear impact on the fuel burn. In particular, the former (Figure 6.39(a)) reveals an U-shaped distribution,

with a minimum located somewhat in the middle of the analyzed range, and the second (Figure 6.39(c)) indicates a linear descending trend, with the best values located towards the higher bound of 0.4. Less pronounced, and less relevant, is the effect of the taper ratio, with all the different MDAOs finding the best configurations at $t_r = 0.25$. As expected, the main feature to focus on is the fuel-vs-$\mathcal{AR}$ relationship, since the determination of a unique optimum turned out to be dubious.

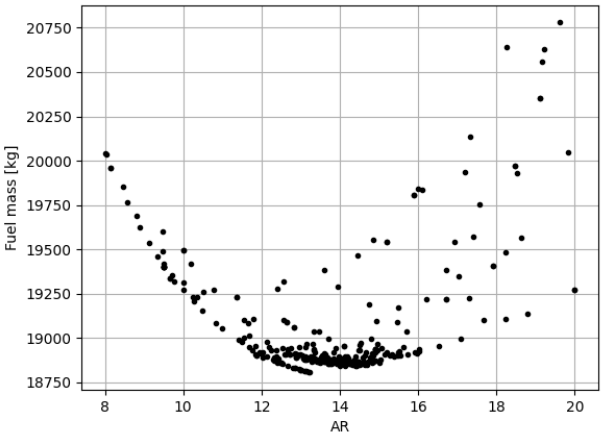

(a)

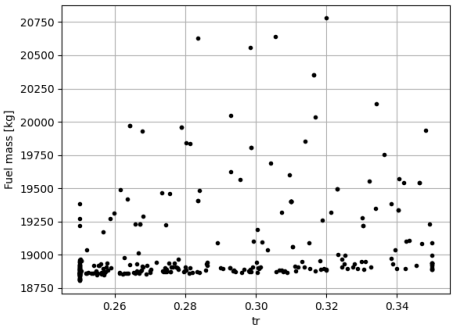

(b)

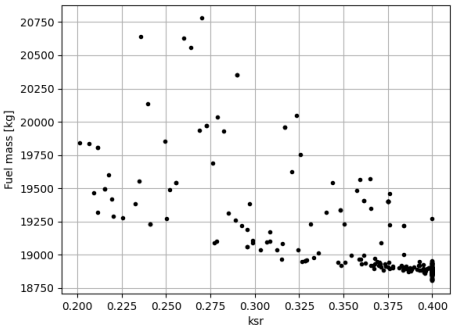

(c)

FIGURE 6.39: Scatter plots of the fuel mass with respect to the three design variables: aspect ratio (a), taper ratio (b) and kink span ratio (c). The data are those collected during the 6 MDAO cases presented above.

Further insights can be achieved by comparing the one-dimensional evolution of the fuel mass with respect to the aspect ratio, obtained from both the rigid and flexible aircraft sizing approaches. This was done by keeping the two remaining variables fixed, and in particular setting them to their optimal values $t_r = 0.25$ and $k_{sr} = 0.4$. The resulting curves are plotted in Figure 6.40. The two curves, originally coincident and then separating at around $\mathcal{AR} = 12.5$, have two different minima. In particular, the `FAST-OAD` curve results smoother and has a distinctly identifiable minimum at $\mathcal{AR} \approx 15$.

The initial descending trend of the fuel-vs-$\mathcal{AR}$ curve is explained by the fact that in that range the improvement in aerodynamic efficiency overcomes the impact of airframe weight increase required by slender wing structures, with a positive overall impact on fuel consumption. However, with increasing $\mathcal{AR}$, the weight penalty, due to the need for more robust wing structures to sustain higher and higher bending loads, starts to prevail over the aerodynamic benefits. This causes a gradual trend inversion after the optimal $\mathcal{AR}$ of 15, where the fuel mass curve exhibits a positive slope.

The flexible aircraft curve, instead, starts fluctuating after departing from the rigid aircraft curve, generating an irregular, plateau-like region between $\mathcal{AR}$ 12.5 and 15 where a minimum is not clearly recognizable. The plateau is physically explained by the fact that there is an aspect ratio range where the gain in fuel burn due to improved aerodynamic efficiency of more slender wings is counterbalanced by the increase in structural weight, with no net positive or negative impacts. The irregular trend in this region is characterized by fluctuations of fuel mass in the order of 20-50 kg. Their presence is to be attributed to the aeroelastic sizing process, where two levels of numerical uncertainty exist: first, the inner wing structural optimization is given a fixed number of evaluations before exiting - 45 in this case - and the outcome is therefore susceptible to a certain degree of randomness; second, when the wing structural weight W_{w2} is more than 2% away from the corresponding value W_{w1} predicted by `FAST-OAD`, the outer loops, as explained in Section 5.2.5, start by adjusting the aircraft configuration to the different wing weight and repeating the structural optimization until the discrepancy is less than the allowed 2%. The exigence of such loops appears to arise always above $\mathcal{AR}$ = 12.5, triggering the split between the two curves. These sources of numerical uncertainty are the reason of the fluctuations of the flexible aircraft curve, and prevent to pursue a fine optimization.

To better quantify these effects, multiple runs have been launched in the $\mathcal{AR}$ range 12 to 15. The results are reported in Figure 6.41, which confirms a noise of about 20 kg in most cases, except a larger error of 50 kg around $\mathcal{AR}$ = 13, where the aeroelastic predictions start to deviate from the rigid aircraft model, making the structural optimization task more likely to find each time slightly different optima.

These considerations explain the differences in the results between cases 1 to 6 in Table 6.14. Anyways, the contained extent of the fluctuations does not necessarily demand an increase of the analysis precision. The configurations in the aspect ratio interval 12.5 - 14 would result virtually equivalent in terms of fuel consumption. A design selection in this case should rather be dictated by other practical considerations - for example the fact that higher aspect ratios are in general more expensive from a manufacturing point of view. Moreover, the wing span could intervene as an additional constraint because of infrastructural requirements (airports, hangars, etc.). These aspects would likely prove more stringent than a 50 kg save in fuel mass, and would lead to the preference of an aspect ratio located at the lower side of the identified optimal region.

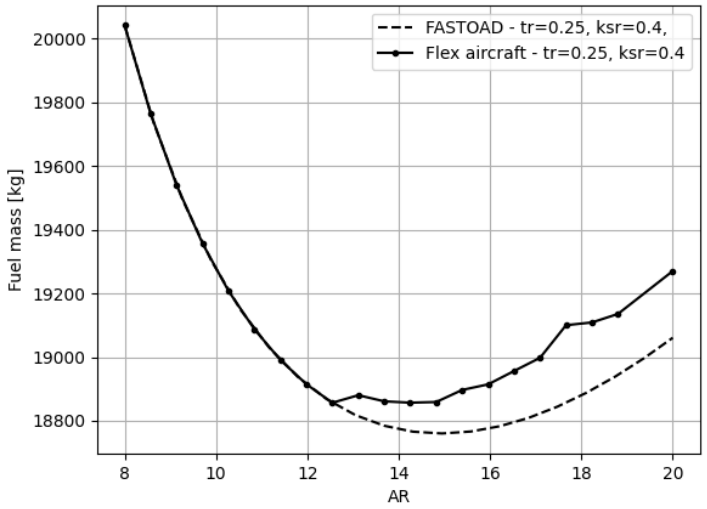

FIGURE 6.40: One-dimensional tracking of the fuel-vs-$\mathcal{AR}$ relationship over the studied space. The two curves correspond to the rigid aircraft sizing process obtained with `FAST-OAD` alone (dashed line), and to the flexible aircraft approach enabled by the developed methods (solid line). The taper ratio and kink span ratio are fixed to $t_r = 0.25$ and $k_{sr} = 0.4$.

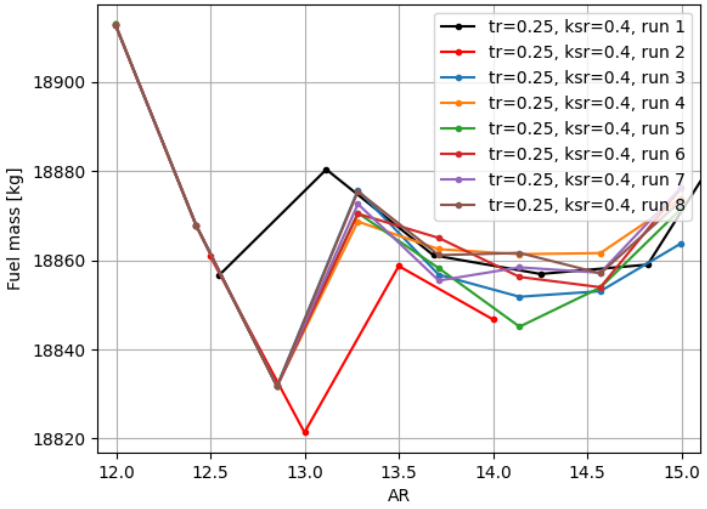

FIGURE 6.41: Overlap of multiple runs over the $\mathcal{AR}$ interval 12 - 15 showing the effect of numerical uncertainty in the flexible aircraft sizing process.

Another interesting aspect to discuss is the role of the enforced aeroelastic constraints. Looking back at Table 6.14, it appears that the real cause of the small discrepancy between the results of cases 1 to 6 is to be found in discussed effect of the numerical fluctuations, and not in the impact of the different enforced constraints. Indeed, the results are all located in the actual optimal region identified as the 'plateau' in Figure 6.40, suggesting that the prevailing driver is the physical dependence of the fuel with

respect to the three variables, and that the constraints are never strict enough to affect the minimization. This is confirmed when looking at the scatter plots of the different constraint values with respect to the three optimization variables. These are given in Figure 6.42, for the flutter speed constraint, and in Figure 6.43 for the gust loads constraints. In all the plots the deterministic constraints are denoted by a cross, and the probabilistic constraints by a dot.

Starting with the flutter constraint, it is evident that the taper ratio and kink span ratio do not have a critical effect (see Figures 6.42(b) and 6.42(c)), and the only relevant role is the one played by the aspect ratio (Figure 6.42(a)). The latter, in fact, shows a clear, almost linear relationship with the flutter speed constraint. However, despite this marked effect, the constraint, as it was defined, starts to be active above $\mathcal{AR} = 16$ in the deterministic case, and above $\mathcal{AR} = 14$ in the probabilistic case. This confirms the fact that such constraint was not decisive during any of the proposed cases.

Analogous conclusions are drawn from the gust loads constraints plots of Figures 6.43(a) to 6.43(c). A few differences can be noted though: first, the trend versus the aspect ratio is non-linear and shows a greater dispersion towards the higher aspect ratios; second, this time also the kink span ratio reveals a noticeable, although modest, linear effect on the three types of loads. However, apart from these secondary remarks, the main fact remains that none of these constraints were strict enough to play a key role in the optimization outcomes.

Nevertheless, this lack of impact is only case-dependent, and a small change in the constraint definition may turn into a totally different optimization outcome. For example, one can imagine that a safety factor is to be imposed on the flutter speed limit as well as on the gust loads. This would translate into an upward shift of the unacceptable region, shaded in red in the previous Figures (such as 6.42(b) and 6.42(c)). The offset would be equal to the imposed safety factor.

To give an idea of what the impact of such a move would be, three cases were compared, corresponding to three different safety factors: 0% (no increased safety, same condition as the discussed examples), 8% and 10%. The same data collected during the previous analyses were used, and the constraints considered are the probabilistic ones. The effects are shown in Figure 6.44. Here, the case with no safety increase is reported first (Figures 6.44(a) and 6.44(b)), corresponding exactly to the case 6 already discussed. It can be seen that the optimal aspect ratio region is only marginally impacted by the constraints, and the minimization results would be the same even without enforcing any constraint. When a safety factor of 0.08 is introduced (Figures 6.44(c) and 6.44(d)), the optimal region in the fuel-vs-$\mathcal{AR}$ space is no longer compliant, and the optimum starts to depend on the severity of the enforced constraints. Both the flutter speed and the gust bending loads show an active role. Increasing the safety factor to 0.1 (Figures

6.44(e) and 6.44(f)) accentuates this trend, showing even less valid candidates, triggering also the vertical shear constraint and further reducing the optimal aspect ratio. The different numerical results are collected in Table 6.15, and a graphical representation of the corresponding wing geometries is given in Figure 6.45. The optimal fuel mass would increase up to about 18,980 kg, more than 150 kg above the loosely constrained optimization, and the best aspect ratio would correspondingly decrease from 13 to 11.5. Similar effects can be expected if the input uncertainty is increased, or if additional uncertainty is injected, for example in the weight estimate provided by the aeroelastic sizing.

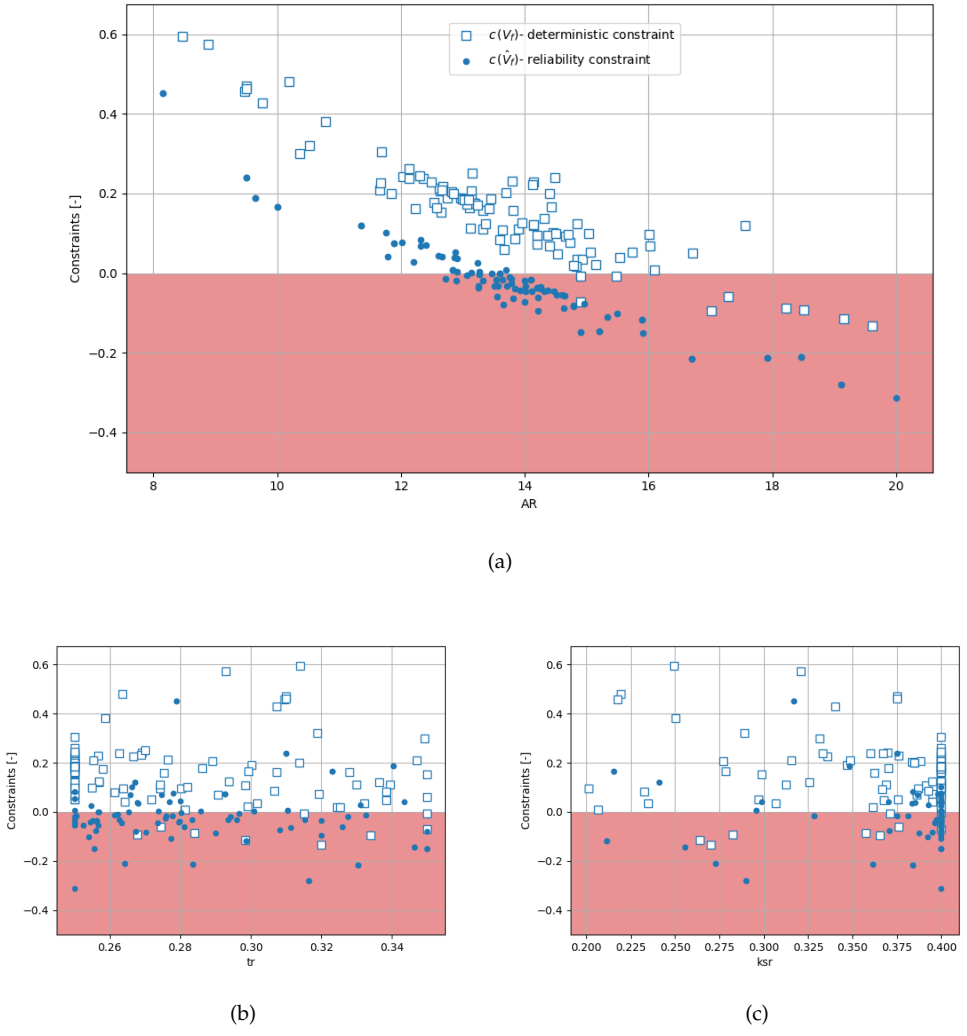

(a)

(b)

(c)

FIGURE 6.42: Scatter plots of the flutter constraint with respect to the three design variables: aspect ratio (a), taper ratio (b) and kink span ratio (c). The data are those collected during the 6 MDAO cases presented above, including the deterministic and probabilistic cases.

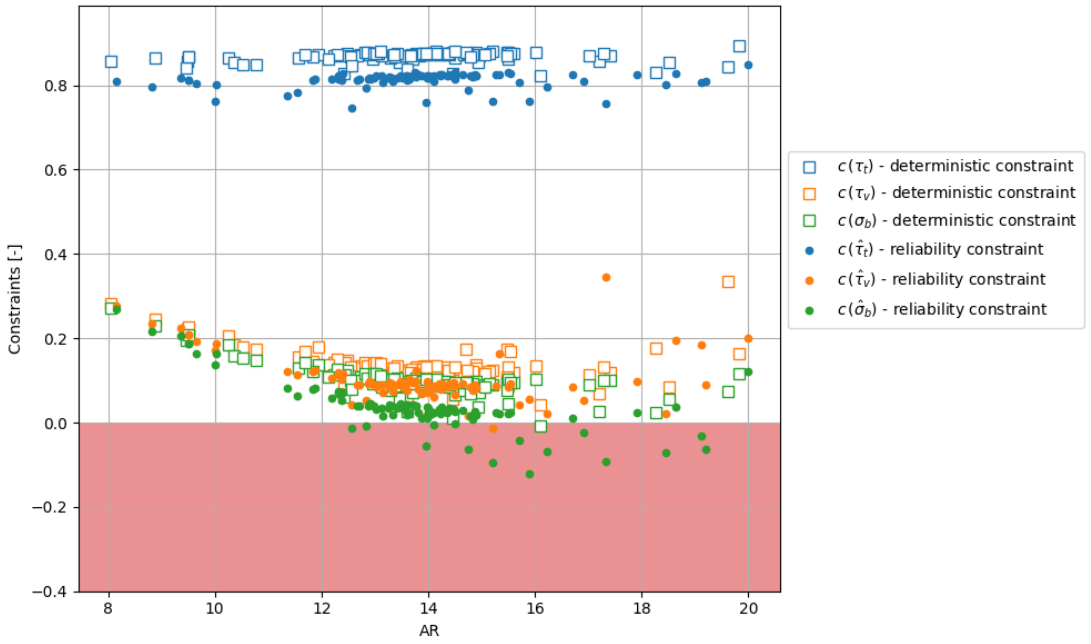

(a)

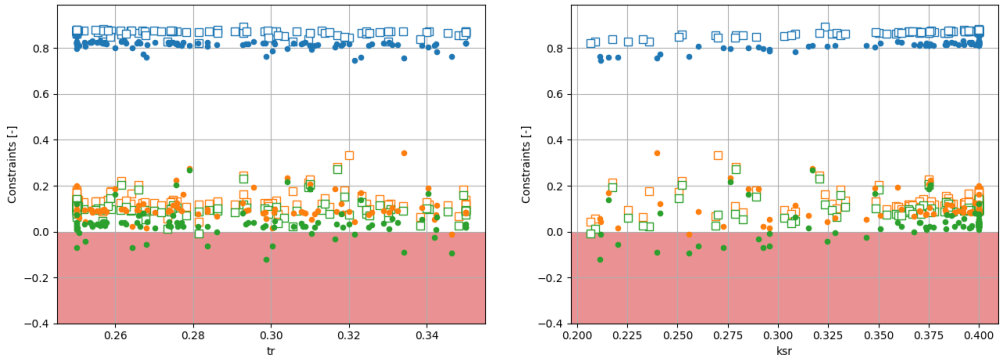

(b) (c)

FIGURE 6.43: Scatter plots of the gust loads constraints with respect to the three design variables: aspect ratio (a), taper ratio (b) and kink span ratio (c). The data are those collected during the 6 MDAO cases presented above, including the deterministic and probabilistic cases.

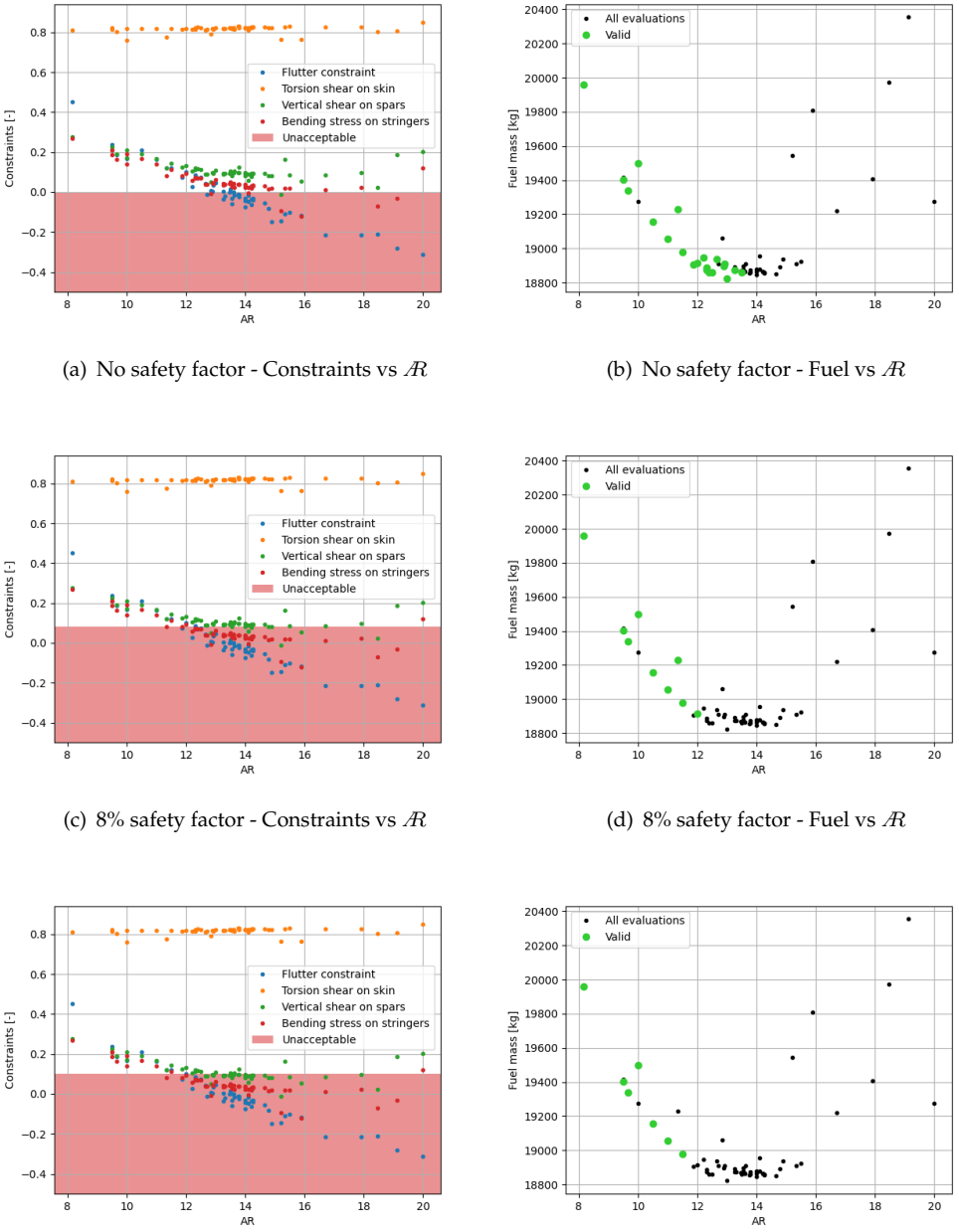

(a) No safety factor - Constraints vs $\mathcal{AR}$

(b) No safety factor - Fuel vs $\mathcal{AR}$

(c) 8% safety factor - Constraints vs $\mathcal{AR}$

(d) 8% safety factor - Fuel vs $\mathcal{AR}$

(e) 10% safety factor - Constraints vs $\mathcal{AR}$

(f) 10% safety factor - Fuel vs $\mathcal{AR}$

FIGURE 6.44: Examples showing the impact of introducing a safety factor in the reliability-constrained MDAO. For each case, the scatter plots of the constraints-vs-$\mathcal{AR}$ and fuel-vs-$\mathcal{AR}$ distributions are reported. The first case (a and b) has no safety factor, corresponding exactly to the MDAO case number 6 discussed above; the second and third case correspond respectively to a safety factor of 8% (c and d) and 10% (e and f). The safety factor is applied to all constraints, and its effect is highlighted by different red-shaded areas in the left Figures, as well as by different numbers of valid points, highlighted in green in the right figures.

ID	Safety factor	$\mathcal{AR}$	t_r	k_{sr}	Fuel mass (kg)
6.1	0%	13.0	0.25	0.4	18,821
6.2	8%	12.0	0.25	0.4	18,912
6.3	10%	11.5	0.25	0.4	18,977

TABLE 6.15: MDAO under flutter and gust loads reliability constraints. Optimization results corresponding to different safety increments applied on the constraint definitions.

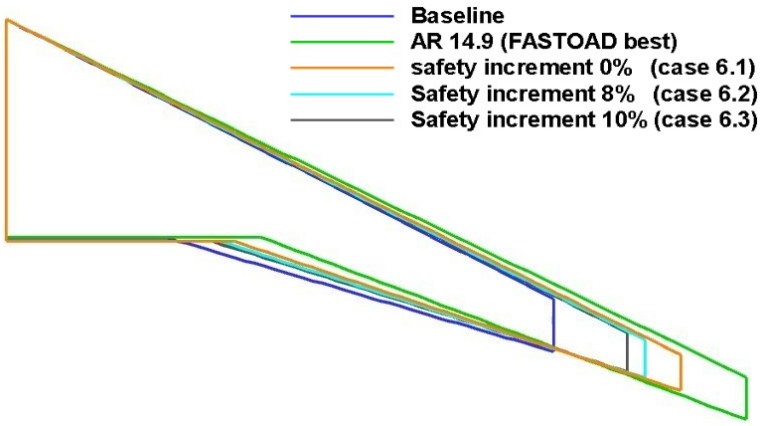

FIGURE 6.45: Best wing planforms corresponding to different safety increments applied on the constraint definitions. The baseline and the best planform from the FAST-OAD rigid aircraft optimization are also reported for comparison.

6.6 Conclusions

This Chapter has demonstrated the application of the framework proposed in Chapter 5 for robust multidisciplinary analysis and optimization for flexible transport aircraft. The specific case study involved the wing planform optimization of the CeRAS baseline for fuel mass minimization over a fixed mission. In particular, three geometric variables were chosen: the wing aspect ratio $\mathcal{AR}$, its taper ratio t_r and the nondimensional kink position (or kink span ratio) k_{sr}. Structural flexibility was taken into account for the main wing, which is considered the only element to undergo significant deformations and oscillations. The term 'robust', as anticipated in Chapter 2, is intended in its wider connotation indicating 'resilience' against uncertainty or design changes. More precisely, the uncertainty, attributed to a few structural parameters, is propagated only onto the constraints on flutter speed and gust loads. Therefore, strictly speaking, the task performed is an optimization under dynamic aeroelastic reliability constraints.

Before addressing this task, some simplified versions of it were performed, with increasing complexity, in order to have some reference results to compare with. The first case, presented in Section 6.2, considers the aircraft as perfectly rigid. In that case, there is no need for the inner structural optimization loop (for flexible wings), and additionally no dynamic aeroelastic constraints are applied. The optimization was performed just by means of the standard `FAST-OAD` sizing routines and of the `SEGOMOE` optimization suite. As aeroelasticity is neglected by `FAST-OAD`, the optimization was left unconstrained, and therefore also the uncertainty propagation was avoided, in favour of a deterministic approach. The results show a clear tendency towards very elongated wings, with an optimal aspect ratio of 14.9, 57% higher than the baseline one, allowing a 3.5% save in fuel mass compared to the baseline configuration.

The following step, after the rigid aircraft optimization, was to employ the new framework to perform a first set of flexible aircraft MDAO in a deterministic context. The problem definition was left unchanged, but this time some aeroelastic constraints were enforced. In particular, a first case was run with the constraint on flutter speed, a second case with three constraints on gust loads (bending, vertical shear and torsion), and a third case with all constraints on both flutter speed and gust loads active at the same time. However, it was found that the main driver affecting the optimization results was the inner wing structural optimization loop. In fact, the constraints applied at that stage, imposing safety against static limit loads on the deformable wing, appeared to be more stringent compared to the outer dynamic aeroelastic constraints, which are evaluated only after the wing is sized for static loads. Therefore, most configurations resulted compliant with respect to the deterministic flutter and gust constraints. However, the inner structural sizing routine, which considers the wing flexibility, already reveals some differences with respect to the standard rigid aircraft approach. In particular, the main effect of the flexible wing sizing was a smaller optimal aspect ratio,

which was found between 13 and 14 in the three cases studied, instead of the almost 15 given by the rigid case. This resulted in a reduced save of fuel mass (about 3% instead of 3.5).

The last and more complex step was to run the same three MDAO cases for the flexible aircraft, but this time introducing uncertainty on a couple of structural parameters (the location of the wing's elastic and center-of-gravity axes). Therefore the dynamic aeroelastic constraints were redefined as reliability constraints, imposed on the probability of violating certain safety limits of flutter speed and/or gust loads. It is true that the choice of such kind of stochastic constraints is somewhat arbitrary, because most specification requirements are deterministic, and the definition of how much 'reliable' or 'robust' the results should be is really up to the designer will for the particular case under examination. Thus, it was shown that the optimization results under reliability constraints are indeed dependent on how restrictive the probabilistic requirements are. For example, the first round of optimization studies under aeroelastic reliability constraints did not provide significant differences compared to the previous deterministic studies. This happened because the probabilistic requirements were not stringent enough to make a difference in the optimization process, which remained dominated by the inner static wing sizing. In fact, the optimal wing planform resulted from the best compromise between aerodynamic efficiency and structural weight, both of which increase with the aspect ratio.

However, it was later shown how a different choice of the reliability requirements can easily change the design outcome. For example, it was found that increasing the safety threshold for flutter speed and gust loads by 8 or 10% makes the aeroelastic constraints (especially flutter and bending gust loads) much more active, with the effect of reducing the best allowable aspect ratio down to 12.5 or 11.5, and further reducing the fuel mass gain to 2.5% or 2.1%.

Overall, this Chapter demonstrated the capability of the proposed framework to tackle complex optimization problems for the design of unconventionally high aspect ratio flexible aircraft, with the possibility of injecting and propagating parameters uncertainty to evaluate the robustness or reliability of the design outcome. The application focused on the wing planform optimization of a transport aircraft to minimize fuel, and structural uncertainty was considered and propagated into some dynamic aeroelastic reliability constraints, including flutter speed and gust loads. Results were compared against those for a conventional rigid aircraft design approach, and the main differences were highlighted and discussed. In particular, it was found that the conventional approach can result in dangerous non-conservative results, as its predictions were too optimistic both with respect to the fuel mass objective function, and to the aeroelastic safety of the optimal configuration.

The proposed framework introduces a great computational cost with respect to the conventional approach, the former requiring around a couple of days of serial calculations on a modern computer for the robust approach and half to one day for the deterministic one, compared to less than an hour for the conventional rigid-aircraft approach. However, an order of magnitude of a few days of calculations during a conceptual design phase represents a minimal cost if compared to all the mitigation activity to be undertaken in case an aircraft project is found unsafe during its advanced development. Moreover, these few days can be significantly reduced by running the optimization in parallel.

6.7 Summary

This Chapter presents some aircraft design and optimization studies involving the developed framework and tools discussed earlier in this manuscript. In particular, the Chapter is structured as follows:

- An overview of the problem is provided. The optimization task targets the fuel minimization for a baseline airliner for a fixed mission, by searching the best combination of a few wing planform parameters, including the aspect ratio. The constraints to be applied concern flutter speed and gust loads, and they are to be treated in both a deterministic and a probabilistic approach.
- Before running the optimization cases taking aeroelasticity into account, one conventional optimization assuming a fully rigid airframe is performed, serving as a reference for the subsequent applications on flexible aircraft.
- A series of three flexible aircraft MDAO cases is performed according to the deterministic approach. The first implements only the flutter speed constraints, the second implements the gust loads constraints only, the third involves all constraints together.
- Three flexible aircraft robust MDAO cases are performed following the same format as the previous ones, but as uncertainty is introduced, the dynamic aeroelastic constraints are expressed in a probabilistic way, taking the form of reliability constraints.
- A comparative review and discussion of all the above results is provided, and conclusions are drawn.

This chapter marks the fulfillment of the last of the technical objectives stated in Section 1.2. With the rest of them being already addressed in the previous chapters, this also marks the accomplishment of this project's overall aim. A conclusive overview of

this Thesis's content and look to the main perspectives for future work are given in the next chapter.

Chapter 7

Conclusions

Contents

6.1 Overview 208
6.2 Rigid aircraft optimization 209
6.3 Deterministic MDAO results 214
6.3.1 Optimization under flutter constraint only 214
6.3.2 Optimization under gust loads constraints only 219
6.3.3 Optimization under flutter and gust loads constraints 225
6.4 Robust MDAO results 231
6.4.1 Optimization under flutter reliability constraint only 232
6.4.2 Optimization under gust loads reliability constraints only . . . 238
6.4.3 Optimization under flutter and gust loads reliability constraints 245
6.5 Results review and discussion 251
6.6 Conclusions 261
6.7 Summary 263

7.1 Thesis summary

In a context where air transport innovation is targeted with increasing urgency, with both research and industry engaged with vibrant determination, this project seeks to propose a new and effective approach for the conceptual design and optimization of novel efficient aircraft concepts, and in particular of those involving flexible, high-aspect-ratio lifting surfaces. As discussed in Chapter 1, this task requires the capability of capturing, as early as possible in the design process, the complex physical phenomena deriving from structural flexibility, generally defined as fluid-structure interaction or aeroelastic problems.

The complexity arises from several aspects: different disciplines have to be treated in a coupled way (at least aerodynamics and structural dynamics, but also flight dynamics and control science are involved), several challenging phenomena have to be taken into account, such as static and dynamic structural response, structural response at high deformations, three-dimensional aerodynamic effects, unsteady aerodynamics, compressibility, flight mechanics. As a result, static and dynamic aeroelastic analyses easily become costly and difficult to set up.

Moreover, conducting such multidisciplinary studies at conceptual design level necessarily introduces and combines uncertainty from different sources, due to the unavoidable assumptions and approximate estimations or guesses in lack of precise and trustable data. Despite this problem is often bypassed in favour of a deterministic approach, such choice can be risky, if not fatal, as it can significantly impact the development costs due to expensive design reviews during the next, more advanced design phases. For this reason, this project aimed not only at the development of adequate multidisciplinary analysis tools to include aeroelastic and flight dynamics information during the conceptual design phase, but also to provide a capability of injecting and propagating uncertainty over the design and optimization process, in order to deliver an assessment about the robustness of the optimization results.

The fundamental aim of this project is summarized as follows:

The development of an analysis and simulation framework to investigate aeroelastic and flight performance of new generation flexible aircraft, capable of handling and propagating input uncertainty, in support of a robust design and optimization process at conceptual design phase.

To achieve this target, the project was built around four technical objectives, stated in Section 1.2 and reported here for convenience:

I the development of a set of adequate analysis tools for the disciplines of interest, namely aerodynamics, flight dynamics and structural dynamics, in response to the need of more physics-based methods for unconventional design exploration;

II the integration of the above modules with an aircraft sizing tool to broaden the design exploration capabilities, including the possibility of taking into account discipline-related uncertainty and constraints;

III the further expansion of the framework's capabilities and set of constraints by enabling coupled aero-structural analyses under uncertainty;

IV the demonstration of a robust design and optimization process for a highly flexible aircraft concept.

In order to effectively address the above objectives, a review of the state of the art was pursued, spanning the main technical domains involved in this research problem. This review is provided in Chapter 2.

Then, the development, integration and validation of all the required tools is documented in Chapter 3. More in detail, those tools respond to the need of suitable computational methods for: steady and unsteady aerodynamics, linear and nonlinear, static and dynamic structural mechanics, static and dynamic aeroelasticity, flight dynamics simulation, simulation post-processing, sensitivity analysis and uncertainty quantification, overall aircraft design and optimization. This development partly fulfills the technical objective I.

A first demonstration of how those tools can be integrated for a robust multidisciplinary analysis and optimization task is provided in Chapter 4. The application involves a transport aircraft planform optimization under uncertainty, targeting the best aerodynamic configuration to minimize the fuel mass for a given reference mission. Some of the developed disciplinary tools (aerodynamics and flight dynamics modules) were used to constrain the optimization under flying qualities requirements, concerning in particular the short period dynamics. The input uncertainty was put on some weight & balance parameters and propagated into the short period characteristics, so that the dynamic constraints took the form of reliability constraints. This study demonstrates the accomplishment of the technical objective II. This objective represents an intermediate step in the project outline, as aeroelasticity was not taken into account yet.

The technical objective III is achieved in Chapter 5, which presents a more complex architecture for robust multidisciplinary analysis of flexible aircraft, where static and dynamic aeroelasticity is finally considered. The structure is similar to the previous example, but this time the reliability constraints are on the dynamic aeroelastic performance of the candidate configurations, and in particular on flutter speed and dynamic gust loads. The Chapter details all the relevant building blocks and their interface, which involves an inner structural sizing and optimization loop for flexible wings, and an outer overall aircraft optimization loop under the new aeroelastic reliability constraints. Some sensitivity studies on the aeroelastic quantities of interest are also

presented, in order to select the most relevant parameters whose uncertainty can significantly impact the design outcome.

Finally, the capabilities of the above framework are demonstrated in Chapter 6. A series of optimization studies was performed with increasing complexity. First, a conventional optimization was carried out under the assumption of rigid aircraft, therefore ignoring any aeroelastic issue. Then, the same optimization was run considering wings flexibility, and adopting deterministic flutter and gust loads constraints. Lastly, the optimization was repeated but introducing some relevant structural uncertainty, according to the sensitivity results of Chapter 5, and propagating it into flutter and gust loads reliability constraints. The results from the different approaches are also discussed and compared at the end of the Chapter. These case studies concretely demonstrate the applicability of the developed approach for robust analysis and optimization of flexible aircraft. This successfully addresses the last technical objective (IV), in fulfillment of the PhD project aim.

7.2 Achievements

7.2.1 Tools development, integration and validation

A robust analysis and optimization process for flexible aircraft is a multidisciplinary task that requires the integration of several disciplinary analysis tools within a numerical framework that also involves aircraft sizing algorithms, optimization algorithms and uncertainty quantification tools. A large part of this project was aimed at the development and integration of such tools. In particular, the flight physics disciplines of interest, as far as this project is concerned, are mainly aeroelasticity and flight dynamics. Aeroealsticity is essential to capture the potentially dangerous response of the flexible airframe subjected to static and dynamic airloads. Flight dynamics is of interest because this research is projected towards the flight simulation of flexible aircraft. Static and dynamic aeroelastic analyses require in turn adequate models for steady and unsteady aerodynamics, static and dynamic, linear/nonlinear structural mechanics, and an effective interface to couple the two domains. For these reasons, the disciplinary tools development and integration was addressed to the implementation of:

- A choice of aerodynamic models, including a classical analytical model based on linear aerodynamic derivatives, and a steady or unsteady implementation of the Vortex Lattice Method (VLM or UVLM);
- A nonlinear structural mechanics solver (GEBT, Geometrically Exact Beam Theory)

- Two possible aeroelastic solvers: *a*) a linear solver based on potential unsteady strip theory coupled with linear beam theory, mainly required for flutter analysis; *b*) a linear/nonlinear solver coupling the GEBT structural solver with the VLM or UVLM aerodynamic solvers;
- A flight dynamics simulation module (FDM) implementing the 6DOFs nonlinear equations of motion;
- A post-processing module to extract the desired quantity of interest (amplitude, frequency, damping) out of the simulation history by use of a Least Square best fit technique of the time-domain data;

All the above disciplinary tools have been developed by the author, except the `GEBT` solver, which was taken off-the-shelf and then integrated with the VLM/UVLM solvers to enable nonlinear aeroelastic analysis. The choice of developing such programs resulted from a combination of reasons: lack of well documented and validated off-the-shelf software matching the different needs, the interest of having a fully mastered code, with deep knowledge of its structure, analytical basis and numerical limitations, the need for flexible interface between the different disciplines.

In addition, the following existing tools have been tested and integrated for aircraft design and optimization under uncertainty:

- An uncertainty quantification and sensitivity analysis module that wraps the above modules and propagates the uncertainty from the input parameters into the desired outputs. It returns the desired statistical metrics to be used in the reliability evaluation;
- An aircraft conceptual sizing tool (`FAST-OAD`) performing the necessary loops until convergence to a consistent configuration;
- An optimization environment (`SEGOMOE`) to be interfaced with the sizing process and with the implemented multidisciplinary deterministic or stochastic constraints (such as flying qualities constraints, flutter speed, gust loads).

The availability of such tools allows performing a variety of analysis, simulation and optimization tasks over flexible aircraft or flexible wings, with the option to introduce uncertainty and propagate it into different figures of merit, such as flying qualities, static loads, flutter speed, gust loads, but also overall parameters such as fuel consumption.

The successful implementation, integration and validation of those tools marks the first achievement of this project, responding to the first objective I set out in the preamble of this work (Section 1.2). This outcome represents an important contribution because it

opens to several different multidisciplinary studies on flexible aircraft robust optimization. The remaining Chapters of this manuscript offer just a glimpse of the research problems that could be addressed.

7.2.2 Application: MDAO of rigid aircraft under flying qualities reliability constraints

A second, intermediate achievement of this work is the demonstration of how some of the proposed tools can be assembled and employed for a multidisciplinary design and optimization process for a transport aircraft under input parameter uncertainty. In particular, the selected case study was about a planform optimization to minimize fuel mass, constrained by some probabilistic constraints on short period characteristics.

To evaluate such dynamic characteristics, some of the developed disciplinary tools were used. In particular, it was shown how the VLM and the UVLM can be used to calculate a set of steady and unsteady aerodynamic derivatives that can be stored in an aerodynamic database useful for flight simulation. Subsequently, the flight dynamics module can be run, with the unsteady aerodynamic loads easily and quickly calculated via simple formulae based on the pre-computed derivatives. This approach allows to perform flight simulation studies that benefit from an enriched aerodynamic model, which is usually not available during early simulation campaigns. It was shown that the computational cost of complex models could be mitigated by the use of surrogate models.

In this particular case, the flight dynamics model was used to simulate the short period response at certain fixed cruise conditions. The post-processing module was then used to extract the desired figures of merit (in this case short period damping and frequency) out of the simulated time history, in a completely automatic fashion. These quantities were compared against some flying qualities requirements, derived from military specifications, in order to constrain the overall optimization.

An additional degree of complexity was introduced by considering that weight and balance estimations from the aircraft sizing tool were uncertain. Such uncertainty was propagated to the short period characteristics by use of the uncertainty quantification module. Therefore, the flying qualities constraints were formulated in probabilistic terms. The overall problem took the form of a reliability-constrained optimization.

This application represents a first example of how the implemented tools can be assembled into an MDAO framework for robust aircraft design, responding to the intermediate objective II. This example, however, did not include all the disciplinary tools developed throughout the project, and in particular did not take airframe flexibility into account. Such problem was addressed in the following activities.

7.2.3 MDAO framework for the design of flexible aircraft under uncertainty

The most ambitious achievement of this project in terms of software architecture is the assembling of a robust MDAO framework for very high-aspect-ratio flexible aircraft. The aim was to allow an overall optimization process for an aircraft configuration by taking into account the major issues arising from wings' flexibility. These include both the static and dynamic aeroelastic characteristics.

The static aeroelastic behaviour is investigated within an inner wing sizing and optimization loop, with the outer optimization variables kept fixed while the wing structural layout is optimized for minimum weight under static manoeuvre loads constraints. This is addressed in an aeroelastic sizing cycle integrating the developed nonlinear aeroelastic model with the `FAST-OAD` aircraft sizing tool and the `SEGOMOE` optimizer. Some validating examples were provided, showing that when applied to conventional wings of moderate aspect ratio, the results of this approach are consistent with standard semi-empirical methods.

The dynamic aeroelastic characteristics of the sized wing is subsequently evaluated not to provide a feedback to the sizing process, which would imply excessive complexity and computational time, but simply to constrain the outer optimization process. The non-compliant configurations are not resized, but just discarded. In particular, the dynamic aeroelastic features considered in this work are flutter speed and gust loads. It was shown how the developed tools can be interfaced with the overall aircraft sizing process and provide the desired output quantities.

Additionally, such a framework can include some uncertainty quantification routines to propagate the required input parameter uncertainty into the desired output quantities. Here, this process was demonstrated for some input structural parameters, whose uncertainty is propagated to the dynamic aeroelastic characteristics of the wing. In this way, the overall optimization problem can take the form of a reliability-constrained optimization, where the flutter speed and gust loads constraints are formulated in a probabilistic way.

Such a process provides another example of the effectiveness of the methods developed and integrated throughout this project to tackle complex MDAO problems for robust aircraft design at conceptual level, fulfilling the third research objective III.

7.2.4 Application: MDAO of flexible aircraft under aeroelastic reliability constraints

The last and most complex achievement of this project is the demonstration of how the developed framework described above, including in particular the linear and nonlinear

aeroelastic tools, can be employed for robust MDAO of high-aspect-ratio flexible aircraft. A case study was set up, consisting in the optimization of a transport aircraft, the CeRAS baseline, aiming at minimizing the fuel mass for a given mission, with respect to a few wing planform variables, including the aspect ratio.

An overview of the framework architecture has already been given in the previous Section. Three main approaches were compared: 1) a conventional optimization based only on the traditional rigid-aircraft approach of `FAST-OAD`, neglecting any aeroelastic effects and constraints; 2) a deterministic MDAO using the newly-developed tools, where aeroelasticity was taken into account both for the inner wing static sizing and for the outer evaluation of the flutter and gust loads constraints; 3) a robust MDAO approach following the same logic as the previous, but this time considering some input uncertainty on a few key structural parameters, and propagating it into the outer flutter and gust loads constraints.

The results obtained with the different methodologies have been compared and discussed. One main outcome is that the proposed method provides equivalent predictions as the conventional rigid-aircraft one when applied to low or medium aspect ratios, up to around 11, but then the two approaches start to deviate from each other. In particular, the rigid-aircraft approach resulted optimistic compared to the flexible-aircraft approach, confirming the potential advantage of the latter in terms of safety and robustness.

Moreover, it was demonstrated how the aeroelastic reliability constraints can significantly impact the optimization outcome, depending on how much uncertainty the designer is prepared to accept. In fact, it was shown that a slight change of the acceptability criteria, especially on flutter speed and gust bending loads, can turn them from inactive to active, in which case their effect is mainly to reduce the optimal feasible aspect ratio and degrade efficiency.

The reported applications represent only an example among the different studies that could be addressed with the available tools. However, to the author's knowledge, there are very little comparable examples in literature of such complex multi-disciplinary tasks where the overall optimization of an entire aircraft configuration is addressed by taking into account both static and dynamic aeroelastic effects, capable at the same time of propagating uncertainty to enable a reliability-constrained optimization. The achievement of this level of performance accomplishes the last objective of this project (IV), and represents the most valuable contribution of this PhD program.

7.3 Perspectives

7.3.1 Possible improvements and future work

The proposed development and studies represent an already rich and complex multi-disciplinary research work. Yet, the presented applications served as first proofs of concept of the implemented approach, so that several aspects were considered only in a limited way. Therefore, there are plenty of areas where the focus can be increased, or shifted, and several ways in which the analysis capabilities can be improved. An exemplifying list of possible improvements and further studies is here briefly provided.

To start with, the same kind of MDAO studies could be addressed with some additional features not considered in this work. For example, the analyses could be extended to include the evaluation of asymmetrical flutter, the inertial effects of wing-mounted engines, lateral flying qualities. Also, the design space could be extended to include not only additional wing geometry variables (such as wing twist, sweep, dihedral angle), but also other variables at the aircraft level. Similarly, the set of constraints could be expanded, for example by considering more sizing mass cases or flight points where to evaluate the gust response and flutter safety. Flying qualities constraints could also be added together with aeroelastic constraints during the same MDAO, whereas this work only presented the two types of constraints in two separate applications.

It would be also interesting to apply the same design approach and available tools to different configurations, such as unconventional wing shapes (box-wing, strut-braced wings, blended-wing-body configurations) or in combination to other design solutions involving electric/hybrid propulsion, distributed propulsion or hydrogen propulsion.

Moreover, some of the available analysis tools could be applied not only to overall aircraft applications, but also to lower level studies involving just the wing, or the wing and tail, or the wing with its control surfaces, for example to design manoeuvre loads alleviation (MLA) and gust loads alleviation (GLA) systems.

Furthermore, it would be interesting to provide some comparison of the proposed strategies against standard high-fidelity methods. A relatively simple example could be to reproduce a wing sizing and optimization case, such as those demonstrated in Section 5.2.4, with a more detailed structural finite element model of the three-dimensional wing structure. More ambitious validation studies could reproduce the entire MDAO cases presented in Chapter 6 and substituting the present aeroelastic models with higher-fidelity structural and aerodynamic tools. Some work could be performed on characterizing the accuracy of the proposed approach, and the gain in computational time. Several aspects could be further investigated, such as the role of mass tolerance in the wing sizing loops, the question of introducing additional surrogate models, or the effect

of restructuring the optimization problem so that planform and structural variables are treated together at the same level, instead of separating them in inner and outer loops.

Finally, as already mentioned earlier in this manuscript, an interest exists at the University of Southampton, where an advanced research flight simulator is being put in place, towards the flight simulation of fully flexible aircraft configurations. The simulation tools developed during this PhD project offer a good starting point in this direction. More details on this are given in the following Section.

7.3.2 Flight simulation of very flexible aircraft

Flight simulation of highly flexible aircraft can be achieved with the tools presented so far by coupling the flight dynamics simulation model of Section 3.5 with the nonlinear steady or unsteady aeroelastic model presented in Section 3.4.2. The tools have all been implemented in order to be compatible and with a dedicated interface. In fact, they are all part of the Fortran suite, where the modules are designed to share the same variables, classes and subroutines, as well as data formats for the inputs and outputs. For example, the flight dynamics module can import the instantaneous aerodynamic loads in three main ways: *a*) from a simple derivative-based aerodynamic function; **b**) from the steady or unsteady VLM; *c*) from the aeroelastic module, that in turn couples the steady/unsteady VLM with the GEBT linear/nonlinear solver. The last option would correspond to the mean-axes simulation approach discussed above, where flight dynamics module propagates the trajectory of the vehicle while at each time step the aerodynamic loads are computed by the aeroelastic solver. An extract of a simple demonstration is represented in Figures 7.1 and 7.2. Here, the level horizontal flight of a wing-plus-stabilizer configuration is simulated after the wing oscillations are excited by a step-change of local angle of attack. The Figures capture an instant after several oscillations occurred. This is visible from the undulated shape of the wake, reproduced by the UVLM solver, which gives an idea of the trajectories of different points along the wing's trailing edge. Additionally, the wake roll-up can be noted in correspondence of the wing tips. It is worth to point out that only the wing is here treated as flexible, whereas the tail is considered rigid. The unevenness of the tail's wake is only due to the interaction with the oscillating wake of the main wing.

This example is aimed at showing the capabilities of the developed analysis and simulation toolbox, and in particular the ability to select and couple the disciplinary tools to perform simulations of different complexity according to the specific needs. However, the unsteady flight simulation of a flexible aircraft, representing highest level of complexity, remains a challenging task when linking its application to robust analysis and optimization process. For instance, it requires a demanding tuning and validation process, involving a consistent definition of geometry and reference frames, as well as an appropriate choice of discretization density for aerodynamics and structure, numerical

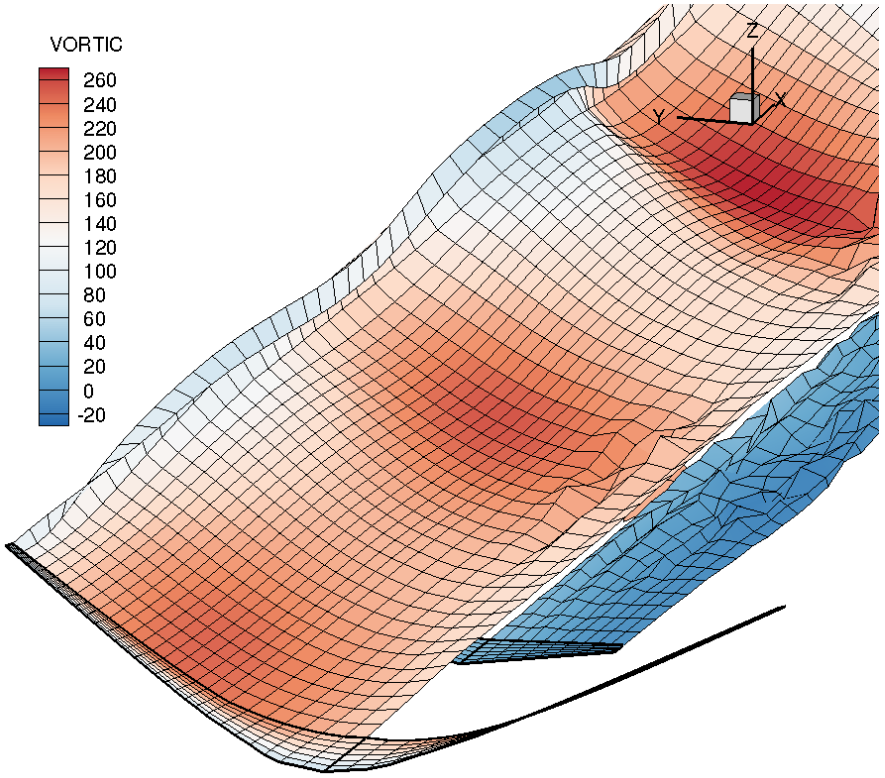

FIGURE 7.1: Snapshot from an unsteady aeroelastic simulation of the response of a flexible wing-plus-stabilizer configuration to a step-change in the angle of attack. The contour plot highlights the distribution of vorticity over the wing, stabilizer and their wakes.

integration method and time stepping adequate both for the structural dynamics and the unsteady aerodynamics. Moreover, those choices are case-specific, meaning that it is not immediate at all to move from a test case to another.

For these reasons, this level of simulation is only shown here for demonstrative purpose. Further validation and software optimization work is required to have this capability ready to be included into wider studies involving aircraft design exploration, optimization and uncertainty quantification. In this project the different disciplinary modules have been employed for different case studies, but without enforcing this full coupling.

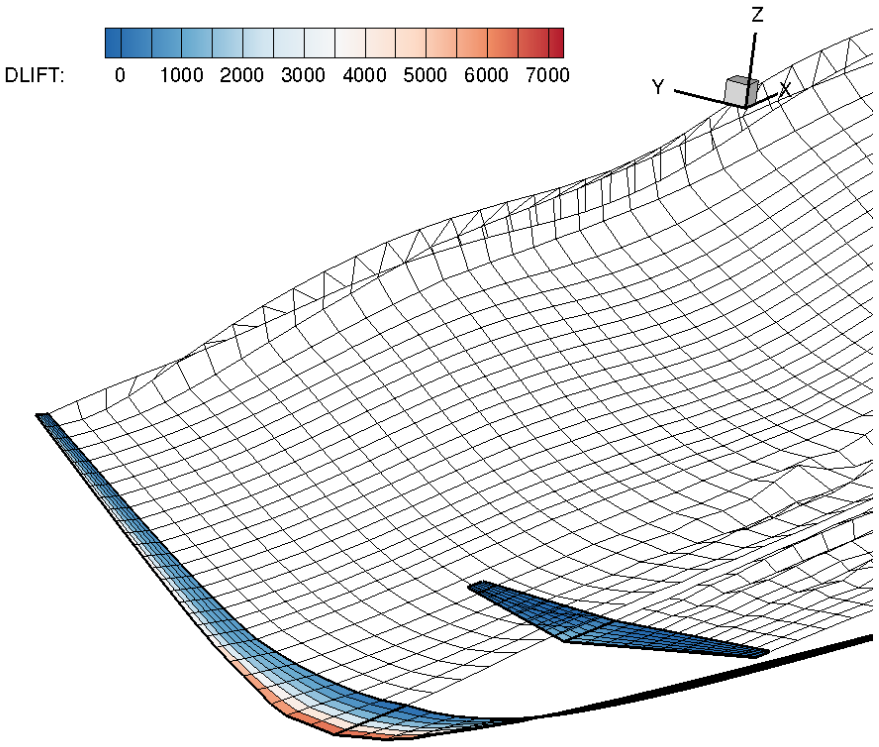

FIGURE 7.2: Snapshot from an unsteady aeroelastic simulation of the response of a flexible wing-plus-stabilizer configuration to a step-change in the angle of attack. The contour plot highlights the distribution of lift over the wing and stabilizer. Their discretized wakes are also represented by a black uncoloured mesh.

Appendix A

Unsteady strip theory formulation

Contents

7.1 Thesis summary 266

7.2 Achievements 268

7.2.1 Tools development, integration and validation 268

7.2.2 Application: MDAO of rigid aircraft under flying qualities reliability constraints 270

7.2.3 MDAO framework for the design of flexible aircraft under uncertainty 271

7.2.4 Application: MDAO of flexible aircraft under aeroelastic reliability constraints 271

7.3 Perspectives 273

7.3.1 Possible improvements and future work 273

7.3.2 Flight simulation of very flexible aircraft 274

A.1 Expressions for unsteady lift and moment

A.1.1 Contribution of aerofoil pitch-plunge motion

The contribution of the aerofoil motion is:

$$\begin{aligned} L_a(t) \;=& \pi\rho\, U^2\, b\, \left[-\frac{b}{U^2}\ddot{u} \;+\; \frac{b}{U}\,\dot{\theta} \;-\; \frac{b^2}{U^2}\,a\,\ddot{\theta}\right] \;- \\ & 2\,\pi\,\rho\,U^2\,b\,\left[w_{3/4}(0)\,\phi(t) \;+\; \int_0^t \frac{d\,w_{3/4}(\tau)}{d\tau}\,\phi(t-\tau)\,d\tau\right] \end{aligned} \tag{A.1}$$

$$\begin{aligned} M_a(t) =& 2\,\rho U^2 b^2\left[-\frac{\pi}{2}a\frac{b}{U^2}\ddot{u}(t) - \frac{\pi}{2}\left(a^2+\frac{1}{8}\right)\frac{b^2}{U^2}\ddot{\theta}(t) - \frac{\pi}{2}\left(\frac{1}{2}-a\right)\frac{b}{U}\dot{\theta}(t)\right] \\ & -\; 2\,\rho\,U^2\,b^2\,\pi\,\left(\frac{1}{2}\;+\;a\right)\left[w_{3/4}(0)\,\phi(t) \;+\; \int_0^t \frac{d\,w_{3/4}(\tau)}{d\,\tau}\,\phi(t-\tau)\,d\tau\right] \end{aligned} \tag{A.2}$$

where:

$$w_{3/4}(t) \;=\; -\left[-\frac{1}{U}\dot{u}(t) \;+\; \theta(t) \;+\; \left(\frac{1}{2} \;-\; a\right)\;\frac{b}{U}\dot{\theta}(t)\right] \tag{A.3}$$

A.1.2 Contribution of flap rotation

The dependence of aerodynamic loads on the flap rotation and its time derivatives is expressed as:

$$\begin{aligned} L_\delta(t) \;=& \rho\,U^2\,b\,\left[-T_4\,\frac{b}{U}\,\dot{\delta}(t) \;-\; T_1\,\frac{b^2}{U^2}\,\ddot{\delta}(t)\right] \;+\; 2\,\pi\,\rho\,U^2\,b\,\left[\frac{1}{\pi}\,T_{10}\,\delta(0) \;+\; \frac{1}{2\,\pi}\,T_{11}\,\frac{b}{U}\,\dot{\delta}(0)\,\phi(t) \;+\right. \\ & \left.\int_0^t\left(\frac{1}{\pi}\,T_{10}\,\frac{b}{U}\,\dot{\delta}(\tau) \;+\; \frac{1}{2\,\pi}\,T_{11}\,\frac{b^2}{U^2}\,\ddot{\delta}(\tau)\right)\,\phi(t\;-\;\tau)\,d\tau\right] \end{aligned} \tag{A.4}$$

$$\begin{aligned} M_\delta(t) \;=& 2\,\rho\,U^2\,b^2\,\left[-\frac{T_4\;+\;T_{10}}{2}\,\delta(t) \;-\; \frac{T_1\;-\;T_8\;-(c\;-\;a)\,T_4\;+\;\frac{1}{2}\,T_{11}}{2}\,\frac{b}{U}\,\dot{\delta}(t)\right. \\ & \left.+\;\frac{T_7\;+\;(c\;-\;a)\,T_1}{2}\,\frac{b^2}{U^2}\,\ddot{\delta}(t)\right] \;+ \\ & 4\,\pi\,\rho\,U^2\,b^2\,\left[\frac{1}{\pi}\,T_{10}\,\delta(0) \;+\; \frac{1}{2\,\pi}\,T_{11}\,\frac{b}{U}\,\dot{\delta}(0)\right)\,\phi(t) \;+ \\ & \left.\int_0^t\left(\frac{1}{\pi}\,T_{10}\,\frac{b}{U}\,\dot{\delta}(\tau) \;+\; \frac{1}{2\,\pi}\,T_{11}\,\frac{b^2}{U^2}\,\ddot{\delta}(\tau)\right)\,\phi(t\;-\;\tau)\,d\tau\right] \end{aligned} \tag{A.5}$$

The coefficients used above are from Theodorsen [18].

A.1.3 Contribution of gust encounter

The response to any arbitrary shape of $W_g(t)$ is obtained as follows:

$$L_g(t) = 2\,\pi\,\rho\,U^2\,b\,\left[W_g(t)\,\psi(t) + \int_0^t \frac{dW_g(\tau)}{d\tau}\,\psi(t-\tau)\,d\tau\right] \tag{A.6}$$

$$M_g(t) = 2\,\rho\,U^2\,b^2\,\pi\,\left(\frac{1}{2}+a\right)\,\left[W_g(t)\,\psi(t) + \int_0^t \frac{dW_g(\tau)}{d\tau}\,\psi(t-\tau)\,d\tau\right] \tag{A.7}$$

A.2 Transformation of Integro-Differential Equations into Ordinary Differential Equations

The introduction of the aerodynamic loads in the form of unsteady aerodynamics formulation makes the problem a coupled set of Integro-Differential Equations (IDEs). This is due to the convolution integral terms present in Equations. (A.1), (A.2) and (A.4) to (A.7) of the Appendix A.1. Those terms account for the past history of the system, which is needed when considering the unsteadiness of the flow field. A mathematical procedure exists to replace the integral terms with additional variables and equations describing their evolution. As a result, the set of IDEs can be expressed in terms of an expanded set of Ordinary Differential Equations (ODEs) with an increased number of state variables. This procedure is described for example in References [165] or [215]. Basically, a new set of variables is defined for those integral terms arising from convolution that cannot be expressed as linear functions of the structural variables (or their time derivatives). To obtain the dynamics of the new variables (the right part of Equations (A.11) of the Appendix A.3.1, the Leibniz integral role is applied, namely:

$$\frac{\partial}{\partial z}\int_{a(z)}^{b(z)} f(x,z)\,dx = \int_{a(z)}^{b(z)} \frac{\partial f}{\partial z}\,dx + f(b(z),z)\,\frac{\partial b}{\partial z} - f(a(z),z)\,\frac{\partial a}{\partial z} \tag{A.8}$$

The new variables and their dynamics are described in details in the Appendix A.3.1.

A.3 Total aerodynamic loads

Developing the above equations, the aerodynamic loads can be expressed as linear functions of the structural and some appropriate aerodynamic variables (see section A.3.1)

$$
\begin{aligned}
L(x,t) =& a_0(x,t) + a_1\,\ddot{u}(x,t) + a_2\,\ddot{\theta}(x,t) + a_3\,\dot{u}(x,t) + a_4\,\dot{\theta}(x,t) \\
&+ a_5\,u(x,t) + a_6\,\theta(x,t) + a_7\,z_1(x,t) + a_8\,z_2(x,t) + a_9\,z_3(x,t) \\
&+ a_{10}\,z_4(x,t) + b_0(x,t) + b_1\,\ddot{\delta}(x,t) + b_2\,\dot{\delta}(x,t) + b_3\,\delta(x,t) \\
&+ b_4\,z_5(x,t) + b_5\,z_6(x,t) + c_1\,W_g(x,t) + c_2\,z_7(x,t) + c_3\,z_8(x,t)
\end{aligned}
\tag{A.9}
$$

$$
\begin{aligned}
M(x,t) =& d_0(x,t) + d_1\,\ddot{u}(x,t) + d_2\,\ddot{\theta}(x,t) + d_3\,\dot{u}(x,t) + d_4\,\dot{\theta}(x,t) \\
&+ d_5\,u(x,t) + d_6\,\theta(x,t) + d_7\,z_1(x,t) + d_8\,z_2(x,t) + d_9\,z_3(x,t) \\
&+ d_{10}\,z_4(x,t) + + e_0(x,t) + e_1\,\ddot{\delta}(x,t) + e_2\,\dot{\delta}(x,t) + e_3\,\delta(x,t) \\
&+ e_4\,z_5(x,t) + e_5\,z_6(x,t) + f_1\,W_g(x,t) + f_2\,z_7(x,t) + f_3\,z_8(x,t)
\end{aligned}
\tag{A.10}
$$

Each of the following coefficients must be calculated for each element if the taper ratio is not unity. Moreover, the following quantities are defined for convenience:

$$
\begin{aligned}
b_{av} &= \frac{1}{3}\,c\,\frac{(1+t_r+t_r^2)}{(1+t_r)} \qquad \text{(Mean aerodynamic half-chord)} \\
\varepsilon_1 &= \frac{b_1\,U}{b_{av}}; \qquad \varepsilon_2 = \frac{b_2\,U}{b_{av}}; \qquad \varepsilon_3 = \frac{b_3\,U}{b_{av}} \qquad \varepsilon_4 = \frac{b_4\,U}{b_{av}} \\
c_X &= \cos X, \qquad X = \text{sweep angle}
\end{aligned}
$$

$$
\begin{aligned}
a_0 &= 2\pi\,c_X\,\rho\,U^2\frac{b}{b_{av}}\left[u(x,0) - b\left(\frac{1}{2}-a\right)\theta(x,0)\right]\left(A_1\,b_1\,e^{-\varepsilon_1 t} + A_2\,b_2\,e^{-\varepsilon_1 t}\right) \\
a_1 &= -c_X\pi\rho\,b^2 \\
a_2 &= -c_X\pi\rho\,a\,b^3 \\
a_3 &= -2c_X\pi\rho\,U\,b(1-A_1-A_2) \\
a_4 &= c_X\pi\rho\,Ua\,b^2 + 2c_X\pi\rho\,U\,b^2\left(\frac{1}{2}-a\right)(1-A_1-A_2) \\
a_5 &= -2c_X\pi\rho\,U^2\frac{b}{b_{av}}(A_1\,b_1 + A_2\,b_2) \\
a_6 &= 2c_X\pi\rho\,U^2 b\left[(1-A_1-A_2) + \frac{b}{b_{av}}\left(\frac{1}{2}-a\right)(A_1 b_1 + A_2 b_2)\right] \\
a_7 &= 2c_X\pi\rho\,U^3 A_1 b_1\frac{b}{b_{av}}\left[1 - \frac{b}{b_{av}}\left(\frac{1}{2}-a\right)b_1\right] \\
a_8 &= 2c_X\pi\rho\,U^3 A_2 b_2\frac{b}{b_{av}}\left[1 - \frac{b}{b_{av}}\left(\frac{1}{2}-a\right)b_2\right] \\
a_9 &= 2c_X\pi\rho\,U^3\frac{b}{b_{av}^2}A_1 b_1^2 \\
a_{10} &= 2c_X\pi\rho\,U^3\frac{b}{b_{av}^2}A_2 b_2^2
\end{aligned}
$$

$$
\begin{aligned}
b_0 &= 0 \\
b_1 &= -\rho\, b^3 T_1 \\
b_2 &= \rho\, b^2 U(-T_4 + T_{11}(1 - A_1 - A_2)) \\
b_3 &= \rho\, b U^2(2T_{10}(1 - A_1 - A_2) + \frac{b}{U} T_{11}(A_1\varepsilon_1 + A_2\varepsilon_2)) \\
b_4 &= \rho\, b U^2(2T_{10}A_1\varepsilon_1 - \frac{b}{U} T_{11}A_1\varepsilon_1^2) \\
b_5 &= \rho\, b U^2(2T_{10}A_2\varepsilon_2 - b/U T_{11}A_2\varepsilon_2^2)
\end{aligned}
$$

$$
\begin{aligned}
c_1 &= \rho\, b U^2 2\pi(1 - A_3 - A_4) \\
c_2 &= \rho\, b U^2 2\pi\, A_3\, \varepsilon_3 \\
c_3 &= \rho\, b U^2 2\pi\, A_4\, \varepsilon_4
\end{aligned}
$$

$$
\begin{aligned}
d_0 &= -2c_X\pi\rho\, U^2 \frac{b^2}{b_{av}} \left(\frac{1}{2} + a\right) \Big[u(x,0) \\
&\qquad - b\left(\frac{1}{2} - a\right) \theta(x,0)\Big] \left(A_1\, b_1\, e^{-\varepsilon_1 t} + A_2\, b_2\, e^{-\varepsilon_1 t}\right) \\
d_1 &= -c_X\pi\rho\, a b^3 \\
d_2 &= -c_X\pi\rho(1/8 + a^2) b^4 \\
d_3 &= -2c_X\pi\rho\, U b^2 \left(\frac{1}{2} + a\right)(1 - A_1 - A_2) \\
d_4 &= -c_X\pi\rho\, U b^3 \left(\frac{1}{2} - a\right) + 2c_X\pi\rho\, U b^3 \left(\frac{1}{2} - a\right)\left(\frac{1}{2} + a\right)(1 - A_1 - A_2) \\
d_5 &= -2c_X\pi\rho\, U^2 \frac{b^2}{b_{av}}(A_1 b_1 + A_2 b_2) \left(\frac{1}{2} + a\right) \\
d_6 &= 2c_X\pi\rho\, U^2 b^2 \left(\frac{1}{2} + a\right)\left[(1 - A_1 - A_2) + \frac{b}{b_{av}}\left(\frac{1}{2} - a\right)(A_1 b_1 + A_2 b_2)\right] \\
d_7 &= 2c_X\pi\rho\, U^3 A_1\, b_1 \frac{b^2}{b_{av}} \left[1 - \frac{b}{b_{av}}\left(\frac{1}{2} - a\right) b_1\right]\left(\frac{1}{2} + a\right) \\
d_8 &= 2c_X\pi\rho\, U^3 A_2\, b_2 \frac{b^2}{b_{av}} \left[1 - \frac{b}{b_{av}}\left(\frac{1}{2} - a\right) b_2\right]\left(\frac{1}{2} + a\right) \\
d_9 &= 2\pi\, c_X\rho\, U^3 A_1\, b_1^2 \frac{b^2}{b_{av}^2} \left(\frac{1}{2} + a\right) \\
d_{10} &= 2\pi\, c_X\rho\, U^3 A_2\, b_2^2 \frac{b^2}{b_{av}^2} \left(\frac{1}{2} + a\right)
\end{aligned}
$$

$$
\begin{aligned}
e_0 &= 0 \\
e_1 &= \rho\, b^4 (T_7 + (c-a)T_1) \\
e_2 &= \rho\, b^3 U(-(T_1 - T_8 - (c-a)T_4 + \frac{1}{2}T_{11}) + (a+\frac{1}{2})T_{11}(1 - A_1 - A_2)) \\
e_3 &= \rho\, b^2 U^2 \left[-(T_4 + T_{10}) + 2T_{10}\left(\frac{1}{2}+a\right)(1 - A_1 - A_2) \right. \\
&\qquad \left. + \frac{b}{U} T_{11}\left(\frac{1}{2}+a\right)(A_1\varepsilon_1 + A_2\varepsilon_2) \right] \\
e_4 &= \rho\, b^2 U \left(\frac{1}{2}+a\right) A_1\varepsilon_1 (2UT_{10} - bT_{11}\varepsilon_1) \\
e_5 &= \rho\, b^2 U \left(\frac{1}{2}+a\right) A_2\varepsilon_2 (2UT_{10} - bT_{11}\varepsilon_2)
\end{aligned}
$$

$$
\begin{aligned}
f_1 &= 2\rho\, b^2 U^2 \pi \left(\frac{1}{2}+a\right)(1 - A_3 - A_4) \\
f_2 &= 2\rho\, b^2 U^2 \pi \left(\frac{1}{2}+a\right) A_3\, \varepsilon_3 \\
f_3 &= 2\rho\, b^2 U^2 \pi \left(\frac{1}{2}+a\right) A_4\, \varepsilon_4
\end{aligned}
$$

A.3.1 Aerodynamic variables

Developing the equations in section A.1, the new variables and their dynamics are expressed as follows:

$$z_1(t) = \int_0^t e^{-b_1 \frac{U}{b}(t-\tau)}\, \theta(\tau)\, d\tau, \qquad \dot{z}_1 = \theta(t) - b_1 \frac{U}{b} z_1(t) \tag{A.11a}$$

$$z_2(t) = \int_0^t e^{-b_2 \frac{U}{b}(t-\tau)}\, \theta(\tau)\, d\tau, \qquad \dot{z}_2 = \theta(t) - b_2 \frac{U}{b} z_2(t) \tag{A.11b}$$

$$z_3(t) = \int_0^t e^{-b_1 \frac{U}{b}(t-\tau)}\, u(\tau)\, d\tau, \qquad \dot{z}_3 = u(t) - b_1 \frac{U}{b} z_3(t) \tag{A.11c}$$

$$z_4(t) = \int_0^t e^{-b_2 \frac{U}{b}(t-\tau)}\, u(\tau)\, d\tau, \qquad \dot{z}_4 = u(t) - b_2 \frac{U}{b} z_4(t) \tag{A.11d}$$

$$z_5(t) = \int_0^t e^{-b_1 \frac{U}{b}(t-\tau)}\, \delta(\tau)\, d\tau, \qquad \dot{z}_5 = \delta(t) - b_1 \frac{U}{b} z_5(t) \tag{A.11e}$$

$$z_6(t) = \int_0^t e^{-b_2 \frac{U}{b}(t-\tau)}\, \delta(\tau)\, d\tau, \qquad \dot{z}_6 = \delta(t) - b_2 \frac{U}{b} z_6(t) \tag{A.11f}$$

$$z_7(t) = \int_0^t e^{-b_3 \frac{U}{b}(t-\tau)}\, W_g(\tau)\, d\tau, \qquad \dot{z}_7 = W_g(t) - b_3 \frac{U}{b} z_7(t) \tag{A.11g}$$

$$z_8(t) = \int_0^t e^{-b_4 \frac{U}{b}(t-\tau)}\, W_g(\tau)\, d\tau, \qquad \dot{z}_8 = W_g(t) - b_4 \frac{U}{b} z_8(t) \tag{A.11h}$$

To obtain the dynamics of the new variables (the right part of Equations (A.11)), the Leibniz integral role has been applied, namely:

$$\frac{\partial}{\partial z}\int_{a(z)}^{b(z)} f(x,\,z)\,dx \;=\; \int_{a(z)}^{b(z)} \frac{\partial f}{\partial z}\,dx \;+\; f(b(z),\,z)\,\frac{\partial b}{\partial z} \;-\; f(a(z),\,z)\,\frac{\partial a}{\partial z} \tag{A.12}$$

A.3.2 Formulation of discretized aerodynamics

Applying the Galerkin's method, the equilibrium equations become defined in integral sense, multiplying them by some assumed weighting functions (here denoted as $\gamma(x)$ and $\chi(x)$) and integrating along the span-wise axis. Doing this, the terms related with the aerodynamics are, in local element coordinates:

$$l_e \int_0^1 \tilde{\gamma}(\zeta)\,L(\zeta,t)\,d\zeta \qquad \text{and} \qquad l_e \int_0^1 \tilde{\chi}(\zeta)\,M(\zeta,t)\,d\zeta \tag{A.13}$$

where:

$$\tilde{\gamma}_e(\zeta) \;=\; \boldsymbol{N}_{\boldsymbol{v}}^T(\zeta)\,\boldsymbol{\gamma_e} \tag{A.14a}$$

$$\tilde{\chi}_e(\zeta) \;=\; \boldsymbol{N}_{\boldsymbol{\theta}}^T(\zeta)\,\boldsymbol{\chi_e} \tag{A.14b}$$

Substituting Eqs. (A.9) and (A.10) in the respective terms of of Eq. (A.13), and applying the same procedure of the previous section to each term, the discretized expressions for the aerodynamic loads are obtained. For example, developing such a procedure for one term of the lift, it gives:

$$\begin{aligned} l_e \int_0^1 \tilde{\gamma}(\zeta)\,a_1\,\ddot{u}(\zeta,t)\,d\zeta \;&=\; \boldsymbol{\gamma_e}^T \left[l_e\,a_1 \int_0^1 \boldsymbol{N_v}(\zeta)\,\boldsymbol{N_v}^T(\zeta)\,d\zeta \right] \boldsymbol{\ddot{u}_e}(t) \;= \\ &=\; \boldsymbol{\gamma_e}^T\,\boldsymbol{a_1}\,\boldsymbol{\ddot{u}_e}(t) \end{aligned} \tag{A.15}$$

It is worthwhile to show also how the procedure is applied to the terms containing the $z-$variables. For instance:

$$\begin{aligned} l_e \int_0^1 \tilde{\gamma}(\zeta)\,a_7\,z_1(\zeta,t)\,d\zeta \;&=\; l_e\,a_7 \int_0^1 \tilde{\gamma}(\zeta) \int_0^t e^{-b_1\frac{U}{b}(t-\tau)}\,\theta(\zeta,\tau)\,d\tau\,d\zeta \;= \\ &=\; \boldsymbol{\gamma_e}^T \left[l_e\,a_7 \int_0^1 \boldsymbol{N_v}(\zeta)\,\boldsymbol{N_\theta}^T(\zeta)\,d\zeta \right] \int_0^t e^{-b_1\frac{U}{b}(t-\tau)}\,\boldsymbol{\theta_e}(\tau)\,d\tau \\ &=\; \boldsymbol{\gamma_e}^T\,\boldsymbol{a_7}\,\boldsymbol{z_1}(t) \end{aligned} \tag{A.16}$$

The aerodynamic loads in matrix form, for each element, become:

$$\begin{aligned} \boldsymbol{f_e} = & \boldsymbol{a_0} + \boldsymbol{a_1}\,\boldsymbol{\ddot{u}_e} + a_2\,\boldsymbol{\ddot{\theta}_e} + \boldsymbol{a_3}\,\boldsymbol{\dot{u}_e} + \boldsymbol{a_4}\,\boldsymbol{\dot{\theta}_e} + \boldsymbol{a_5}\,\boldsymbol{u_e} + \\ & + \boldsymbol{a_6}\,\boldsymbol{\theta_e} + \boldsymbol{a_7}\,\boldsymbol{z_{1,e}} + \boldsymbol{a_8}\,\boldsymbol{z_{2,e}} + \boldsymbol{a_9}\,\boldsymbol{z_{3,e}} + \boldsymbol{a_{10}}\,\boldsymbol{z_{4,e}} + \\ & + \boldsymbol{b_0} + \boldsymbol{b_1}\,\ddot{\delta}_e + \boldsymbol{b_2}\,\dot{\delta}_e + \boldsymbol{b_3}\,\delta_e + \boldsymbol{b_4}\,z_{5,e} + \boldsymbol{b_5}\,z_{6,e} + \\ & + \boldsymbol{c_1}\,W_g + \boldsymbol{c_2}\,z_{7,e} + \boldsymbol{c_3}\,z_{8,e} \end{aligned} \tag{A.17}$$

$$\begin{aligned} \boldsymbol{m_e} = & \boldsymbol{d_0} + \boldsymbol{d_1}\,\boldsymbol{\ddot{u}_e} + d_2\,\boldsymbol{\ddot{\theta}_e} + \boldsymbol{d_3}\,\boldsymbol{\dot{u}_e} + \boldsymbol{d_4}\,\boldsymbol{\dot{\theta}_e} + \boldsymbol{d_5}\,\boldsymbol{u_e} + \\ & + \boldsymbol{d_6}\,\boldsymbol{\theta_e} + \boldsymbol{d_7}\,\boldsymbol{z_{1,e}} + \boldsymbol{d_8}\,\boldsymbol{z_{2,e}} + \boldsymbol{d_9}\,\boldsymbol{z_{3,e}} + \boldsymbol{d_{10}}\,\boldsymbol{z_{4,e}} + \\ & + \boldsymbol{e_0} + \boldsymbol{e_1}\,\ddot{\delta}_e + \boldsymbol{e_2}\,\dot{\delta}_e + \boldsymbol{e_3}\,\delta_e + \boldsymbol{e_4}\,z_{5,e} + \boldsymbol{e_5}\,z_{6,e} + \\ & + \boldsymbol{f_1}\,W_g + \boldsymbol{f_2}\,z_{7,e} + \boldsymbol{f_3}\,z_{8,e} \end{aligned} \tag{A.18}$$

A.3.3 Unsteady aileron hinge moment

The procedure to obtain the hinge moment is analogue to that shown in the previous section, thus, developing Eq. (29) of the main document:

$$\begin{aligned} M_h(x,t) = & m_0(x,t) + m_1\,\ddot{u}(x,t) + m_2\,\ddot{\theta}(x,t) + m_3\,\dot{u}(x,t) + \\ & + m_4\,\dot{\theta}(x,t) + m_5\,u(x,t) + m_6\,\theta(x,t) + m_7\,z_1(x,t) + \\ & + m_8\,z_2(x,t) + m_9\,z_3(x,t) + m_{10}\,z_4(x,t) + \\ & + n_0(x,t) + n_1\,\ddot{\delta}(x,t) + n_2\,\dot{\delta}(x,t) + n_3\,\delta(x,t) + \\ & + n_4\,z_5(x,t) + n_5\,z_6(x,t) \end{aligned} \tag{A.19}$$

Coefficients in Eq. (A.19) are:

$$
\begin{aligned}
m_1 &= -\rho\ b^3\, T_1 \\
m_2 &= -2\,\rho\ b^4\, T_{13} \\
m_3 &= \rho\ U\ b^2\, T_{12}\ (1 - A_1 - A_2) \\
m_4 &= -\rho\ U\ b^3\ \left(-2\,T_9 - T_1 + T_4\ (a - 0.5) + T_{12}\ \left(\frac{1}{2} - a\right)\ (1 - A_1 - A_2)\right) \\
m_5 &= \rho\ U^2\, b\, T_{12}\ (A_1\, b_1 + A_2\, b_2) \\
m_6 &= -\rho\ U^2\, b^2\, T_{12}\ \left(\left(\frac{1}{2} - a\right)\ (A_1\, b_1 + A_2\, b_2) + (1 - A_1 - A_2)\right) \\
m_7 &= \rho\ U^3\, b\, T_{12}\, A_1\, b_1\ \left(\left(\frac{1}{2} - a\right)\ b_1 - 1\right) \\
m_8 &= \rho\ U^3\, b\, T_{12}\, A_2\, b_2\ \left(\left(\frac{1}{2} - a\right)\ b_2 - 1\right) \\
m_9 &= -\rho\ U^3\, T_{12}\, A_1\, b_1^2 \\
m_{10} &= -\rho\ U^3\, T_{12}\, A_2\, b_2^2
\end{aligned}
$$

$$
\begin{aligned}
n_1 &= \frac{\rho\ b^4\, T_3}{\pi} \\
n_2 &= \frac{\rho\ U\ b^3\, T_{11}}{2\,\pi}\ \left(T_4 - 0.5\,T_{12}\ \left(\frac{1}{2} + a\right)\ (1 - A_1 - A_2)\right) \\
n_3 &= -\frac{\rho\ U\ b^2}{\pi}\ \left[U\ (T_5 - T_4\, T_{10}) + 0.5\,T_{12}\, U\ T_{10}\ \left(\frac{1}{2} + a\right)\ (1 - A_1 - A_2)\right. \\
&\qquad \left. + \frac{1}{4}\, T_{12}\, T_{11}\, b\ \left(\frac{1}{2} + a\right)\ (A_1\, \varepsilon_1 + A_2\, \varepsilon_2)\right] \\
n_4 &= \frac{T_{12}\,\rho\ U\ b^2}{4\,\pi}\ \left(\frac{1}{2} + a\right)\ A_1\, \varepsilon_1\ (T_{11}\, b\, \varepsilon_1 - 2\,U\ T_{10}) \\
n_5 &= \frac{T_{12}\,\rho\ U\ b^2}{4\,\pi}\ \left(\frac{1}{2} + a\right)\ A_2\, \varepsilon_2\ (T_{11}\, b\, \varepsilon_2 - 2\,U\ T_{10})
\end{aligned}
$$

The same procedure discussed above was followed to obtain discretized expressions for the hinge moment. Therefore, each term in Eq. (A.19) is manipulated such as the first one shown below:

$$
\begin{aligned}
l_e \int_0^1 \tilde{\xi}(\zeta)\, m_1\, \ddot{u}(\zeta, t)\, d\zeta \ &= \ \boldsymbol{\xi}_e^T\ \left[l_e\, m_1 \int_0^1\ \boldsymbol{N_t}(\zeta)\, \boldsymbol{N_v^T}(\zeta)\, d\zeta\right]\ \ddot{\boldsymbol{u}}_{\boldsymbol{e}}(t)\ = \\
&= \ \boldsymbol{\xi}_e^T\, \boldsymbol{m_1}\, \ddot{\boldsymbol{u}}_{\boldsymbol{e}}(t)
\end{aligned}
\tag{A.20}
$$

where $\boldsymbol{\xi_e}$ represents the nodal values of the weighting function for the Galerkin's method:

$$\tilde{\xi}(\zeta) \;=\; \boldsymbol{N_t^T}(\zeta)\,\boldsymbol{\xi_e} \tag{A.21}$$

Applying this procedure for each contribution, it yields the following matrix expression:

$$\begin{aligned}\boldsymbol{M_{h,e}} \;=\; & \boldsymbol{m_0} \;+\; \boldsymbol{m_1}\,\ddot{\boldsymbol{u}}_e \;+\; m_2\,\ddot{\boldsymbol{\theta}}_e \;+\; \boldsymbol{m_3}\,\dot{\boldsymbol{u}}_e \;+\; \boldsymbol{m_4}\,\dot{\boldsymbol{\theta}}_e \;+\; \boldsymbol{m_5}\,\boldsymbol{u}_e \;+ \\ & +\; \boldsymbol{m_6}\,\boldsymbol{\theta}_e \;+\; \boldsymbol{m_7}\,\boldsymbol{z_{1,e}} \;+\; \boldsymbol{m_8}\,\boldsymbol{z_{2,e}} \;+\; \boldsymbol{m_9}\,\boldsymbol{z_{3,e}} \;+\; \boldsymbol{m_{10}}\,\boldsymbol{z_{4,e}} \;+ \\ & +\; \boldsymbol{n_0} \;+\; \boldsymbol{n_1}\,\ddot{\delta}_e \;+\; \boldsymbol{n_2}\,\dot{\delta}_e \;+\; \boldsymbol{n_3}\,\delta_e \;+\; \boldsymbol{n_4}\,z_{5,e} \;+\; \boldsymbol{n_5}\,z_{6,e}\end{aligned} \tag{A.22}$$

Rearranging it in a more compact form, and assembling for multiple flapped elements, it brings to Eq. (30) of the main document.

Appendix B

Verification of the surrogate modelling approach

Contents

Appendix A.1 Expressions for unsteady lift and moment 278
Appendix A.1.1 Contribution of aerofoil pitch-plunge motion 278
Appendix A.1.2 Contribution of flap rotation 278
Appendix A.1.3 Contribution of gust encounter 279
Appendix A.2 Transformation of Integro-Differential Equations into Ordinary Differential Equations 279
Appendix A.3 Total aerodynamic loads 279
Appendix A.3.1 Aerodynamic variables 282
Appendix A.3.2 Formulation of discretized aerodynamics 283
Appendix A.3.3 Unsteady aileron hinge moment 284

The verification of the surrogate model for the aircraft sizing and unsteady aerodynamic calculation processes is here reported. The model depends on 5 variables (the 4 geometric optimization variables V_g plus the error on the CG location Δx_{CG}) and returns 8 aerodynamic derivatives plus 2 aircraft parameters (wing reference area and MAC) and the objective function (fuel mass). Figures B.1 to B.3 show that all the predicted outputs are in good agreement with the training points, used to train the Gaussian process, and with the test points, excluded from the training and used only for verification. The RMS error was always below 0.3%.

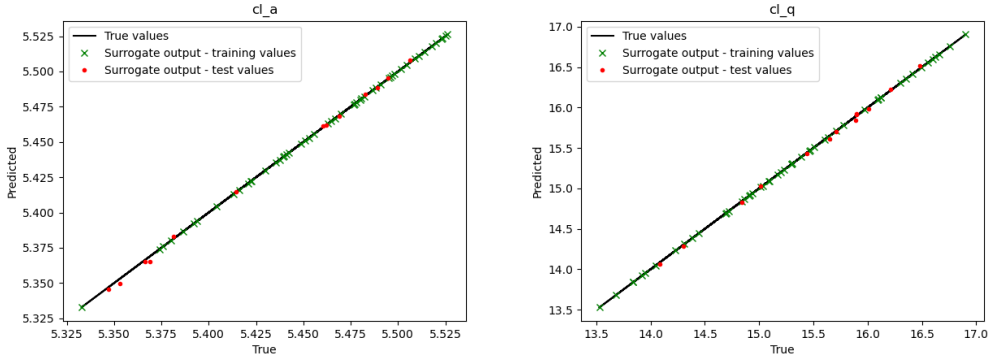

(a) C_{L_α}

(b) C_{L_q}

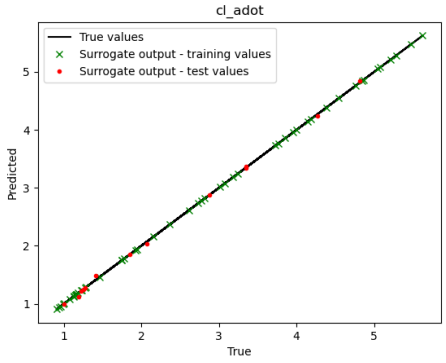

(c) $C_{L_{\dot{\alpha}}}$

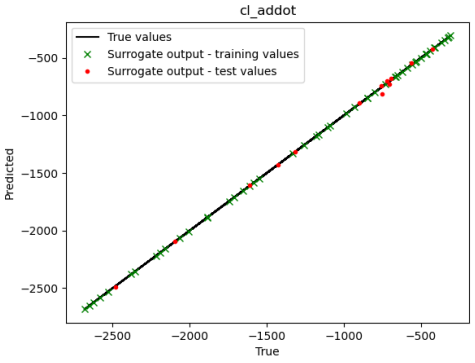

(d) $C_{L_{\ddot{\alpha}}}$

FIGURE B.1: Validation of the surrogate models - Lift coefficient derivatives.

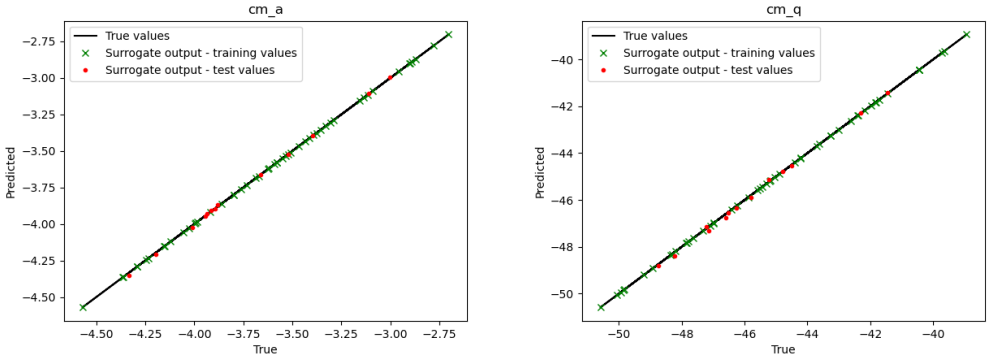

(a) C_{M_α}

(b) C_{M_q}

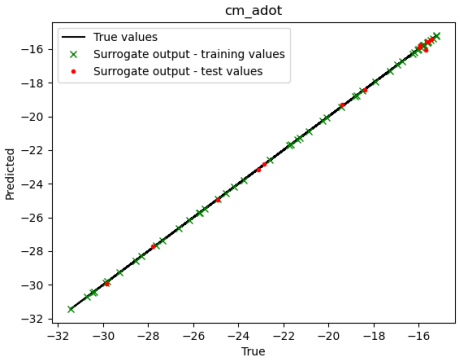

(c) $C_{M_{\dot{\alpha}}}$

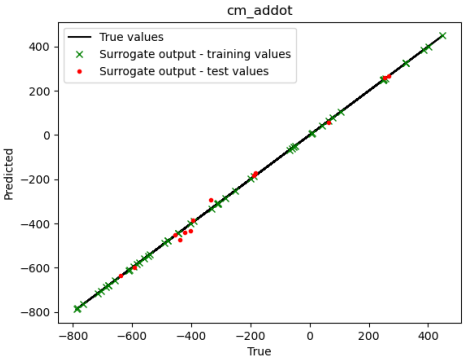

(d) $C_{M_{\ddot{\alpha}}}$

FIGURE B.2: Validation of the surrogate models - Moment coefficient derivatives.

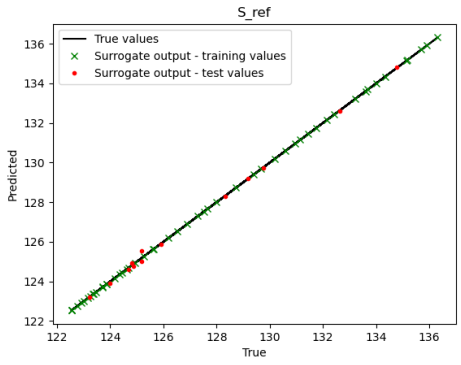

(a) Wing area

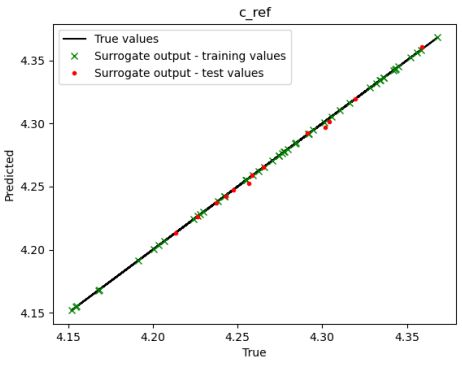

(b) Mean aerodynamic chord

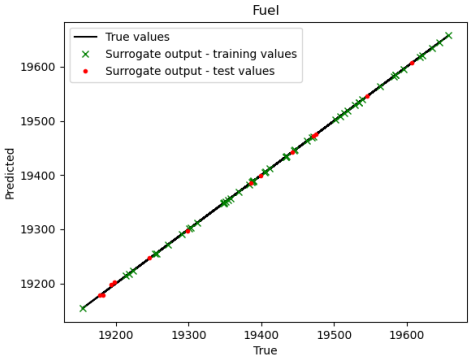

(c) Fuel mass

FIGURE B.3: Validation of the surrogate models - Aircraft parameters.

Appendix C

Initial analytical sizing of the main wing-box components

C.1 Skin sizing

The skin is supposed to withstand the torsional moment. The total moment acting at the wing root for a swept wing is calculated as the estimated moment of a straight wing plus the contribution of sweep:

$$M_t = \frac{1}{2}\rho V^2 \frac{S}{2} c_{\text{mgc}} C_m + \frac{L}{2} \frac{y_{\text{mgc}}}{\cos \Lambda_{1/4}} \tag{C.1}$$

where y_{mgc} is the location of the mean geometric chord along the y body axis, which divided by the cosine of the quarter chord sweep angle $\Lambda_{1/4}$ gives the arm in the x direction generated by the sweep.

The thickness needed to withstand the limit loads is found by inverting the Bredt's formula for thin-walled cross sections:

$$\tau = \frac{|M_t|}{2\,\Omega_{wb}\,t_s} \quad \Rightarrow \quad t_s = \frac{|M_t|}{2\,\Omega_{wb}\,\tau_m} \tag{C.2}$$

where Ω_{wb} is the wing-box cross section area, that for the present rectangular shape is simply given by the product of its two dimensions c_b and h_b. Recall that these are obtained from the `FAST-OAD` output: the former is known from the front and rear spar positions, the latter is derived from the profile thickness ratio, by applying a reduction factor of 0.9.

The skin thickness is subject to a lower bound dictated by lighting strike requirements, imposing a minimum thickness commonly set to 2.7 mm (as from [212]).

C.2 Web sizing

With the discussed assumption that the shear force of the wing half is entirely reacted by the spars, and that these are considered of identical cross section, the two of them are equivalent to a single shear web of thickness t_w and height h_b. Each spar has therefore a thickness of $t_w/2$. Under these assumptions, stress analysis theory provides the analytical expressions for the stress distribution over a uniform rectangular cross section subjected to vertical shear. Such a distribution is of parabolic shape, with the maximum located at the neutral axis. With a total vertical force of $n_L\,W/2$ applied on each wing, neglecting the contributions of fuselage and tail, the maximum shear stress at the root section is:

$$\tau = \frac{3}{2}\frac{n_L\,W}{h_b\,t_w} \tag{C.3}$$

The required thickness is therefore:

$$t_w = \frac{3}{2}\frac{n_L W}{h_b \tau_m} \tag{C.4}$$

The lower bound for the spar thickness is set to the minimal technological limit of 1.2 mm, following [212].

C.3 Stringers sizing

The wing stringers are sized to react the whole wing bending moment generated by lift. As discussed above, the adopted procedure does not require any other quantities than the overall stringers cross section. Their shape, number and spacing is not of concern at this stage. The overall cross-sectional area at wing root is here denoted as $2\,A_s$, with A_s being the area located on the upper and lower skin, in a specular fashion. Therefore, considering half of the total lift applied at the mean geometric chord, the total bending moment at root, and the required stringers area to counteract it are as follows:

$$M_b = \frac{n_L W}{2} y_{\text{mgc}} = \sigma\, A_s\, h_b \quad \Rightarrow \quad A_s = \frac{\frac{n_L W}{2} y_{\text{mgc}}}{\sigma_m\, h_b} \tag{C.5}$$

No specific technological bounds are applied to A_s. It is just imposed that once A_s is calculated at the wing root, the corresponding value at the wing tip is $0.05\,A_s$, as suggested in [27], so that the span-wise distribution is a linear function between these two values.

C.4 Ribs sizing

Within the hypotheses discussed above, the only quantity related with ribs that is relevant to this approach is their weight contribution. Their contribution to structural stiffness and integrity is not analyzed here. Therefore, no analytical expressions are derived for their detailed sizing, and no variables linked with ribs are added to the optimization problem. Instead, an approximate estimation is made, adapted from the approach of [27]. Here, the authors suggest to assign ribs the same thickness of the local skin, neglect any lightening holes, consider a semi-elliptic geometry and a spacing of half the local chord. The approach proved to give realistic prediction in the domain of general aviation aircraft. In the present case, with a completely different category of aircraft, it was found that this approach does not match satisfactorily with the available data on the CeRAS baseline. Instead, it was found more accurate to assign them half the local thickness of one spar, considering the same rectangular cross-section of the

wing box, and a spacing of about 60-70 cm (as from [8, 212]). The higher value of 70 cm was adopted here.

C.5 Reinforcements and secondary parts

The total wing mass is given by the primary structure mass, composed by spars, stringers, skin and ribs and estimated as above, plus the mass of reinforcements, mainly needed by the landing gear, and of secondary parts. These two last contributions are difficult to estimate in a direct way as done for the primary structure, and it is more realistic at this stage to rely on experience and existing data for the given class of airplane. Therefore, this mass is here set equal to the value estimated by `FAST-OAD`, where a statistical regression is adopted from [9]. Here, the expressions for landing gear reinforcements mass m_r and secondary parts mass m_s are in the forms:

$$m_r = c_1 \, k_1 \, (\mathrm{MLW})^{c_2} \tag{C.6}$$

$$m_s = c_3 \, k_1 \, (\mathrm{MTOW})^{c_4} \, S_{\mathrm{PF}} \, c_5 \tag{C.7}$$

where the coefficients c_i are fixed coefficients, k_1 depends on the number and location of the engines, MLW and MTOW are the Maximum Landing Weight and Maximum Take-Off Weight, respectively, and S_{PF} is the surface of the overhanging wing.

Appendix D

Numerical methods for solving nonlinear equations

Contents

Appendix C.1 Skin sizing 292
Appendix C.2 Web sizing 292
Appendix C.3 Stringers sizing 293
Appendix C.4 Ribs sizing 293
Appendix C.5 Reinforcements and secondary parts 294

D.1 Classic chord method

The *classic chord* method is based on the approximation of local linearity of the real non-linear function $f(x)$, so that at each iteration the new point x_{n+1} is given by:

$$x_{n+1} = x_n + m_n f(x_n) \tag{D.1}$$

where m_n is the inverse of the slope of the linear approximation. Differently from the simpler *chord* method, where such a slope is kept fixed, so that $m_n = m$, in the *classic chord* method m_n is updated at each iteration, which greatly accelerates convergence. The value of m_n is set equal to the inverse of the slope of the straight line connecting the points $[x_n, f(x_n)]$ and $[x_{n-1}, f(x_{n-1})]$:

$$x_{n+1} = x_n + \frac{x_n - x_{n-1}}{f(x_n) - f(x_{n-1})} f(x_n) \tag{D.2}$$

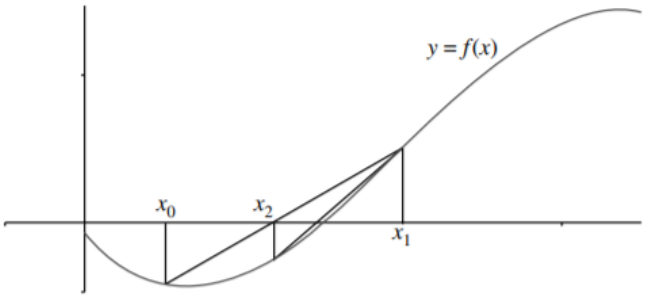

FIGURE D.1: *Classic chord* method, from Reference [28].

D.2 Regula falsi method

The difference of the *regula falsi* method with respect to the *classic chord* method is that the coefficient m_n is computed using the points $[x_n, f(x_n)]$ and $[x_{n'}, f(x_{n'})]$, where n' is the highest index for which $f(x_n) \cdot f(x_{n'}) < 0$:

$$x_{n+1} = x_n + \frac{x_n - x_{n'}}{f(x_n) - f(x_{n'})} f(x_n) \tag{D.3}$$

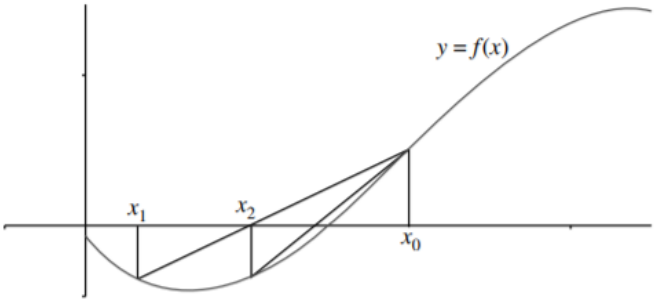

FIGURE D.2: *Regula falsi* method, from Reference [28].

References

[1] Bocola, F., Muscarello, V., Quaranta, G., and Masarati, P., "Pilot In The Loop Aeroservoelastic Simulation in Support to the Conceptual Design of a Fly By Wire Airplane," *AIAA paper 2015-2557, AIAA Atmospheric Flight Mechanics Conference, 22-26 June, Dallas,TX*, 2015. .

[2] Pressman, A., "Integrated practice in perspective: A new model for the architectural profession," *Architectural Record. May 16, 2007*, 2007. URL http://archrecord.construction.com/practice/projDelivery/0705proj-2.asp.

[3] Hamel, P. G., and Jategaonkar, R. V., "Evolution of flight vehicle system identification," *Journal of Aircraft*, Vol. 33, No. 1, 1996, pp. 9–28. , URL https://doi.org/10.2514/3.46898.

[4] Shah, J., and Hazelrigg, H., "Research opportunities in engineering design," *NSF Strategic Planning Workshop, Final Report*, 1996.

[5] Rizzi, A., "Modeling & Simulating Aircraft Stability & Control - SimSAC Project," *AIAA paper 2010-8238, AIAA Atmospheric Flight Mechanics Conference*, 2010. , URL https://arc.aiaa.org/doi/abs/10.2514/6.2010-8238.

[6] Hesse, H., and Palacios, R., "Consistent structural linearisation in flexible-body dynamics with large rigid-body motion," *Computers & Structures*, Vol. 110-111, 2012, pp. 1 – 14. , URL http://www.sciencedirect.com/science/article/pii/S0045794912001368.

[7] Shearer, C. M., and Cesnik, C. E. S., "Nonlinear Flight Dynamics of Very Flexible Aircraft," *Journal of Aircraft*, Vol. 44, No. 5, 2007, pp. 1528–1545. , URL https://doi.org/10.2514/1.27606.

[8] Calderon, D., Cooper, J., Lowenberg, M., Neild, S., and Coetzee, E., "Sizing High-Aspect-Ratio Wings with a Geometrically Nonlinear Beam Model," *Journal of Aircraft*, Vol. 56, No. 4, 2019, pp. 1455–1470.

[9] Dupont W. P., C. C., "Preliminary design of commercial transport aircraft," *Didactic material, ISAESupaero, Toulouse, France*, 2012.

[10] *U.S. Federal Aviation Administration, Advisory Circular No 25.341-1 - Dynamic Gust Loads*, 2014.

[11] Opgenoord, M. M., Drela, M., and Willcox, K. E., "Influence of transonic flutter on the conceptual design of next-generation transport aircraft," *AIAA Journal*, Vol. 57, No. 5, 2019, pp. 1973–1987.

[12] Colas, D., Roberts, N. H., and Suryakumar, V. S., "HALE multidisciplinary design optimization part I: solar-powered single and multiple-boom aircraft," *2018 Aviation Technology, Integration, and Operations Conference*, 2018, p. 3028.

[13] Colas, D., Roberts, N. H., and Suryakumar, V. S., "HALE multidisciplinary design optimization part II: solar-powered flying-wing aircraft," *2018 Aviation Technology, Integration, and Operations Conference*, 2018, p. 3029.

[14] Frazier, P. I., "A tutorial on Bayesian optimization," *arXiv preprint arXiv:1807.02811*, 2018.

[15] Lelièvre, N., Beaurepaire, P., Mattrand, C., Gayton, N., and Otsmane, A., "On the consideration of uncertainty in design: optimization-reliability-robustness," *Structural and Multidisciplinary Optimization*, Vol. 54, No. 6, 2016, pp. 1423–1437.

[16] Katz, J., and Plotkin, A., *Low-Speed Aerodynamics, Second Edition*, Cambridge University Press, 2001.

[17] Deporrois, A., "Overview of the theoretical background in XFLR5," *Presentation document*, March 2009.

[18] Theodorsen, T., "General theory of aerodynamic instability and the mechanism of flutter," *NACA Report No. 496*, 1935, p. 24. .

[19] Murua, J., "Flexible Aircraft Dynamics with a Geometrically-Nonlinear Description of the Unsteady Aerodynamics," *PhD thesis, Imperial College London, May 2012*, 2012.

[20] Bisplinghoff, R. L., Ashley, H., and Halfman, R., "Aeroelasticity," *Dover Publications, Inc.*, 1955.

[21] Smith, M., Patil, M., and Hodges, D., "CFD-based analysis of nonlinear aeroelastic behavior of high-aspect ratio wings," *19th AIAA Applied Aerodynamics Conference*, 2001, p. 1582.

[22] Kharlamov, D., "Computational aeroelasticity for next-generation aircraft," Ph.D. thesis, University of Southampton, 2021.

[23] Sequeira, C., Willis, D., and Peraire, J., "Comparing Aerodynamic Models for Numerical Simulation of Dynamics and Control of Aircraft," *44th AIAA Aerospace Sciences Meeting and Exhibit, 09 - 12 January 2006, Reno, Nevada, USA.*, 2006. , URL https://arc.aiaa.org/doi/abs/10.2514/6.2006-1254.

[24] Fang, H., Gong, C., Su, Y., H. Zhang, Li, C., and Da Ronch, A., "A gradient-based uncertainty optimization framework utilizing dimensional adaptive polynomial chaos expansion," *Struct Multidisc Optim*, 2019, pp. 1199–1219.

[25] David, C., Delbecq, S., Defoort, S., Schmollgruber, P., Benard, E., and Pommier-Budinger, V., "From FAST to FAST-OAD: An open source framework for rapid Overall Aircraft Design," *IOP Conference Series: Materials Science and Engineering*, Vol. 1024, No. 1, 2021, p. 012062. , URL https://doi.org/10.1088/1757-899x/1024/1/012062.

[26] Schmollgruber, P., "Enhancement of the conceptual aircraft design process through certification constraints management and full mission simulations," Phd thesis, Doctorat de l'Université de Toulouse délivré par l'Institut Supérieur de l'Aéronautique et de l'Espace (ISAE), Dec. 2018. URL https://hal.archives-ouvertes.fr/tel-02146110.

[27] Gudmundsson, S., *General aviation aircraft design: Applied Methods and Procedures*, Butterworth-Heinemann, 2013.

[28] Esch, L., Kieffer, R., and Lopez, T., *Asset and risk management: risk oriented finance*, John Wiley & Sons, 2005.

[29] Patil, M. J., and Hodges, D. H., "On the importance of aerodynamic and structural geometrical nonlinearities in aeroelastic behavior of high-aspect-ratio wings," *Journal of Fluids and Structures*, Vol. 19, No. 7, 2004, pp. 905–915.

[30] Saporito, M., and Da Ronch, A., "Aeroelastic energy harvesting from statistically representative gust encounters," *Journal of Fluids and Structures*, Vol. 94, 2020, p. 102869. , URL http://www.sciencedirect.com/science/article/pii/S0889974619306656.

[31] Saporito, M., da Ronch, A., Schmollgruber, P., and Bartoli, N., "Framework development for robust design of novel aircraft concept," *3AF Aerospace Europe Conference, Feb 2020, BOR-DEAUX, France. hal-02904365*, 2020.

[32] Saporito, M., Da Ronch, A., Bartoli, N., and Defoort, S., "Flying qualities reliability constraints in aircraft conceptual design using time-marching simulations," *AIAA paper 2021-3101, AIAA AVIATION 2021 FORUM, August 2-6, 2021, Virtual event*, 2021, p. 3101.

[33] Saporito, M., Da Ronch, A., Bartoli, N., and Defoort, S., "Robust multidisciplinary analysis and optimization for conceptual design of flexible aircraft under dynamic aeroelastic constraints," *Aerospace Science and Technology*, Vol. 138, 2023, p. 108349. , URL https://www.sciencedirect.com/science/article/pii/S1270963823002468.

[34] Cumpsty, N., Mavris, D., and Kirby, M., "Aviation and the environment: Outlook," *ICAO environmental report 2019, Chapter 1*, 2019. URL https://www.icao.int/environmentalprotection/Pages/environmentpublications.aspx.

[35] Green et al., J., "Air Travel - Greener by Design. Mitigating the environmental impact of aviation: Opportunities and priorities," *The Aeronautical Journal, Cambridge University Press*, Vol. 109, No. 1099, 2005, pp. 361–416. , URL https://doi.org/10.1017/S0001924000000841.

[36] Rogers, H. L., Lee, D. S., Raper, D. W., Foster, P. M. d. F., Wilson, C. W., and Newton, P. J., "The impacts of aviation on the atmosphere," *The Aeronautical Journal, Cambridge University Press*, Vol. 106, No. 1064, 2002, pp. 521–546. , URL https://doi.org/10.1017/S0001924000018157.

[37] Cai, Y., Chakraborty, I., and Mavris, D. N., "Integrated Assessment of Vehicle-level Performance of Novel Aircraft Concepts and Subsystem Architectures in Early Design," *AIAA paper 2018-1741, New Technologies and Aircraft System Architectures, AIAA Aerospace Sciences Meeting, 8-12 January 2018, Kissimmee, Florida*, 2018. , URL https://arc.aiaa.org/doi/abs/10.2514/6.2018-1741.

[38] Bendarkar, M. V., Behere, A., Briceno, S. I., and Mavris, D. N., "A Bayesian Safety Assessment Methodology for Novel Aircraft Architectures and Technologies Using Continuous FHA," *AIAA paper 2019-3123, AIAA Aviation Forum, 17-21 June 2019, Dallas, Texas*, 2019. , URL https://arc.aiaa.org/doi/abs/10.2514/6.2019-3123.

[39] Sgueglia, A., Schmollgruber, P., Bartoli, N., Atinault, O., Bénard, E., and Morlier, J., "Exploration and Sizing of a Large Passenger Aircraft with Distributed Electric Ducted Fans," *AIAA paper 2018-1745, AIAA Scitech Forum, 8-12 January 2018, Kissimmee, US*, 2018, pp. 1–33. , URL https://arc.aiaa.org/doi/abs/10.2514/6.2018-1745.

[40] Afonso, F., Vale, J., Lau, F., and Suleman, A., "Performance based multidisciplinary design optimization of morphing aircraft," *Aerospace Science and Technology*, Vol. 67, 2017, pp. 1 – 12. URL https://doi.org/10.1016/j.ast.2017.03.029.

[41] Smith, M. S., Sandwich, C., and Alley, N. R., "Aerodynamic analyses in support of the spanwise adaptive wing project," *Presentation at the AIAA Aviation Forum, 25-29 June 2018, Atlanta, GA.*, 2018.

[42] Wilson, T., Castrichini, A., Azaball, A., Cooper, J. E., Ajaj, R., and Herring, M., "Aeroelastic behaviour of hinged wing tips," *IFASD Paper 2017-216, International Forum on Aeroelasticity and Structural Dynamics (IFASD), 25-28 June 2017, Como, Italy*, 2017.

[43] Sgueglia, A., Schmollgruber, P., Bénard, E., Bartoli, N., and Morlier, J., "Preliminary Sizing of a Medium Range Blended Wing-Body using a Multidisciplinary Design Analysis Approach," *MATEC Web of Conferences, EDP Sciences*, Vol. 233, 2018, pp. 1–9. .

[44] Mody, P., Sato, S., Hall, D., la Rosa Blanco, E. D., Hileman, J., and Wen, E., "Conceptual Design of an N+3 Hybrid Wing Body Subsonic Transport," *AIAA paper 2010-4812, 28th AIAA Applied Aerodynamics Conference, 28 June - 1 July 2010, Chicago, Illinois*, 2010. , URL https://arc.aiaa.org/doi/abs/10.2514/6.2010-4812.

[45] Cipolla, V., Salem, K. A., Scardaoni, M. P., and Binante, V., "Preliminary design and performance analysis of a box-wing transport aircraft," *AIAA paper 2020-0267, AIAA Scitech Forum,6-10 January 2020, Orlando, FL*, 2020. , URL https://arc.aiaa.org/doi/abs/10.2514/6.2020-0267.

[46] Sieradzki, A., Dziubiński, A., and Galiński, C., "Performance comparison of the optimized inverted joined wing airplane concept and classical configuration airplanes," *Archive of Mechanical Engineering*, Vol. LXIII, No. 3, 2016, pp. 455–470. .

[47] Gagnon, H., and Zingg, D. W., "Aerodynamic Optimization Trade Study of a Box-Wing Aircraft Configuration," *Journal of Aircraft*, Vol. 53, No. 4, 2016, pp. 971–981. , URL https://doi.org/10.2514/1.C033592.

[48] Gray, J. S., and Martins, J. R. R. A., "Coupled aeropropulsive design optimisation of a boundary-layer ingestion propulsor," *The Aeronautical Journal,, Cambridge University Press*, Vol. 123, No. 1259, 2019, pp. pp 121–137. , URL https://doi.org/10.1017/aer.2018.120.

[49] Maldonado, D., Viken, S. A., Housman, J. A., Hunter, C. A., Duensing, J. C., Frink, N. T., Jensen, J. C., McMillin, S. N., and Kiris, C. C., "Computational Simulations of a Mach 0.745 Transonic Truss-Braced Wing Design," *AIAA Scitech 2020 Forum, 6-10 January 2020, Orlando, Forida*, 2020. , URL https://arc.aiaa.org/doi/abs/10.2514/6.2020-1649.

[50] Vos, J., Charbonnier, D., Ludwig, T., Merazzi, S., Timmermans, H., Rajpal, D., and Gehri, A., "Aero-elastic Simulations Using the NSMB CFD Solver Including results for a Strut

Braced Wing Aircraft," *Flexible Engineering Toward Green Aircraft. Lecture Notes in Applied and Computational Mechanics, Springer.*, Vol. Vol 92, 2020, pp. pp. 71–94. URL https://doi.org/10.1007/978-3-030-36514-1_5.

[51] Secco, N. R., and Martins, J. R. R. A., "RANS-Based Aerodynamic Shape Optimization of a Strut-Braced Wing with Overset Meshes," *Journal of Aircraft*, Vol. Vol 56, No. 1, 2019, pp. pp. 217–227. , URL https://doi.org/10.2514/1.C034934.

[52] Potter, G., "Conceptual Design of a Strut-Braced Wing Configuration," *UTIAS National Colloquium on Sustainable Aviation, June 21-23, 2017*, 2017.

[53] The Airbus Company, "AlbatrossONE - A revolutionary approach to aircraft wing design," *Airbus innovation portal*, 2019. URL https://www.airbus.com/en/innovation/disruptive-concepts/biomimicry/albatrossone.

[54] Uranga, A., Drela, M., Greitzer, E., Titchener, N., Lieu, M., Siu, N., Huang, A., Gatlin, G. M., and Hannon, J., "Preliminary Experimental Assessment of the Boundary Layer Ingestion Benefit for the D8 Aircraft," *AIAA paper 2014-0906, 52nd Aerospace Sciences Meeting, 13-17 January 2014, National Harbor, Maryland*, 2014. , URL https://arc.aiaa.org/doi/abs/10.2514/6.2014-0906.

[55] Banke, J., "Beauty of Future Airplanes is More than Skin Deep," *nasa.org online article*, 2017. URL https://www.nasa.gov/topics/aeronautics/features/future_airplanes.html.

[56] Trifari, V., Ruocco, M., Cusati, V., Nicolosi, F., and De Marco, A., "Multi-disciplinary analysis and optimization JAVA tool for aircraft design," *31st ICAS Congress, Belo Horizonte, Brazil, September 9-14, 2018*, 2018.

[57] Sødahl, A., Lædre, O., Svalestuen, F., and Lohne, J., "Early Contractor Involvement: Advantages and Disadvantages for the Design Team," *22nd Annual Conference of the International Group for Lean Construction 2014 (IGLC 2014), 25-27 June 2014, Oslo, Norway*, Vol. 1, 2014.

[58] Price, N. B., Kim, N.-H., Haftka, R. T., Balesdent, M., Defoort, S., and Le Riche, R., "Deciding Degree of Conservativeness in Initial Design Considering Risk of Future Redesign," *Journal of Mechanical Design*, Vol. 138, No. 11, 2016, p. 13p. , URL https://hal-emse.ccsd.cnrs.fr/emse-01351036.

[59] US Federal Aviation Administration, "Airworthiness Directives; The Boeing Company Airplanes," *US Department of Transportation, FAA, 14 CFR Part 39, Federal Register, Rules and Regulations, 16 July 2015*, Vol. 80, No. 136, 2015.

[60] Goetzendorf-Grabowski, T., "Multi-disciplinary optimization in aeronautical engineering," *Proceedings of the Institution of Mechanical Engineers, Part G: Journal of Aerospace Engineering*, Vol. 231, No. 12, 2017, pp. 2305–2313. , URL https://doi.org/10.1177/0954410017706994.

[61] Goetzendorf-Grabowski, T., and Mieloszyk, J., "Common computational model for coupling panel method with finite element method," *Aircraft Engineering and Aerospace Technology*, Vol. 89, No. 5, 2017, pp. pp. 654–662. , URL https://doi.org/10.1108/AEAT-01-2017-0044.

[62] Reitenbach, S., Vieweg, M., Hollmann, C., and Becker, R. G., "Usage of Data Provenance Models in Collaborative Multidisciplinary Aero-Engine Design," *Journal of Engineering for Gas Turbines and Power*, Vol. 142, No. 10, 2020. , URL https://doi.org/10.1115/1.4048436, 101006.

[63] Kim, D., Druot, T. Y., and Liem, R. P., "Data-driven Operation-based Aircraft Design Optimization," *AIAA paper 2020-3156, Session Aircraft Design and Optimization, AIAA Aviation 2020 Forum, Virtual event, June 15-19, 2020*, 2020. , URL https://arc.aiaa.org/doi/abs/10.2514/6.2020-3156.

[64] Kharlamov, D., Drofelnik, J., Da Ronch, A., and Walker, S., "Rapid load calculations using an efficient unsteady aerodynamic solver," *AIAA paper 2018-3621, AIAA AVIATION Forum, 25-29 June, Atlanta, Georgia, USA*, 2018. , URL https://doi.org/10.2514/6.2018-3621.

[65] Şugar-Gabor, O., Koreanschi, A., and Botez, R. M., "A new non-linear vortex lattice method: Applications to wing aerodynamic optimizations," *Chinese Journal of Aeronautics*, Vol. 29, No. 5, 2016, pp. 1178 – 1195. , URL http://www.sciencedirect.com/science/article/pii/S1000936116300954.

[66] Paul, R. C., and Gopalarathnam, A., "Iteration schemes for rapid post-stall aerodynamic prediction of wings using a decambering approach," *International Journal for Numerical Methods in Fluids, John Wiley & Sons, Ltd.,*, Vol. 76, No. 4, 2014, pp. 199–222. , URL https://onlinelibrary.wiley.com/doi/abs/10.1002/fld.3931.

[67] Da Ronch, A., Ghoreyshi, M., and Badcock, K., "On the generation of flight dynamics aerodynamic tables by computational fluid dynamics," *Progress in Aerospace Sciences*, Vol. 47, 2011, pp. 597–620. .

[68] Choi, S., Alonso, J. J., and Kroo, I. M., "Two-Level Multifidelity Design Optimization Studies for Supersonic Jets," *Journal of Aircraft*, Vol. 46, No. 3, 2009, pp. 776–790. , URL https://doi.org/10.2514/1.34362.

[69] Piperni, P., DeBlois, A., and Henderson, R., "Development of a multilevel multidisciplinary-optimization capability for an industrial environment," *AIAA Journal*, Vol. 51, No. 10, 2013, pp. 2335–2352. .

[70] Wang, L., Xiong, C., Hu, J., Wang, X., and Qiu, Z., "Sequential multidisciplinary design optimization and reliability analysis under interval uncertainty," *Aerospace Science and Technology*, 2018. .

[71] Toal, D. J. J., "On the Potential of a Multi-Fidelity G-POD Based Approach for Optimization and Uncertainty Quantification," *Turbo Expo: Power for Land, Sea, and Air, Volume 2B: Turbomachinery, Düsseldorf, Germany. June 16-20, 2014*, Vol. 2B, No. n V02BT45A002, 2014. , URL https://doi.org/10.1115/GT2014-25184.

[72] Sgueglia, A., "Methodology for sizing and optimising a Blended Wing-Body with distributed electric ducted fans," Phd thesis, ISAE - Institut Supérieur de l'Aéronautique et de l'Espace, Dec. 2019. URL https://hal.archives-ouvertes.fr/tel-02487044.

[73] Palladino, V., Bartoli, N., Dubreuil, S., Bénard, E., Pommier-Budinger, V., Jordan, A., Schmollgruber, P., and Defoort, S., "A comparative study of different propulsion models for hybrid electric aircraft," *3AF Aerospace Europe Conference 2020, Bordeaux, France*, 2020. URL https://hal.archives-ouvertes.fr/hal-02904367.

[74] Savin, E., and Hantrais-Gervois, J.-L., "Uncertainty quantification of an aeroelastic model with sparse polynomial surrogates," *Proceedings of the 8th International Conference on Computational Stochastic Mechanics (CSM 8), 2019*, 2019. .

[75] Mines, J. M., "A bi-Level framework for aircraft design uncertainty quantification and management," Phd thesis, Georgia Institute of Technology, 2019.

[76] Jategaonkar, R. V., "Flight Vehicle System Identification: A Time-Domain Methodology, Second Edition," *Progress in Astronautics and Aeronautics,American Institute of Aeronautics and Astronautics, Inc.,1801 Alexander Bell Drive, Reston, VA 20191-4344*, Vol. 245, 2015. , URL https://doi.org/10.2514/4.102790.

[77] Allen, L., "Evolution of flight simulation," *Flight Simulation and Technologies, 09 – 11 August 1993, Monterey, CA, USA*, 1993. , URL https://arc.aiaa.org/doi/abs/10.2514/6.1993-3545.

[78] Cavagna, L., Ricci, S., and Riccobene, L., "A Fast Tool for Structural Sizing, Aeroelastic Analysis and Optimization in Aircraft Conceptual Design," *AIAA paper 2009-2571, 50th AIAA/ASME/ASCE/AHS/ASC structures, structural dynamics and materials conference. 4-7 May, Palm Springs, California*, 2009.

[79] Cavagna, L., Ricci, S., and Travaglini, L., "NeoCASS: an integrated tool for structural sizing, aeroelastic analysis and MDO at conceptual design level," *Progress in Aerospace Sciences*, Vol. 47, No. 8, 2011, pp. 621–635.

[80] Baalbergen, E., Lammen, W., Noskov, N., Ciampa, P., and Moerland, E., "Integrated collaboration capabilities for competitive aircraft design," *EASN-CEAS Conference 2018, Glasgow, UK*, 2018. URL https://www.agile4.eu/cloud/index.php/s/WyZzFLGSG9xE6N6.

[81] Torrigiani, F., Bussemaker, J., Ciampa, P., Fioriti, M., Tomasella, F., Aigner, B., Rajpal, D., Timmermans, H., Savelyev, A., and Charbonnier, D., "Design of the Strut Braced Wing aircraft in the AGILE Collaborative MDO Framework," *ICAS Conference 2018, Belo Horizonte, Brazil*, 2018. URL https://www.agile4.eu/cloud/index.php/s/kBczAEHPoqo5k67.

[82] Mieloszyk, J., and Goetzendorf-Grabowski, T., "Introduction of full flight dynamic stability constraints in aircraft multidisciplinary optimization," *Aerospace Science and Technology*, Vol. 68, 2017, pp. 252 – 260. URL https://doi.org/10.1016/j.ast.2017.05.024.

[83] MIL-F-8785CMilitarySpecification, "Flying Qualities of Piloted Airplanes," *US Military Specs/Standards/Handbooks, 5 November 1980.*, 1980.

[84] EuropeanAviationSafetyAgency, "Certification Specifications for Normal, Utility, Aerobatic, and Commuter Category Aeroplanes," *CS-23, Amendment 3, 2012*, 2012.

[85] Goetzendorf-Grabowski, T., "PANUKL potential solver, Software package," *Warsaw University of Technology*, 2020. URL http://www.meil.pw.edu.pl/add/ADD/Teaching/Software/PANUKL.

[86] Goetzendorf-Grabowski, T., "SDSA - Simulation and Dynamic Stability Analysis - software package," *Warsaw University of Technology*, 2019. URL http://www.meil.pw.edu.pl/add/ADD/Teaching/Software/SDSA.

[87] Goetzendorf-Grabowski, T., Mieszalski, D., and Marcinkiewicz, E., "Stability analysis using SDSA tool," *Progress in Aerospace Sciences*, Vol. 47, No. 8, 2011, pp. 636 – 646. , URL http://www.sciencedirect.com/science/article/pii/S037604211100073X, special Issue - Modeling and Simulating Aircraft Stability and Control.

[88] Morris, C. C., "Flight Dynamic Constraints in Conceptual AircraftMultidisciplinary Analysis and Design Optimization," *PhD Thesis, Virginia Polytechnic Institute and State University, December 4, 2013, Blacksburg, Virginia, USA*, 2013.

[89] Saussié, D., Saydy, L., and Akhrif, O., "Longitudinal flight control design with handling quality requirements," *The Aeronautical Journal,Cambridge University Press*, Vol. 110, No. 1111, 2006, p. 627–637. , URL https://doi.org/10.1017/S0001924000001494.

[90] Paulino, J. A., Da Ronch, A., Guimarães Neto, A. B., Silvestre, F. J., and Morales, M. A. V., "On real-time simulation of flexible aircraft with physics-based models," *ICAS paper 2018-501, 31st Congress of the International Council of the Aeronautical Sciences (ICAS), 09-14 September, Belo Horizonte, Brazil*, 2018.

[91] Guimarães, A. B., Silva, R. G. A., Paglione, P., and Silvestre, F. J., "Formulation of the Flight Dynamics of Flexible Aircraft Using General Body Axes," *AIAA Journal*, Vol. 54, No. 11, November 2016. .

[92] Andrews, S., "Modelling and Simulation of Flexible Aircraft: Handling Qualities with Active Load Control," *PhD Thesis, Cranfield University*, 2011.

[93] Lopez, G., and Portapas, V., "Pilot-in-the-loop simulation of flexible aircraft in MATLAB/Simulink: implementation and coding peculiarities," *AIAA paper 2018-0426, Proceedings of AIAA 2018 Modeling and Simulation Technologies Conference, 8-12 January, Kissimmee, Florida, USA*, 2018. .

[94] Su, W., and Cesnik, C. E., "Nonlinear aeroelasticity of a very flexible blended-wing-body aircraft," *Journal of Aircraft*, Vol. 47, No. 5, 2010, pp. 1539–1553.

[95] Milne, R. D., "Dynamics of the deformable aeroplane," *Her Majesty s Stationary Office TR RM 3345, London*, 1964.

[96] Hesse, H., and Palacios, R., "Reduced-Order Aeroelastic Models for Dynamics of Maneuvering Flexible Aircraft," *AIAA Journal*, Vol. 52, No. 8, 2014, pp. 1717–1732. , URL https://doi.org/10.2514/1.J052684.

[97] Kroo, I., "Drag due to lift: concepts for prediction and reduction," *Annual review of fluid mechanics*, Vol. 33, 2001, p. 587.

[98] Raymer, D. P., "Aircraft design: a conceptual approach," *American Institute of Aeronautics and Astronautics, Inc., Reston, VA*, 2012. URL https://doi.org/10.2514/4.869112.

[99] Wakayama, S., and Kroo, I., "Subsonic wing planform design using multidisciplinary optimization," *Journal of Aircraft*, Vol. 32, No. 4, 1995, pp. 746–753.

[100] Kennedy, G., Kenway, G. K., and Martins, J. R., "High aspect ratio wing design: Optimal aerostructural tradeoffs for the next generation of materials," *52nd Aerospace Sciences Meeting*, 2014, p. 0596.

[101] Conlan-Smith, C., and Schousboe Andreasen, C., "Aeroelastic Optimization of Aircraft Wings Using a Coupled Three-Dimensional Panel-Beam Model," *AIAA Journal*, Vol. 59, No. 4, 2021, pp. 1374–1386.

[102] Elsayed, M. S., Sedaghati, R., and Abdo, M., "Accurate stick model development for static analysis of complex aircraft wing-box structures," *AIAA journal*, Vol. 47, No. 9, 2009, pp. 2063–2075.

[103] Gray, A. C., and Martins, J. R., "Geometrically Nonlinear High-fidelity Aerostructural Optimization for Highly Flexible Wings," *AIAA Scitech 2021 Forum*, 2021, p. 0283.

[104] Cestino, E., Frulla, G., Spina, M., Catelani, D., and Linari, M., "Numerical simulation and experimental validation of slender wings flutter behaviour," *Proceedings of the Institution of Mechanical Engineers, Part G: Journal of Aerospace Engineering*, Vol. 233, No. 16, 2019, pp. 5913–5928.

[105] Hodges, D. H., and Pierce, G. A., *Introduction to Structural Dynamics and Aeroelasticity*, Cambridge University Press, 2002.

[106] Hassig, H. J., "An approximate true damping solution of the flutter equation by determinant iteration." *Journal of Aircraft*, Vol. 8, No. 11, 1971, pp. 885–889.

[107] Abel, I., "An analytical technique for predicting the characteristics of a flexible wing equipped with an active flutter-suppression system and comparison with wind-tunnel data," *National Aeronautics and Space Administration, Scientific and Technical Information Office*, Vol. 1367, 1979.

[108] Hounjet, M. H., "H Flutter Analysis: A Direct Harmonic Interpolation Method," *Journal of aircraft*, Vol. 46, No. 1, 2009, pp. 348–352.

[109] Gu, Y., and Yang, Z., "Modified pk method for flutter solution with damping iteration," *AIAA journal*, Vol. 50, No. 2, 2012, pp. 507–510.

[110] Megson, T. H. G., *Aircraft Structures for Engineering Students, Fifth Edition*, Elsevier Ltd., 2013.

[111] Pratt, K. G., and Walker, W. G., "A revised gust-load formula and a re-evaluation of vg data taken on civil transport airplanes from 1933 to 1950," *NASA Technical Report, NACA-TR-1206*, 1954.

[112] EuropeanAviationSafetyAgency, "Certification Specifications and Acceptable Means of Compliance for Large Aeroplanes - "Gust and turbulence loads"," *CS-25, 25.341, Amendment 27*, Dec 2021.

[113] US Federal Aviation Administration, "Airworthiness Standards: Transport Category Airplanes - "Gust and turbulence loads."," *CFR-25.341*, 2021.

[114] Fung, Y., "Fundamentals of Flutter Analysis," *An Introduction to the Theory of Aeroelasticity*, 1993, pp. 186–245.

[115] Wright, J. R., and Cooper, J. E., "Introduction to aircraft aeroelasticity and loads," *John Wiley & Sons*, Vol. 20, 2008.

[116] Tang, D., and Dowell, E. H., "Experimental and theoretical study on aeroelastic response of high-aspect-ratio wings," *AIAA journal*, Vol. 39, No. 8, 2001, pp. 1430–1441.

[117] Cavagna, L., Ricci, S., and Travaglini, L., "Aeroelastic analysis and optimization at conceptual design level using NeoCASS suite," *52nd AIAA/ASME/ASCE/AHS/ASC Structures, Structural Dynamics and Materials Conference 19th AIAA/ASME/AHS Adaptive Structures Conference 13t*, 2011, p. 2079.

[118] Drela, M., "TASOPT 2.00," *Tech. rep., Massachusetts Institute of Technology*, 2010.

[119] Seywald, K., Hellmundt, F., Wildschek, A., and Holzapfel, F., "Airworthiness investigation of a highly nonplanar flexible wing concept," *Proceedings of the 29th Congress of the International Council of the Aeronautical Sciences, St. Petersburg, Russia*, 2014, pp. 7–12.

[120] Drela, M., "ASWING 5.99 Technical Description - Unsteady Extension," *Tech. rep., Massachusetts Institute of Technology*, 2015.

[121] Drela, M., "Integrated simulation model for preliminary aerodynamic, structural, and control-law design of aircraft," *40th Structures, Structural Dynamics, and Materials Conference and Exhibit*, 1999, p. 1394.

[122] Sale, D., Aliseda, A., Motley, M., and Li, Y., "Structural optimization of composite blades for wind and hydrokinetic turbines," *Proceedings 1st Marine Energy Technology Symposium*, 2013.

[123] Lambe, A. B., and Martins, J., "A unified description of MDO architectures," *9th World Congress on Structural and Multidisciplinary Optimization, Shizuoka, Japan*, 2011.

[124] Simpson, T. W., and Martins, J. R., "Multidisciplinary design optimization for complex engineered systems: report from a national science foundation workshop," *Journal of Mechanical Design*, Vol. 133, No. 10, 2011.

[125] Bartoli, N., Lefebvre, T., Dubreuil, S., Panzeri, M., d'Ippolito, R., Anisimov, K., and Savelyev, A., "Robust nacelle optimization design investigated in the AGILE european project," *2018 Multidisciplinary Analysis and Optimization Conference*, 2018, p. 3250.

[126] Gray, J. S., Hwang, J. T., Martins, J. R. R. A., Moore, K. T., and Naylor, B. A., "OpenMDAO: an open-source framework for multidisciplinary design, analysis, and optimization," *Structural and Multidisciplinary Optimization*, Vol. 59, 2019, pp. 1075–1104. , URL https://doi.org/10.1007/s00158-019-02211-z.

[127] Yong, H. K., Wang, L., Toal, D. J., Keane, A. J., and Stanley, F., "Multi-fidelity Kriging-assisted structural optimization of whole engine models employing medial meshes," *Structural and Multidisciplinary Optimization*, Vol. 60, No. 3, 2019, pp. 1209–1226.

[128] Priem, R., Gagnon, H., Chittick, I., Dufresne, S., Diouane, Y., and Bartoli, N., "An efficient application of Bayesian optimization to an industrial MDO framework for aircraft design." *AIAA AVIATION 2020 FORUM*, 2020, p. 3152.

[129] Williams, C., and Rasmussen, C. E., "Gaussian processes for machine learning, vol. 2, no. 3," *Cambridge, MA, USA: MIT Press*, 2006.

[130] Clark, C. E., "The greatest of a finite set of random variables," *Operations Research*, Vol. 9, No. 2, 1961, pp. 145–162.

[131] Jones, D. R., Schonlau, M., and Welch, W. J., "Efficient Global Optimization of Expensive Black-Box Functions," *Journal of Global Optimization*, Vol. 13, 1998, pp. 455–492. , URL https://doi.org/10.1023/A:1008306431147.

[132] Močkus, J., "On Bayesian methods for seeking the extremum," *Optimization techniques IFIP technical conference*, 1975, pp. 400–404.

[133] Sasena, M. J., Papalambros, P., and Goovaerts, P., "Exploration of metamodeling sampling criteria for constrained global optimization," *Engineering optimization*, Vol. 34, No. 3, 2002, pp. 263–278.

[134] Priem, R., Bartoli, N., Diouane, Y., Lefebvre, T., Dubreuil, S., Salaün, M., and Morlier, J., "SEGOMOE: Super Efficient Global Optimization with Mixture of Experts," *Workshop CIMI Optimization & Learning*, 2018.

[135] Bartoli, N., Lefebvre, T., Dubreuil, S., Olivanti, R., Priem, R., Bons, N., Martins, J., and Morlier, J., "Adaptive modeling strategy for constrained global optimization with application to aerodynamic wing design," *Aerospace Science and Technology*, Vol. 90, 2019, pp. 85–102. , URL https://www.sciencedirect.com/science/article/pii/S1270963818306011.

[136] Priem, R., Bartoli, N., Diouane, Y., and Sgueglia, A., "Upper trust bound feasibility criterion for mixed constrained Bayesian optimization with application to aircraft design," *Aerospace Science and Technology*, Vol. 105, 2020, p. 105980.

[137] S., T., G., H., and T., E. G., "Uncertainpy: A Python Toolbox for Uncertainty Quantification and Sensitivity Analysis in Computational Neuroscience," *Front. Neuroinform*, 2018, pp. 12–49. .

[138] Saltelli, A., Ratto, M., Andres, T., Campolongo, F., Cariboni, J., Gatelli, D., Saisana, M., and Tarantola, S., *Global sensitivity analysis: the primer*, John Wiley & Sons, 2008.

[139] Sobol, I. M., "On sensitivity estimation for nonlinear mathematical models," *Matematicheskoe Modelirovanie*, Vol. 2, 1990, pp. 112–118.

[140] Glen, G., and Isaacs, K., "Estimating Sobol sensitivity indices using correlations," *Environmental Modelling & Software*, Vol. 37, 2012, pp. 157 – 166. , URL http://www.sciencedirect.com/science/article/pii/S1364815212001065.

[141] Saltelli, A., Annoni, P., Azzini, I., Campolongo, F., Ratto, M., and Tarantola, S., "Variance based sensitivity analysis of model output. Design and estimator for the total sensitivity index," *Computer Physics Communications*, Vol. 181, No. 2, 2010, pp. 259 – 270. , URL http://www.sciencedirect.com/science/article/pii/S0010465509003087.

[142] Homma, T., and Saltelli, A., "Importance measures in global sensitivity analysis of nonlinear models," *Reliability Engineering & System Safety*, Vol. 52, No. 1, 1996, pp. 1–17.

[143] Sobol', I. M., "On the distribution of points in a cube and the approximate evaluation of integrals," *Zhurnal Vychislitel'noi Matematiki i Matematicheskoi Fiziki*, Vol. 7, No. 4, 1967, pp. 784–802.

[144] Hammersley, J. M., "Monte Carlo methods for solving multivariable problems," *Annals of the New York Academy of Sciences*, Vol. 86, No. 3, 1960, pp. 844–874. , URL https://nyaspubs.onlinelibrary.wiley.com/doi/abs/10.1111/j.1749-6632.1960.tb42846.x.

[145] Xiu, D., "Numerical Methods for Stochastic Computations: A Spectral Method Approach," *Princeton University Press, ISBN: 9780691142128*, 2010.

[146] Sudret, B., "Global sensitivity analysis using polynomial chaos expansions," *Reliability engineering & system safety*, Vol. 93, No. 7, 2008, pp. 964–979.

[147] Crestaux, T., Le Maıˆtre, O., and Martinez, J.-M., "Polynomial chaos expansion for sensitivity analysis," *Reliability Engineering & System Safety*, Vol. 94, No. 7, 2009, pp. 1161 – 1172. , URL http://www.sciencedirect.com/science/article/pii/S0951832008002561, special Issue on Sensitivity Analysis.

[148] Clark, D. L., Allison, D. L., Bae, H., and Forster, E. E., "Effectiveness-Based Design of an Aircraft Considering Mission Uncertainties," *Journal of Aircraft*, Vol. 56, No. 5, 2019, pp. 1961–1972. , URL https://doi.org/10.2514/1.C035402.

[149] Bae, H., Clark, D. L., and Forster, E. E., "Nondeterministic Kriging for Engineering Design Exploration," *AIAA Journal*, Vol. 57, No. 4, 2019, pp. 1659–1670. , URL https://doi.org/10.2514/1.J057364.

[150] Schmollgruber, P., J. Bedouet, J., Sgueglia, A., Defoort, S., Lafage, R., Bartoli, N., Gourinat, Y., and Benard, E., "Use of a Certification Constraints Module for Aircraft Design Activities," *17th AIAA Aviation Technology, Integration, and Operations Conference, 5-9 June, Denver, Colorado*, 2017. .

[151] Lambe, A. B., and Martins, J. R., "Extensions to the design structure matrix for the description of multidisciplinary design, analysis, and optimization processes," *Structural and Multidisciplinary Optimization*, Vol. 46, No. 2, 2012, pp. 273–284.

[152] Meckstroth, C. M., and nez, R. O., "Multi-fidelity Aerodynamic Analysis for MADO S&C Analysis of Tailless Fighter Aircraft," *AIAA Aviation 2020 Forum,June 15-19, 2020, virtual event*, 2020. , URL https://arc.aiaa.org/doi/abs/10.2514/6.2020-3177.

[153] Azabi, Y., Savvaris, A., and Kipouros, T., "Initial Investigation of Aerodynamic Shape Design Optimisation for the Aegis UAV," *Transportation Research Procedia*, Vol. 29, 2018, pp. 12 – 22. , URL http://www.sciencedirect.com/science/article/pii/S2352146518300036, aerospace Europe CEAS 2017 Conference.

[154] Drela, M., and Youngren, H., "AVL 3.36," *Online page*, 2006. URL http://web.mit.edu/drela/Public/web/avl/.

[155] Bryan, G. H., "Stability in aviation," *Macmillan Co., London*, 1911.

[156] Etkin, B., *Dynamics of atmospheric flight, pp. 134-145*, Dover Publications, Inc, 1972.

[157] Stevens, B. L., Lewis, F. J., and Johnson, E., *Aircraft Control and Simulation, 3rd Edition*, John Wiley & Sons, Inc., 2015.

[158] Berndt, J. S., *JSBSim - An open source, platform-independent, flight dynamics model in C++.*, 2011.

[159] Williams, J. E., and Vukelich, S. R., "The USAF stability and control digital dATCOM. Users manual." Tech. rep., McDonnell Douglas Astronautics Co., St Louis, Mo, 1979.

[160] CeRAS, "Central Reference Aircraft Data System," *[on line database]*, 2015. URL https://ceras.ilr.rwth-aachen.de.

[161] Roux, E., "Pour un Approche Analytique de la Dinamique du Vol," *PhD Thesis, ISAESU-PAERO, Toulouse.*, 2005.

[162] Monaghan, R., "A review and assessment of various formulae for turbulent skin friction in compressible flow," *Aeronautical Research Council Tech. Rep., C.P. 142 (15.464)*, 1953.

[163] Anderson, J. D., "Fundamentals of aerodynamics - 5th edition," *McGraw-Hill*, 2011.

[164] Niţă, M., and Scholz, D., "Estimating the oswald factor from basic aircraft geometrical parameters," *German Aerospace Congress 2012, 10–12 September 2012, Berlin, Germany*, 2012.

[165] Da Ronch, A., Tantaroudas, N. D., Badcock, K. J., and Mottershead, J., "A Nonlinear Controller for Flutter Suppression: from Simulation to Wind Tunnel Testing," *AIAA paper 2014-0345, 55th AIAA/ASME/ASCE/AHS/ASC Structures, Structural Dynamics, and Materials Conference*, 2014, pp. 1–19. , URL http://arc.aiaa.org/doi/10.2514/6.2014-0345.

[166] Zhou, Q., Li, D., Da Ronch, A., Chen, G., and Li, Y., "Computational fluid dynamics-based transonic flutter suppression with control delay," *Journal of Fluids and Structures*, Vol. 66, 2016, pp. 183–206. , URL http://dx.doi.org/10.1016/j.jfluidstructs.2016.07.002.

[167] Wang, Y., Li, F., and Da Ronch, A., "Adaptive feedforward control design for gust loads alleviation of highly flexible aircraft," *Proceedings of AIAA Atmospheric Flight Mechanics Conference, Dallas, Texas, 2015*, 2015.

[168] Wang, Y., Da Ronch, A., and Ghandchi-Tehrani, M., "Adaptive feedforward control for gust-induced aeroelastic vibrations," *Aerospace*, Vol. 3, No. 86, 2018. , URL www.mdpi.com/journal/aerospace.

[169] Ghandchi Tehrani, M., Da Ronch, A., Ghandchi-Tehrani, M., and Li, E., "Adaptive feedforward control design for gust loads alleviation and lco suppression," *in: Proceedings of the 29th Congress of the International Council of the Aeronautical Sciences, St. Petersburg, Russia, 2014.*, 2014.

[170] Ghandchi Tehrani, M., and Ronch, D., "Gust load alleviation using nonlinear feedforward control," *in: Proceedings of the EURODYN IX International Con- ference on Structural Dynamics, Porto, Portugal, 2014.*, 2014.

[171] Saporito, M., "Energy harvesting from gust-induced vibrations for active aerolastic control," Master thesis, Università degli studi di Palermo, Scuola Politecnica, Corso di Laurea Magistrale in Ingegneria Aerospaziale, 2018. URL http://aleph22.unipa.it:8991/F/?func=direct&doc_number=001159859&local_base=PAL01.

[172] Jones, R. T., "The unsteady lift of a wing of finite aspect ratio," *NACA report Nr. 681 (1940)*, 1940.

[173] Leishman, J. G., "Unsteady lift of a flapped airfoil by indicial concepts," *Journal of Aircraft*, Vol. 31, No. 2, 1994, pp. 288–297. , URL https://arc.aiaa.org/doi/abs/10.2514/3.46486.

[174] Takahashi, T. T., "A Bad Moon Rising: The Puzzling Inaccuracies of the Work-Energy Theorem in Aircraft Performance," *AIAA Scitech 2019 Forum, 7-11 January 2019 San Diego, California*, 2019. , URL https://arc.aiaa.org/doi/abs/10.2514/6.2019-1305.

[175] Da Ronch, A., Badcock, K., Wang, Y., and Palacios, R., "Nonlinear Model Reduction for Flexible Aircraft Control Design," *AIAA paper 2012-4404, AIAA Atmospheric Flight Mechanincs Conference*, 2012.

[176] McDonald, R. A., "Advanced Modeling in OpenVSP," *AIAA paper 2016-3282, 16th AIAA Aviation Technology, Integration, and Operations Conference, 13-17 June 2016 Washington, D.C.*, 2016. , URL https://arc.aiaa.org/doi/abs/10.2514/6.2016-3282.

[177] Carre, A. D., Muñoz-Simón, A., Goizueta, N., and Palacios, R., "SHARPy: A dynamic aeroelastic simulation toolbox for very flexible aircraft and wind turbines," *Journal of Open Source Software*, Vol. 4, No. 44, 2019, p. 1885. , URL https://doi.org/10.21105/joss.01885.

[178] Stanford, B. K., and Beran, P. S., "Analytical Sensitivity Analysis of an Unsteady Vortex-Lattice Method for Flapping-Wing Optimization," *Journal of Aircraft*, Vol. 47, No. 2, 2010, pp. 647–662. , URL https://doi.org/10.2514/1.46259.

[179] Murua, J., Hesse, H., Palacios, R., and Graham, J. M. R., "Stability and Open-Loop Dynamics of Very Flexible Aircraft Including Free-Wake Effects," *52nd AIAA/ASME/ASCE/AHS/ASC Structures, Structural Dynamics and Materials Conference*, 2011.

[180] Papadopoulos, P., *Introduction to the Finite Element Method, Department of Mechanical Engineering, University of California, Berkeley*, 2010. URL https://www.mm.ethz.ch/CSM/FEMNotes.pdf.

[181] Yu, W., and Wang, Q., "Geometrically Exact Beam Theory," *Composites Design and Manufacturing HUB*, 2014. URL https://cdmhub.org/resources/gebt.

[182] Yu, W., and Blair, M., "GEBT: A General-Purpose Nonlinear Analysis Tool for Composite Beams," *Composite Structures*, Vol. 94, 2012, pp. 2677–2689.

[183] Wang, Q., Yu, M. A., W.and Sprague, and Jonkman, J., "Geometric Nonlinear Analysis of Composite Beams using Wiener-Milenkovic Parameters," *Proceedings of the 54th Structures, Structural Dynamics, and Materials Conference, 8-11 April 2013, Boston, Massachusetts, USA*, 2013.

[184] Murua, J., Hesse, H., Palacios, R., and Graham, J. M. R., "Stability and Open-Loop Dynamics of Very Flexible Aircraft Including Free-Wake Effects," *52nd AIAA/ASME/ASCE/AHS/ASC Structures, Structural Dynamics and Materials Conference*, 2011, pp. 1–21. , URL http://arc.aiaa.org/doi/10.2514/6.2011-1915.

[185] Hodges, D. H., Shang, X., and Cesnik, C. E., "Finite element solution of nonlinear intrinsic equations for curved composite beams," *Journal of the American helicopter society*, Vol. 41, No. 4, 1996, pp. 313–321.

[186] Goland, M., and Luke, Y., "The flutter of a uniform wing with tip weights," *American Society of Mechanical Engineers*, 1948.

[187] Patil, M. J., Hodges, D. H., and Cesnik, C. E., "Nonlinear aeroelastic analysis of complete aircraft in subsonic flow," *Journal of Aircraft*, Vol. 37, No. 5, 2000, pp. 753–760.

[188] Patil, M. J., Hodges, D. H., and Cesnik, C. E., "Limit-cycle oscillations in high-aspect-ratio wings," *Journal of fluids and structures*, Vol. 15, No. 1, 2001, pp. 107–132.

[189] Quaranta, G., Masarati, P., and Mantegazza, P., "A conservative mesh-free approach for fluid-structure interface problems," *International Conference on Computational Methods for Coupled Problems in Science and Engineering, Santorini, Greece, May 25-28, 2005*, 2005.

[190] Schaback, R., and Wendland, H., "Characterization and construction of radial basis functions," *Multivariate approximation and applications*, 2001, pp. 1–24.

[191] Schy, A. A., and Hannah, M. E., "Prediction of jump phenomena in roll-roupled maneuvers of airplanes," *Journal of Aircraft*, Vol. 14, No. 4, 1977, pp. 375–382. , URL https://doi.org/10.2514/3.58787.

[192] Roskam, J., "Airplane Design," *DAR corporation, Lawrence, Kansas, USA*, 2002.

[193] Ronch, A. D., McCracken, A. J., and Badcock, K. J., "Assessing the Impact of Aerodynamic Modelling on Manoeuvring Aircraft," *AIAA Atmospheric Flight Mechanics Conference, 13-17 January 2014, National Harbor, Maryland, USA.*, 2014. , URL https://arc.aiaa.org/doi/abs/10.2514/6.2014-0732.

[194] Schmid, P. J., "Dynamic mode decomposition of numerical and experimental data," *Journal of fluid mechanics, Cambridge University Press*, Vol. 656, 2010, pp. 5–28.

[195] Laszuk, D., "Python implementation of Empirical Mode Decomposition algorithm," *GitHub Repository*, 2017. URL https://github.com/laszukdawid/PyEMD.

[196] The SciPy Community, "Signal Processing (scipy.signal)," *SciPy.org, Jul 23, 2020*, 2020. URL https://docs.scipy.org/doc/scipy/reference/signal.html#module-scipy.signal.

[197] Lobos, T., Rezmer, J., and Schegner, J., "Parameter estimation of distorted signals using Prony method," *2003 IEEE Bologna Power Tech Conference Proceedings,*, Vol. 4, 2003, pp. 5–pp. , URL https://ieeexplore.ieee.org/abstract/document/1304801.

[198] The SciPy Community, "Curve_fit (scipy.optimize)," *SciPy.org, Jul 23, 2020*, 2020. URL https://docs.scipy.org/doc/scipy/reference/generated/scipy.optimize.curve_fit.html.

[199] MathWorks, "Signal Processing Toolbox - Perform signal processing and analysis," *Matlab products online store*, 2020. URL https://www.mathworks.com/products/signal.html.

[200] Klein, V., and Morelli, E., *Aircraft System Identification: Theory And Practice*, American Institute of Aeronautics & Astronautics, 2006. .

[201] Rifkin, R. M., and Lippert, R. A., "Notes on Regularized Least Squares," *Computer Science and Artificial Intelligence Laboratory, Technical Report (MIT-CSAIL-TR-2007-025), Massachusetts Institute of Technology, Cambridge, Ma, 02139 USA - www.csail.mit.edu*, 2007.

[202] Narayan, A., and Jakeman, J., "Adaptive Leja sparse grid constructions for stochastic collocation and high-dimensional approximation," *Cornell University [online at arXiv.org > math > arXiv:1404.5663]*, 2014.

[203] Smolyak, S. A., "Quadrature and interpolation formulas for tensor products of certain classes of functions," *Russian Academy of Sciences, Doklady Akademii Nauk*, Vol. 148, No. 5, 1963, pp. 1042–1045.

[204] Yang, D., and Liu, L., "Reliability analysis of structures with complex limit state functions using probability density evolution method," *Structural and Multidisciplinary Optimization*, Vol. 50, 2014, pp. 275–286. , URL https://doi.org/10.1007/s00158-014-1048-4.

[205] Bouhlel, M. A., Hwang, J. T., Bartoli, N., Lafage, R., Morlier, J., and Martins, J. R. R. A., "A Python surrogate modeling framework with derivatives," *Advances in Engineering Software*, 2019, p. 102662. .

[206] Saves, P., Bartoli, N., Diouane, Y., Lefebvre, T., Morlier, J., David, C., Van, E. N., and Defoort, S., "Constrained Bayesian optimization over mixed categorical variables, with application to aircraft design," *Proceedings of the International Conference on Multidisciplinary Design Optimization of Aerospace Systems (AEROBEST 2021)*, 2021, pp. 1–758.

[207] Klein, V., Murphy, P. C., Curry, T. J., and Brandon, J., "Analysis of Wind Tunnel Longitudinal Static and Oscillatory Data of the F-16XL Aircraf," *NASA TM–97–206276*, December, 1997.

[208] Pedregosa, F., Varoquaux, G., Gramfort, A., Michel, V., Thirion, B., Grisel, O., Blondel, M., Prettenhofer, P., Weiss, R., Dubourg, V., Vanderplas, J., Passos, A., Cournapeau, D., Brucher, M., Perrot, M., and Duchesnay, E., "Scikit-learn: Machine Learning in Python," *Journal of Machine Learning Research*, Vol. 12, 2011, pp. 2825–2830.

[209] Cook, M. V., *Flight dynamics principles: a linear systems approach to aircraft stability and control*, Butterworth-Heinemann, 2012.

[210] US Federal Aviation Administration, "Airworthiness Standards: Transport Category Airplanes - "Strength and deformation."," *CFR-25.305*, 2021.

[211] Burden, R., Faires, J., and Reynolds, A., "Numerical Analysis, Prindle, Weber & Schmidt, 1981," *R. Siegel and JR Howell, Thermal Radiation Heat Transfer, Hemisphere Pub. Corp*, 1981, pp. 437–450.

[212] Panettieri, E., Montemurro, M., Fanteria, D., and Coccia, F., "Multi-scale least-weight design of a wing-box through a global/local modelling approach," *Journal of Optimization Theory and Applications*, Vol. 187, No. 3, 2020, pp. 776–799.

[213] EuropeanAviationSafetyAgency, "Certification Specifications and Acceptable Means of Compliance for Large Aeroplanes - "Aeroelastic Stability requirements"," *CS-25, 25.629, Amendment 27*, Dec 2021.

[214] US Federal Aviation Administration, "Airworthiness Standards: Transport Category Airplanes - "Aeroelastic stability requirements."," *CFR-25.629*, 2021.

[215] Lee, B. H. K., Gong, L., and Wong, Y. S., "Analysis and Computation of Nonlinear Dynamic Response of a Two-Degree-of- Freedom System and its Application in Aeroelasticity," *Journal of Fluids and Structures*, Vol. 11, 1997, pp. 225–246.